HIGH-FREQUENCY ULTRASOUND IMAGING OF THE AUDITORY SYSTEM

by

Zahra Torbatian

Submitted in partial fulfillment of the requirements
for the degree of Doctor of Philosophy

at

Dalhousie University
Halifax, Nova Scotia
October 2012

DALHOUSIE UNIVERSITY

SCHOOL OF BIOMEDICAL ENGINEERING

The undersigned hereby certify that they have read and recommend to the Faculty of Graduate Studies for acceptance a thesis entitled "HIGH-FREQUENCY ULTRASOUND IMAGING OF THE AUDITORY SYSTEM" by Zahra Torbatian in partial fulfillment of the requirements for the degree of Doctor of Philosophy.

Dated: October 22, 2012

External Examiner: ____________________________________

Research Supervisors: ____________________________________

____

Examining Committee: ____________________________________

____

Departmental Representative: ____________________________________

DALHOUSIE UNIVERSITY

DATE: October 22, 2012

AUTHOR: Zahra Torbatian

TITLE: HIGH-FREQUENCY ULTRASOUND IMAGING OF THE AUDITORY SYSTEM

DEPARTMENT OR SCHOOL: School of Biomedical Engineering

DEGREE: PhD CONVOCATION: May YEAR: 2013

Signature of Author

To my parents, Maryam & Mehdi

and my lovely sister, Sara

TABLE OF CONTENTS

LIST OF FIGURES

ABSTRACT

Current technology used to diagnose hearing disorders is limited. This is mostly due to the fact that the auditory structures are very small and not easily accessible with existing imaging technologies. The objective of this dissertation was to investigate the potential of high-frequency ultrasound as a tool for exploring the anatomy of the auditory system. Three studies were conducted in order to demonstrate the feasibility of high-frequency ultrasound as a diagnostic technology for hearing disorders.

In the first study, an in-house developed 50 MHz annular array-based ultrasound system was used to provide ex-vivo images of auditory structures in cadaveric temporal bones. It was shown that the spatial resolution was sufficient to visualize a high level of detail of the ossicular bones of the middle ear as well as intra-cochlear structures of the inner ear. In the second study, a 50 MHz 1.26λ pitch phased array ultrasound transducer was designed for imaging intra-cochlear structures through the round window membrane. As this element pitch results in large grating lobe artifacts, novel transmit beamforming techniques were developed to suppress grating lobes resulting from this large-pitch array. Theoretical techniques using the impulse-response simulation method and experimental verification using high-frequency linear array ultrasound system (Vevo 2100, VisualSonics, Canada) showed that these techniques were able to suppress grating lobe levels up to 40 dB. In the third study, a needle mounted 45 MHz single-element ultrasound probe was fabricated in order to measure the vibrations of intra-cochlear structures on human cadavers. Basilar membrane velocimetry measurements were successfully performed using pulsed-wave Doppler ultrasound in the frequency range between 100 Hz-2 KHz. The measured velocity of the basilar membrane and the round window membrane showed that the middle ear resonance frequency near 1 KHz was present over multiple temporal bones. This is the first work that has explored the human auditory system with high resolution ultrasonic visualization and Doppler velocimetry.

LIST OF ABBREVIATIONS AND SYMBOLS USED

Abbreviation/Symbol	Description	Unit
AAOHNS	American Academy of Otolaryngology Head and Neck Surgery	-
ABR	Auditory Brainstem Response	-
A/D	Analog to Digital	-
A	Peak of normal velocity	m/s
$a(t)$	Envelope of the echo	V
BM	Basilar Membrane	-
BW	BandWidth	Hz
b_i	Sign bit of the echo	-
BW	-6 dB bandwidth	Hz
BW_{FWHM}	Bandwidth of full width at half maximum	Hz
$\mathrm{BW}_{\mathrm{3dB}}$	3 dB beamwidth (lateral resolution)	m
CAP	Compound Action Potential	V
CF	Characteristic Frequency	Hz
CHL	Conductive Hearing Loss	-
CM	Cochlear Microphonic	V
CMUT	Capacitive Micromachined Ultrasonic Transducer	-
CT	Computed Tomography	-
CW	Continuous Wave	-
c	Speed of sound in the medium	m/s
c_b	Speed of sound in blood	m/s
c_p	Velocity of the sound in the piezoelectric transducer	m/s
$[c^{\zeta}]$	Stiffness matrix	N/m
DOCT	Doppler Optical Coherence Tomography	-
DOF	Depth Of Field	m
DPOAE	Distortion-Product Otoacoustic Emission	-

Abbreviation/Symbol	Description	Unit
d	Thickness of the piezoelectric transducer	m
d	The virtual point depth considered at the back of transducer	m
d_{max}	Maximum displacement of the membrane	m
d_{33}	Piezoelectric coefficient	C/N
D	Diameter of the transducer (Full transducer aperture)	m
$[D]$	Electric displacement matrix	C/m^2
ECoG	Electrocochleaography	-
$[e]$	Piezoelectric stress matrix	Pa
FFT	Fast Fourier Transform	-
FIR	Finite Impulse Response	-
FOV	Field of View	-
FPGA	Field Programmable Gate Arrays	-
FWHM	Full Width at Half Maximum	-
f	Frequency	Hz
f_a	Anti-resonance frequency	Hz
f_d	Doppler shift	Hz
f_r	Resonance frequency	Hz
f_s	Sampling frequency	Hz
f_{stim}	Acoustic stimulation frequency	Hz
f_u	Ultrasound pulse center frequency	Hz
f_1, f_2	Two-tone frequencies	Hz
F	f-number	-
$f(r, t)$	Source vibration force	N
GUI	Graphical User Interface	-
g_{33}	Piezoelectric coefficient	Vm/N
$h(r, t)$	Impulse-response	-
IHC	Inner Hair Cell	-
I-Q	In phase-Quadrature	-
$I(t), Q(t)$	In-Phase, Quadrature components of the echo	V
k_{eff}	Effective electromechanical coupling	-
k_t	Electromechanical coupling	-
K	Number of splits for transmit aperture	-

Abbreviation/Symbol	Description	Unit
LDV	Laser Doppler Vibrometer	-
LPF	Low Pass Filter	-
LUT	Look Up Table	-
l	Thickness of matching layer	m
$L1, L2, L3$	Distances between the grating lobe point and the points on the virtual curved aperture	m
MD	Meniere's Disease	-
MRI	Magnetic Resonance Imaging	-
m_1, m_2, m_r	Signal amplitude	V
M	Length of recorded echoes at each PRF	-
n	Integer	-
n_s	Number of sub-arrays	-
N	Number of elements	-
OAE	Otoacoustic Emission	-
OCT	Optical Coherence Tomography	-
OHC	Outer Hair Cell	-
OSL	Osseous Spiral Lamina	-
PC	Personal Computer	-
PCI	Phase Coherence Imaging	-
PMN-PT	Lead magnesium niobate-lead titanate	-
PRF	Pulse Repetition Frequency	Hz
PVDF	Polyvinylidene fluoride	-
PW Doppler	Pulsed Wave Doppler	-
PZT	Lead zirconate titanate	-
p	Inter-element pitch	m
$p(r,t)$	Wave pressure	Pa
P_i	Pressure of incident wave	Pa
P_r	Pressure of reflected wave	Pa
$p_{rec}(r,t)$	Receive pressure pulse	Pa
P_{tr}	Pressure of transmitted wave	Pa
$p_{tr}(r,t)$	Transmit pressure pulse	Pa
PRF	Pulse repetition frequency	Hz

Abbreviation/Symbol	Description	Unit
RF	Radio Frequency	Hz
RWM	Round Window Membrane	-
r	Radius between a spatial point and the center of transducer	m
R	Focal radius	m
$R_j(n)$	Cross-correlation between successive echoes	-
R_s	Distance between a point on the transducer and a spatial point	m
Rx(t)	Receive echo	V
SCF	Sign Coherence Factor	-
SNHL	Sensorineural Hearing Loss	-
SNR	Signal-to-Noise Ratio	-
SP	Summating Potential	V
SPL	Sound Pressure Level	dB
S	Surface of the transducer	m^2
$[S]$	Strain matrix	-
SCF^α	Sign coherence factor	-
TM	Tympanic Membrane	-
TOAE	Transient Otoacoustic Emission	-
t	Time	s
t_{PRI}	Pulse repetition interval	s
$\triangle t_j$	Time shift between successive echoes	s
$[T]$	Stress matrix	Pa
T_I	Transmission intensity coefficient	-
Tx(t)	Transmit pulse	V
v_b	Blood cell velocity	m/s
$v_e(t)$	Echo	V
$max(\triangle v_j)$	Maximum velocity of the membrane echo	m/s
v_m	Velocity of moving object	m/s
v_{m-max}	Upper limit on the measurable velocity of the moving object	m/s
$v(r,t)$	Particle velocity	m/s
$v_{no}(t)$	Normal surface velocity of the transducer	V
$V_{PRF}(t,i)$	Instantaneous echogram amplitude at i th PRF	V

Abbreviation/Symbol	Description	Unit
$velocity_{pk-pk}$	Peak to peak velocity of the membrane	m/s
WBER	Wide-Band Energy Reflectance	-
w_e	Element width	m
W	Bandwidth	Hz
x, y, z	Cartesian coordinate unit vectors	m
(x_{fp}, z_{fp})	Coordinate of the focal point	m
$(x_i, 0)$	Coordinate of the i th element	m
x_j	Echo recorded at j th PRF	V
$\triangle x_j$	Displacement of the membrane echo	m
(x_o, z_o)	Origin of the array transducer	m
x_0	Element for splitting the aperture	-
z_p	Focal depth	m
Z	Acoustic impedance of the material	Rayl
Z_i	Acoustic impedance of incident medium	Rayl
Z_r	Acoustic impedance of reflecting medium	Rayl
Z_{01}	Acoustic impedance of transducer	Rayl
Z_{02}	Acoustic impedance of matching layer	Rayl
Z_{03}	Acoustic impedance of the tissue	Rayl

Greek symbol	Description	Unit
α	Sensitivity factor for SCF calculation	-
α_d	Angle between transmit and receive transducers	rad
$[\epsilon^S]$	Permittivity matrix	F/m
${\epsilon_{33}}^S/\epsilon_0$	Relative dielectric constant	-
$[\zeta]$	Electric field matrix	N/C
θ	Grating lobe angle versus the center of transducer array	rad
θ_d	Angle between ultrasound probe and the vessel	rad
θ_m	Angle between the probe and the moving object	rad
Θ	Grating lobe angle	rad
λ	Wavelength	m
ρ	Density of the material	kg/mm^3
σ	Standard deviation of sign-bits	-
σ_W	Standard deviation of the Gaussian function	Hz
τ_i	Applied delay for array element i	s
τ_r	Time-shift of Gaussian function	s
τ_{ti}	Beamforming delay to generate defocused pulse	s
$\phi(r,t)$	Velocity potential	m^2/s
$\phi_a(t)$	Time dependent phase of the echo	rad
Φ	Phase of the echo	rad
Φ_d	Phase difference between received echo and transmitted pulse	rad

ACKNOWLEDGEMENTS

I would like to thank sincerely from my co-supervisors, Dr. Jeremy Brown and Dr. Manohar Bance for their constructive supervision and enormous support during my PhD. This work was not possible without knowledge and guidance of Dr. Brown. In these years, I had the opportunity to have access to the facilities in the microfabrication lab and ear-lab in order to complete my study. I thank my supervisory committee, Dr. Geoff Maksym and Dr. Kamal El-Sankary for their positive guidance. I am very grateful to Dr. Rob Adamson whose scientific support was essential in my PhD. I am thankful to Dr. Phil Garland whose assistance and support was very effective in this period. I would like to thank individuals of microfabrication lab and ear-lab especially Andre Bezanson, Craig Arthur, Dr. Akhilesh Kotiya, Michael Leung, and Helga Ross for their collaboration and assistance. I am very grateful to the engineers at VisualSonics Inc. especially Jim Mehi, Andrew Needles, and Stanley Poon for their help and support. I would like to thank the staff and colleagues at School of Biomedical Engineering especially Sandy Mansfield and Sandra Pereira for their kind support during my PhD study. I could not survive the grey days in this period without huge kindness of my lovely sister, Sara. Finally, many thanks to my lovely friends Glareh, Zhila, Helga, Ehsan, Sina, and Mohammad who greatly supported me emotionally in these years.

CHAPTER 1

INTRODUCTION

Currently, there are no truly accurate diagnostic tools available for hearing disorders. These disorders are diagnosed primarily based on symptoms described by the patient, the threshold of hearing measured by an audiometric test, middle ear acoustic impedances, and the status of external ear canal and tympanic membrane visualized through an optical microscope (*Bess and Humes*, 2003; *Couzos et al.*, 2001; *Dalebout*, 2008). These tests, however, do not provide enough information to differentiate between a wide variety of pathologies. Moreover, the small structures of the auditory system cannot be properly visualized using current imaging techniques such as computed tomography (CT) or magnetic resonance imaging (MRI), which only possess between 0.5 and 1 mm spatial resolution (*Vassiliou et al.*, 2011).

The aim of this dissertation was to develop new technologies that could potentially be used for exploring the auditory system in-vivo with much higher image resolution. The first focus of this thesis was the preliminary development of an ultrasound imaging tool for in-vivo visualization of the auditory structures with high spatial resolution. The thesis shows proof of concept that such a device is feasible as long as a novel signal processing algorithm is applied. Such an imaging tool could be used in clinics as a diagnostic tool for real-time monitoring of the auditory system. The second focus of this thesis was to develop a velocimetry technique for measuring the dynamics of intra-cochlear structures, which could potentially provide valuable diagnostic information and be incorporated into the imaging probe. Direct measurements of the auditory system could remove many of the inaccuracies incurred with the perceptual nature of conventional audiometric tests.

1.1 Motivation

Hearing loss is a rapidly growing disorder, affecting both children and adults. According to the 2006 Statistic Canada Participation and Activity Limitation Survey report (*Statistics Canada PLAS*, 2006), more than one million Canadian adults (about 5% of the population) are suffering from different types of hearing disabilities. The annual economic burden of hearing loss in Canada is estimated at about 18-billion dollars (*The Hearing Foundation of Canada*, 2010). Hearing disorders are also a big concern in the United States where 1 in 10 people suffer from hearing impairment as well as in Europe, where about 16% of the adult population is affected by hearing loss (*Shield*, 2006; *Dalebout*, 2008). Unfortunately, the available diagnostic tools in this field are relatively crude and for the most part indirect. They do not have high accuracy, with both limitations of low sensitivity and high false positive rates.

Hearing disorders may be the result of damage to the structures within the middle ear or the inner ear (*Bess and Humes*, 2003). These auditory structures are very small and difficult to access. This introduces obvious challenges for clinicians trying to accurately diagnose the main causes of impairment. Currently, microscopic otoscopy is used in clinics to examine the ear for possible causes of impairment. However, since the tympanic membrane is not transparent, or at best semi-transparent, physicians cannot visualize beyond this membrane due to its optical scattering properties (*Dalebout*, 2008). On the functional level, audiometry is a popular technique used to evaluate the level of hearing in patients (*Bess and Humes*, 2003). Although it is helpful to differentiate impairments associated with the middle ear from those of the inner ear, the root source of the disorder cannot be detected. Various other physiological and physical tests have been developed specifically for the middle ear (eg. tympanometry, wide-band reflectance) and the inner ear (eg. brainstem auditory evoked response, electrocochleography, otoacoustic emission). In all of these objective measurement techniques, signals are generated within or reflected from the auditory system in response to a stimulus. They are then recorded and analyzed to characterize and delineate the damaged structure (*Burkard et al.*, 2007). Several studies have shown that no specific signal pattern could be assigned with high confidence to a known hearing disorder, mostly because there are large signal variations within the healthy subject population and the patient population (*Burkard et al.*, 2007). Moreover, these tests are indirect indicators of functionality of the auditory system that might be affected by different parameters involved in the system set-up, or by a combination of more than one pathology contributing to the hearing loss. Often, they point to a range of disorders rather than a specific disorder.

In-vivo visualization of the micro-scale structures within the auditory system would obviously be the most reliable method for the diagnosis of hearing disorders, especially if the structures can be examined in real-time. Unfortunately, the currently available imaging techniques such as magnetic resonance imaging (MRI) and computed tomography (CT) do not offer sufficient resolution for clear visualization of the middle ear structures (ossicles, ligaments, and spaces) and the inner ear components (the cochlear ducts, vestibular organs, membranes, and vasculature) (*Vassiliou et al.*, 2011). The focus of first part of this dissertation was on developing a high-resolution imaging technique that could potentially be used for visualizing the auditory structures in-vivo.

The cochlea is a snail-shaped structure with complex mechanics and is the part of the inner ear responsible for hearing. It houses an essential hearing component called the basilar membrane, along which the travelling wave is decomposed into its fundamental frequencies when the membrane is displaced, triggering action potentials in the auditory nerve and producing the perception of sound (*Møller*, 2006). Measuring the motion of the basilar membrane in-vivo could potentially be used to diagnose inner ear disorders such as Meniere's Disease which can affect the mechanics of this membrane (*Salt and Plontke*, 2010). Laser Doppler vibrometer is currently the standard technique used to measure the vibration of basilar membrane in ex-vivo/in-vivo animal studies (*Robles and Ruggero*, 2001), however, it is not practical for in-vivo application in humans because the cochlea needs to be surgically opened in order to place reflective beads on the membrane for improved reflectivity. The focus of second part of this dissertation was to develop a new technique for measuring the dynamics of basilar membrane motion that would be practical for in-vivo diagnostics (ie. without damaging the cochlea).

Ultrasound imaging with operating frequencies less than 10 MHz is commonly used in clinical practice as a diagnostic tool for non-invasively generating real-time images of internal physiologic structures. This modality is cost-effective, fast, real-time, and safe in comparison with MRI or CT. In order to resolve finer structures, the resolution of ultrasound images can be improved by increasing the transducer frequency at the cost of reducing penetration depth (*Bushberg*, 2002).

High-frequency ultrasound imaging (>20 MHz) has proven to be an effective high-resolution imaging tool for the posterior portion of the eye, the skin, the vascular system (intravascular imaging), and in small animals for biological studies (*Lockwood et al.*, 1996; *Foster et al.*, 2000). Conventionally, high-frequency ultrasound systems have been based on a single-element transducer which is translated mechanically in order to capture 2D image space (*Foster et al.*, 2000). This is not desirable for applications where a high-frame rate, large depth of field, and small probe profile are desired. The frame-rate and depth-of-field can be increased by moving to an array-based imaging system. Development of high-frequency array-based ultrasound systems however is challenging because fabrication of small size arrays and implementation of high-speed electronic beamformers are very difficult (*Brown*, 2005). Despite these issues, successful development of high-frequency linear array and annular array ultrasound systems are reported in multiple studies, which have shown promising results in small animal imaging and ophthalmic imaging (*Brown et al.*, 2004b, 2007; *Cannata et al.*, 2006). Moreover, the first commercially available high-frequency linear array ultrasound system (Vevo 2100, VisualSonics, ON, CA) was released to the market in 2008 for pre-clinical studies (*Foster et al.*, 2009). The number of clinical applications for this high-resolution imaging modality is still growing. In addition to high-frequency imaging, high-frequency pulsed-wave Doppler ultrasound has also been shown to be an effective technique for measuring blood velocity within small micro-vasculature (*Christopher*, 1998; *Lockwood et al.*, 1996).

As mentioned previously, currently no real-time imaging technique is available for visualizing the auditory system. The middle ear is enclosed by the tympanic membrane and the inner ear is embedded deep inside the temporal bone, and from the middle ear side, is only accessible through two openings: the oval window and the round window (*Møller*, 2006). Moreover, since the auditory structures are very small (<100 μm), high-resolution imaging is required for proper visualization of the anatomy, the physiology, and the pathophysiology. Considering the growing success of high-frequency ultrasound imaging in its ability to visualize sub-surface micro-scaled structures, the first aim of this thesis was to investigate the feasibility of high-frequency ultrasound in capturing high-resolution images of these very small auditory structures. The second goal of this dissertation was to design a high-frequency ultrasound transducer specifically for imaging the inner ear through the round window, and make the probe practical for in-vivo imaging.

The main reason that no technique is currently available for clinical measurements of basilar membrane vibrations is because it has been conventionally required that the cochlea be opened in order to have direct access to basilar membrane, with substantial risk of hearing loss resulting. Because of the effectiveness of high-frequency pulsed-wave Doppler ultrasound in measuring blood velocity within small vessels non-invasively, the third goal of this research was to investigate the potential of high-frequency pulsed-wave Doppler in measuring the vibration of the basilar membrane through the round window, without damaging the cochlea. The success of this approach would again demonstrate the potential as an in-vivo diagnostic tool.

1.2 Research Objectives and Hypotheses

The overall objective of this dissertation was to investigate the feasibility of high-frequency ultrasound for exploring the auditory system in a form factor practical as a minimally invasive clinical tool. To achieve this objective, three independent but related studies were designed and conducted.

Study One-Ex-vivo High Frequency Ultrasound Imaging of the Auditory System

In this study, it was hypothesized that high frequency ultrasound could offer sufficient resolution for visualising the small structures within the middle ear and the inner ear. To test this hypothesis, a previously developed high-frequency annular array ultrasound system was used to image auditory structures of cadaveric temporal bones (*Brown*, 2005). In separate experiments, the individual ossicles, the middle ear structures across the tympanic membrane, and the intra-cochlear structures through the round window were imaged.

Study Two-Design of a High-frequency Ultrasound Transducer for In-vivo Imaging of the Inner Ear

The first study showed that the intra-cochlear structures such as the basilar membrane could be visualized through the round window opening with high-frequency ultrasound. However, available high-frequency imaging transducers are not suitable for in-vivo intra-cochlear imaging because of the large size of their packaging/aperture. In the second study, it was hypothesized that an endoscopic ultrasound probe could be developed for in-vivo imaging of the inner ear with minimally invasive procedure. Therefore, the objective of this study was to design a high-frequency ultrasound transducer which would be suitable for in-vivo intra-cochlear imaging through the round window using current transducer fabrication technology. The optimized design of the proposed array was empirically determined by simulating the radiation profiles of transducers with different parameters. Moreover, effective techniques for suppressing grating lobes resulting from arrays with large inter-element spacing (pitch) were developed theoretically and tested experimentally in order to show that such an array could be manufactured using established array fabrication technology.

Study Three-Measuring the Vibration of Basilar Membrane using High-frequency Pulsed-wave Doppler Ultrasound

The first study showed that the basilar membrane could be visualized through the round window without damaging the cochlea. This led to to the third study where the objective was to use a high-frequency pulsed-wave Doppler technique for measuring the vibration of basilar membrane without opening the cochlea. It was hypothesized that this technique would be able to detect the motion of the basilar membrane while the ear canal was stimulated acoustically. To test this, a high-frequency single-element needle-mounted transducer was fabricated and a Doppler system was developed in order to collect Doppler information from cadaveric temporal bones.

1.3 Dissertation Structure

In chapter 1 of the dissertation, the problem definition is first introduced; that current diagnostics in otology are relatively crude. The proposed solution to this problem is the development of new high resolution ultrasonic imaging technology specifically for imaging the auditory system. The three research studies described in chapters 3, 4, and 5 to demonstrate the feasibility of high frequency ultrasound for imaging the auditory system, are summarized. Lastly, the dissertation structure and author contribution are laid out.

In chapter 2, the background literature relevant to this dissertation is presented. Literature specific to the anatomy of the ear, the mechanics of the cochlea, common hearing disorders, available diagnostic tools and their shortcomings, and background on high-frequency ultrasound technology and grating lobe suppression techniques are reviewed.

In chapter 3, the motivation behind study one is described as well as the experimental methods, results and discussion. This study resulted in an original manuscript entitled ”Ex-vivo High-frequency Ultrasound Imaging of the Auditory System” authored by Dr. Jeremy

Brown, co-authored by Zahra Torbatian, Rene Van Wijhe, Dr. Manohar Bance, published in journal of Ultrasound in Medicine and Biology 2009. Chapter three is modified version of this publication with additional details surrounding the experiment (*Brown et al.*, 2009; *Torbatian et al.*, 2009).

In chapter 4, the motivation behind study two, the proposed design and experimental results are presented and discussed. The theoretical component to this study resulted a scientific paper entitled ”A Split-Aperture Transmit Beamforming Technique with Phase Coherence Grating Lobe Suppression”, published in IEEE in Ultrasonics, Ferroelectrics and Frequency Control 2010. The experimental component to this study has recently resulted in a scientific manuscript entitled ”Experimental Verification of Pulse-Probing Technique for Improving Phase Coherence Grating Lobe Suppression” submitted for publication. Both papers are authored by Zahra Torbatian, and co-authored by Drs Rob Adamson, Manohar Bance, and Jeremy Brown. This chapter combines both of these manuscripts along with additional details surrounding the theory and experimental set-up (*Torbatian et al.*, 2010, 2011a,b, 2012a).

In chapter 5, the motivation behind study three, the experimental set-up, transducer fabrication, and experimental results are presented and discussed. This study resulted in an original manuscript entitled ”Listening to the Cochlea With High-Frequency Ultrasound” authored by Zahra Torbatian, co-authored by Drs Phil Garland, Rob Adamson, Julian Savage, Manohar Bance, and Jeremy Brown. This manuscript is currently published online and the print article is scheduled for the October 2012 issue of the journal of Ultrasound in Medicine and Biology. This chapter is a modified version of the manuscript that contains more details surrounding the experimental set-up and interpretation of results (*Torbatian et al.*, 2012b).

In chapter 6, a general discussion is provided to conclude the key results of three studies and the future directions are highlighted.

Appendix A is related to study two (chapter 4) which includes the math behind the split-aperture transmit beamforming technique (appendix A.1), and the recipe for making the in-house tissue-mimicking phantom used in experiments of this dissertation (appendix A.2).

Appendix B is related to study three (chapter 5) which includes information about the required phase correction for ER-7 probe microphone.

Appendix C includes the code which was developed for study two and study three of this dissertation. The first section includes the MATLAB code developed for study two used to design the proposed high-frequency phased array ultrasound transducer for auditory imaging (appendix C.1.1) and the code used to test the proposed grating lobe suppression techniques theoretically (appendices C.1.2, C.1.3). The MATLAB code for offline processing of the experimental data collected to verify the proposed grating lobe suppression techniques, using the Vevo 2100 high frequency imaging system is included in appendices C.2.1, C.2.2. The third section (appendix C.3) includes the MATLAB code developed for study three to capture and process the Doppler data.

Appendix D includes the copyright permission letters for the use of published manuscripts and figures in this dissertation.

The authors of the manuscripts included within this dissertation were involved in different stages of this research. I was mainly responsible for defining the hypothesis, designing the experiments, data collection, data analysis,and interpretation of the results for each study. I was the first author of all manuscripts presented in this dissertation except study one (*Brown et al.*, 2009).

1.4 Contribution

In study one (chapter 3), I was responsible to formulate the hypothesis, recode the the available high-frequency imaging system, set-up the experiments, collect the data, reconstruct 3D images using Osirix, and interpret the results. A journal paper was prepared by my supervisor Dr. Jeremy Brown based on these findings and accepted to Ultrasound in Medicine and Biology (*Brown et al.*, 2009). Besides that, a proceeding was prepared by me and published and presented in IEEE International Ultrasonics Symposium 2009 (*Torbatian et al.*, 2009). The other authors helped in preparing the temporal bones and editing the papers.

In study two (chapter 4), I was responsible to develop all necessary codes for simulating the radiation patterns of phased array transducers with conventional transmit beamforming and along with phase coherence imaging technique. I figured out the deficiency of phase coherence imaging for suppressing grating lobes of large-pitch phased arrays through simulation investigations and I was involved in formulating the split aperture and pulse probing techniques. For theoretical validation, I was responsible to develop necessary codes in order to simulate these techniques. I developed wire phantoms and tissue phantoms in the lab for imaging. To collect data for experimental validation, I was responsible to learn how to reprogram Vevo 2100 using engineering mode and automate the procedure using script coding. It was my responsibility to develop codes to import and process the experimental data offline. I interpreted the results and prepared 2 journal papers and 3 proceeding papers based on them. The theoretical verification results are published as a journal paper in IEEE Ultrasonics, Ferroelectric, and Frequency Control (*Torbatian et al.*, 2010) and published and presented as a proceeding paper in SPIE Medical Imaging 2011 (*Torbatian et al.*, 2011a). The experimental results are published and presented as two proceeding papers in IEEE International Ultrasonics Symposium 2011, 2012 (*Torbatian et al.*, 2011b, 2012a) and submitted as a journal paper to IEEE Ultrasonics, Ferroelectrics, and Frequency Control. Other authors collaborated in interpreting the results and editing the papers.

For study three (chapter 5), I was responsible to formulate the hypothesis, fabricate the probe, set up the experiment, and develop necessary codes to collect data and automate the procedure. Then I was in charge of processing, analyzing, and interpreting the data. I prepared a journal paper based on findings of this part which is accepted to journal of Ultrasound in Medicine and Biology (*Torbatian et al.*, 2012b). Other authors collaborated in interpreting the results and editing the papers.

CHAPTER 2

REVIEW OF RELEVANT LITERATURE

2.1 The Auditory System and Current Diagnostic Technology

2.1.1 Anatomy of the Ear

The ear is a complex sensory organ which can be divided into three main sections: the outer ear, the middle ear, and the inner ear (figure 2.1). The outer ear includes the pinna and the external ear canal. The middle ear consists of the eardrum (tympanic membrane (TM)) and three small bones called ossicles (malleus, incus, and stapes). External pressure waves (sounds) reach the eardrum, and are transmitted via vibrations of the middle ear ossicles (malleus, incus, then stapes) into the oval window at the base of the inner ear cochlea. The inner ear consists of the cochlea, a sensory organ for hearing, and the vestibular system (the otoliths and three semi-circular canals), which is responsible for the balance (*Møller*, 2006). It is embedded deep inside the temporal bone which is one of the hardest bones in the body. The cochlea is a small snail-shaped structure which is divided into three fluid-filled canals: scala tympani, scala vestibuli, and scala media (cochlear duct). The scala media is separated from the scala tympani by the basilar membrane (BM) and from the scala vestibuli by the Reissner's membrane. The pressure difference between scala tympani and scala vestibuli, displaces the basilar membrane (*Møller*, 2006). The cross-section of the cochlea with these structures is shown in figure 2.2. The scala media is filled with a fluid called *endolymph* while the scala vestibuli and scala tympani contain *perilymph*. The ion composition of endolymph is similar to the intracellular fluid (rich is potassium and low in sodium) while perilymph is similar to the extracellular fluid (rich in sodium and low in potassium). The footplate of stapes is attached to one end of the cochlea (scala vestibuli) at the oval window, to allow the transfer of the mechanical vibrations into the perilymph

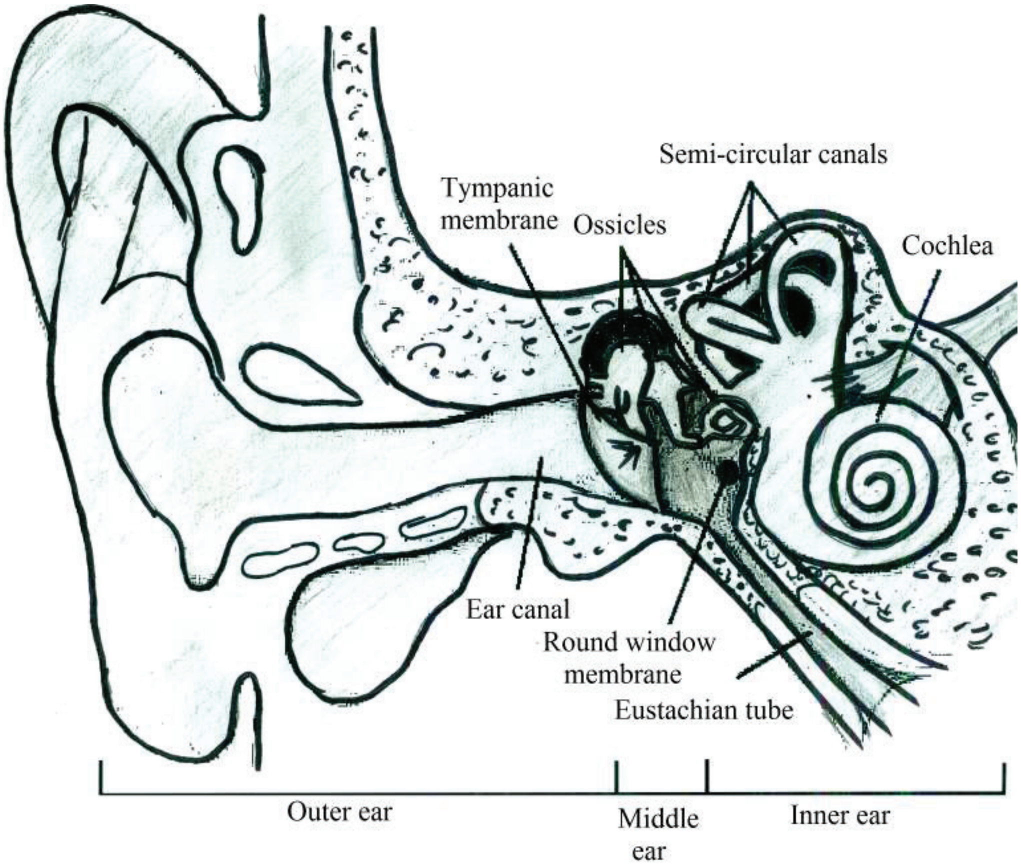

Figure 2.1: Anatomy of the ear (Redrawn from *Ear Anatomy*).

fluid. Perilymph is an incompressible fluid, so the round window membrane (RWM) on the other side of the cochlea (scala tympani) acts as a pressure release valve. Within the scala media is the *organ of Corti* which contains hair cells. The inner hair cells (IHC) and outer hair cells (OHC) are situated on the basilar membrane and their stereocilia are intimately associated with the tectorial membrane. The outer hair cells act as amplifiers by actively increasing vibrations of the basilar membrane for low intensity sounds while the inner hair cells convert mechanical vibrations into electrical impulses to trigger auditory nerves (*Møller*, 2006; *Dalebout*, 2008; *Robles and Ruggero*, 2001). With BM vibrations, there is a shearing between the reticular lamina at the apex of the organ of Corti and the tectorial membrane, which acts to tilt the stereocilia of the hair cells. When they are tilted, ionic channels in the hair cell membrane are opened, hair cells are depolarized, and action potentials are generated in the auditory nerve fibers which are carried to the brain for processing (*Møller*, 2006; *Dalebout*, 2008; *Robles and Ruggero*, 2001).

2.1.2 Mechanics of the Cochlea

Humans can hear sounds in the frequency range of 20 Hz to 20 KHz, at least in childhood, with sound pressure level (SPL) up to 120 dB (*Møller*, 2006). The large range of frequency

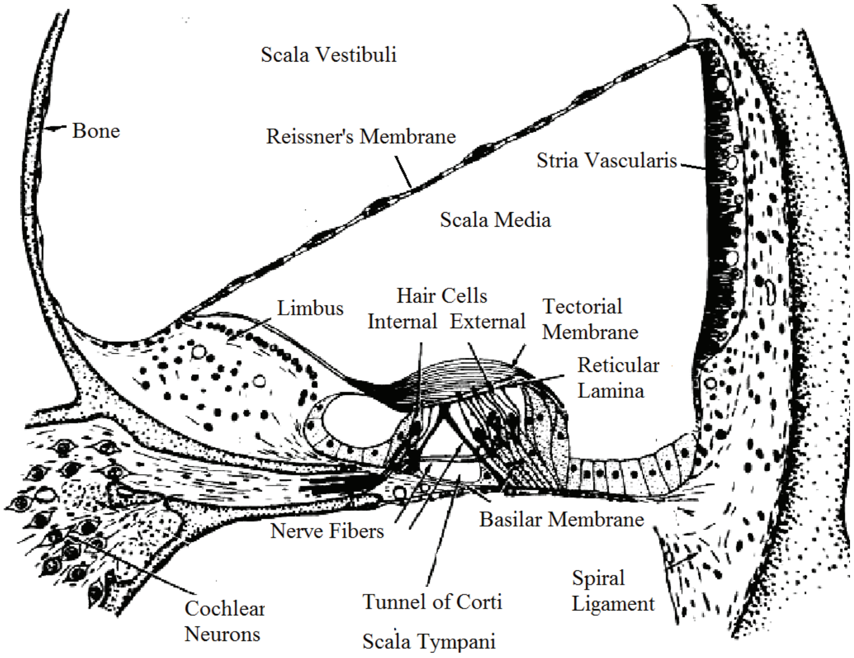

Figure 2.2: A cross-section of the cochlea (*Davis* (1962), with permission of the Journal of the Acoustical Society of America).

and intensity is dependent on the mechanical and biophysical process in the cochlea. The basilar membrane is the primary transducing mechanical structure within the cochlea. It is where the sound is decomposed into its constituent frequencies, and the site where the auditory nerves are stimulated (*Møller*, 2006; *Robles and Ruggero*, 2001). While hearing loss can be caused by damage to the sensory structures themselves (i.e. inner hair cells, auditory nerve), any deficiency in the mechanical vibrations of the basilar membrane can also result in sensorineural hearing loss (SNHL). Indeed, many pathologies primarily affect the outer hair cells, which are involved with amplifying mechanical vibrations of the basilar membrane. Several studies on cadaveric temporal bones and animal models have focused on discovering the mechanical characteristics of this membrane which are quite complex.

The first measurements of basilar membrane vibrations were performed by von Bekesy on human cadavers, using a stereoscopic microscope for which he was awarded the Nobel prize in 1961 (*Von Békésy*, 1960). He showed that the cochlea acts as a Fourier analyzer, mapping frequencies along the longitudinal position of the BM. In other words, each location along the BM resonates at a different frequency, called characteristic frequency (CF). The CF location of high frequencies are at the base of the cochlea while the low frequency region is located at the apex of the cochlea (*Robles and Ruggero*, 2001). A tonopic cochlear map has been defined in the literature based on in-vitro measurements of the CF at various BM sites (CF-to distance mapping). Bekesy also described that a displacement 'travelling wave' moves along the BM from base to apex which grows in amplitude until it reaches to a maximum at the location corresponding to the CF, and then decays in amplitude. In 1971, Rhode discovered a compressive nonlinearity of the basilar membrane using the Mossbauer technique in live squirrel monkeys (*Rhode*, 1971). He showed that the nonlinearity was mostly present near the CF and that it disappeared after death. Later, the presence of this nonlinearity was confirmed with more accurate measurements performed by Laser Doppler Vibrometer (LDV) (*Robles and Ruggero*, 2001).

The mechanics of the BM are better known at the basal turn in the literature because it is more accessible. The basal turn can be accessed through the scala tympani, either through the round window or via cochleostomies in the promontary, whereas the apical turns are more deeply embedded in bone and cannot be accessed without destroying more of the cochlea. The few studies at the apex of the cochlea in chinchillas and guinea pigs show that the BM responses at the apex are somewhat different from the base in that the compressive nonlinearity is less pronounced (*Robles and Ruggero*, 2001). However, these results are not entirely reliable because Reissner's membrane is usually damaged in order to access the apical turn of the cochlea which might alter the cochlear response. In figure 2.3, the velocity of basilar membrane motion at the site of a chinchilla BM 3.5 mm from the basal end, is plotted versus applied sound pressure at the ear canal. Their measurements were performed using LDV technique with a tone applied to the ear canal (*Robles and Ruggero*, 2001). As shown, the BM motion has linear growth at frequencies above and below the characteristic frequency (CF=10 KHz), however, it is compressive at the CF, with much higher velocity for lower sound pressure levels than would be expected from a linear growth. This nonlinearity is also apparent in sensitivity function of the BM (displacement per unit of stimulus pressure as a function of frequency) (figure 2.4). As shown, at the low frequencies which are away from the CF, the BM acts linearly while it is compressive about the CF. It is also shown that the sensitivity of BM is more sharply tuned about the CF for low intensity stimulus and it has higher values which suggest that the BM amplifies the low intensity sounds about the CF while it compresses high intensity stimulus at the CF. This compressive characteristic is essential to translate a large range of vibration (120 dB) of the auditory stimulus into a range of vibration suitable for transduction by inner ear hair cells (30-40 dB) (*Robles and Ruggero*, 2001). These curves suggest that damage to the outer hair cells would linearize the BM function.

The nonlinearity characteristic of the BM is thought to be the source of two-tone suppression and intermodulation distortions. Two-tone suppression is the reduction of the response to one tone when another tone is presented simultaneously. The suppression is

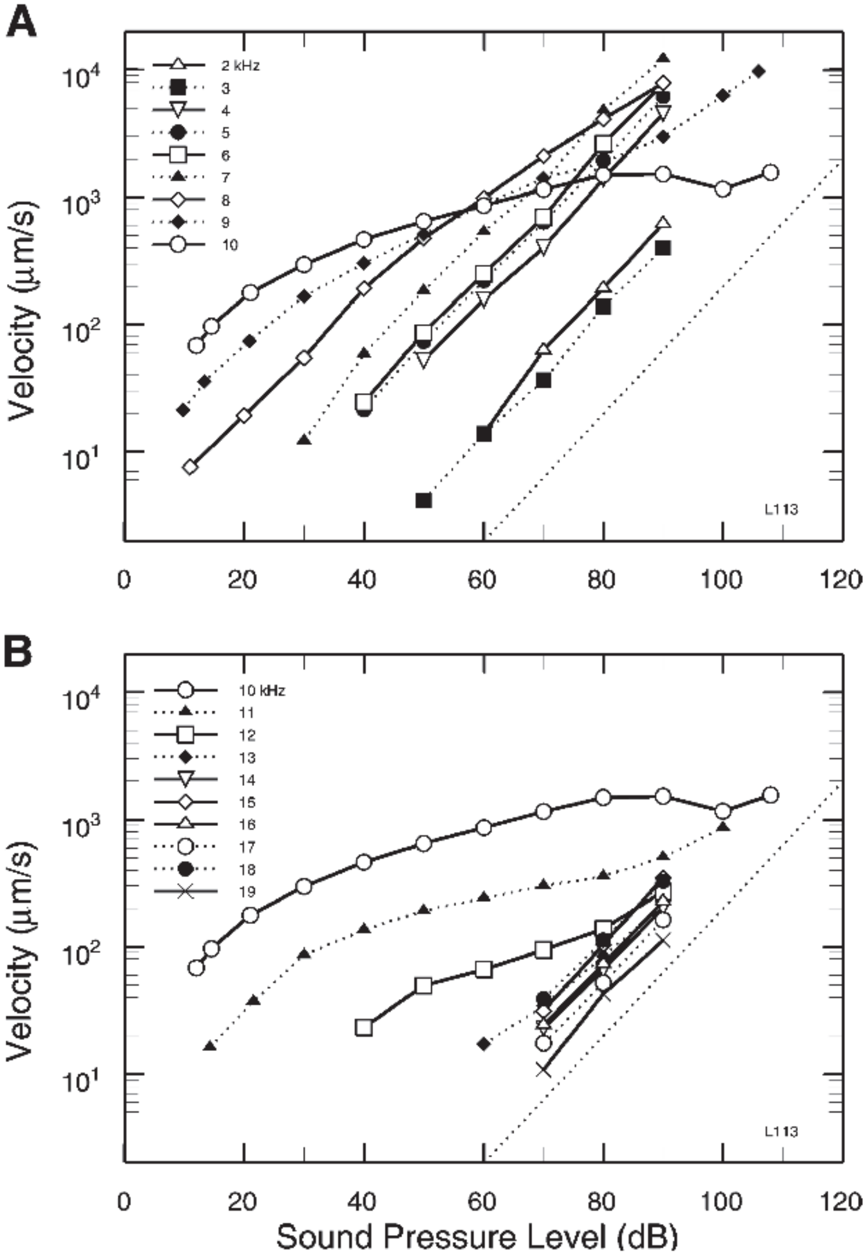

Figure 2.3: Velocity-intensity of the BM response to tones for chinchilla cochlea. A) Responses to tones with frequency equal to and lower than CF (10 KHz). B) Responses to tones with frequency equal to and higher than CF (*Ruggero et al.* (1997), with permission of the Journal of Acoustical Society of America).

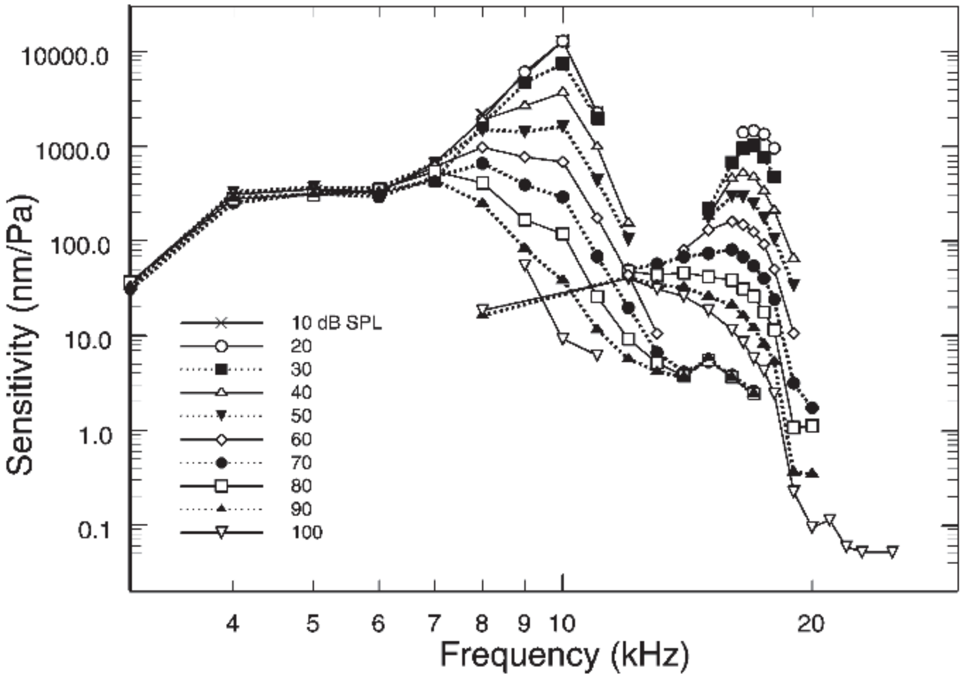

Figure 2.4: The sensitivity of BM response to tones versus frequency for two sites (CF=10 KHz, CF=17 KHz) measured of a chinchilla cochlea (*Robles and Ruggero* (2001), ©The American Physiological Society).

highest at the CF and it gets larger when the second tone is applied at a frequency close to CF. When two-tone sounds (f_1, f_2) are applied, the additional combinations of these frequencies ($f_2 - f_1, 2f_1 - f_2, 2f_2 - f_1$) are also detected by the auditory system. The amplitude of these intermodulation distortions depends on the frequency separation of the two tones (*Robles and Ruggero*, 2001).

Since the sound wave propagates from base to apex in the cochlea, phase lags have been demonstrated in the BM response to the applied tones. In figure 2.5, the phase of BM vibration relative to the middle ear measured at various basal sites of the cochlea for squirrel monkey, guinea pig, and cat are shown. The measured phase is relatively flat for the low frequencies and it has a steep slope around the CF. The slope of phase curve corresponds to the group delay between the sound wave near the stapes and its arrival at the measuring point on BM (*Robles and Ruggero*, 2001). As shown, the phase slope is decreased when the CF is higher because the measured site is closer to the basal turn where the delay is shorter. It has also been shown that the phase-lag is intensity dependent for frequencies near the CF.

Bekesy in fact discovered the cochlear mechanical travelling wave, defined as slow moving bending waves that propagate on the BM from base to apex (*Von Békésy*, 1960). Travelling wave characteristics depend on the ”passive” mechanical characteristics (mass, stiffness,

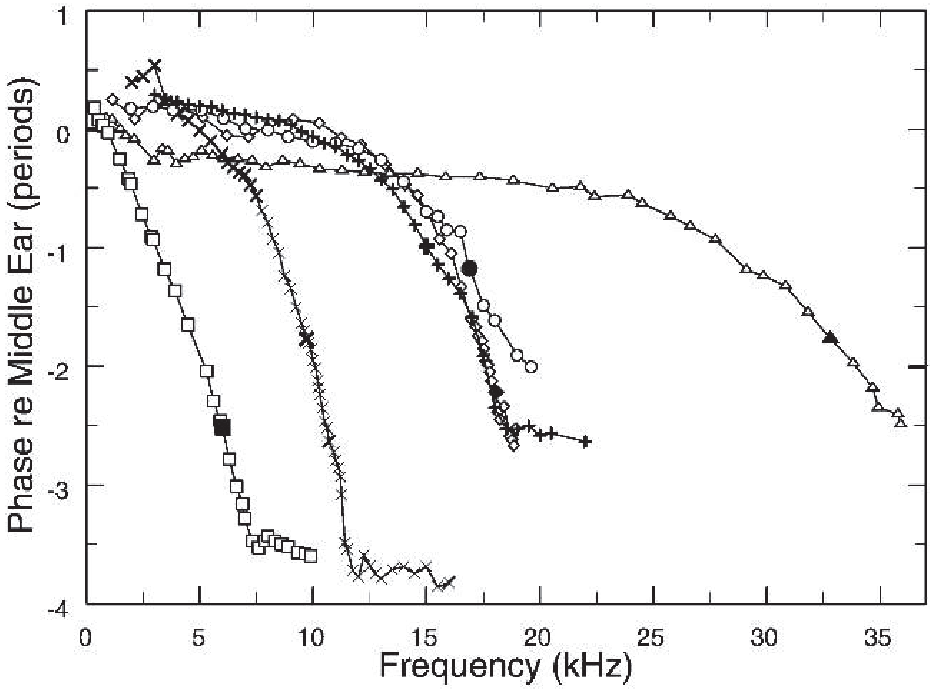

Figure 2.5: The phase of BM response (relative to the middle ear) to tones vs. frequency measured at various basal sites of the animals for guinea pig (circles and diamonds), chinchilla (X and crosses), squirrel monkey (squares), and cat (triangles). The closed symbols indicate the CFs. (*Robles and Ruggero* (2001), ©The American Physiological Society).

and damping) of the cochlear tissues and fluids. The velocity of this wave decreases as it approaches the cochlear apex and its wavelength increases. The difference in the travelling wave velocity along the BM, causes delays in the onset of BM and neural responses to impulse clicks (latency) (*Robles and Ruggero*, 2001). Bekesy's experiments revealed that the stiffness of BM decreases by 2-4 orders of magnitude as a function of distance from the stapes while the mass does not change much (*Robles and Ruggero*, 2001). This is the main cause of the reduction in travelling wave velocity along the BM. Since the BM is stiffer at the basal end, the bending wave velocity is higher at that site and gets slower as it approaches the less stiff regions at the apical end. By assuming that the stiffness of BM decreases exponentially with a mass that is almost constant, the CF-to-distance map can be explained. At the basal end where it is stiffer, the resonance frequency (CF) is higher while it gets lower as the BM becomes less stiff at the apical end.

Currently, it is believed that the outer hair cells (OHC) are responsible for the amplification of low intensity sounds about the CF and also for sharp tuning of the BM sensitivity function. It has been shown that when OHCs are electrically stimulated, their length changes (somatic electromotility) which results in a positive feedback loop for BM vibrations (*Lagarde et al.*, 2008). This effect can amplify the BM displacement at low-level intensities. This phenomenon is called the *cochlear amplifier* which refers to positive feedback for BM vibrations via *reverse transduction* (the conversion of electrical energy to mechanical vibration). When the OHCs are damaged which is the case for instance immediately postmortem, there is a large decrease in the sensitivity of responses to low level intensities near the CF, a loss in the sharpness of tuning curve, and downward shift of the CF (*Robles and Ruggero*, 2001). There are further proof of positive feedback of OHCs to BM motion in the cochlea. Spontaneous otoacoustic emissions are narrow-band sounds which can be measured continuously in the absence of acoustic stimulation and are believed originated from within the cochlea due to somatic electromotility of the OHC (*Robles and Ruggero*, 2001).

The current knowledge surrounding BM motion is mostly based on animal studies. Even with ex-vivo studies, animal studies are typically used because the round window membrane is more accessible in animals than humans and it is much more optically transparent in most animals (*Roeser et al.*, 2007). In fact the human RWM is often covered with dense soft tissue *folds*. Aside from the Bekesy study, there are only two studies that have measured BM vibration on human cadavers both at a 12 mm distance from the stapes (*Gundersen et al.*, 1978; *Stenfelt et al.*, 2003). In *Stenfelt et al.* (2003), the vibration of the BM and the osseous spiral lamina (OSL) which is attached to the BM on the modiolus side, were measured at the basal turn of the cochlea using a laser Doppler Vibrometer (LDV). In figure 2.6(a), the velocity of BM and OSL at two different positions (OSL1: close to BM, OSL2 close to cochlear wall) relative to the stapes are shown and compared with the results of *Gundersen et al.* (1978). As shown, all curves showed a resonance frequency at around 1.5-2 KHz. The vibration of OSL was similar to BM when the measured site was close to the BM (OSL1) while it was lower as the site was probed further away (OSL2). Further, the measured phase of BM/OSL relative to the stapes had a flat response at low frequencies with a rapid decrease about the resonance frequency (figure 2.6(b)).

Several studies have measured the vibration of the round window membrane on human cadavers using LDV, as a way to estimate the amount of input to the cochlea (*Stenfelt et al.*, 2004; *Asai et al.*, 1999; *Stieger et al.*, 2012). As mentioned, the oval window and round window membranes cover the two ends of the cochlea which is filled with perilymph. Since the perilymph is incompressible, the motion of the oval window which is triggered by the stapes footplate is reflected at the round window with opposite phase, at least for low frequencies (*Stenfelt et al.*, 2004). In figure 2.7, the magnitude and phase of RWM velocity measured at 80 dB sound pressure level (SPL) are shown for different points on the round window of human temporal bones. As shown, the RWM velocity has a resonance frequency centred at 1 KHz with a 6 dB/octave slope on the rise and fall region. As expected, the RW

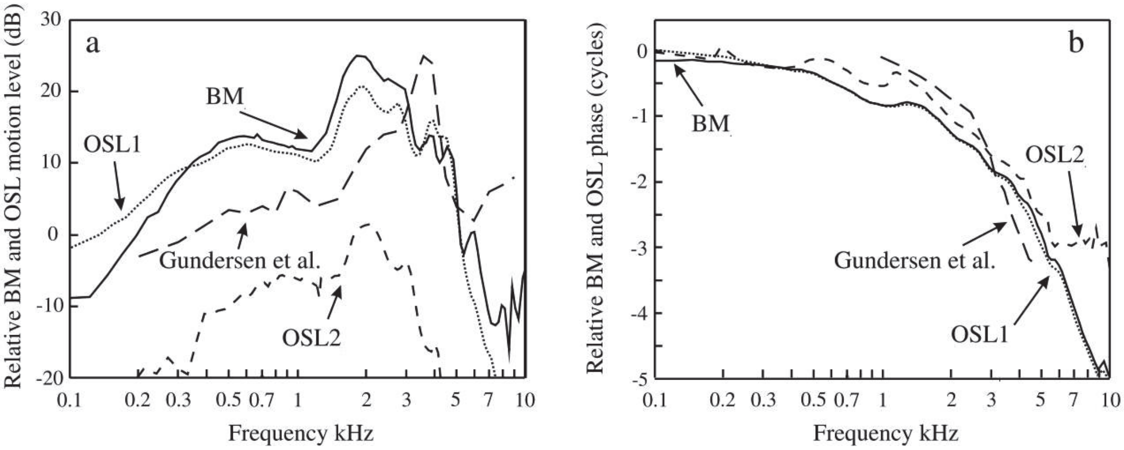

Figure 2.6: The velocity of BM (solid line) and OSL at two different locations (OSL1 (dotted line): close to BM, OSL2 (short dashed line): close to cochlear wall) relative to stapes footplate at the basal turn of human temporal bone. a) Magnitude b) Phase.The measurements are compared with *Gundersen et al.* (1978) study (long dashed line) (*Stenfelt et al.* (2003), with permission of the Elsevier).

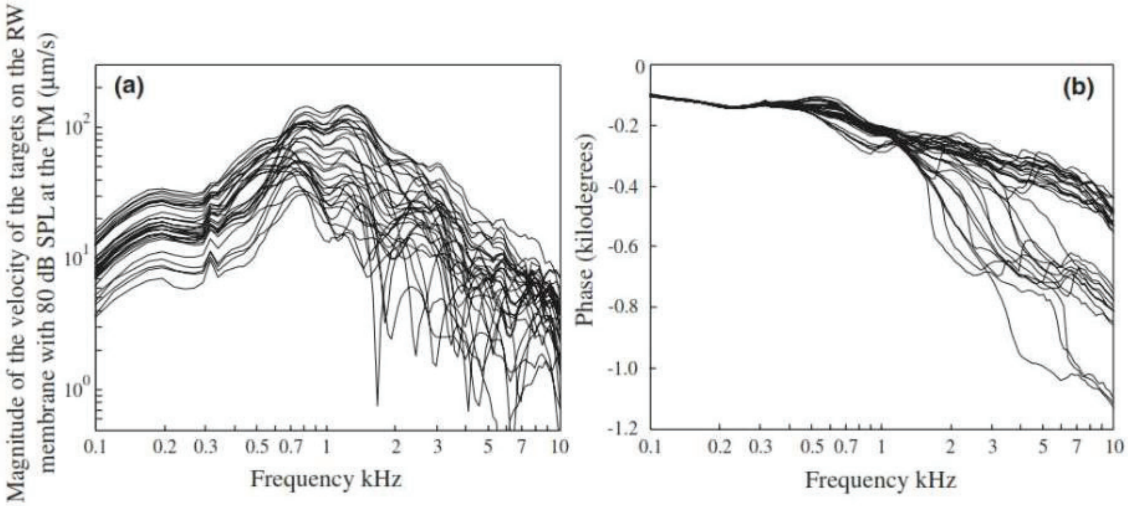

Figure 2.7: The magnitude (a) and phase (b) of RWM velocity for 31 different membrane locations measured at 80 dB SPL of human temporal bone. The phase is relative to sound pressure measured at tympanic membrane (*Stenfelt et al.* (2004), with permission of the Elsevier).

resonance frequency is very similar to the resonance frequency reported for the middle ear in several studies (*Goode et al.*, 1994; *Voss et al.*, 2000; *Aibara et al.*, 2001; *Hato et al.*, 2003; *Homma et al.*, 2009). The phase of the RW relative to sound pressure at the tympanic membrane is flat up to 0.5-0.6 KHz and it decays afterwards. The spread in the phase plots above .5 KHz suggest that the vibration of RW membrane is not in phase over its entire surface (*Stenfelt et al.*, 2004). At low frequencies, the entire vibration of RW is in-phase with a single maximum close to the center of the membrane. The RW motion between 1.5 KHz-3 KHz can be approximated by the motion of two sections with 180 degrees phase difference. Above 3 KHz, it has multi-modal vibration pattern (*Stenfelt et al.*, 2004). Due to this nonlinear motion of RWM at higher frequencies, high spatial resolution is required for measuring the vibration of round window membrane at higher frequencies.

Although a great deal is known about the mechanics of the cochlea today, it is still questionable how various sites of the organ of Corti, the BM, and the tectorial membrane move in relation to each other and how their vibrations result in the deflection of inner hair cell stereocilia (*Robles and Ruggero*, 2001).

2.1.3 Current Techniques for Measuring Basilar Membrane Vibrations

Measuring basilar membrane vibrations is quite tricky because 1) the amplitude of vibration is very small and therefore the measuring technique needs to be very sensitive (*Tonndorf*, 1977) and 2) the cochlea is surrounded with dense bone (temporal bone) which makes it very difficult to access the intra-cochlea structures without violating the cochlea. The round window membrane is the only accessible soft tissue opening into the cochlea. Because of this limitation, only the basal turn of the BM can be studied adjacent to the round window. The three techniques that have been used to date for studying the BM motion characteristics are the Mossabuer technique (*Johnstone and Boyle*, 1967; *Rhode*, 1971; *Gundersen et al.*, 1978), Laser Doppler Viobrometry (LDV) (*Khanna and Leonard*, 1981; *Khanna et al.*, 1989; *Nuttall et al.*, 1991; *Khanna*, 1991; *Kössl and Russell*, 1995; *Khanna et al.*, 1998; *Cooper*, 1999; *Ren*, 2002; *Overstreet et al.*, 2002; *Ren et al.*, 2003; *Stenfelt et al.*, 2003; *Lukashkin et al.*, 2005; *Dong and Olson*, 2009), and Optical Coherence Tomography (OCT) (*Hong and Freeman*, 2006; *Choudhury et al.*, 2008; *Wang and Nuttall*, 2010; *Chen et al.*, 2011; *Subhash et al.*, 2012). In the Mossbauer technique, a small radioactive source is placed on the BM to produce gamma rays (γ-ray) at specific frequencies. The motion of BM causes Doppler shifts of the emitted γ-rays. A fixed absorber is used to measure the γ-ray intensity, which varies with the frequency shift (*Kliauga and Khanna*, 1983). The velocity of the source is a function of γ-ray absorption, however this function is nonlinear, and therefore the velocity can only be measured over a narrow range (*Robles and Ruggero*, 2001). The other issue with this technique is that the cochlea must be opened in order to place the radioactive sources, which might disturb the normal function and the fluid surrounding the BM. Also, the radiation dose in these experiments may damage the receptor cells and cause loss of response (*Kliauga and Khanna*, 1983).

Laser Doppler Vibrometry (LDV) has been widely used to measure the vibrations of BM and RWM in ex-vivo and in-vivo animal studies. In this technique, the cochlea is typically opened near the round window and microscopic mirrors (beads) are placed on the BM to improve the optical reflectivity so that reasonable signal strength can be attained. When a sound with known sound pressure level (SPL) is applied at the eardrum, the Doppler shift in reflected laser light caused by the vibration of BM is measured by laser interferometry and the motion of BM can be obtained. This technique again involves opening of the cochlea, which, as mentioned earlier, may change the transfer function of BM and certainly makes this technique unsuitable for in-vivo human measurements. The need for the reflective beads to be placed on the BM is due to the low reflectivity inherent to its high level of transparency. Moreover, the motion of the reflective beads do not always accurately follow the motion of BM (*Khanna et al.*, 1998). In some studies, revisions of LDV technique such as self-mixing laser-diode interferometry, confocal heterodyne velocimetry, and heterodyne displacement interferometry have been suggested in order to avoid opening of the cochlea while measuring BM motion (*Khanna*, 1991; *Kössl and Russell*, 1995; *Cooper*, 1999; *Lukashkin et al.*, 2005; *Dong and Olson*, 2009). All of these techniques however are at the mercy of the low reflectivity of the BM surface and the low optical transparency of the RWM. As described above, for humans the round window membrane is thicker than that of animals and it is often covered with optically dense soft tissue folds which further scatter the light source and reduce measurement sensitivity. Another drawback of these LDV-based techniques is that they cannot range differentiate, and therefore the BM measurements might be influenced by the reflection off of the round window membrane.

Recently, Doppler optical coherence tomography (DOCT) has been introduced as another alternative for measuring BM vibration (*Hong and Freeman*, 2006; *Choudhury et al.*, 2008; *Wang and Nuttall*, 2010; *Chen et al.*, 2011). In this technique, a broadband light source is split into two beams; one is transmitted toward the sample while the other is transmitted toward a reference mirror located at a known distance. The motion of the sample is measured by monitoring the difference in optical path length between sample and the reference point. Although results presented to date are promising, the OCT penetration depth is very low and because of this, it might not properly capture the motion of the BM through the round window, especially if tissue folds are present. The other issue with this technique is that the reference mirror must be translated mechanically in order to follow the sample motion, which may introduce some limitations for in-vivo measurements.

In spite of the large amount of research directed at measuring the basilar membrane vibrations using these techniques, the mechanics of the BM are still not well understood. Again, this is primarily because the BM is very difficult to access without violating the cochlea, which will ultimately change its true mechanical characteristics. Opening the cochlea also makes human in-vivo measurements out of the question. For these reasons, there is a huge need for developing a sensitive, reliable, and real-time technique for measuring BM vibration without opening the cochlea which could potentially be used in-vivo.

2.1.4 Hearing Disorders

There are two main types of hearing loss: conductive hearing loss (CHL), affecting the middle ear and external ear structures, and sensorineural hearing loss (SNHL), affecting the inner ear and auditory nerve structures. Hearing loss can be any mixture of both. CHL is the most common type of hearing loss in children while SNHL is the most common overall, particularly with aging. CHL is usually due to middle ear fluid, otitis media, or other middle ear disorders, and can sometimes be treated by surgery, or drugs. SNHL is difficult to treat and can be caused by numerous insults, including noise, genetic causes, ototoxicity, aging and barotrauma. In general, for this kind of loss, the only rehabilitation option is hearing aids, unless it is severe, in which case cochlear implants are typically needed (*Bess and Humes*, 2003). One of the most frequent middle ear disorders is otitis media which causes inflammation of middle ear cavity and the accumulation of fluid in this cavity (middle ear effusion). It is a common disease in children with high prevalence in this population. The cause of this disorder is thought to be obstruction of the Eustachian tube, which provides ventilation to the middle ear. Hearing loss is the most significant consequence of otitis media. The air conduction loss in this disorder is typically around 25 dB over a frequency range of 500-2000 Hz. Cholesteatoma, meningitis, brain abscess, perforation of eardrum and facial paralysis are other medical complications that can be associated with the otitis media. In adults, otosclerosis is another common conductive hearing loss disorder that is the result of build-up of the calcification around the oval window, fixing the annular ligament around the stapes. In this case, the stapes footplate is immobilized and sound is not efficiently transmitted into the cochlea. Similarly, tympanosclerosis can cause the fixation of the malleus or incus. In other cases, there is discontinuity of the ossicles. In these cases, the patient typically suffers from 50-60 dB hearing loss (*Bess and Humes*, 2003).

Meniere's Disease (MD) is a chronic inner ear disorder which causes hearing loss, often initially fluctuant, and low frequency. This disease is mostly characterized by vertigo, hearing loss, aural fullness, and tinnitus. The histopathology associated with this disorder is an increase in the endolymph volume in the scala media of the cochlea (*Harris and Salt*, 2008). Histological study of MD patient's temporal bones have shown rupture of labyrinth membrane, loss of cochlear hair cells, poor vascularity in the stria vascularis, and dilated endolymph duct. Yet another kind of SNHL is caused by autoimmune inner ear disease which is an inflammatory condition caused by immune system dysfunction resulting in the body attacking cells in the inner ear, or producing antibodies that are detrimental to inner ear function. It is accompanied by rapidly progressive hearing loss, tinnitus, and aural fullness and currently is very difficult to distinguish from bilateral MD. In other causes of SNHL, sudden changes in the middle ear pressure as the result of diving, flying or sneezing might cause rupture of the round window membrane and the leakage of perilymph into the middle ear cavity (perilymphatic fistula), which can also follow stapedectomy surgery (replacement of stapes with micro prosthesis) (*Martin and Clark*, 1997). Many other inner ear disorders are the result of aging, high level of noise exposure, head injuries, bacterial diseases, or ototoxic drugs which cause loss of inner ear hair cells or damage to the cochlea structures and auditory nerve (*Martin and Clark*, 1997).

Since the focus of this thesis is on developing a new diagnostic tool for inner ear disorders, further details are provided about Meniere's Disease which is a complex SNHL and conventionally very difficult to diagnose.

2.1.4.1 Meniere's Disease

Meniere's Disease (MD) is a chronic inner ear disorder that affects about 97000 Americans annually, with a substantial impact on the primary healthcare system (*Harris and Salt*, 2008; *Vassiliou et al.*, 2011). It is characterized by episodic vertigo, fluctuating hearing loss, tinnitus, and aural pressure (*Harris and Salt*, 2008). The presence of these symptoms varies over time and at different stages of the disease. The American Academy of Otolaryngology-Head and Neck Surgery (AAOHNS) has considered three categories (Definite, Probable, and Possible) for diagnosis of Meniere's Disease based on the presence of symptoms (number of episodic vertigo, hearing loss, tinnitus). To be absolutely certain in diagnosing MD, histopathologcal confirmation is required (*Vassiliou et al.*, 2011). Endolymphatic hydrops is recognized as the most probable underlying manifestation and possible cause of the disease, however, in some cases it is not present (*Vassiliou et al.*, 2011). Endolymphatic hydrops is the result of over pressurization of the endolymph within the scala media which might be caused by dysfunction in the mechanisms of production or absorption of endolymph (*Vassiliou et al.*, 2011). The stria vascularis [1] is recognized as the site of endolymph production while it is thought to be absorbed in the endolymphatic sac [2] (*Sando et al.*, 2002). At the early stages, endolymphatic hydrop mostly involves the cochlear duct and saccule (vestibular membrane) while the entire endolymphatic system is affected in the later stages (*Harris*, 1999). In the cochlea, the endolymphatic hydrops usually starts at the apical portion and it progresses into the basal turn as the disease progresses (*Mancini et al.*, 2002).

Currently, the only certain way to diagnose MD is by histopathologic study whereby the temporal bones of patients are analyzed microscopically. Based on these histopathological studies, atrophy in the structure of stria vascularis and blockage of endolymph sac with fibrosis structures have been identified in MD patients (*Sando et al.*, 2002). The narrowing of endolymphatic duct [3] and distension of cochlear membranes such as Reissner's memebrane, is described in some cases as well (*Mancini et al.*, 2002; *Salt and Plontke*, 2010; *Harris and Salt*, 2008). The degree of distension depends on the mechanical compliance of the membrane (*Salt and Plontke*, 2010). In some cases, membrane ruptures have been detected which might contribute to the recurrent episodic vertigo attacks. When the membranes rupture, there is a sudden admixture between endolymph and perilymph, which results in highly toxic high potassium endolymph fluid bathing the afferent nerve endings, and other physical and chemical changes in the cochlear and vestibular system ultimately resulting in hair cell damage (*Vassiliou et al.*, 2011). At early stages of the disease, the hair cells and neurons in the organ of Corti are mostly normal, but the damage occurs to these structures over time (*Harris and Salt*, 2008). The loss of spiral gangolian cells, damage to stereocilia of the hair cells, and loss of inner and outer hair cells have all been reported. These changes occur earliest, and most severely in the apical turns of the cochlea (*Harris and Salt*, 2008). Hearing loss in MD usually occurs at low frequencies initially, but with time this can extend to all frequencies, and there is significant hearing deterioration over time (*Belinchon et al.*, 2011). Although, the pathophysiology of Meniere's Disease has been studied for many years, it is still quite unknown how these pathological changes interact with each other or which are the primary and/or secondary changes (*Harris and Salt*, 2008).

2.1.4.2 The Impact of Meniere's Disease on the Basilar Membrane

Based on histopathological studies, over pressurization of endolymph in the scala media causes some deformation to the basilar membrane. Displacement of basilar membrane in

---

[1] Stria vascularis is the upper part of the spiral ligament of the scala media.

[2] One end of the membranous labyrinth is the apical end of the cochlea and the other end is endolymphatic sac.

[3] The endolymphatic sac is linked to the vestibule by the endolymphatic duct.

the apical segments of the cochlea is reported, to a degree whereby the basilar membrane contacts the bony wall of scala tympani (*Salt and Plontke*, 2010). In two studies it was shown that for some Meniere's patients, the basilar membrane was displaced outward in the apical and middle segments of the cochlea (*Xenellis et al.*, 2004; *Nageris et al.*, 1996). It is assumed that the distortion of basilar membrane is a consequence of an increase of endolymph pressure over the perilymphatic pressure. Since the BM is thinner and broader in the apex than in the base of the cochlea, it is more compliant in the apex and yields more easily toward the scala tympani in the presence of endolymphatic pressure (*Xenellis et al.*, 2004) which might be the cause of hearing loss being more pronounced at low frequencies. Moreover, a strong correlation has been reported between the reduced size of the endolympahtic sac and the severity of basilar membrane deformation (*Xenellis et al.*, 2004). In *Xenellis et al.* (2004), it was reported that in the ears without BM deformity or with mild deformity, the hearing was significantly better in the 250-2000 Hz frequency range than those with severe deformity. In yet another study, it was shown that the BM impairment did not affect the threshold of hearing, but was speculated to be the cause of loudness recruitment experienced in MD patients (*Braun*, 1996). Loudness recruitment is an abnormal rapid growth of loudness with the applied sound intensity. The hypothesis for this phenomenon is that since the BM is impaired in endolymphatic hydrops, the nonlinear compression of the travelling wave does not occur, which results in rapid growth of loudness with sound intensity (*Braun*, 1996).

2.1.5 Current Diagnostic Tools for Hearing Disorders

Diagnosis of auditory disorders with high accuracy is an unsolved issue for otologists. Optical microscopy (i.e. examining the external ear and eardrum with a microcope, or with a handheld magnifying otoscope) is the first step for evaluating anatomical structures of the auditory system in clinics, but this is useful mostly for visualizing the tympanic membrane (TM) (*Bess and Humes*, 2003; *Couzos et al.*, 2001; *Dalebout*, 2008). The ossicles are barely visible because of the presence of the semi-opaque TM which causes optical scattering. Other techniques have been developed over the years to diagnose auditory disorders based on behavioural hearing tests or physiological responses of the ear, however, they are not accurate in identifying any specific type of deficiency.

2.1.5.1 Audiometry

The first and foremost test for hearing evaluation is pure-tone or speech audiometry. In this test, the psychoacoustic hearing threshold is measured for a variety of pure tone frequencies and for speech sounds. The threshold is the sound level that the subject can detect the signal

50% of the time. A graph that shows the hearing threshold versus frequency is called an audiogram. Pure-tone audiometry is measured for air-conduction and bone-conduction. In the air-conduction test, the stimulus is applied through either an earphone or room speaker and it passes through the outer ear, middle ear, and the inner ear. For the bone-conduction test, a vibrator is placed on the mastoid prominence of the skull and the sound directly reaches (vibrates) the cochlea (the outer ear and middle ear are bypassed). Results are normalized to reference threshold hearing levels which are based on the average levels for healthy young population at each frequency, for both the bone conduction and air conduction results (i.e. in dB Hearing Level, or dB HL). The comparison of these two audiograms (bone and air) is helpful for the differentiation of conductive hearing loss from sensorineural hearing loss. If there is a gap between air-conduction and bone-conduction hearing levels, diagnosis is narrowed to conductive hearing loss pathologies, which are typically in the middle ear. If the two conduction curves are almost the same (within 5 dB) and have lower values than the normal levels, SNHL (inner ear hearing loss) is diagnosed (*Bess and Humes*, 2003). The damaged structure or pathology cannot be localized by audiometry alone. Specific diagnostic tests are needed to differentiate different types of auditory disorders.

2.1.5.2 Tympanometry and Wideband Energy Reflectance

Tympanometry and wideband energy reflectance (WBER) are diagnostic tests for CHL. In these tests, the acoustic impedance of middle ear is calculated based on the amount of reflected energy from the TM while stimulating it with a known sound pressure, typically with a 226 Hz probe tone, and measuring the reflected sound pressure. In tympanometry, the stimulator is a pure-tone sound and the recording is done at different levels of pressurization within the ear canal. This allows an estimate of middle ear pressure, as admittance of the probe tone is highest at when the pressure in the ear canal is the same as the middle ear pressure. In general, this is a very good test for detecting fluid in the middle ear, or negative pressure, but while there are described patterns for ossicular discontinuity (e.g. Ad pattern) and fixation (e.g. As pattern), it is generally insensitive for these disorders (*Bess and Humes*, 2003). Since the middle ear is a dynamic system, multi-frequency tests such as wideband energy reflectance (WBER) are theoretically better able to evaluate the performance of the middle ear cavity, with its complex arrangement of ossicles, ligaments and suspensory folds. In WBER, a click or chirp (wideband signal) is applied at atmospheric air pressure within the ear canal, and the reflected energy at each frequency is calculated. Recent studies have shown that WBER is more accurate than tympanometry for diagnosis of middle ear disorders such as otitis media (*Feeney et al.*, 2009). The presence of otosclerosis or ossicular discontinuity can change the pattern of the recorded signal (*Feeney et al.*, 2009), but again the changes in the test results are relatively subtle and not very sensitive. The main drawback of these two tests is that the mobility of tympanic membrane can affect and dominate the outcomes. The section of tympanic membrane that surrounds the ossicles has the highest influence on the measurement results and it might mask contributions from deeper structures (*Rosowski et al.*, 2008).

2.1.5.3 Laser Doppler Vibrometry

Laser Doppler vibrometry (LDV) is another test to measure the vibration of the umbo (tip of malleus attached to the TM) and evaluate the functionality of the ossicles. In this test, the effect of various pathologies can cause loss in vibration amplitude of the malleus, but it is not typically possible to localize the deficiencies in the ossicular chain. This technique is capable of measuring the velocity of a moving object based on Doppler principle. Recent studies have shown that the pattern of umbo velocity measured by LDV for a normal ear could be differentiated from ears with different ossicular pathologic conditions (*Rosowski et al.*, 2003). This method potentially outperforms tympanometry and WBER in diagnosis of the middle ear disorders, but is difficult to set-up, subject to background vibration noise, requires expensive not easily available equipment, and has poor normative values in living subjects. For these reasons, it has not really been widely adopted. One of the issues with LDV is that the type of ossicular pathologic condition is decided based on the velocity pattern of the umbo. These patterns have large variation from patient to patient and it likely is not possible to assign different velocity patterns to various disorders. Moreover, evaluating solely the umbo does not provide enough information typically to localize the damaged structure in the ossicular chain.

2.1.5.4 Electrocochleaography

Amongst tests of the inner ear, electrocochleaography (ECoG) is a method for recording electrophysiological potentials of the cochlea in response to an acoustic stimulus. The measured electric signals are the results of ionic currents associated with transduction processes in cochlear hair cells and the generation of action potentials in the auditory nerve (*Burkard et al.*, 2007). For this measurement, an active electrode is placed close to the cochlea and a reference electrode at the ipsilateral mastoid. The potentials near the cochlea are recorded while a stimulus is applied to the ear. The commonly used stimuli are clicks or brief tone bursts. Since the responses are typically in the range of 0.1-10 μV, stimuli are applied repeatedly for averaging and to improve the signal-to-noise ratio. An ECoG response can be broken down into three signals called the cochlear microphonic (CM), the summating potential (SP), and the compound action potential (CAP). The CM is related to the AC component of the transduction currents in the cochlear hair cells which directly reflects the oscillation of basilar membrane movement induced by the stimuli. The SP is a DC component of the signal which is the result of nonlinear transduction processes in the haircells (both OHC and IHC). CAP reflects the synchronous firing of a number of auditory nerve fibers in response to hair cell depolarization. The important parameters of the ECoG signals are usually the amplitude of CAP, the latency of the CAP, and the SP level. The latency of the CAP is the time delay between the CAP and the onset of the stimulus. It is related to the cochlear travelling wave characteristics and decreases by increasing the frequency of tone burst stimulus because the signal is from the more proximal basal segment of the cochlea.

Since SP is generated by the hair cells, a reduction of its amplitude is an indication of sensorineural hearing loss (loss of hair cells). For a normal cochlea, the amplitude of the CAP increases and its latency decreases by increasing the stimulus intensity because more neural fibers are activated mostly from the basal turn of the cochlea. For MD patients, the slope of CAP amplitude versus stimulus level is increased which is an indication of loudness recruitment, the CAP latencies are larger, and the SP/CAP ratio is greater than normal values (*Burkard et al.*, 2007). The mechanism behind the large SP is thought to be in the difference of resting position of the BM due to increased pressure in the scala media which leads to a different working point of the hair cells and therefore to a different amplitude of their nonlinear DC response (*Burkard et al.*, 2007; *Harris*, 1999). Many groups have investigated the difference of SP levels between MD and normal subjects (*Burkard et al.*, 2007; *Iseli and Gibson*, 2010). It is mostly reported that the difference in SP amplitude is statistically significant between these two groups however, there is a great overlap between normal and MD patients, resulting in poor accuracy, and difficulty defining an operating point for the test that yields satisfactory sensitivity and false positive rates. The large variability within MD patients is partly related to the dynamic nature of this disorder. Some studies show that the SP/CAP ratio increases from early to intermediate and late stage of the disease. When the disease progresses over time, the overall condition of the cochlea deteriorates which results in lower SP and CAP amplitudes (*Burkard et al.*, 2007). Since there is no means to determine underlying state and phase of this disorder, the measurements are usually subject to large variability. Other definitive techniques are clearly required to diagnose endolymphatic hydrops with higher accuracy.

2.1.5.5 Auditory Brainstem Responses

The auditory brainstem responses (ABR) technique is used to measure evoked potentials which originate from neural structures peripheral to the auditory midbrain in response to auditory stimuli. Various waves are present in the recorded signal to form the ABR. Wave I is identical to CAP which is generated by the auditory nerve. The cochlear nucleus is the source of wave III and wave V is generated by cells in the lateral leminiscus (*Burkard et al.*, 2007). Other, later waves (middle and late latency waves) are generated by the midbrain and auditory cortex, and will not be reviewed here. In this technique, a click or tone bursts are transmitted into the auditory system and the ABR signals are measured by placing surface electrodes at the vertex of the scalp and earlobes (*Burkard et al.*, 2007). The amplitude of ABR signals are usually small and do not exceed 1μV (*Burkard et al.*, 2007), and hence typically require averaging over more than 1000 stimulation samples.

Wave V is the most robust response and it is often the only observable wave. The latency of the recorded waves corresponds to the various generating neural sites in the brainstem and different parts of the cochlea which are activated by the stimulus (*Burkard et al.*, 2007). For instance, the wave latencies increase with progressive activation from base to apex of the cochlea because the travelling wave takes a finite time to traverse the cochlea from its basal high frequency end to its apical low frequency end. The amplitude of waves can be affected by the stimulus level, degree of hearing, and the gender. Since click stimuli are broadband, they affect large portions of the cochlea, generating large amplitude waves with low latencies.The ABR in response to a click stimulus is mostly dominated by the base of the cochlea. The activation at the apical cochlea is less synchronized and hence contributes less to the recorded ABR. This problem can be avoided by applying low intensity pure tone burst stimuli or using masking techniques to generate frequency specific ABR.

In the ABR masking technique, the response is recorded from a limited region of the cochlea, by applying high-pass filtered noise along with click stimulus. The latency of wave V increases because the travelling wave takes longer to reach the apical regions, which are now the only regions generating the ABR. The amplitudes of derived-band ABRs are also lower than click-alone ABR because a smaller portion of the cochlea is activated (*Burkard et al.*, 2007). The difference between wave V latencies of two derived-band ABRs (i.e. from two different parts of the cochlea with a known distance apart) can be measured to study the travelling wave velocity along the basilar membrane. Any pathology that affects the BM properties can results in deviation of travelling wave velocity from normal values (*Burkard et al.*, 2007).

Some studies have focused on the application of the ABR technique for diagnosis of MD (*Don et al.*, 2005, 2007; *Claes et al.*, 2008). In 1991, the measurement of the travelling wave velocity test was proposed to diagnose endolymphatic hydrops. This test is based on the hypothesis that the chronic endolymphatic hydrops makes the basilar membrane stiff, and therefore the speed of the travelling wave should increase because of the higher rigidity of the BM (*Claes et al.*, 2008). The ABR latencies obtained with high-pass noise masking techniques (assuming normal frequency-place mapping), reviewed above, can be used to calculate the travelling wave velocity of the BM (*Don et al.*, 2005). Based on this method, high travelling wave velocities are reported for patients with MD (*Don et al.*, 2005). Recently, it has been shown that latencies measured by ABR evoked by clicks and 0.5 KHz high-pass masking noise can separate MD from normal subjects with high accuracy (*Don et al.*, 2005). In this study, it was shown that although the masking noise reduced the amplitude of wave V, the latency of wave V was not affected much in MD patients. This can be an indicator of higher stiffness of the basilar membrane at lower frequencies, resulting in higher travelling wave velocity. The other reason might be a change in the mechanical properties of the BM that affects the masking (*Don et al.*, 2005). Despite these promising results, the accuracy of this technique in diagnosis hearing disorders is questionable due to the large variations of recorded signals within the patients and normal subjects, and the results have yet to be verified in large scale populations.

2.1.5.6 Otoacoustic Emissions

Otoacoustic emissions (OAE) are low intensity sounds caused by the expansion and contraction of outer hair cells inside the cochlea, causing movement of the basilar membrane. This test is mostly intended for evaluating the function of outer hair cells in the cochlea by recording very weak radiated OAE signals in response to a broadband click or tone burst. Transient evoked OAE (TOAE) have latencies of about 5-10 ms which are initiated by the BM vibration in response to an applied stimulus sound (*Burkard et al.*, 2007). The presence of an OAE signal usually implies an almost normal cochlear mechanism, but not necessarily normal retrocochlear hearing. However this measurement is greatly affected by the middle ear pathology. TOAE are usually absent when the cochlear loss is greater than 30-35 dB but in MD the emissions might still be detected with a hearing loss of up to 40 dB. Distortion-product OAE (DPOAE) are generated by simultaneous application of two tones (f_1, f_2) which are separated by a frequency ratio, with the resultant OAE primarily produced at the $2f_1 - f_2$ frequency (*Burkard et al.*, 2007). In most MD patients, the DPOAE levels are reduced below the normal average while in some cases they are normal (*Burkard et al.*, 2007). One interpretation is that in MD the hearing loss is not caused by OHC pathology but from dysfunction of other neural components of the cochlea (*Burkard et al.*, 2007). The incidence of OAE in the affected ear of MD patients is reported to be lower than the unaffected ear of the same group. Again, the OAEs in MD are not very different from those in non-Meniere's ears with equivalent hearing loss (*de Kleine et al.*, 2002). Therefore, OAE are mainly helpful in detecting the presence of hearing loss and confirming that outer hair cells are functioning, but not to find the cause of the loss.

2.1.5.7 Imaging

The main issue with the above reviewed inner ear physiological hearing tests (ECoG, ABR, OAE) is that the pathologic conditions of the external and middle ear can hugely affect the recorded signals (*Muzzi et al.*, 2008). Moreover, it is difficult to associate a specific pattern of the recorded signals to a particular inner ear disorder due to the large variations of signals within patients and normal populations, and the non-specific nature of any abnormalities detected. Visualizing intra-cochlear structures with high resolution would, theoretically, be almost revolutionary in advancing diagnosis of inner ear disorders, if specific anatomical deficits can be identified with different pathologies.

Computed Tomography (CT) and Magnetic Resonance Imaging (MRI) are the two modalities that are typically used for diagnosis of cochlear or auditory nerve disorders or pre-operative cochlear implant surgical planning (*Sennaroglu et al.*, 2002). Since CT is not well suited for imaging soft tissues, its practical value lies only in detection of abnormalities affecting the bony structures of the otic capsule, or disease in the temporal bone such as cholesteatoma (*Sennaroglu et al.*, 2002). MRI is useful for imaging soft tissues such as the auditory nerve, and detecting retrocochlear pathology. It can identify the fluid signal in the cochlea, show fibrosis or obliteration of the cochlea, and show inflammation if used with gadolium dies, but primarily has poor spatial resolution, and is weak in imaging bony structures (*Sennaroglu et al.*, 2002). The major drawback of both of these modalities however is that they do not have sufficient spatial resolution for imaging intra-cochlear structures and fine details of the middle ear ossicles (both modalities have approximately 0.5-1 mm resolution).

Currently, many researchers have focused on the application of micro-CT and high resolution MRI in auditory imaging. It has been shown that with micro-CT techniques the intra-cochlear spaces can be visualized however the intra-cochlear membranes can not be imaged properly due to the low absorption of X-rays in soft tissues (*Postnov et al.*, 2006). High-resolution MRI with 9.4 Tesla magnetic resonance scanner offers sufficient resolution to visualize Reissner's membrane and osseous spiral lamina within the human cochlea in ex-vivo studies (*Silver et al.*, 2002), however safety is a big concern in in-vivo applications due to the strong magnetic field, and such magnet strengths have not been clinically available.

For MD patients, high-resolution CT is applicable to study the size, shape, or position of the bony vestibular aqueduct, but the membranous portion within it cannot be visualized (*Vassiliou et al.*, 2011). Magnetic resonance imaging (MRI) of the inner ear has been used to visualize endolymphatic and perilymphatic spaces in patients. It was shown that Reissner's membrane of the guinea pig cochlea could be visualized using 7.1 T MRI (*Ghiz* *et al.*, 2001; *Koizuka*, 2002). The contrast agent gadolinium in a 4.7 T MRI could discriminate perilymphatic and endolymphatic spaces in live guinea pigs. Since the magnetic fields required for this imaging approach are high, cost, safety, and availability become big issues. Moreover, the use in humans for inner ear disorders has not yet been certified (*Horii et al.*, 2011). Recently, 3T MRI with intratympanic gadolinium injection has been reported to be helpful in diagnosis of endolympahtic hydrops. With this contrast injection, the intensity of perilymphatic space is enhanced because of the presence of gadolinium while endolympahtic space appears dark on the image. It has been reported that after injection of gadolinium, vestibular enhancement is observed first, followed by the enhancements of basal cochlear turn, semicircular canals, and finally the apical turn of the cochlea (*Vassiliou et al.*, 2011). The perilymphatic space is either small or cannot be visualized for these MD patients (*Vassiliou et al.*, 2011). A recent study has shown that the intratympanic gadolinium injection along with 3T MRI with 2D FLAIR sequence could differentiate MD from control subjects with sudden deafness based on the size of enhanced perilymphatic space signal (*Horii et al.*, 2011). However, the size of study group was quite small in this work, and further investigation is needed to confirm the potential of this technique in detecting hydrops at different stages of MD. The safety of gadolinium intratympanically in hearing ears is also not yet determined. According to histopathological studies, in endolymphatic hydrops the Reissner's membrane and basilar membrane bulge out toward scala vestibuli and scala tympani, respectively. The main drawback of MRI imaging systems are that they do not provide sufficient resolution to visualize these membranes or the hair cells within the organ of Corti of the inner ear which would be essential to diagnose MD at different stages.

Optical Coherence Tomography (OCT) has been suggested as an alternative for imaging the cochlea and is shown to achieve very high spatial resolution in animal models (*Wong et al.*, 2004; *Sepehr et al.*, 2008; *Lin et al.*, 2008). Although these results are promising, the OCT penetration depth in soft tissue is usually less than 2 mm. In OCT cochlear imaging studies, the temporal bone is typically thinned out prior to the imaging in order to provide optical transparency which makes it an invasive approach, not suitable for humans. In addition, OCT requires a mechanical scanning mechanism, which can generate dangerously high sound levels in the ear canal.

Some literature has reported the effectiveness of ultrasound in detection of middle-ear effusion caused mostly by otitis media (*Alvord and Fine*, 1990; *Wu et al.*, 1998; *Discolo et al.*, 2004). In this technique a 20 MHz single-element ultrasound transducer is placed against the tympanic membrane to transmit ultrasound pulse and receive echo. If the middle ear is a normal air cavity, only a small reflected echo is expected because of large impedance mismatch between the air and the transducer. However, if the middle ear is filled with fluid, increased reflections from the air/eardrum interface will be present. The results reported in the literature are promising for detection of middle ear effusion, but this technique has not yet been further explored to diagnose any other types of hearing disorders, and is unlikely to be able to distinguish other causes of hearing loss. An unpublished study from John Hopkins university (presented on-line) has reported the application of high-frequency ultrasound for imaging the intra-cochlear structures. In this work, a 70 MHz focused single-element transducer was fabricated and mechanically translated in order to image the cochlea through the round window. They reported that the basal turn of basilar membrane and the Reissner's membrane could be visualized through the round window (*Rothbaum et al.*). If this technique was applied in-vivo, it would be a very effective tool for diagnosis hearing disorders since there is direct observation of the anatomical characteristics of the auditory structures in real-time.

Unfortunately, until this research, there has been no published studies using high resolution ultrasound for imaging the ear. This is likely due to the fact that developing high-frequency ultrasound systems is a challenging task. With the right combination of microfabrication technology, RF electronics, and high-frequency ultrasound expertise, the development of a valuable diagnostic tool for auditory disorders such as MD is possible. The intention of this dissertation is to show the potential of high-frequency ultrasound in auditory imaging through the development of novel technology specific to this application. In the following section, fundamentals of ultrasound imaging along with its current applications will be reviewed.

2.2 High-Frequency Ultrasound Imaging

Ultrasound imaging is a widely used diagnostic tool for imaging structures within the human body. This imaging modality is real-time, safe (no ionizing radiation), and cheap in comparison with MRI and CT, which makes it a very popular diagnostic tool. Most clinical ultrasound imaging systems operate in the frequency range between 3 to 10 MHz, which provides between 0.25 and 1 mm resolution (*Lockwood et al.*, 1996). High-frequency ultrasound (>20 MHz) is a relatively new area of ultrasonic imaging that can provide high-resolution images from micro-scaled structures. Since the resolution of these systems is proportional to the wavelength, by increasing the ultrasound frequency from 5 MHz to 50 MHz for instance, the wavelength decreases tenfold and in turn the axial and lateral resolution of images improves tenfold. High-frequency ultrasound is very useful where resolution is critical and has found widespread use in certain niche applications. These systems can resolve tissue structures ranging between 20 to 100 μm (*Brown*, 2005).

It has been shown for many years that high-frequency ultrasound can resolve many tissue structures which cannot be visualized with CT or MRI. For instance, with a 60 MHz high-frequency ophthalmic imaging system that provides 50 μm resolution, the cornea, the sclera, lens surface, iris, and ciliary muscle can be visualized (*Lockwood et al.*, 1996; *Foster et al.*, 2000), far beyond what can be seen with MRI and CT. One of the largest applications of high-frequency ultrasound to date is in in-vivo small animal imaging for biological studies. It can be extremely effective in cancer, drug, and phenotyping research (*Lockwood et al.*, 1996; *Foster et al.*, 2000).

There has also been some recent work showing that high-frequency Doppler ultrasound provides the necessary temporal resolution and sensitivity to measure the blood flow in micro-vessels, which can be helpful in evaluating the stages of wound healing or the progression of tumor vasculature. For example, a 38 MHz pulsed Doppler system has been used to measure slow blood flow in 100 μm diameter vessel of a rabbit eye (*Lockwood et al.*, 1996; *Foster et al.*, 2000).

As mentioned, available clinical imaging modalities cannot resolve the micro structures within the cochlea such as the basilar membrane, tectorial membrane, or hair cells. The microanatomical study in (*Wysocki*, 1999) shows that the height and width of scala tympani and scala vestibuli change over the length of the cochlea from base to apex (mostly decreasing). The height of scala tymapni varies between 0.3-1.3 mm while its width changes between 1.3-2.1 mm. For scala vestibuli, the height is between 0.4-1.2 mm and the width is in the range of 0.8-1.75 mm. Therefore, an imaging system should provide about 50-80 μm resolution in order to visualize the intra-cochlear spaces clearly. Since the required resolution for imaging intra-cochlear structures is between 50-80 μm and it is accessible through a membrane (round window), it has been inferred based on previous studies that an ultrasound frequency range between 40 and 50 MHz would be sufficient.

In the following sections, the basics of ultrasound imaging, design and fabrication of transducers, arrays, and beamformers will be reviewed.

2.2.1 Ultrasound Imaging

Pulse-echo ultrasound was suggested as a new diagnostic tool by Wild in 1950 (*Wild*, 1950). With this technique, a pulsed sound wave is transmitted into a sample, and it is reflected back from the interface between tissues of dissimilar acoustic properties. The received echo is recorded as an electronic signal and its amplitude is detected to form an A-scan line. The amplitude of reflected echo depends on the amount of acoustic mismatch between neighbouring tissues. The acoustic impedance (Z) for an inviscid medium when a plane ultrasonic wave propagates through it, is as follows:

$$Z = \rho \cdot c \tag{2.1}$$

where c is the speed of sound and ρ is the density of the material. If the ultrasound wave is normally incident on an interface of two mediums, the transmitted and reflected pressures are as follows:

$$\begin{aligned} P_{tr} &= P_i \frac{2Z_i}{Z_i + Z_r} \\ P_r &= P_i \frac{Z_r - Z_i}{Z_i + Z_r} \end{aligned} \tag{2.2}$$

where P_i is the amplitude of the incident wave, Z_i, Z_r are the impedances of the incident and reflecting mediums, P_r is the pressure of reflected wave, and P_{tr} is the pressure of transmitted wave to the second medium. If the incident angle of the ultrasound wave is not normal on the interface, the incidence, reflected, and transmitted angles calculated from Snell's law would result in a modified (2.2) which is fully described in *Cobbold* (2007). When the received echoes are recorded as an electrical signal (A-scan), the envelope is detected and the amplitude is assigned to grey scale values. Quadrature sampling is a popular technique for envelope detection especially at high frequencies because the data can be sampled at a rate equal to the signal bandwidth, instead of a rate of twice to the highest frequency (above the nyquist frequency) (*Mucci*, 1984). A received ultrasound A-scan line ($v_e(t)$) can be represented as (2.3).

$$v_e(t) = a(t)\cos(2\pi f - \Phi) \tag{2.3}$$

where $a(t)$ is the envelope of the ultrasound echo, the '$\cos$' term is the carrier signal with frequency f and phase Φ. By expanding (2.3), the in-phase ($I(t)$) and the quadrature ($Q(t)$) component of the signal can be derived.

$$\begin{aligned} v_e(t) &= a(t)(\cos(2\pi f)\cos(\Phi) + \sin(2\pi f)\sin(\Phi)) \\ &= I(t)\cos(2\pi f) + Q(t)\sin(2\pi f) \end{aligned} \tag{2.4}$$

If $v_e(t)$ has a frequency bandwidth of W, then $I(t), Q(t)$ have a frequency band of $[-W/2, W/2]$ and can be sampled at a sampling rate of W without aliasing, which is much less than Nyquist rate. The envelope function ($a(t)$) can be calculated using in-phase and quadrature components (*Cobbold*, 2007; *Brown*, 2005).

$$a(t) = \sqrt{I(t)^2 + Q(t)^2} \tag{2.5}$$

Since a ’$\sin$’ wave is a ’$\cos$’ wave delayed by a quarter of wavelength ($\lambda/4$), the recorded signal can be splitted into two channels, one delayed by a quarter of wavelength with respect to the other, to sample I and Q directly from the signal. When two channels are sampled directly, the envelope ($a(t)$) is calculated by taking square root of the sum of the squares of the two channels (2.5). The quarter wavelength delay is only accurate for the center frequency of the ultrasound pulse, so I and Q are not separated properly when a broadband pulse is used. However, it is a good approximation sampling technique which is commonly used in commercial ultrasound systems (*Cobbold*, 2007; *Brown*, 2005).

To generate a 2-D ultrasound image, a series of adjacent A-scans are collected throughout a field-of view (FOV). The envelope signals of the A-scans ($a(t)$) are detected and mapped to gray scale values ranging from black for the smallest signal to white for the largest signal to generate B-mode images.

2.2.2 Ultrasound Transducers

Ultrasound transducers are electromechanical devices which are triggered electrically to transmit mechanical pulses into the medium, and in turn are triggered mechanically by the reflected echoes and convert them into electrical signals. Careful mechanical and electrical matching design of transducers is important to produce ultrasound pulses with large bandwidth for good axial resolution and high sensitivity to improve signal to noise (*Cobbold*, 2007; *Brown*, 2005). The main components of an ultrasound transducer are piezoelectric resonator, matching layer, and backing layer (figure 2.8).

The piezoelectric element converts mechanical vibrations into electrical signals and vice versa. Since there is impedance mistmatch between the piezoelectric material and imaging medium (tissue), matching layers are used to maximize the amount of energy transmitted through the front face of the transducer to the tissue (*Cobbold*, 2007). Backing layers are used to increase bandwidth of the ultrasound pulse and also provide rigidity to the transducer stack.

2.2.2.1 Piezoelectricity

A piezoelectric material is described by its elastic, dielectric, and piezoelectric coefficients (*Cobbold*, 2007). A set of constitutive relations govern the behaviour of piezoelectric material at different electrical and mechanical boundary conditions. These equations relate mechanical variables (stress and strain) to the electrical variables (electric displacement,

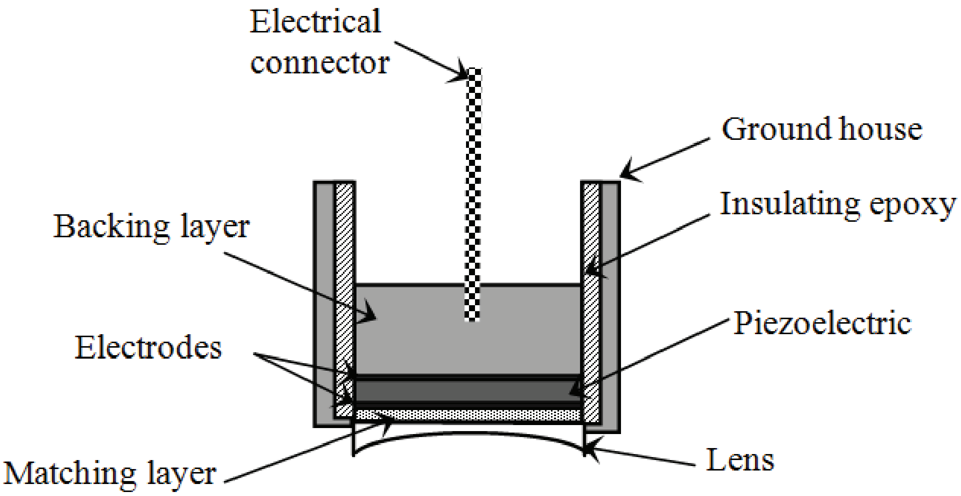

Figure 2.8: The cross-section of an ultrasound single-element transducer (Redrawn from *Brown* (2005)).

and electric field). Since piezoelectric is not an isotropic medium, the variables should be considered for 3 Cartesian coordinates (x, y, z), indexed as 1,2,3 (*Cobbold*, 2007). It can be shown that the constitutive equations in matrix format are as follows:

$$\begin{aligned}[T] &= [c^{\zeta}][S] - [e]^t[\zeta] \\ [D] &= [e][S] + [\epsilon^S][\zeta]\end{aligned} \tag{2.6}$$

where $[T]$ is the 6×1 stress matrix, $[S]$ is the 6×1 strain matrix, $[D]$ is the 1×3 electric displacement matrix, $[\zeta]$ is the 1×3 electric field matrix, $[c^{\zeta}]$ is the 6×6 stiffness matrix, $[e]$ is the 3×6 piezoelectric stress matrix, and $[\epsilon^S]$ is 3×3 permittivity matrix (*Cobbold*, 2007).

Electromechanical coupling is the ability of the material to convert one form of energy to another, defined as $\frac{\text{stored mechanical energy}}{\text{total stored energy}}$ (*Shung et al.*, 2007). Among the piezoelectric coefficients, d_{33} and g_{33} are especially important for the design if the vibration along the thickness mode is desired. The d_{33} coefficient expresses the deformation of piezo in the z direction for a given applied electric field in that direction (*Cobbold*, 2007). The g_{33} coefficient describes the amount of electric field generated for a given received pressure (*Cobbold*, 2007). Essentially, the best piezoelectrics for ultrasound transducers have the highest d_{33} and g_{33} coefficients. Other important factors for transducer design include relative dielectric constant (${\epsilon_{33}}^S/\epsilon_0$) for electrical impedance matching, thickness mode electromechanical coupling (k_t) for sensitivity, and acoustic impedance (Z) for acoustic coupling with tissue (*Cobbold*, 2007).

There are several different piezoelectric materials with different characteristics that can be considered for fabrication of ultrasound transducers. The popular materials include piezoceramics, piezoelectric polymers, and single crystals (*Shung et al.*, 2007). Piezoceramics such as lead zirconate titanate (PZT) have high electromechanical coupling coefficients and large dielectric constants, which are ideal for electrical impedance matching of small sized transducer elements. However, they have high acoustic impedance ($\sim$ 35 MRayl) which is problematic for acoustic impedance matching with human tissue ($\sim$ 1.5 MRayl). The typical grain size of ceramics ranging from 3 to 10 μm can also be an issue for fabrication of thin active elements at high frequencies (*Shung et al.*, 2007). Piezoelectric polymers such as polyvinylidene fluoride (PVDF) have low acoustic impedance ($\sim$ 3.9 MRayl) which is good for acoustic matching of the transducer to the human tissue and they are flexible, which is good for geometrical focusing of the transducer. Their dielectric constant however is low which can result in undesirably high electrical impedance and they have a poor thickness mode coupling coefficient which can result in poor sensitivity (*Shung et al.*, 2007). Relaxor-PT single crystals such as lead magnesium niobate-lead titanate (PMN-PT) usually display very high electromechanical coupling which is ideal for designing sensitive transducers. Also, they do not have finite grain size which makes them ideal for high frequency ultrasonic micro-arrays with microscopic dimensions (*Shung et al.*, 2007). The resonant frequency of an ultrasound transducer is proportional to its thickness as shown in (2.7).

$$f = \frac{c_p}{2d} \tag{2.7}$$

where f is the desired resonant frequency of the transducer, c_p is the velocity of the sound in the piezo, and d is the thickness of the transducer.

2.2.2.2 Backing & Matching layers

As mentioned, the acoustic impedance of tissue is about 1.5 MRayl which is much smaller than acoustic impedance of commonly used piezoelectric materials such as PZT. Therefore, a matching layer is usually needed between the front face of the transducer and the imaging medium to maximize the transmission of the acoustic pressure to the tissue. It can be shown that the transmission coefficient ($T_I = \frac{P_{tr}}{P_i}$) through a thin medium is governed by (2.8) (*Kinsler et al.*, 1999). Therefore, 100% transmission can be achieved when the matching layer has a quarter wavelength thickness and its acoustic impedance is equal to (2.9).

$$T_I = \frac{4Z_{01}Z_{03}}{(Z_{01}+Z_{03})^2\cos^2\frac{2\pi l}{\lambda} + (Z_{02}+\frac{Z_{01}Z_{03}}{Z_{02}})^2\sin^2\frac{2\pi l}{\lambda}} \tag{2.8}$$

$$Z_{02} = \sqrt{Z_{01} \cdot Z_{03}} \qquad (2.9)$$
$$l = \frac{\lambda}{4}$$

where l is the thickness of the matching layer and Z_{01}, Z_{02}, Z_{03} are the acoustic impedances of the transducer, matching layer, and the tissue, respectively. The designed matching layer is only perfect for the resonant frequency, however it acts as a band-pass filter, which can be problematic when a broadband pulse is desired. Therefore, transducers with two or three matching layers are usually designed (*Brown*, 2005). Other modified equations are proposed in the literature for calculation of optimum acoustic impedance of matching layers based on transmission line transducer model to obtain high-efficient, broadband transducers (*Desilets et al.*, 1978).

A backing layer is needed at the back of transducer to provide support for the transducer, to damp the resonator, and to attenuate the energy transmitted into the backing layer. The higher the acoustic impedance of the backing layer, the higher the bandwidth of transmitted pulse as there will be less reflections within the piezoelectric resonator (*Brown*, 2005). There is also a trade-off for choosing the acoustic impedance of backing layer between the bandwidth of transmitted pulse and transducer sensitivity.

2.2.3 Beam Focusing

The spatial resolutions (axial and lateral) of an ultrasound system are proportional to the ultrasound transducer geometry, frequency, and its bandwidth. The axial resolution is the ability of the system for resolving targets along the beam direction while lateral resolution is its capability for resolving the targets perpendicular to the beam direction (*Cobbold*, 2007). A single-element transducer can be geometrically shaped into a concave surface as shown in figure 2.9 to focus the beam at a specific depth. The lateral resolution refers to the width of the beam 3 dB below the peak. The depth-of-field (DOF) refers to a region where the ultrasound pressure is greater than -3 dB of the maximum pressure.

For a focused single-element transducer shown in figure 2.9, the DOF and the lateral resolution ($\mathrm{BW}_{3\,\mathrm{dB}}$) can be calculated using following equations:

$$\mathrm{BW}_{3\,\mathrm{dB}} = 1.02\lambda\frac{z_p}{D} = 1.02\lambda F \qquad (2.10)$$
$$\mathrm{DOF} = 7.2\lambda F^2$$

where D is the diameter of the transducer, z_p is the focal depth, and λ is the wavelength. The ratio of focal depth to transducer diameter is called f-number ($F = z_p/D$) (*Cobbold*, 2007). As shown, there is a trade-off between lateral resolution and depth-of-field for a

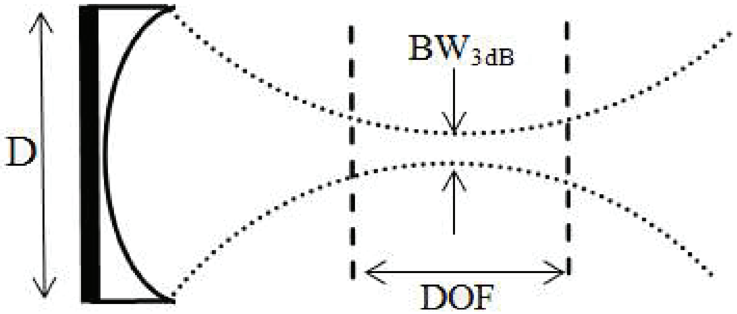

Figure 2.9: A focused single-element transducer with diameter D (Redrawn from *Brown* (2005)).

single-element transducer focused at a specific depth. By increasing the focal depth (z_p), the depth-of-field becomes larger while the lateral resolution increases as well. By increasing the frequency, the spatial resolution improves while depth-of-field decreases. Moreover, since the ultrasound attenuation coefficient is proportional to the center frequency of the transducer, it attenuates exponentially at higher frequencies which limits the imaging depth. In order to avoid the trade-off between lateral resolution and depth-of field, an array transducer can be used. Array transducers are discussed in section 2.2.5.

2.2.4 *Theoretical Basis for Field Calculations*

To design a transducer, it is essential to simulate the propagation of pressure waves in the medium theoretically. Hence, the characteristics of the transducer can be optimized in order to achieve the desired axial and lateral resolution. The transducer can be considered as a small vibrating source within a large, isotropic, and homogeneous medium. Thus, the wave equation can be used to predict the velocity and pressure of ultrasound wave propagating in the medium at different times and spatial locations. The wave equation shown in (2.11) is the result of combining the equation of motion, the continuity equation, and the equation of state for a compressional wave in homogeneous inviscid medium (*Cobbold*, 2007; *Brown*, 2005).

$$\begin{aligned}
&\nabla^2\phi(r,t) - \frac{1}{c^2}\frac{\partial^2\phi(r,t)}{\partial t^2} = f(r,t) \qquad (2.11)\\
&v(r,t) = -\nabla\phi(r,t)\\
&p(r,t) = \rho\frac{\partial\phi(r,t)}{\partial t}
\end{aligned}$$

where $v(r,t)$ is the particle velocity, $p(r,t)$ is the pressure, $\phi(r,t)$ is the velocity potential, c is the speed of sound in the medium, and $f(r,t)$ is the source of vibration at location r

and time t. It can be shown that the Rayleigh integral solution of (2.11) can be reduced to the following convolution equation (*Cobbold*, 2007; *Brown*, 2005):

$$\begin{aligned} \phi(r,t)|_{r=R_s} &= \frac{1}{2\pi}\iint_S \frac{v_{no}(t-\frac{R_s}{c})}{R_s}\,dS \\ &= v_{no}(t) * \iint_S \frac{\delta(t-\frac{R_s}{c})}{2\pi R_s}\,dS \\ &= v_{no}(t) * h(r,t)|_{r=R_s} \end{aligned} \tag{2.12}$$

where, $v_{no}(t)$ is surface velocity normal to the transducer face, S is the surface of the transducer, R_s is the distance between a point on transducer surface and spatial point, and $h(r,t)|_{r=R_s}$ is the *impulse response* of transducer at the spatial point (r,t) which is dependent on the geometry of transducer. The analytical expressions for the impulse response of transducers with different geometries such as disk or rectangle are available in the literature (*San Emeterio and Ullate*, 1992; *Stepanishen*, 1971; *Arditi et al.*, 1981). As shown in (2.12), the velocity potential ($\phi(r,t)$) is calculated by convolving impulse response ($h(r,t)$) with the transducer surface velocity. For a broadband surface velocity, $v_{no}(t)$ can be modelled as a Gaussian modulated cosine wave with full width at half maximum (FWHM) bandwidth of FWHM $= \frac{2.36\sigma_W}{2\pi f}$ (*Cobbold*, 2007).

$$v_{no}(t) = A\cos(2\pi f t)e^{-\sigma_W^2\frac{t^2}{2}} \tag{2.13}$$

where A is the peak of normal velocity, σ_W is the standard deviation of Gaussian function, and f is the frequency of ultrasound transducer. The transmit pressure pulse $p_{tr}(r,t)$ at each point of the space can be derived using $\phi(r,t)$ as shown in (2.11). For echo signals that are received by the transducer, the transmit pressure is convolved with the impulse response ($h(r,t)$) once more as shown in (2.14).

$$\begin{aligned} p_{tr}(r,t) &= \rho\frac{\partial\phi(r,t)}{\partial t} \\ p_{rec}(r,t) &= p_{tr}(r,t) * h(r,t) \end{aligned} \tag{2.14}$$

where p_{tr} and p_{rec} are the transmit and receive pressure pulses, respectively.

By calculating the sound pressure at each point of the space and considering the peak value, a contour map of pressure distribution generated by the transducer in the medium can be modelled which is referred to as *radiation pattern* (*Cobbold*, 2007). A one way radiation pattern is the outcome of transmitted sound pressures while a two-way radiation pattern is the result of received echo pressures calculated by an extra convolution of transmitted pressure with the impulse response (2.14). The lateral resolution, depth-of-field, focal point, or imaging artifacts such as side-lobes or grating lobes can be visualized and assessed based on the simulations of radiation patterns.

2.2.5 Arrays & Beamforming

As discussed in section 2.2.3, single element transducers can be geometrically shaped to focus the ultrasound beam at a specific depth. However, there is a trade-off between the lateral resolution and the depth of field. This issue can be avoided by using an array of elements which are triggered in a way that approximates the radiation pattern of a single-element transducer. By applying appropriate delays to the excitation pulses of the elements, the ultrasound beam can be focused at different depths or it can be steered to different angles. The same applies on receive when the echoes are delayed properly to focus/steer the beam at a spatial location. Since the ultrasound energy can be refocused to any depth, the trade-off between depth-of-field and lateral resolution is avoided (*Cobbold*, 2007).

An array-based ultrasound system usually consists of an analog front-end circuit, receive beamformer, synchronization control unit, and a computer for displaying the image. The front-end circuitry is responsible for exciting the transducer elements with appropriate delays, receiving the echoes, amplifying, and applying time gain control (TGC), which compensates for the attenuation of the ultrasound pulse at different depths. In the following sections, the fabrication of array-based transducers and the design of electronic beamformers (specifically at high frequencies) will be reviewed.

2.2.5.1 Transducer arrays

The two main types of 1-D array-based transducers are the linear array, and the linear phased array (phased array). With a linear array transducer, a subset of elements are pulsed (sub-aperture) for each A-scan line and the beam is focused to different depths along the central axis of this sub-aperture. The sub-aperture is then stepped across the full aperture electronically in order to collect many parallel image lines (A-scans) and produce a full 2D image. The linear array transducer usually has large number of elements and cannot steer the ultrasound beam, which results in a relatively large aperture. In phased array transducers, the whole aperture is pulsed for each image line (A-scan), and the beam can be focused at different depths and steered to various steering angles. In this array, a large field of view can be achieved with small aperture.

The main issue with linear/phased array ultrasound imaging at high frequencies is the

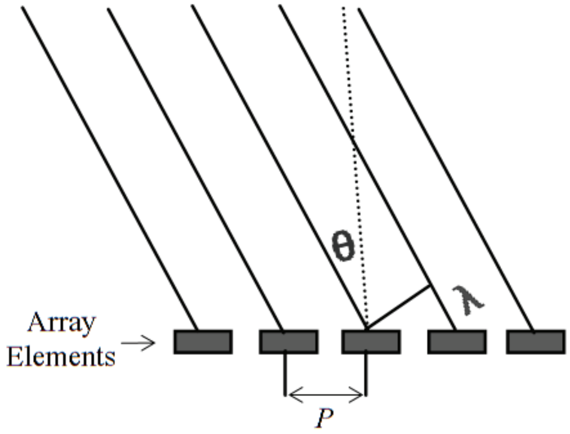

Figure 2.10: The grating lobe angle (Redrawn from *Ustuner and Gee* (2007)).

presence of grating lobe artifacts in the field of view because of periodicity of the element spacing. Grating lobes are the result of unwanted constructive interference outside of the main lobe (*Cobbold*, 2007). As shown in figure 2.10, it occurs at an angle where the difference between path length (after beamforming delays) between the spatial point and adjacent elements is an integer multiple of wavelength. Because of this, the received echoes from the grating lobe region are in-phase, producing unwanted constructive interference. The grating lobe angle for a continuous wave ultrasound can be calculated using (2.15).

$$\Theta = \sin^{-1} \frac{n\lambda}{p} \tag{2.15}$$

where p is the element-to-element pitch, λ is the wavelength, n is an integer, and Θ is the grating lobe angle. For linear arrays where the beam is only focused along the main axis of the sub-aperture, the element pitch of the array can be reduced to λ, to push the grating lobes to 90° angle versus to the main lobe (2.15). At large angles, the transducer elements will not accept any energy from the tissue therefore grating lobes coming from large angles is not an issue. For phased arrays where the beam steers off to different angles, the element-to element pitch should be approximately half of a wavelength to prevent this artifact from entering into the field of view (*Cobbold*, 2007). These constraints impose big challenges for the fabrication of high frequency linear/phased arrays where the wavelength is quite small (30 μm at 50 MHz).

At high-frequencies, the required thickness of the piezoelectric material ($\lambda/2$) is quite small which makes the handling of substrate very difficult during the fabrication process. Moreover, cutting the substrate to form the array elements is very challenging due to the small element-to-element pitch required to avoid grating lobes. In addition, connecting cabling system wires to the microscopic elements is another challenge (*Brown*, 2005). Despite these challenges, some success has been reported in the literature for fabrication of high-frequency linear array transducers with element-to-element pitch between $(1\lambda - 2\lambda)$. Dicing methods such as diamond-nickle blade (*Cannata et al.*, 2006; *Ritter et al.*, 2002) or laser cutting (*Lukacs et al.*, 2006; *Foster et al.*, 2009) have been used to cut small elements into the substrate. The problem with mechanical dicing is that the size of space left between elements (kerf) is limited to the smallest thickness of available dicing saw blade ($\sim 10\ \mu$m). Laser micromachining is another technique for fabrication of fine and tightly packed array elements of high frequency transducers (*Lukacs et al.*, 1999). This technique is also limited to kerf sizes on the order of 10 μm and the generated heat at the focused spot might result in the permanent destruction of the remaining piezoelectric material. Reactive ion etching (*Liu et al.*, 2008, 2012; *Zhou et al.*, 2010) and interdigital pair bonding (*Chabok et al.*, 2011; *Liu et al.*, 2001; *Cannata et al.*, 2011; *Yin et al.*, 2004) have also been suggested as alternative techniques for fabricating high-frequency arrays with very small kerfs; however, the accuracy of these methods is still questionable and they are very labour intensive. It has also been shown that dicing kerfs can be avoided by designing *kerfless* arrays where the electrodes are patterned on the piezoelectric using simple photolithography (*Wu et al.*, 2009; *Brown et al.*, 2007; *Chabok et al.*, 2011; *Morton and Lockwood*, 2002; *Cannata et al.*, 2005). Although the fabrication of high frequency ultrasound transducers is simplified using this technique, the coupling between adjacent elements is increased. The result of increased cross coupling between transducer elements is the reduction of element directivity. Element directivity determines the angular pressure distribution of an element, which is dependent on the width of the element (*Cobbold*, 2007). The directivity of a rectangular element decreases by increasing the element width and in the kerfless array design the effective element width is increased (*Morton and Lockwood*, 2002).

Recently, capacitive micromachined ultrasonic transducers (CMUTs) are also suggested as an alternative for piezoelectric transducers (*Ergun et al.*, 2003; *Yeh et al.*, 2005; *Oralkan et al.*, 2002; *Ergun et al.*, 2002). These devices are composed of two thin membranes separated by a very small cavity in between. On transmit, a voltage is applied to the CMUT to cause electrostatic attraction forces and put the membranes in vibration which generates acoustic waves in the medium. On receive, the acoustic wave vibrates the membrane and causes a capacitance variation, which is detected by the change in the current flow (*Ergun et al.*, 2003). CMUTs are fabricated using semiconductor microfabrication technology which avoids the size limitations associated with the fabrication of piezoeletric-based high frequency ultrasound transducers. It is also possible to integrate the electronic circuits on

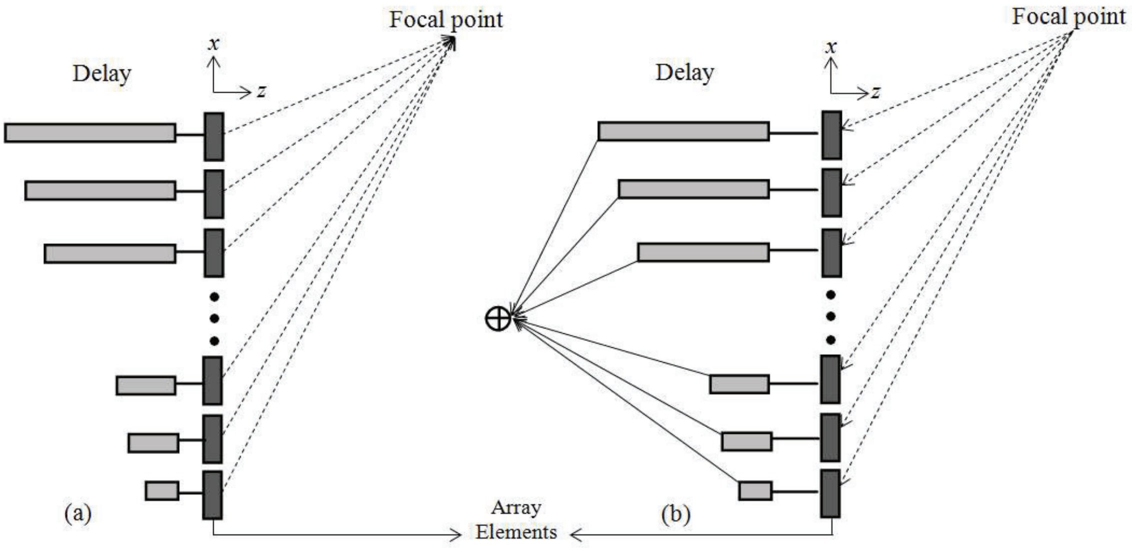

Figure 2.11: Beamforming on a) transmit and b) receive (Redrawn from *Cobbold* (2007)).

the same wafer of the transducer in order to miniaturize the packaging.

2.2.5.2 Beamforming

Applying the focusing delays to the ultrasound excitation pulses during transmit is called transmit beamforming (figure 2.11a). Delays are also inserted upon receive for receive focusing, and then the signals are subsequently added together (figure 2.11b). The delays for each transducer element versus origin of the array can be calculated using (2.16) to focus the beam at any spatial location in the tissue (figure 2.11)(*Thomenius*, 1996).

$$\tau_i = \frac{\sqrt{\left(x_i - x_{fp}\right)^2 + {z_{fp}}^2} - \sqrt{{x_{fp}}^2 + {z_{fp}}^2}}{c} \tag{2.16}$$

where, τ_i is the applied delay for element i, $(x_i, 0)$ is the coordinate of the i th element, (x_{fp}, z_{fp}) is the focal point, and c is the velocity of sound in water (typically assumed to be a constant). For transmit, there is usually a fixed focal zone while on receive delays can be applied at all spatial locations as if the signals are individually digitized. This is referred to as dynamic receive beamforming (*Thomenius*, 1996). In dynamic receive beamforming, the ultrasound pulse is optimally focused at all spatial locations within the tissue. In transmit beamfomring, pulse should be allowed to dispersed before any subsequent transmit events, therefore dynamic focusing for transmit is not possible (*Brown*, 2005). Conventional ultrasound systems usually have 2 to 4 transmit focal zones in combination with dynamic receive beamforming. The accuracy of applied delays is essential to avoid any unwanted destructive interference resulting degraded image quality. Careful electronic delay design is especially important at high frequencies where the wavelength is shorter. As a general rule, the delay error should be kept less than 1/30 of the wavelength.

The first generation of beamformers was based on analog circuits that tapped the signals along the delay circuits at fixed locations and then summed them using an adder circuit (*Thomenius*, 1996). In these beamformers, a large number of delay taps was needed to keep delay errors small. Rapid switching of the delay lines which is required by dynamic beamforming could cause smearing noise artifact (*Manes et al.*, 1988). Insertion loss and impedance mismatch were the other factors that degraded signal-to-noise ratio (*Brown*, 2005).

Digital ultrasound beamformers were developed in the early 80's when analog-to-digital (A/D) convertors with high sampling frequency and large number of bits were available (*Thomenius*, 1996). The echoes are digitized using A/D converters for each individual element, digitally delayed, and then summed. This is the simplest form of a digital beamformer and it should be obvious that the delay accuracy increases with sampling frequency. In general, increasing the sampling frequency of the A/D decreases the dynamic range (bit-depth). This is critical in medical imaging applications where a large dynamic range is required. Also, large amount of memory is needed to store the digitized data (*Mucci*, 1984). These problems are more pronounced in high frequency ultrasound where the center frequency is greater than 20 MHz. Therefore, modifications beyond conventional beamforming systems are usually implemented at high frequencies.

There is currently one commercially available high-frequency beamfomer which is based on several field programmable gate arrays (FPGA) (*Foster et al.*, 2009). FPGAs have high clock rate and can achieve required accuracy for high-frequency beamforming delays. Since the required delays are barely an integer multiple of sampling period, they are broken down into coarse delays and fine delays. Coarse delays are an integer multiplication of the sampling frequency while fine delays are a fraction of it that can be generated with a number of different techniques. One way to generate fine delays is to sample the signals at varying sampling frequency, so that only the samples that are required for focusing will be recorded. Then by adding the recorded samples, the beam can be focused at the specific depth and no delay insertion is needed (*Brown*, 2005). Interpolation filters are the other option for generating very small fine delays to improve the accuracy of delaying the echoes prior to summation (*Hu et al.*, 2006b,a, 2011; *Foster et al.*, 2009).

Up until now, no fully sampled high-frequency phased array ultrasound system (with beam steering) has been developed. This is mostly because of small element-to-element pitch required to avoid large grating lobe artifacts. It will be discussed later that phased-array transducers are the best choice for auditory imaging because of the small opening available for imaging the inner ear across the round window membrane. Therefore, it is certainly in our interest to investigate potential methods for suppressing grating lobes with large-pitch phased array transducers. The only other option would be to develop a fabrication process that can produce arrays with smaller pitch. In the following section, proposed solutions for suppressing grating lobes in the literature will be reviewed.

2.2.5.3 Methods for Suppressing Grating Lobes

As mentioned in section 2.2.5.1, the grating lobes are the result of unwanted constructive interference of the points along an angle where the difference in path length between adjacent transducer elements (after beamforming delays) are an integer multiple of wavelength. According to (2.15), by reducing the element-to-element pitch of transducer, the grating lobes will eventually be pushed to an angle that is too large to accept any energy from the tissue. However, the fabrication of high-frequency transducers with small element pitch becomes challenging. Several methods have been proposed in the literature to avoid grating lobes while fabricating arrays with larger element-to-element pitch.

In one approach, the array structure is manipulated in a way to avoid the periodicity of elements and in return the grating lobes. A sub-array rotation technique is proposed in *Agrawal* (1978) to suppress grating lobes of 2D phased arrays. In this method, the 2D array is divided into equal sub-arrays which are physically rotated by specific angles. If the fast Fourier transform (FFT) of array radiation pattern is considered, the main-lobe is at the center while the grating lobes form a ring around it. When the sub-arrays are rotated and combined, the main lobe remains at the center and adds up while the grating lobes will be displaced and positioned over the null of the others. Therefore, the difference between the level of main lobe and grating lobe increases (*Agrawal*, 1978). The grating lobe level is expected to be about $20log_{10}(n_s)$ lower than the main lobe where n_s is the number of sub-arrays. However based on the simulated radiation patterns, the suppression is lower than expected and some conditions needs to be considered while choosing the number of sub-arrays, the angle of rotations, and their dimensions (*Agrawal*, 1978).

Arrays with randomly spaced elements are designed for thermotherapy applications in order to avoid periodicity of the elements however the reported suppression is not significant (*Hutchinson et al.*, 1996; *Gavrilov and Hand*, 2000; *Wang et al.*, 2008; *Goss et al.*, 1996). In *Hutchinson et al.* (1996), the distribution of unequally sized elements is optimized by defining a cost function as the ratio of maximum grating lobe power to the main lobe power. The simulation results have shown that the grating lobes can be suppressed about 30%-45% over a conventional periodic element distribution while the pitch varies between $.5\lambda$ to 1.4λ. In *Gavrilov and Hand* (2000), a theoretical study was done to evaluate the effect of random distribution of circular elements in a 2D spherical array on grating lobe suppression. It is shown that the grating lobe level can be pushed up to 20 dB below the main lobe in an array with 5.5λ pitch when the beam is steered to $\pm 8.13°$. In *Goss et al.* (1996), a theoretical investigation has shown that for a large-pitch hexagonally packed array with randomly distributed circular elements, the grating lobe levels can be suppressed about 8 dB lower than main lobe for steering angles of $\pm 2.86°$. In *Wang et al.* (2008), a combined approach of using random sub-arrays and random staggering of the rows is proposed to suppress grating lobes in 2D arrays. It was shown that the grating lobe level can be pushed to about 20 dB below the main lobe with this technique. The main issue with these techniques is that the fabrication of array elements with complex geometries in a 1D phased array becomes virtually impossible, especially at high frequencies where the size of elements is extremely small. In addition, the grating lobe suppression is not significant and the range of steering angles is very limited.

In other proposed techniques, the elements of the transducers are removed randomly during transmit or receive to form a *sparse array* (*Gavrilov et al.*, 1997; *Turnbull and Foster*, 1991). In *Gavrilov et al.* (1997), practical recommendations are presented about the use of subsets of elements for suppressing grating lobes of large-pitch phased arrays ($\sim \lambda$). The experimental hydrophone measurements have shown that the grating lobe level can be pushed to about 10 dB lower than the main lobe at $\sim 18°$ steering angle when a subset of elements at the contralateral part of the array is switched off. The theoretical studies in *Turnbull and Foster* (1991) show that for broadband ultrasound pulse, the grating lobes are present even when the pitch is close to 0.5λ due to grating lobe contribution from the higher frequencies in the pulse. The main drawbacks of sparse arrays are: 1) the signal-to-noise ratio (SNR) is reduced because lower number of elements are present in transmit and/or receive and 2) the level of side-lobes increases since it is proportional to the inverse of number of elements (*Cobbold*, 2007).

In another study (*Talman and Lockwood*, 2000), it is suggested that the transmit and receive apertures be separated creating non-overlapping phased arrays with large pitch. The suppression theory is based on the fact that the effective aperture is defined as the convolution of transmit and receive apertures. Therefore, these apertures can have elements with larger pitch which results in the same effective aperture as the one with $\lambda/2$ pitch. The simulation results in this work have shown that the grating lobes can be suppressed up to 60 dB below the main lobe with up to 2λ pitch. The issue with this technique is that the transmit and receive arrays must to be fabricated separately.

A different approach in the literature is to apply weighting factors to the element echoes in order to minimize the effect of grating lobes and emphasize the main lobe. Different features of the received echoes can be measured in order to calculate these weighting factors, between 0-1. Weighting factors can be defined based on the cross-correlation of delayed echoes as a measure of time-shifts between them (*Ustuner and Gee*, 2007). Echoes originating from the main lobe have no time-shift after inserting the proper delays on receive while the grating lobe echoes are shifted versus each other. With this technique, the grating lobes can be differentiated from the main lobe and properly suppressed. This work is published as a patent which does not include any simulation or experimental results. Some methods have been proposed in the literature for defining weights in order to suppress the sidelobe levels generated from the edges of transducer elements. These techniques might be applicable for grating lobe suppression with some modifications. In *Li and Li* (2003), the weights are defined based on receiving direction of the echoes in order to compensate for the errors resulted from sound-velocity inhomogeneities in tissue. The echoes direction is estimated from the FFT of echoes received along the aperture. It is demonstrated that the low frequency portion of the spectral energy of echoes received along the aperture corresponds to the coherent part of echoes while the high-frequency components are related to the incoherent part. Therefore, a coherence factor is defined as the ratio of spectral energy at low frequency range to the total energy. The simulation results have shown that the side-lobe levels can be pushed to more than 20 dB below the main lobe with this technique. A method called minimum variance is developed to suppress sidelobe levels by applying optimized weights on the received echoes. The weights are calculated in a way to minimize the power of summed echoes while having unit gain at the focal point (*Synnevag et al.*, 2007; *Asl and Mahloojifar*, 2010). The simulated results have shown that the sidelobe levels can be suppressed about 20 dB, however, the suppression is shown to be smaller in experimental results (*Synnevag et al.*, 2007). Although some of these techniques (generally called adaptive beamformering) have shown promising results, they are not suitable options for high frame-rate imaging systems because the computational cost of calculating the weighting factors is very high.

Recently however, a simple signal processing technique called phase coherence imaging (PCI) has been proposed for suppressing grating lobes of large-pitch arrays (*Camacho et al.*, 2009). In this method, weighting factors are defined based on the instantaneous phase coherence between delayed echoes at each time point. After inserting proper delays on receive, the echoes of the main lobe are in-phase, so the variance of phases at each time point is close to zero. On the other hand if the echoes originated from the grating lobe region, they are shifted by one wavelength between adjacent elements. Therefore, these echoes are less in phase in the time domain and in the case that they are broadband, result in high phase variance. PCI experimental results have shown that the grating lobes of large pitch arrays when using synthetic aperture beamforming can be suppressed greater than 40 dB (eg. grating lobe levels from -40 dB to -85 dB) (*Camacho et al.*, 2009). In this relatively unconventional type of beamforming (synthetic aperture), the grating lobe echoes are in fact quite broadband because only one element is pulsed during each transmit event. In the case of conventional transmit beamforming however, the grating lobe echoes are not broadband and this technique is not effective. In the same study, it was also suggested that the sign bit of recorded echoes at each time point can be considered as a coarse estimation of the signal phase to calculate sign coherence factor (SCF). This means that the computational cost for this technique is very low.

Since this technique is able to suppress the grating lobes with broadband echoes significantly (>40 dB experimentally) and its implementation is very simple, I decided to adopt the PCI in the design of a large-pitch phased array for auditory imaging. However, as previously mentioned, this technique is not practical for suppressing grating lobes of phased arrays with conventional transmit beamforming because the grating lobe echoes are narrowband. Hence, other techniques have been developed in this dissertation in order to increase the effectiveness of PCI with conventional transmit beamforming, suitable for intra-cochlear imaging.

2.3 Doppler Ultrasound

When an acoustic source is moving relative to a stationary observer, the frequency of the sound that the observer hears is different from the source. If the source is moving toward the observer, the detected frequency is higher than the emitted frequency while it is lower when it is moving away. This is referred to as the Doppler effect. The difference between the emitted and the detected frequency is called the *Doppler shift* and is proportional to the velocity of wave source (*Christopher*, 1998; *Evans*, 1989). Thus by measuring the Doppler shift, the velocity of sound source can be calculated.

The Doppler effect was applied to the ultrasound waves by Satomura for the first time in 1959 in order to measure the blood flow of peripheral vessels, in-vivo (*Satomura*, 2005). Since then, Doppler ultrasound in the frequency range of 1 MHz-10 MHz has been widely used in the clinics for measuring the blood flow of the vascular system, non-invasively. The first medical Doppler ultrasound systems were based on transmission and reception of a continuous wave (CW) to estimate the velocity of moving blood cells. In CW Doppler ultrasound, since the transducer continuously transmits the ultrasound wave into the tissue, a separate transducer is needed for receiving the continuous echo. Both transducers are usually placed on the same housing and the sample volume is within the overlap of two ultrasound beams (*Christopher*, 1998; *Evans*, 1989).

The transmit ultrasound pulse and the received echo for a single scatterer can be defined as follow:

$$\begin{aligned} \text{Tx}(t) &= m_1 \cos(2\pi f t) \\ \text{Rx}(t) &= m_2 \cos(2\pi (f + f_d) t + \Phi_d) \end{aligned} \tag{2.17}$$

where f is the ultrasound frequency, f_d is the Doppler shift, m_1, m_2 are the amplitudes, and Φ_d is the phase difference between Rx (received echo) and Tx (transmitted pulse). In order to extract the Doppler shift from the received echo, coherent demodulation is done where the echo (Rx(t)) is multiplied by the master oscillator signal and is low-pass filtered (LPF).

$$\begin{aligned} \text{I}(t) &= \text{LPF}(\text{Rx}(t) \cdot m_r \cos(2\pi f t)) \\ &= \frac{m_2 m_r}{2} \cos(2\pi f_d t + \Phi_d) \end{aligned} \tag{2.18}$$

Then, the Doppler equation is used to estimate the velocity of blood cells.

$$f_d = \frac{2 f v_b \cos(\theta_d) cos(\alpha_d/2)}{c_b}, v_b << c_b \tag{2.19}$$

where v_b is the blood cell velocity, θ_d is the angle between the transducer axis and the vessel, α_d is the angle between two transducers, and c_b is the speed of ultrasound in the blood. This equation is only valid when the blood velocity is smaller than the speed of sound in the blood which is always the case in vivo (*Christopher*, 1998). Although the velocity of blood cells is estimated with the mentioned signal processing method, the direction of blood flow is unknown. The quadrature coherent demodulation technique can be used to extract the in-phase and quadrature components of the Doppler signal and separate forward flow from reverse flow (*Christopher*, 1998; *Cobbold*, 2007). The main drawback of CW Doppler systems is that since the transmit pulse is continuous, there is no depth discrimination. In other words, it is not possible to measure the blood flow of a single vessel at a specific depth precisely and the measured signal is usually the result of the blood velocity of all vessels within the sample volume. It is a big problem in studying deep vascular structures such as the heart. To overcome this issue, Pulsed-wave Doppler ultrasound has been developed which is based on the pulse-echo technique (*Christopher*, 1998; *Evans*, 1989).

In Pulsed-wave Doppler ultrasound (PW Doppler), short bursts of ultrasound pulses are

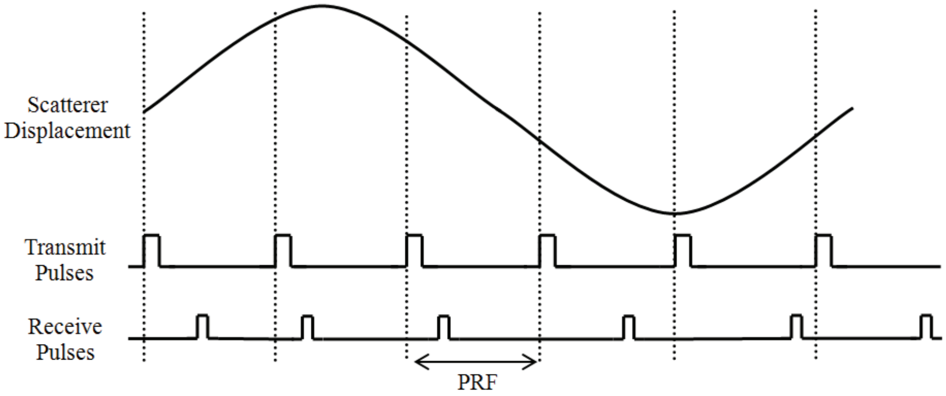

Figure 2.12: Pulsed-wave Doppler Ultrasound (Redrawn from *Cobbold* (2007)).

transmitted into the tissue at regular intervals called the pulse repetition frequency (PRF). The echoes are received by the same transducer a short period of time later (after a delay) which is adjusted based on the range of measurement called range gate (figure 2.12).

PW Doppler ultrasound is usually combined with B-mode imaging as the duplex mode, for accurate positioning of the sample volume within a single blood vessel (*Christopher*, 1998; *Evans*, 1989). Since the transmitted ultrasound pulse is broadband in this technique, the Doppler shift cannot be extracted from the coherent demodulation method reviewed for CW Doppler. The Doppler effect is actually detectable from the phase change of recorded echoes at successive PRFs. When an object is stationary, the successive echoes have the same time-of-flight while it increases or decreases if the object is moving away or toward the transducer (figure 2.12). Thus, the time-shift between echoes recorded at successive PRFs can be calculated to estimate the velocity of moving object (v_m) using following equation (*Cobbold*, 2007).

$$v_m = \frac{c \triangle t_j}{2t_{PRI} \cos\theta_m} \tag{2.20}$$

where $\triangle t_j$ is the time-shift, the t_{PRI} is the pulse repetition interval, c is the velocity of sound in the medium (e.g. water), and the θ_m is the angle between the probe and the scatterer. In order to estimate the time shift ($\triangle t_j$), the cross-correlation between successive echoes ($R_j(n)$) is computed.

$$R_j(n) = \sum_{i=1}^{M} x_0(i)x_j(i+n) \tag{2.21}$$

$$\triangle t_j = \frac{n_{R_j=max(R_j)}}{f_s}$$

where x_j is the echo recorded at each PRF, x_0 is the first recorded echo considered the reference, M is the length of recorded echoes at each PRF, and f_s is sampling frequency of the echoes. The main drawback of PW Doppler ultrasound is that there is an upper limit on the measurable velocity (v_{m-max}) as shown in (2.22) because of the Nyquist criteria. In PW Doppler technique, the displacement of moving object is actually sampled by sending broadband ultrasound pulse and receiving echoes with variable phase at sampling frequency of PRF. Therefore velocity of the moving object should be less than half of PRF in order to measure it without aliasing (*Cobbold*, 2007).

$$v_{m-max} = \frac{c \cdot \mathrm{PRF}}{4f \cos\theta_m} \tag{2.22}$$

where c is the velocity of sound in water, f is the transducer frequency, and θ_m is the angle between the probe and the moving object.

Despite this issue, PW Doppler is currently a preferable technique for measuring blood velocity of vascular systems mostly because of the depth resolution that it offers. High-frequency PW Doppler ultrasound (>20 MHz) is practical for measuring blood velocity in the microcirculation system within the body because increasing the operating frequency results in higher spatial resolution, better velocity resolution, and an increase in the blood echo intensity relative to the tissue (*Christopher*, 1998). However, the depth of penetration is limited and only microvessels at shallower depths can be measured. There have been a few high-frequency PW Doppler systems reported in the literature with the ability to detect blood velocity less than 2 mm/s in vessels smaller than 50 μm (*Berson et al.*, 1989; *Ferrara et al.*, 1996; *Christopher et al.*, 1997). In *Xu et al.* (2008), the first high frequency PW Doppler linear array ultrasound system is developed for assessing the cardiovascular function in small animals which has shown promising results. Recently, a very small 44 MHz single element ultrasound transducer with 0.4 mm aperture has been fabricated to measure blood flow in the microcirculation of the retina. The small size of the probe is essential since it should be inserted through the sclera to access the posterior portion of the eye (*Zhou et al.*, 2007).

As mentioned, currently there is no in-vivo technique available for measuring vibration of basilar membrane which is located within the cochlea and is only accessible through the round window membrane. Considering the capability of high-frequency PW Doppler ultrasound in measuring blood velocity of microvessels within the body (ie posterior portion of the eye) and the possibility of miniaturizing the probe size, it is hypothesized that this technique might be applicable for studying the mechanics of basilar membrane with minimally-invasive procedure.

2.4 General Summary

The cochlea is a snail-shaped structure in the inner ear which consists of fluid-filled scala tympani, scala media, and scala vestibuli. It is embedded deeply inside the temporal bones and is only accessible through the oval window and the round window membrane. The vibration of stapes footplate attached to the oval window initiates a travelling wave on the basilar membrane which causes the deflection of hair cells and stimulation of the auditory nerve. The vibration of the basilar membrane is essential to the transduction of perceived sound. This membrane has a nonlinear compressive response about the characteristic frequency, which is essential for amplifying low level sounds and suppressing high level intensities. Also, the low level intensity sounds are highly tuned at the CF. Animal models and postmortem studies have shown that these nonlinear patterns are not present when the cochlea is damaged. Therefore, the mechanics of basilar membrane could potentially be exploited to diagnose inner ear disorders such as Meniere's Disease. MD is a chronic inner ear disorder which is accompanied by vertigo, tinnitus, and hearing loss. These symptoms fluctuate over time and their presence is dependent on the stage of the disease. Histopathological studies show that endolymphatic hydrops is usually present for MD patients. The over-pressurization of the endolymph in the scala media displaces basilar membrane mostly at the apical end to a degree that it is adhered to the scala tympani. Several studies have shown that none of the currently used diagnostic techniques are reliable for the diagnosis of MD because there is such a large variation in the recorded signals within the patients and normal subjects.

The problem with existing techniques is that the assessment of intra-cochlear structures, such as the basilar membrane, are based on indirect approaches for the diagnosis of inner ear disorders. The accuracy of diagnosis of inner ear disorders could be highly improved if intra-cochlear structures such as the basilar membrane can be monitored and measured directly by visualizing the cochlea in-vivo.

Laser Doppler vibrometer is widely used in literature for measuring the vibration of basilar membrane through and around the round window. Since the basilar membrane is not very reflective, the cochlea is usually opened up in order to place reflective beads on it. Not only does this affect the true mechanical response of the cochlea, this method is also impractical for in-vivo applications due to the violation of the cochlea. Moreover, the recorded BM signal might be contaminated with the round window vibrations because the range cannot be properly differentiated with this technique. Doppler optical coherence tomography is suggested as another alternative for measuring the basilar membrane vibration through the round window. However, the depth of penetration is quite small in this technique, which prevents the imaging of human temporal bones that have soft tissue folds in the round window niche. One of the aims of this thesis is to develop a reliable Doppler-based technique for measuring the basilar membrane vibration without damaging the cochlea which can be applicable in in-vivo as a diagnostic tool.

High-frequency Pulsed-wave Doppler ultrasound is currently used for measuring blood velocity of the microcirculation system. Large velocity range (50-300 μm/s) within small vessels ($\sim$50 μm) can be measured using this technique. Promising results have been reported on fabrication of small size high frequency ultrasound transducers for studying microcirculation of posterior portion of the eye in small animals. Considering the high spatial resolution and large velocity range that can be detected with this technique, high-frequency PW Doppler ultrasound could potentially be applicable for measuring the velocity of basilar membrane vibrations through the round window membrane.

Visualizing intra-cochlear structures is another direct technique for assessing functionality of the cochlea. However, structures within the cochlea such as the basilar membrane cannot be visualized using current imaging techniques such as MRI because they do not have sufficient resolution. Considering the fact that auditory disorders such as MD can affect anatomical characteristics of the cochlea such as the static position of basilar membrane, real-time intra-cochlear imaging could potentially be an effective method for diagnosing inner ear disorders.

Ultrasound imaging is a safe, real-time, and cheap imaging modality that is widely used in clinics to visualize intra-structures within the body, non-invasively. The resolution of these systems is increased by increasing the operating frequency. High-frequency ultrasound imaging ($>$20MHz) can provide high resolution images from micro-scaled structures and is widely used in small animal imaging, intravascular imaging, and ophthalmic imaging. High-frequency array-based ultrasound systems are usually desirable in order to have high lateral resolution with large depth-of-field and high frame rate.

Since the structures within the cochlea are quite small and the round window membrane is the only soft tissue window into the cochlea, high-frequency array-based ultrasound might be applicable for visualizing intra-cochlear structures. However, development of these systems is problematic due to the challenges associated with the fabrication of small inter-element pitch array transducers required to avoid grating lobe artifacts. Although some high frequency linear array systems have recently been developed, no high-frequency phased array has been successfully developed. Phased array transducer provides large field of view with a small aperture by steering the beam to different angles. It is a suitable option for inner ear imaging where large field of view within the cochlea is desired through the small opening of the round window. Several techniques have been proposed in the literature to suppress grating lobes resulting from phased arrays with large element pitch. They are mostly based on the design of arrays with aperiodic element patterns or the calculation of weighting factors to apply on the recorded echoes. Phase coherence imaging is a simple signal processing method which has shown promising results in suppression of grating lobes with broadband echoes. This method might be feasible for the proposed application as it allows for the development of high-frequency phased arrays with large element-to-element pitch.

In the next section, proposed studies for assessing the feasibility of high frequency ultrasound in visualization of inner ear structures and study of the basilar membrane mechanics will be presented.

CHAPTER 3

STUDY ONE: EX-VIVO HIGH-FREQUENCY ULTRASOUND IMAGING OF THE AUDITORY SYSTEM

3.1 Introduction and Motivation

Hearing loss typically takes one of two forms: 1) sensorineural hearing loss, which affects the inner ear (cochlea) or auditory nerve and 2) conductive hearing loss, which is a condition primarily affecting the middle ear (ossicles and tympanic membrane) or external ear canal. Mixed forms are also possible.

In the middle ear, direct visualization of pathologic tissue or fluid, and the ability to evaluate the state of the ossicles would greatly enhance the diagnosis of conductive hearing disorders and also provide a non-surgical means of assessing the performance of middle ear implants commonly used to reconstruct the ossicular chain. For the cochlea, in-vivo visualization of the basilar membrane, the round window membrane (RWM), and stria vascularis could reveal morphologic changes associated with inner ear disorders such as Meniere's Disease, sudden and sub-acute sensorineural hearing loss, autoimmune inner ear disease, and perilymphatic fistula, and could revolutionize the ability to diagnose and understand these poorly understood conditions. Visualization of the auditory system could also be used as an intra-operative guidance tool during cochlear implantation surgery (to visualize the placement of electrodes) and acoustic neuroma surgery (to visualize remaining tumor from brainstem).

Current in-vivo imaging techniques such as MRI and CT do not have the spatial resolution to visualize micro-anatomy in the cochlea, such as the basilar membrane (*Sennaroglu*

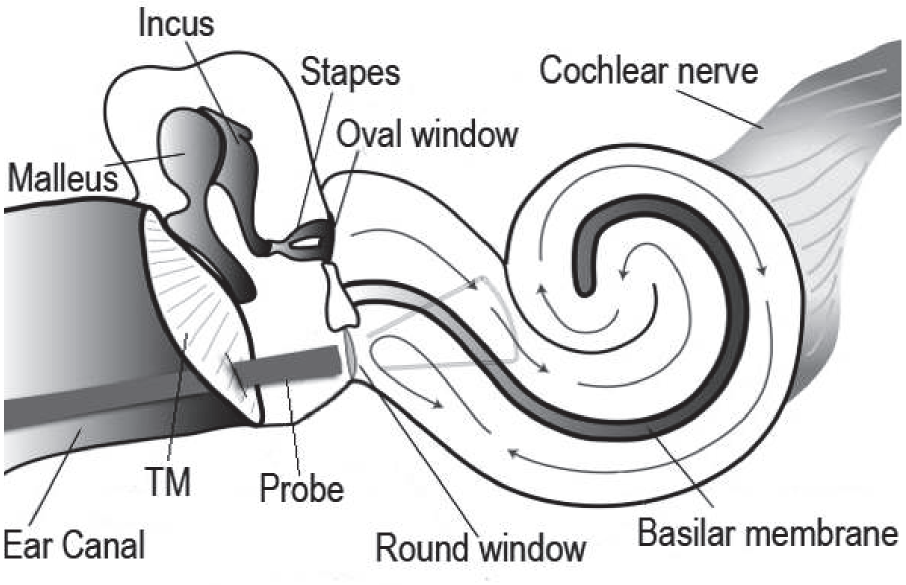

Figure 3.1: Diagram illustrating the major components in the human auditory system. The tympanic membrane and ossicular chain vibrate the cochlear fluid and in turn the basilar membrane (*Brown et al.* (2009), with permission of the Elsevier).

et al., 2002). Recently, it has been shown that micro-CT can offer sufficient resolution to visualize the intra-cochlear spaces on human cadaveric temporal bones (*Postnov et al.*, 2006) however the membranes within the cochlea can not be imaged properly with this modality, not to mention the fact that the chamber size of micro-CT scanners is far too small for in-vivo use. High-resolution MRI (9.4 T magnetic resonance scanner) has shown promising results in visualizing intra-cochlear structures in ex-vivo studies, however, safety is a big concern due to the strong magnetic field in high MRI and the immense cost associated with a 9.4 T magnet prevents wide scale adoption (*Silver et al.*, 2002). This chapter describes preliminary images obtained of cadaveric ear tissues using an in-house developed high-resolution ultrasound system, showing that high-frequency ultrasound has great potential as a diagnostic tool in otology.

Figure 3.1 shows some of the larger clinically relevant structures of the auditory system. Other than the round and oval windows, the cochlea is completely surrounded by dense bone. There are some channels directed intra-cranially, such as the vestibular and cochlear aqueducts, but these are not accessible. Therefore, the most logical approach to image the cochlea with ultrasound is through the RWM. Potentially a RWM imaging probe could be designed similar to a conventional catheter-based probe used in intravascular imaging, but three to four times larger (due to the larger diameter of the access route). To access the cochlea in-vivo, one would need to pass the imaging probe through the middle ear by creating a small hole in the eardrum. This can be created during a routine and minor clinical procedure (myringotomy). This is the same extremely common procedure required for the insertion of ventilation tubes in children. An example of such an endoscopic probe is depicted in figure 3.1. The direction of the ultrasound beam from the front face of the probe would not exactly be forward looking, as is shown in figure 3.1, but actually need to be directed to a mild angle from the true forward direction (approximately 20 degrees) to optimally image the cochlea through the RWM.

The middle ear can be imaged even less invasively by running an endoscopic probe through the ear canal to the tympanic membrane. Such a probe, which could be up to 5 mm in aperture, would image across the tympanic membrane to the middle ear. In an in-vivo situation, the middle ear would need to be filled with a liquid such as water or saline in order to provide the necessary acoustic coupling. This can be relatively easily accomplished in the clinic with a transtympanic needle such as those routinely used for injection of drugs such as Gentamicin or steroids.

In order to evaluate the feasibility of high frequency ultrasound for imaging the auditory system, several ex-vivo preliminary studies were conducted. A previously developed 50 MHz annular array imaging system (*Brown et al.*, 2004a; *Brown and Lockwood*, 2005) was used to collect series of 2D high-resolution ex-vivo images of the cadaveric human auditory system. The imaging system consisted of a 2 mm diameter, 7-element, equal- area annular-array transducer (*Brown et al.*, 2004a), and a FPGA-based beamformer covering a 5.12 mm scan depth from 3 mm to 8.12 mm (*Brown and Lockwood*, 2005). This chapter presents the details of this ex-vivo high frequency ultrasound imaging study.

3.2 Materials and Methods

In-house 50 MHz Annular array Ultrasound System

The available high-frequency ultrasound system was originally developed by Dr. Brown during his PhD (*Brown*, 2005). The high frequency annular array transducer was a kerfless array, based on a fine-grained PZT-5H substrate. The array elements were fabricated by depositing the annular electrode pattern onto the surface of substrate, using high-resolution photolithography (*Brown et al.*, 2004a). The array had a -6 dB bandwidth of 52% and an insertion loss of -16 dB. The -6 dB two-way beamwidth at f/2 was 75 μm (*Brown et al.*, 2004a).

A cross-section diagram of the proposed transducer is shown in figure 3.2 that lists the ten major features of the transducer. The array is patterned with electrodes on top of the piezoelectric resonator, and wire bonds are used to connect them to an interposer. An interposer sits elevated and insulated from the piezoelectric, with bonding pads used to complete the array connections to coaxial cables. Above the insulating backing layer,

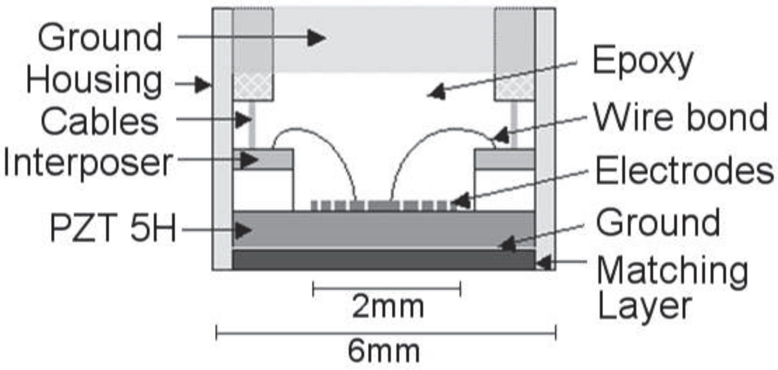

Figure 3.2: Cross-section diagram of the 7-element annular array transducer showing the major elements. These include the housing, wire-bonds, interposer, miniature coax cables, array electrodes, piezoelectric substrate, and matching layer (*Brown et al.* (2009), with permission of the Elsevier).

located immediately behind the array, is a conductive epoxy that connects the ground sheaths of the coaxial cables to the transducer housing.

The transmit beamformer was based on digitally programmable delay circuit which could be adjusted to generate up to four focal zones. The digital receive beamformer was based on two high-speed field programmable gate arrays (FPGA) used to capture the in-phase component ($I(t)$) and quadrature component ($Q(t)$) in parallel. These components were separated prior to the sampling by using a quarter wavelength delay line. With quadrature sampling, the sampling frequency of the circuit was reduced to the bandwidth of the demodulated signal rather than Nyquist sampling rate. Instead of inserting delays, a continuously varying sampling frequency was used to trigger analog-to-digital converters (A/D) in order to sample only data points that were required for focusing. The varying sampling frequency was generated by FPGAs, using a coarse term as the integer multiple of the clock and a fine term based on logic buffers. The digital receive beamformer dynamically focused at all depths between 3 and 8.12 mm and the transmit beamformer cycled between four transmit focal zones at depths of 3.5, 4.5, 5.9 and 7.4 mm. The signal gain of the system was controlled by a potentiometer used to adjust the amplitude of the excitation pulses.The transmit beamformer, receive beamformer, transducer, and front-end electronics were all integrated into one system controlled by a PC and software written in Visual C++. The data was transferred to PC by a high-speed I/O interface card to generate 2D ultrasound images. The software also controlled a high precision linear servomotor to translate the annular array mechanically in order to collect each line of the image (*Brown and Lockwood*, 2005).

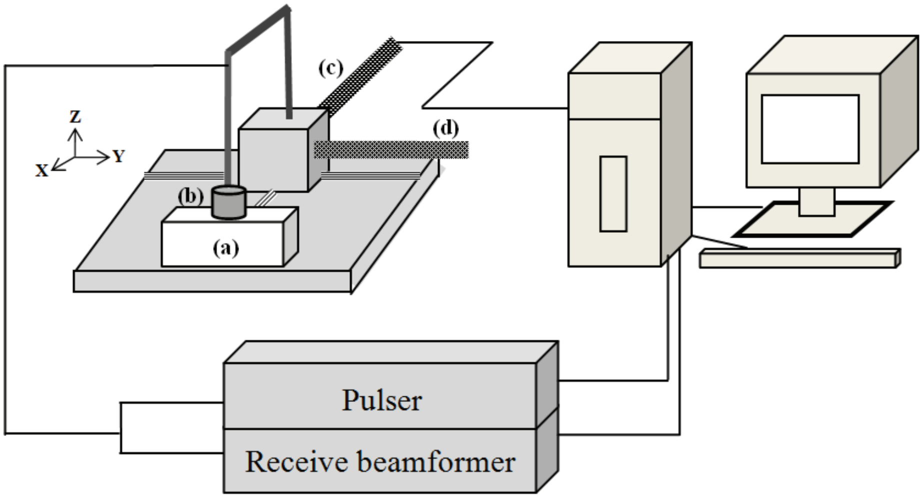

Figure 3.3: Diagram showing the experimental set-up for ex-vivo imaging of the cadaveric temporal bones. The container for the tissue sample (a), the high-frequency annular array (b), the servo motor (c), micrometer positioning stage (d), the pulser for transmit, and the digital receive beamformer are shown.

The Ex-vivo Auditory Imaging Experiments

As shown in figure 3.3, the transducer was mounted on the arm of the Z-axis positioning stage. This arm extends into an acrylic container used as a water tank for imaging tissues. The entire positioning platform on which the acrylic water tank was situated contains X-Y-Z positioning micrometers as well as two separate tilt control micrometers. A computer controlled high precision linear servo-motor (figure 3.3(c)) was used to mechanically scan the transducer in the X direction. The motor had a minimum step size of 0.015 μm, making the system ideal for experimentally measuring radiation patterns or imaging phantoms but too slow for real-time imaging. If a faster motor were used, the system could be run in real-time. For generating the three-dimensional (3-D) images, two-dimensional (2-D) slices spaced 100 μm apart were collected by translating the probe manually in the Y direction and were stitched together using a commercially available software package (Osirix Viewer; Osirix, Geneva, Switzerland). All of the images generated during this study are displayed with a dynamic range of 54 dB. The handling and imaging of the cadaveric tissues described throughout this chapter were approved by the Ethics Review Board at Dalhousie University, Faculty of Medicine.

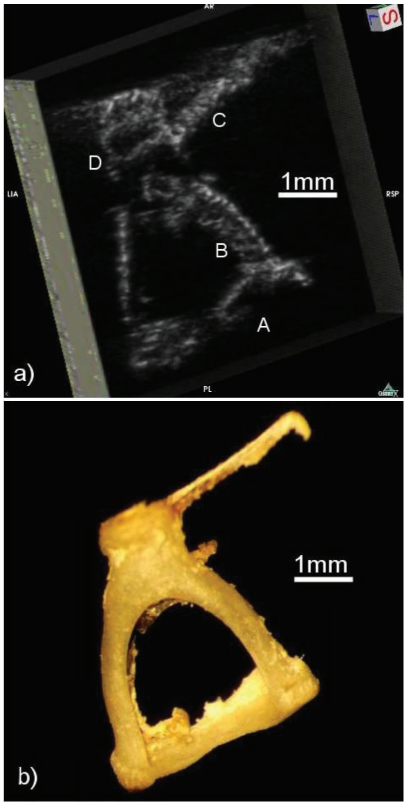

Figure 3.4: a) 50 MHz ultrasound image of the stapes and b) Photograph of the stapes bone through a microscope (*Brown et al.* (2009), with permission of the Elsevier).

3.3 Imaging Results

For imaging the three cadaveric ossicles, the bones were each individually mounted onto a small toothpick using cyanoacrylate adhesive. The toothpick extended off to an angle so that the individual bones could be imaged clear of any obstructions. The mounted ossicles were then submersed in a water bath and imaged. Figure 3.4a shows a preliminary 3D image of the stapes generated by the annular array system. Figure 3.4b shows a photograph of this stapes through a microscope. Images such as this could potentially be generated in a minimally invasive manner in-vivo with a much smaller endoscopic probe resting against the tympanic membrane. Again, in an in-vivo situation, the middle ear would be filled with a saline solution using a transtympanic needle in order to provide the necessary acoustic coupling required for ultrasound imaging. The stapes is the smallest bone in the human body and is situated at the end of the ossicular chain. It rests up against the oval window at the basal end of the cochlea. Most features of the stapes are clearly visualized in figure 3.4a such as the stapedial footplate (A), the suprastructure or crura stapedis (B), the stapedial tendon (C), and the head of the stapes (D). The footplate (A) is perfectly fitted into the oval window of the cochlea and provides excellent mechanical coupling from the ossicular

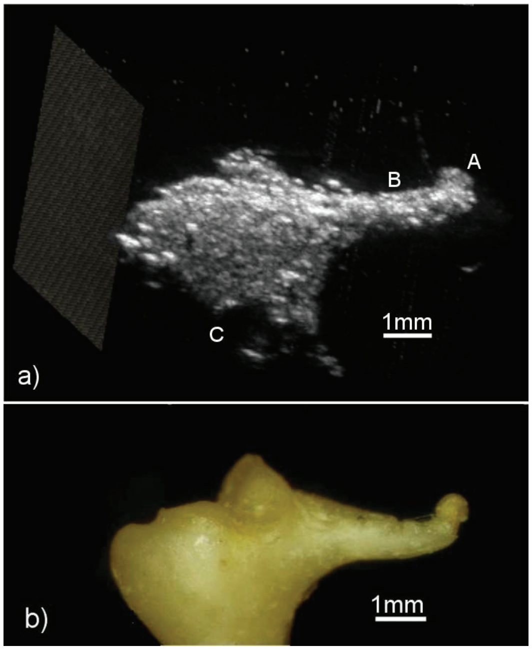

Figure 3.5: a) 50 MHz ultrasound image of the incus and b) Photograph of the incus bone through a microscope (*Brown et al.* (2009), with permission of the Elsevier).

chain to the cochlear fluid. The average length of stapes footplate is 2.68 mm and its width is 1.26 mm (*Harneja and Chaturvedi*, 1973). The crura, the ”arch-shaped” structure (B), distributes the force delivered to the footplate and the stapedial tendon attaches to the stapedius muscle, which contracts in response to loud sounds and protects the inner ear by damping transmission of acoustic energy to it. The stapes head (D) forms part of the incudo-stapedial joint, which is a complex structure that transmits the 3 dimensional lateral ossicular motion to the stapes. Like most joints in the human body these can become inflamed and arthritic, and worsen with age (*Jahn and Santos-Sacchi*, 2001).

Figure 3.5a shows a 3D image of the incus and figure 3.5b shows a photograph of the incus through a microscope. This is the second bone in the ossicular chain and its features can be clearly visualized in the ultrasound image. The three main incus sub-structures are the lenticular process (A), the long process of the incus (B), and the short process of the incus (C). The lenticular process (A) forms part of the incudo-stapedial joint with the stapes head. The long process (B) is a long thin process that reaches from the attic of the ear from the head of the incus to the stapes. Its length relative to the length of the malleus is one part of the lever that provides a pressure gain from the tympanic membrane to the cochlear fluids for acoustic impedance matching. The short process (C) is part of the suspensory mechanism that allows the rocking movements of the incus about a rotational axis. This process is connected to the surrounding bone via the incudal ligaments in the incudal fossa.

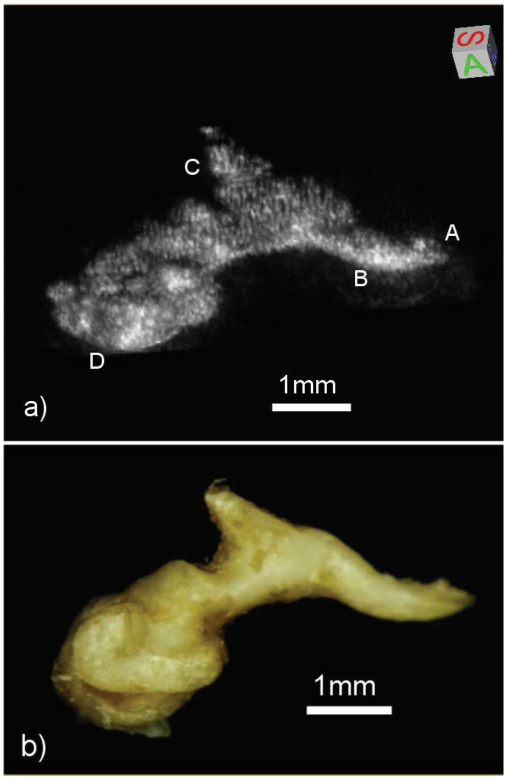

Figure 3.6: a) 50 MHz ultrasound image of the malleus and b) Photograph of the malleus bone through a microscope (*Brown et al.* (2009), with permission of the Elsevier).

The maximum length of incus is about 3.14 mm and its width is 1.82 mm (*Harneja and Chaturvedi*, 1973).

Figure 3.6a shows a 3D ultrasound image of the malleus and figure 3.6b shows a photograph of the malleus through a microscope. The maximum length of malleus is about 7.15 mm (*Harneja and Chaturvedi*, 1973). Again many of the sub-malleus features can clearly be visualized in the ultrasound image. The umbo (A) is situated at the tip of the malleus and connects the malleus to the tympanic membrane (eardrum). The manubrium (B) is the long arm of the malleus and rests up against the tympanic membrane. The anterior malleolar ligament and short process of the malleus (C) connects the malleus anteriorly to the temporal bone, and again forms part of the suspensory ligaments that allow a rotational axis of movment. These ligaments can become calcified in disorders such as tympanosclerosis, and cause conductive hearing loss. The head of the malleus (D) forms an articulating joint with the head of the incus, the incudo-malleolar joint. The head of the malleus can become fixed, either acquired or congenital, and this can be difficult to diagnose cause of conductive hearing loss.

To investigate the feasibility of imaging the middle ear across the tympanic membrane, a cadaveric temporal bone was imaged with the middle ear completely intact. Because of

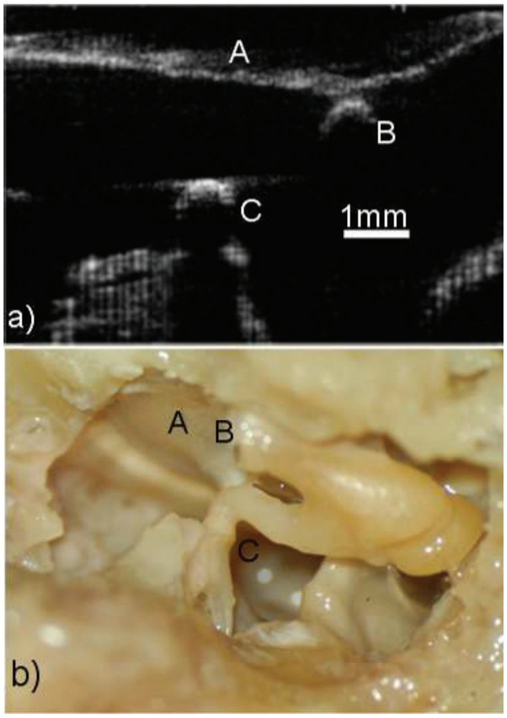

Figure 3.7: High-frequency ultrasound image of the middle ear across the tympanic membrane. The middle ear has been injected with water. a) 50 MHz ultrasound image of a cadaveric middle ear through the tympanic membrane and b) Microscopic photograph of the cadaveric middle ear through a hole drilled into the side post-imaging (*Brown et al.* (2009), with permission of the Elsevier).

the large packaging of the probe, the ear canal had to be removed in order to have wide access to the tympanic membrane for placing the probe. The middle ear was filled with water through a small hole drilled through the temporal bone around the eardrum so as not to disturb it. The bone was then placed in a water bath and 2D and 3D images were generated. Figure 3.7a shows an example of a 2D image of the middle ear across the tympanic membrane, where many middle ear structures can clearly be visualized. The tympanic membrane (A) is intact and located along the top portion of the image. The 2D slice has also captured a cross-sectional view of the umbo (B), the stapes, and the incudo-stapedial joint (C). It should be noted that in this image the ultrasound was not powerful enough to fully penetrate all the way to the most medial limit of the ossicles. This is in part due to the fact that this relatively high-frequency (50 MHz) system attenuates in bone very rapidly due to the age and stiffness of the ossicles in this formaldehyde fixed temporal bone. In-vivo, the ossicles can be expected to be less stiff and therefore more acoustically transparent. Figure 3.7b shows a photograph from a hole drilled into the side of the middle ear where the features visualized in the ultrasound image can be clearly seen. Again the plane of the ultrasound image is perpendicular to the long axis of the incus and

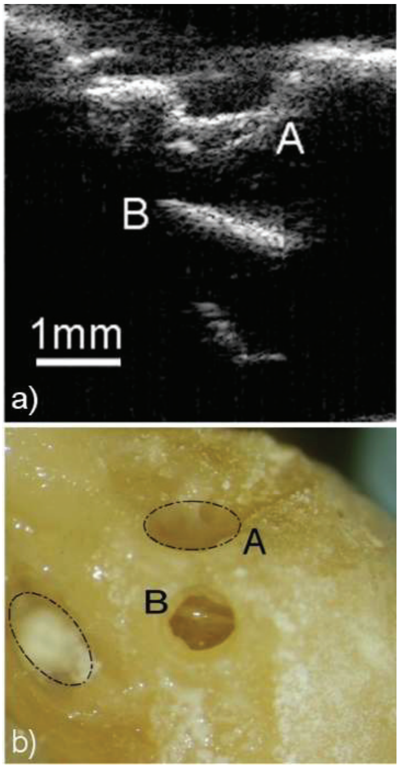

Figure 3.8: a) 50 MHz ultrasound image of a cadaveric cochlea through the round window membrane and b) Photograph of the cadaveric cochlea through a microscope with a hole drilled into the side (*Brown et al.* (2009), with permission of the Elsevier).

malleus but in plane with the stapes.

Images of the cochlea were also generated through the round window membrane. Because the cochlea is surrounded by dense bone, the round window is one of only two acoustically transparent points of access (the other is the oval window where the stapes is normally situated). Because the probe has relatively large packaging, it was needed to drill away some of the posterior canal wall to adequately seat this probe over the RWM. This was only necessary because of the large packaging and not because the transducer aperture was too big. Figure 3.8a shows a 2D image of the cochlea generated with the annular array system through the round window membrane. Although virtually nothing can be imaged underneath the dense bone that surrounds the round window membrane, underneath the round window (A), the ultrasound is able to penetrate into the cochlea where the basilar membrane can clearly be visualized (B). Figure 3.8b shows a photograph through a microscope of the cochlea. The two windows into the cochlea (round and oval) have been highlighted with dotted lines and a hole was also carefully drilled into the basal end of the cochlea in order to photograph the position of the basilar membrane and confirm the anatomical accuracy of the ultrasound images. The ultrasound imaging was performed before this hole was drilled into the cochlea. The ability to visualize the basilar membrane in-vivo has great clinical importance and could be used to diagnose a wide range of inner ear disorders such as Meniere's Disease. It should be noted however that because the aperture of the array is 2 mm in diameter and the round window is only approximately 3 mm in diameter, the beam becomes distorted after 1 to 2 mm of linear translation. Ideally a goniometric rotational motor could be used to create a sector scan so that the image window inside the cochlea is maximized and the distortion due to the bone is minimized.

3.4 Discussion

Middle Ear Imaging

There are two main areas in otology in which this kind of very high resolution *in-vivo* ultrasound has great potential. The first is imaging of the middle ear. A simple non-invasive middle ear probe could provide information about the presence of fluid in the middle ear resulting from serous otitis media or suppurative otitis media, which is not always clear in thickened or opaque tympanic membranes. Another major diagnostic challenge is determining the cause for conductive hearing loss in the presence of an intact eardrum. In these cases, imaging could differentiate ossicular discontinuity from fixation of the ossicles (e.g. otosclerosis, tympanosclerotic fixation etc). It may also allow to determine the site of the fixation. This would avoid the need for surgical exploration for diagnosis, and would provide accurate guidance for correct surgical intervention. Granulation tissue in the middle ear could be detected and possibly differentiated from the more dangerous cholesteatoma, which has a different internal micro-architecture. There are numerous other opportunities to use this probe as an intra-operative middle ear tool. For instance, the ultrasound probe may be able to diagnose labyrinthine fistulas before they are accidentally opened, differentiate the facial nerve from similar looking granulation tissue, or determine if there is residual cholesteatoma in the sinus tympani or behind intact ossicles. Other possible uses include as a tool to diagnose conditions such as perilymphatic fistula (micro-tear in the round window), position of a prosthesis in the oval window during revision stapedotomy surgery, and to verify that prostheses used for ossicular reconstruction have not moved after the tympanic membrane is replaced back into its normal position, a common cause of dislodgement of an otherwise perfectly placed prosthesis.

The quality of the middle ear ultrasound images has been compared with the two other possible competing imaging for this application, CT and OCT. Figure 3.9 shows an X-ray image generated of an intact cadaveric middle ear. The image was generated with a commercial scanner (GE Medical Systems, Lightspeed Pro 16) with the resolution on the

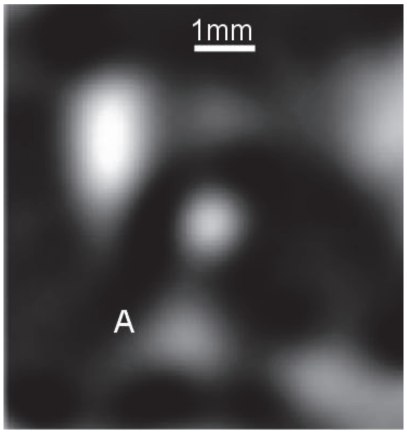

Figure 3.9: A CT image of the middle ear using a commercially available scanner (*Brown et al.* (2009), with permission of the Elsevier).

highest setting (largest number of X-ray projections). There is only one slice that actually captures any of the stapes (A) in the CT data set since the slice thickness is limited to 1 mm. The in-plane resolution was measured to be approximately 700 μm and as a result this image provides very little detail in comparison with the high-frequency ultrasound images of the middle ear (figures 3.4, 3.5, 3.6, 3.7). The stapes crura (A) however, can be crudely visualized but in an in-vivo situation, there would also be motion artifacts due to the low temporal resolution. OCT images have also been generated across the TM (figure 4 *Pitris et al.* (2001)) in an orientation almost identical to that shown in figure 3.7. The OCT image can only properly resolve the TM and the ossicles beneath the TM are extremely blurred due to optical scattering. Only small portion on the surface of the malleus is resolved with OCT clearly showing that the ultrasound images provide much better visualization.

Inner Ear Imaging

Imaging the inner ear is the other major imaging application of this technology. The ability to visualize the basilar membrane in-vivo has great clinical importance and could be used to diagnose a wide range of inner ear disorders. Conditions such as endolymphatic hydrops result in enlargement of the endolymphatic compartment, with ballooning of Reissner's membrane, and displacement of the basilar membrane. In the specimen of this work, the delicate Reissner's membrane has been dessicated and therefore could not be imaged or photographed, but the imaging resolution is sufficient that visualization should be possible. Endolymphatic hydrops is thought to result clinically from Meniere's Disease. This disorder is a clinical diagnosis, and while easy to recognize in its full blown form with tinnitus, hearing loss and episodic vertigo, it can be very difficult to diagnose in its early stages, or in variant forms. Other diagnoses such as cochlear hydrops are speculatively thought to be associated with endolymphatic hydrops because of the similar kinds of hearing loss, but the actual inner ear pathology is not known. Similarly, this is the case with delayed endolymphatic hydrops. The ability to actually visualize inner ear morphology in these conditions could revolutionize understanding of them.

In other conditions such as sudden hearing loss or autoimmune inner ear disease, the end result of sudden or subacute hearing loss may represent a final common pathway that may result from many different inner ear pathologies, and being able to visualize the basilar membrane or the vascular components of the cochlea in the stria vascularis in-vivo may finally allow clinicians to shed light on these somewhat mysterious conditions. In addition, it is not clear how many current treatments for inner ear conditions (such as steroids or betahistidine for instance) work. Observing their impact directly on the inner ear may lead to important insights into pharmacologic actions and evidence based management.

Another inner ear application for this kind of imaging might be in checking placement of the electrode in cochlear implantation. In difficult cases with fibrosis in the basal turn, or altered anatomy such as in cochlear otosclerosis, being able to visualize the basilar membrane and the relative final position of the cochlear implant would be useful in verifying accurate placement.

Since such an ultrasonic imaging approach has never been attempted in-vivo, it is unknown whether or not this technique could result in harmful bio-effects within the cochlea. It is believe that since the cochlea is only sensitive to acoustic frequencies, it will not be harmed by acoustic waves at frequencies that are in the tens of MHz, but this is ultimately a question that can only be answered through in-vivo animal trials.

Other current in-vivo imaging techniques such as MRI and CT do not have the spatial resolution to visualize the micro-anatomy in the cochlea such as the basilar membrane. There is one group that has attempted OCT imaging of the cochlea in human cadaveric bones through the round window membrane (figures 2&3 , *Lin et al.* (2008)). It has been shown that the intra-cochlear spaces could be visualized with this technique. Although these images have much higher resolution than the ultrasound images (figure 3.8), in in-vivo applications the presence of folds on the niche of round window might degrade the quality of these images due to the optical scattering.

One limitation of the current incarnation of this device is that visualization through the RWM is limited to the basal turn of the cochlea. While this presents a limitation, it may be possible to image other areas of the cochlea through surgically thinned bone or to develop a new phased-array imaging probe that has the ability to beam-steer and increase the cochlear view and/or focus at deeper depths.

3.5 Conclusions

Because the middle ear and inner ears are not normally visible, clinical diagnoses are based on indirect inferences from symptoms, end results on hearing, and macroscopic visualization tools such as CT scanning. Improved visualization is the key to refining many important diagnostic classifications. Better imaging will also lead to further insights into many current pathologies that are classified based on symptoms, which may actually represent a disparate myriad of disorders causing similar end-level deficits, as well as providing improved understanding of the effects of treatment.

In this first study of this dissertation, a custom built high-resolution (50 MHz) array-based ultrasound imaging system was used to obtain images of the middle and inner ear in cadaveric temporal bones. These images have shown excellent potential as a diagnostic tool for otologists and surgeons. The 50 MHz imaging annular array used in this chapter had a total active aperture of 2 mm, however, with the additional interposer, wire bonds, and housing, the total size of the packaged device was approximately 6 mm. This total packaged size makes it too large for an in-vivo approach into either the inner ear or the middle ear.

The promising results of this chapter leaded to the second proposed study of this dissertation (chapter 4) where a high-frequency phased array ultrasound probe is designed specifically for imaging the inner ear structures, which should allow for much better images of the cochlea by generating sector scans with a relatively small aperture. For the inner ear, the total active aperture should not exceed 3 mm due to the limited window into the cochlea. In addition, the total packaged transducer should be limited to approximately 3 mm in total to keep the incision for the probe access route through the eardrum to a reasonable size.

Ultrasound has the further advantage of allowing the velocity of the various parts of the auditory system to be measured. This could be very useful in diagnosing problems such as fixation of the ossicles and could provide an unprecedented view port into the dynamical functioning of the living cochlea. Ultrasound velocimetry will be significantly less invasive than the currently-used technology of laser Doppler velocimetry (*Nilsen and Russell*, 2000), which requires a hole to be made in the cochlea. This is the focus of the third study (chapter 5) proposed in this dissertation.

CHAPTER 4

STUDY TWO: DESIGN OF A HIGH-FREQUENCY ARRAY-BASED TRANSDUCER SPECIFICALLY FOR IMAGING THE INNER EAR

4.1 Introduction

The promising results of the ex-vivo study in the first part of this dissertation (chapter 3) suggest that high frequency ultrasound offers sufficient resolution to visualize the ossicles and the inner ear structures such as basilar membrane. Imaging the middle ear is fairly straightforward since the tympanic membrane is directly accessible with an ultrasound endoscope. Inner ear imaging, however, is more challenging since the cochlea is embedded deeply inside the temporal bone and it is only accessible through the two openings, the oval window and the round window. The oval window is obstructed with the footplate of stapes, so the round window is a more suitable site for imaging inside the cochlea. The focus of second study of this dissertation is on design of a high-frequency ultrasound probe specifically optimally imaging inner ear. Design limitations are the size of the soft tissue opening as well as current transducer fabrication technology.

Although the high-frequency annular array system was shown to provide high-resolution images of the inner ear in the first study, it required mechanical translation, which limits not only the packaging size but also the size of acoustically transparent opening that the probe can image through.

A linear/phased array ultrasound probe could potentially, however, be rested up against

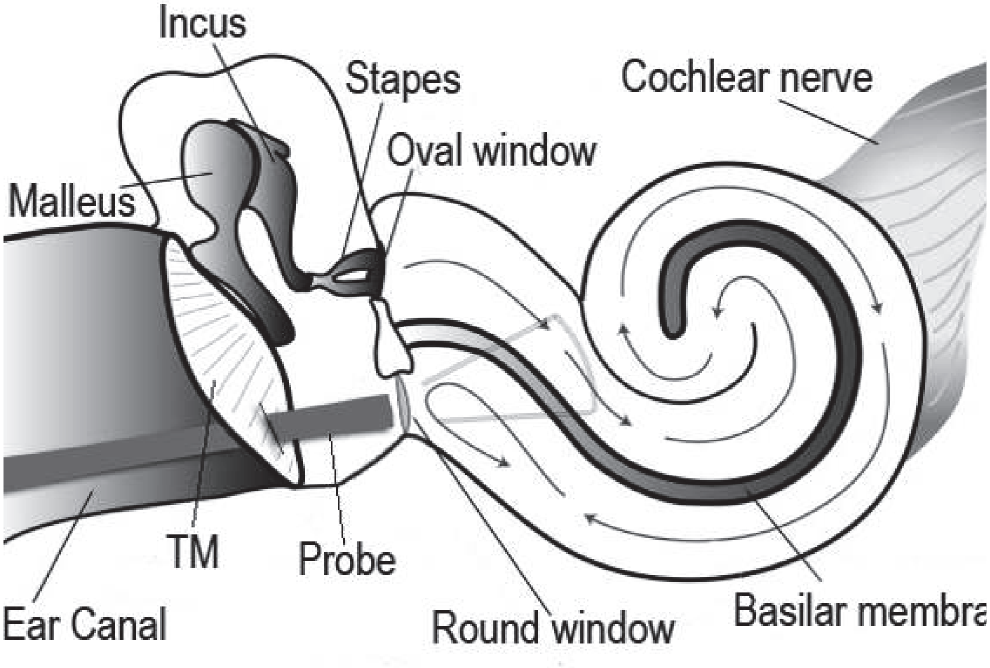

Figure 4.1: The proposed high-frequency phased array ultrasound probe for in-vivo intra-cochlear imaging. The probe is inserted through the tympanic membrane to be rested up against the round window for in-vivo intra-cochlear imaging (*Brown et al.* (2009) with permission of the Elsevier).

the round window for in-vivo intra-cochlea imaging as shown in figure 4.1. These arrays do not require any mechanical translation and can generate a large image volume through a small acoustically transparent opening. The main criterion in designing the probe is the size of transducer aperture be limited to the width of round window ($<$ 3mm). As mentioned previously, phased array transducers are desirable in situations where large field-of-view is required through a narrow opening. In a phased array, the beam is steered to different angles and that is what generates a large field-of view. In contrast, linear arrays generate a focused beam that is perpendicular to the active sub-aperture and therefore, the field-of-view and packaging size are limited to the full aperture of the array.

The main issue in fabricating array-based transducers is the size of element-to-element pitch in order to avoid grating lobes in the field of view. For linear arrays, since the beam is only focused along the main axis, the element-to-element pitch is conventionally limited to approximately 1λ, while for phased arrays, where the beam is steered to ±45 degrees, the element-to-element pitch has been conventionally limited to $\lambda/2$ to avoid grating lobes (*Cobbold*, 2007). These extremely small element pitches introduces big challenges in the fabrication of high-frequency array-based transducers. Some success, however, has been reported in the development of high-frequency linear arrays with element-to-element pitch between 1λ-2λ using modern micro-fabrication techniques (*Cannata et al.*, 2006; *Brown et al.*, 2004a, 2007; *Lukacs et al.*, 2005; *Ritter et al.*, 2002; *Ketterling et al.*, 2005; *Snook* *et al.*, 2003; *Kim et al.*, 2009; *Sisman et al.*, 2009). To date, no group has successfully developed a phased array transducer operating over 30 MHz as a result of the element pitch limitation (*Zemp et al.*, 2008). For example, at a 50 MHz center frequency, and a steering angle of 45 degrees, the element pitch needs to be reduced to 15 μm in order to push the grating lobe angle to 90 degrees (*Ziomek*, 1995). This is beyond current fabrication capabilities because the smallest kerf size that can be cut into these arrays is approximately 10 μm. This would leave only 5 μm of active piezoelectric and most of this 5 μm would be permanently damaged by heating and vibrations from whichever cutting tool is used. Transducers designers will often cheat the $\lambda/2$ slightly as the grating lobe angle does not need to be pushed to the full 90 degrees but only beyond the directivity angle of the elements. Even with cheating the $\lambda/2$ rule slightly, the element pitch required is still well below 1λ and beyond what can be fabricated with current fabrication techniques. This second study is focussed on developing a low computational cost beamforming technique that will effectively suppress grating lobes in arrays with 1λ - 1.5λ wavelength pitch.

Several techniques for suppressing grating lobes have been developed in the past. In one such technique, the array is designed with aperiodic element spacing so as to avoid constructive interference at particular angles that are sensitive to grating lobes (*Rew et al.*, 1993; *Gavrilov et al.*, 1997; *Talman and Lockwood*, 2000; *Hutchinson et al.*, 1996; *Wang et al.*, 2008). In this approach, the elements of the transducers are removed randomly during transmit or receive to form a 'sparse array'. However, the signal-to-noise ratio (SNR) is reduced in these designs because a lower number of elements is present in transmit or receive. Moreover, since the level of side-lobes is proportional to the inverse of the number of elements, the side lobes are larger in sparse arrays, offsetting some of the advantage of reducing grating lobes (*Cobbold*, 2007).

An alternate signal processing approach is to apply weighting factors on the received echoes of the elements in such a way as to minimize the effect of grating lobes without reducing the main lobe (*Ustuner and Gee*, 2007; *Li and Li*, 2003; *Synnevag et al.*, 2007; *Asl and Mahloojifar*, 2010). These weighting factors (between 0-1) can be calculated based on a number of characteristics that distinguish grating lobe echoes from main lobe echoes such as inter-element group delay (cross-correlation (*Ustuner and Gee*, 2007)), the receiving direction of the echoes (FFT (*Li and Li*, 2003)), or the power of the summed echoes (minimum variance (*Synnevag et al.*, 2007; *Asl and Mahloojifar*, 2010)). However, these 'adaptive beamforming' techniques are not suitable for high frame-rate imaging because of the high computational complexity of weighting factor calculation.

A promising new approach called phase coherence imaging (PCI) has been proposed recently for suppressing the grating lobes of large-pitch arrays at low computational cost

(*Camacho et al.*, 2009). It has been shown that this technique is also effective for improving the lateral resolution and suppressing the side-lobes which improves the image contrast. In this method, a weighting factor is defined based on the instantaneous phase coherence of delayed echoes at each time point. The echoes arriving at the array elements from points in the focus are in-phase with zero relative group delay after inserting the beamforming and beamsteering delays, so the variance of the phases measured at different elements from main lobe echoes is close to zero. The echoes originating from a grating lobe are also in phase across elements, but only because these echoes experience a group delay of one period per element. If the grating lobe echoes are broadband (short in time domain), then after a small number of elements the total group delay exceeds the echo length and the received reflections over a large number of elements do not overlap. The phase coherence of the whole array will be low for echoes from the grating lobe region since at any point in time the echo amplitude will only be large at a few adjacent elements and on the rest of the elements the phase will be determined by noise and hence will be random. This is in contrast to echoes from the main lobe region where there is no group delay or phase delay across the array after the beamforming delays are inserted and hence the phase coherence is close to unity across the array. At each sampled point in time a phase coherence factor can be calculated and used to weight the image pixel. Pixels corresponding to reflections from the main lobe will be strongly weighted while those corresponding to grating lobe reflections will have a low weight. This is the Phase Coherence Imaging (PCI) grating lobe suppression technique (*Camacho et al.*, 2009).

This PCI technique is very effective for synthetic aperture beamforming where the grating lobe echoes are highly broadband because only one element is pulsed at each transmit event. However, synthetic aperture beamforming is not desired in many imaging applications since it is susceptible to motion artifacts due to the long time interval that occurs while completing all of the pre-beamforming transmit events. This technique can also suffer from a lower signal to noise ratios as a result of pulsing one single defocused element at a time (*Jensen et al.*, 2006). In contrast, transmit focal-zone beamforming uses the full aperture on transmit and receive beamforming is performed immediately following each transmit event. Because of this, transmit focal zone beamforming is a preferred option for most in vivo ultrasound imaging applications, particularly at high-frequencies. However, grating lobe echoes received in transmit focal-zone beamforming as will be shown in the following section, are narrowband (long in time domain) because the transmit pulse itself has one period group delay between adjacent elements at the grating lobe region. This makes the PCI technique impractical for suppressing grating lobes in conventional transmit beamforming as the signals received from the grating lobe region will have a high instantaneous phase coherence over a large group of elements, making it indistinguishable from the focal region.

In this chapter, the design of a high-frequency large-pitch phased array for imaging the inner ear is presented; the limitation of phase coherence imaging with transmit beamforming is examined more closely and two transmit beamforming techniques are proposed in order to overcome the limitations associated with PCI. These two transmit beamforming techniques are theoretically and experimentally validated in combination with the PCI method for suppressing grating lobes of phased array transducers with unconventionally large element pitch. With these beamforming techniques, the fabrication of phased arrays with current transducer fabrication technology is possible.

4.2 Materials and Methods

4.2.1 Design of a Phased Array Transducer for Intra-cochlea Imaging

It should be possible to resolve structures inside the cochlea with a 40-50 MHz ultrasound transducer as disscussed in section 2.2. A 50 MHz transducer with moderate bandwidth offers an axial resolution of about 50 μm and a lateral resolution of 75 μm at f/2.5 (2.10). In designing a phased array transducer, the number of elements (N), element-to-element pitch (p), full aperture (D), and the width of elements (w_e) need to be defined. The optimal parameters of an array transducer are usually determined by calculating the transient radiation pattern of transducers with various dimensions until the desired radiation pattern is obtained (*Brown et al.*, 2004a). The transient radiation pattern of a phased array transducer is calculated using the impulse response method that was explained in section 2.2.4 (equation (2.12)) using the MATLAB code attached in appendix C.1.1. For all simulations shown below, the pulse in (2.12) ($v_{no}(t)$) was defined as a Gaussian modulated sinusoid with 50% bandwidth (*Cobbold*, 2007).

$$\begin{aligned} v_{no}(t) &= \sin(2\pi f(t-\tau_r)) \exp \frac{-\sigma_W^2 (t-\tau_r)^2}{2} \\ \sigma_W &= \frac{BW(2\pi f)}{2.36} \end{aligned} \tag{4.1}$$

where BW is the -6 dB bandwidth, f is the frequency of the transducer, and τ_r and σ_W are the center and standard deviation of the Gaussian function. For spatial impulse response ($h(r,t)$), the analytical expression proposed in (*San Emeterio and Ullate*, 1992) for a rectangular-shaped transducer was used. In order to simulate the radiation pattern of a phased array, the impulse response of each element at the desired spatial points in the

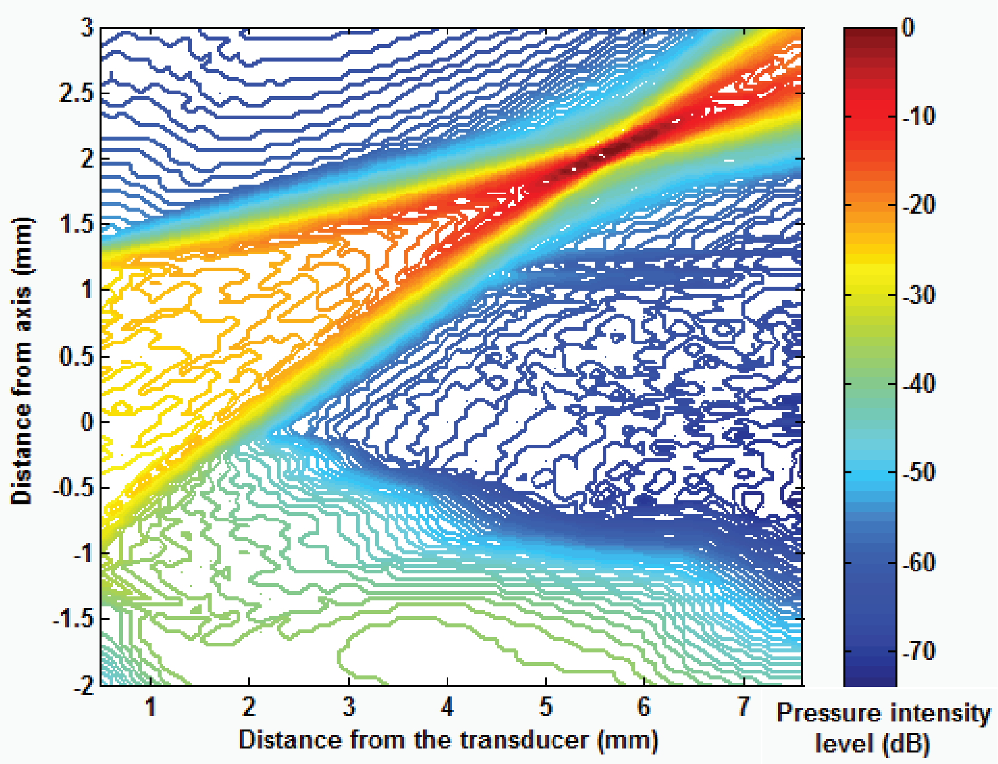

Figure 4.2: The contour map of sound pressure radiated from a 50 MHz, 64-element, 1.25λ pitch phased array focused at 20°, f/2.5. The color bar indicates the pressure intensity distribution between 0 to -75 dB.

FOV was calculated first ($h_i(r,t)|r = R$). The delays were pre-calculated using (2.16) for focusing the beam at the focal point and were inserted into each element's impulse response ($h_i(R, t - \tau_i)$). The final impulse response was the summation of all the delayed impulse responses $\sum_{i=1}^{N} h_i(R, t - \tau_i)$. Then, the received echoes were calculated using (2.14) and the envelope maximum was used to derive 2-way radiation patterns. In figure 4.2, the contour map of the sound pressure radiated from a 50 MHz phased array with 1.25λ pitch and 64 elements steered to 20 degrees, and focused at f/2.5 is shown. As shown, the pressure intensity is highest at the focal point (0 dB) and it degrades for points located outside the focal region.

For this application, the full aperture is limited to the width of round window which is about 3 mm in diameter. If the width of the elements is equal to the pitch, the total number of elements would be D/p. As mentioned in section 2.2.5.1, the linear/phased array transducers suffer from grating lobe artifacts because of the periodicity of the array elements. In a conventional design, it has been shown that the pitch of phased array transducers is required to be about half of the ultrasound wavelength in order to avoid grating lobes in a ± 45 degrees FOV (*Ziomek*, 1995). Therefore, for a 50 MHz phased array transducer the pitch should be limited to 15 μm. As previously mentioned, this pitch

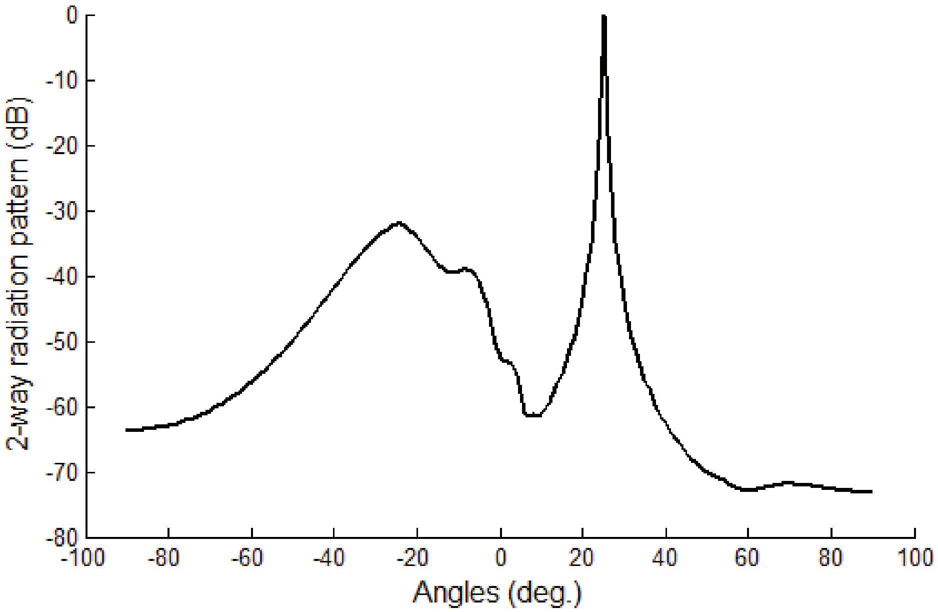

Figure 4.3: 2-way radiation pattern of a 50 MHz , 1.25λ pitch phased array transducer steered at 25° and focused at f/2.5.

is beyond modern transducer fabrication technologies and as a result no high-frequency phased array has been successfully developed with this small of an element pitch. In order to keep the element pitch within practical fabrication limits (>30 μm), but still operate the array as a 'phased array'with beamsteering, grating lobe artifacts will ultimately result. If the number of transducer elements is chosen to be 64 with a 50 MHz 1.26λ pitch, 2.5 mm full aperture can be achieved. 64 elements is chosen out of convenience as high-frequency beamformers are typically 64 parallel channels. The impulse response simulation shown in figure 4.3, illustrates the high level of grating lobes present when the ultrasound beam of a 50 MHz, 1.25λ pitch array is steered to an angle of 25 degrees. This is a cross sectional radiation pattern plotted over a wide range of steering angles while maintaining a constant f-number (f/2.5). The grating lobe artifact arising at approximately -30 degrees will show up in the image as a ghost artifact if there is a scatterer at the grating lobe location. Among the reviewed techniques in section 2.2.5.3, phase coherence imaging (PCI) is the most computationally effective method which offers promising grating lobe suppression results in large-pitch arrays when synthetic aperture beamforming is used (*Camacho et al.*, 2009). Because synthetic aperture is not desired in the proposed application, two novel transmit beamforming techniques were developed in order to make PCI suitable for conventional transmit focal zone beamforming. The theory and experimental results for these techniques are described in the following sections. In practice, it is preferred to consider some space (kerf) between the array elements in order to reduce coupling between them. For a 64-element 50 MHz array, the width of elements can be set to $0.75p$ in order to reduce the coupling between elements.

4.2.2 Grating lobe Suppression of Large-pitch Phased Arrays

4.2.2.1 Phase Coherence Imaging with Conventional Transmit Beamforming

In the phase coherence imaging technique, a weighting factor is defined based on the standard deviation of instantaneous phase of element echoes to suppress the grating lobe and preserve the main lobe. In order to simplify the implementation of PCI and reduce computational power, the sign bit of echoes alone can be measured as an estimation of the phase. This simplified PCI weighting factor is referred to as sign coherence factor (SCF) (*Camacho et al.*, 2009) and is calculated by:

$$SCF^{\alpha} = |1-\sigma|^{\alpha} \tag{4.2}$$

$$\sigma = \sqrt{1-[\frac{\sum_{i=1}^{N} b_i}{N}]^2}$$

where, b_i is the sign bit for the echo of each element, $\alpha \geq 1$ is the sensitivity factor which is set to 2 in this study, σ is the standard deviation of sign-bits, and N is the number of transducer elements (64). Higher values of α result in a larger suppression of grating lobes but also make the main lobe much more sensitive to artifacts (*Camacho et al.*, 2009). In figure 4.4, a typical set of received echoes on neighbouring transducer elements are shown after inserting the beamforming delays. This would be the case in which there was a scatterer at both the focal region and the grating lobe region. In addition, short (broadband) echoes returning from the grating lobe region only result for the case of synthetic aperture beamforming, which is not suitable for high-frequency imaging due to motion artifact. In the focal region where all the echoes are lined up after inserting the delays, the standard deviation of sign-bits of echoes is small, resulting in SCF close to 1 (point A at figure 4.4). For broadband grating lobe echoes where the overlap between echoes detected at over several elements is small, the standard deviation of sign-bits is large because the echoes mostly have a random phase determined by noise, resulting in an SCF close to zero (point B at figure 4.4).

If the grating lobe echoes are long in the time domain however (ie. narrowband), they will in fact overlap in the time-domain after the beamforming delays are inserted. Although the echoes of adjacent elements are shifted by one wavelength, there will still be a region where all echoes are in-phase and as a result carry the same sign-bit. This results in

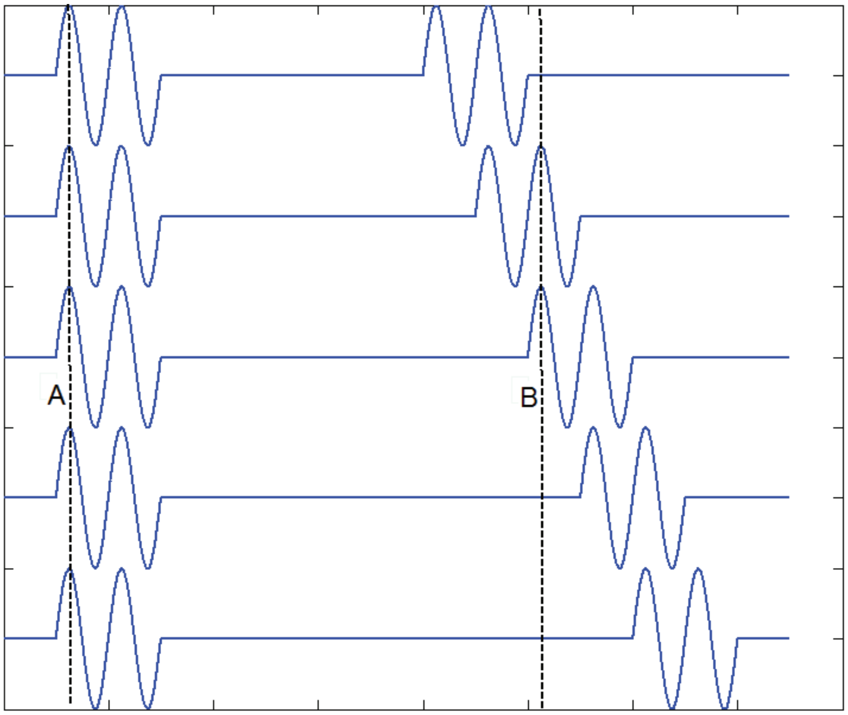

Figure 4.4: Calculating the SCF weights based on instantaneous phases of element echoes. The phases of echoes at time point A which is located at the main lobe are the same while they are different for time point B coming from the grating lobe (Redrawn from *Camacho et al.* (2009)).

an undesirably high SCF factor and no grating lobe suppression. Figure 4.5a shows an example of the 64 individually received echoes from the grating lobe region resulting from transmit beamforming. The signals are for a 64-element, 40 MHz phased array with an element pitch of 1.25λ steering at an angle of 25 degrees and focusing at f/2. The pulse echoes were simulated using the two-way impulse response method (*San Emeterio and Ullate*, 1992). The sum of the one-way transmit pulses in the grating lobe region is calculated and then used as the point source for the received echoes. As described in section 4.2.1, based on *San Emeterio and Ullate* (1992), the impulse-responses of each element at each point in space are first calculated. Then, the delays are inserted for focusing/steering the beam and all 64 individual impulse-responses are summed in order to calculate the final impulse-response of the aperture. The one-way -3 dB pulse echo is then convolved with the final impulse-response of the aperture to generate the transmit pulse. To calculate the echo, the transmit pulse is now used as the point source and it is convolved again with the delayed impulse-responses of the elements. The -3 dB bandwidth of the one-way Gaussian-modulated sinusoidal pulse echo (*Cobbold* (2007)) is 50% of the centre frequency in the simulations. In the grating lobe region, the transmit pulse length is NT (number of elements times pulse period), much longer than in the main lobe region.

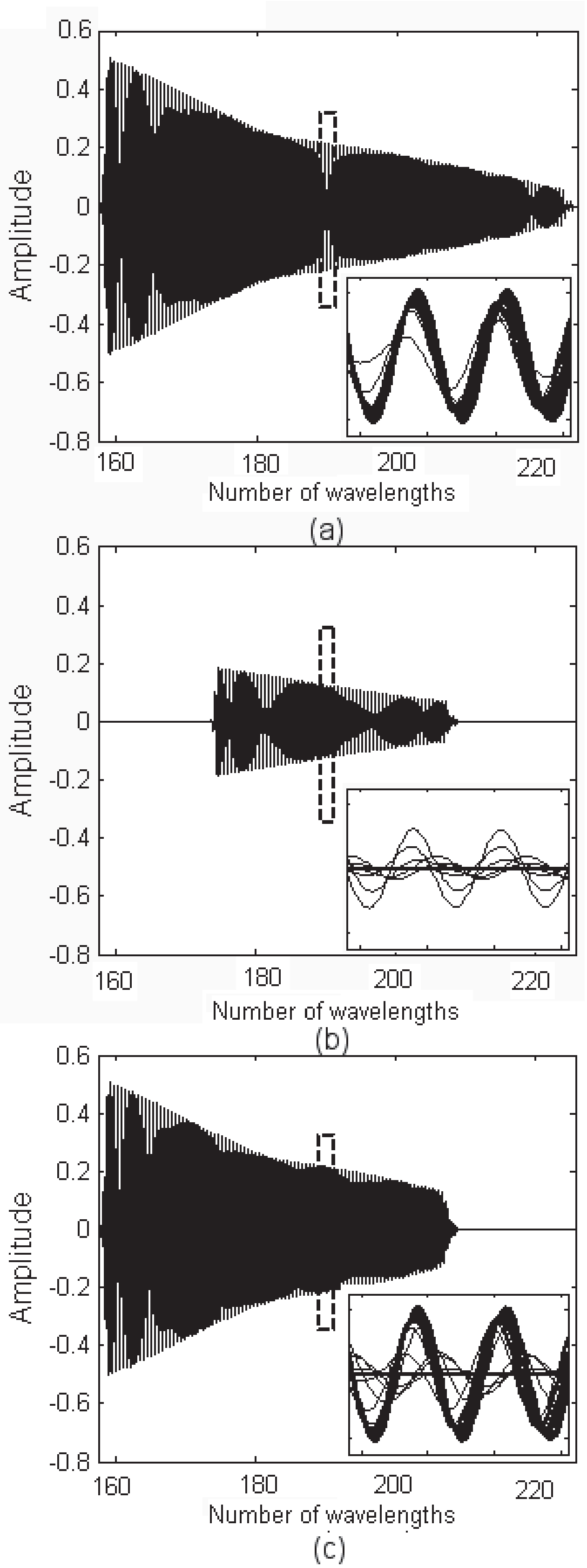

Figure 4.5: Comparison of grating lobe echoes for a 40 MHz, 64-element phased array with 1.25λ pitch using a) transmit beamforming, b) synthetic aperture pulsing with only the central element, and c) split-aperture transmit beamforming (K=2). The receive beamforming delays have been inserted (*Torbatian et al.* (2010), Copyright ©2010, IEEE).

Figure 4.5a shows how the overlapping echoes from the grating lobe region are stretched out in the time domain. Because the grating lobe signals at the different elements are virtually all in phase over a temporal window similar to the main lobe, a large weighting factor results. This prevents SCF from effectively suppressing grating lobes when transmit beamforming is used.

The SCF method is however quite effective at suppressing grating lobes when synthetic aperture transmit beamforming is used. The main difference is that for synthetic aperture, only one element is pulsed at a time which results in broadband echoes returning to the array, even from the grating lobe region. After the receive beamforming delays are inserted, these broadband echoes have very small overlap in the time domain and hence a large sign-bit standard deviation, since many of the elements measure noise or incoherent echoes (random phase) at any given moment in time. This produces a very low SCF weighting coefficient. Figure 4.5b shows an example of the received grating lobe echoes from a 40 MHz, 64 element, 1.25λ pitch phased array steering to 25 degrees when pulsed with a single defocused element (element 32). This is the case for synthetic aperture beamforming. The grating lobe echoes are predominantly out of phase in the temporal region of the main lobe signal. In fact, the received signals are so short that at any given moment most elements are seeing only noise and have a random phase.

As mentioned earlier, synthetic aperture beamforming is susceptible to motion artifacts because many transmit events are required before the signals are beamformed (i.e. 64 transmit events before beamforming for a 64-element transducer). The pre-beamformed signals are susceptible to phase distortions from small tissue movements during the relatively long pulsing sequence. High-frequency arrays are particularly sensitive to small tissue movements since the wavelengths are extremely short and therefore only a couple microns of tissue motion can result in a relatively large change in the echo phase. Transmit beamforming avoids these phase distortions because only one transmit event is required before beamforming. In this application it is the time delay between the transmit event and beamforming that determines the susceptibility to motion artifacts, not the total time required for frame capture. Synthetic aperture typically has a higher frame rate than transmit beamforming, but is still more susceptible to phase distortion due to tissue motion because the beamforming is not done until each element in the array has transmitted.

If transmit beamforming is desired for large pitch phased arrays, a new method for increasing the effectiveness of the SCF for suppressing grating lobes is needed. Since the underlying problem in applying SCF to an array using transmit beamforming is the long time-stretched signal resulting in the grating lobe region, a method that produces shorter time-domain signals should result in reduced received echo overlap and make the

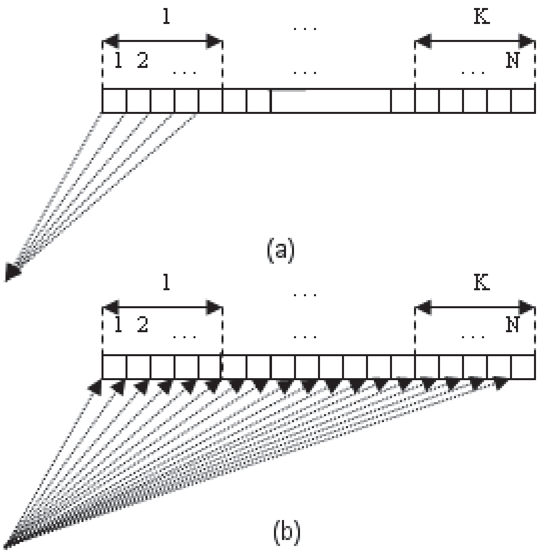

Figure 4.6: Diagram showing the proposed transmit and receive apertures. Each sub-aperture (K) is focused separately during transmission (a) and the echoes are received by all elements (b). One line of the image is constructed after all sub-apertures are pulsed (*Torbatian et al.* (2010), Copyright ©2010, IEEE).

SCF weighting technique more effective. Below are two novel transmit beamforming techniques developed to essentially reduce the temporal length of the transmit pulse in the grating lobe region, but still minimize the number of transmit events before beamforming.

4.2.2.2 The Split-aperture Transmit Beamforming Technique

Since the length of the time domain signal is approximately equal to the difference in arrival times between the closest and furthest elements in the array, it is simply proposed to split the transmit aperture into K sub-apertures, where K potentially varies from 1 to N (number of elements) in order to shorten the length of the time-stretched signal in the grating lobe region (figure 4.6a). The case K=N corresponds to synthetic aperture, while K=1 corresponds to transmit beamforming. In intermediate region 1<K< N, the trade-off between grating lobe suppression and motion artifact susceptibility can be explored. It is desirable to keep K as low as possible in order minimize the total amount of time expired before the signals are beamformed and hence the amount of motion-related phase aberration between pre-beamformed signals. With any K< N, there will be some transmit focusing along the different lines of sight. N/K of the elements will form a transmit aperture and will be pulsed together with transmit focusing delays. For each transmit event all N elements participate in the receive aperture (figure 4.6b). After each transmission, the SCF is calculated based on the time-shifted echoes and is used to weight each time point in the beamformed signal. After K transmit events, all weighted echoes are added together to generate one line in the image. The reduced size of the aperture to N/K elements for transmission makes the grating lobe signal shorter due to the reduced difference in distance between the closest and furthest elements in the transmit aperture. A surprisingly large reduction in overlap for the grating lobe echoes can be obtained even for low values of K, resulting in a much lower SCF weighting with only a small increase in delay between transmit and beamforming. Figure 4.5c shows an example of the received grating lobe echoes resulting from a split transmit aperture of 32 elements after the receive beamforming delays have been inserted on all 64 receive elements (K=2). Similar to figure 4.5a,b, this simulation is for a phased array with an element pitch of 1.25λ, steering angle of 25 degrees, and a focal depth of f/2. It is evident from this plot that there is much lower phase coherence between the echoes for the split transmit aperture technique which results in a much lower SCF weighting factor.

From the discussion so far, it is not clear whether there is a preferred way of dividing the aperture into the K sub-apertures, i.e. which elements should be grouped together as a sub-aperture. To determine the optimal method of splitting the aperture, several simulations were conducted, with the aperture divided into K sections with variable split point positions (x_0). The length of the simulated transmit pulse for each sub-aperture was compared with that of the others to find the optimal configuration. From these simulations it was determined that, as might be guessed intuitively, approximately equal-width sub-apertures ($D/2$ for K=2, $D/4$ for K=4, etc.) produce approximately equally short grating lobe transmit signals. Figure 4.7 shows the geometry of a phased array where ’O’ is the origin of the $x - z$ Cartesian plane. It has been assumed that the focal point (F) is on the main axis and the grating lobe point (G) is located on the same radius (R) at an angle from the central axis calculated by equation (4.3) (*Hoen*, 1982).

$$\Theta = \sin^{-1} \frac{\lambda}{p} \tag{4.3}$$

An expression was derived for determining exactly where to split the transmit aperture in the case of K=2 in order to obtain equal length grating lobe signals from both transmit apertures. Of course, this occurs when the difference in distance between the closest and furthest elements in each sub-aperture are equal. In order to approximate the effect of an array of elements having transmit beamforming delays inserted to focus at point F (f-number=F), a virtual curved aperture is considered for the rest of the derivation. $L1, L2,$ and $L3$ are the distances between the grating lobe point (G) and the points on the virtual curved aperture. In order to have transmit pulses with the same length in the time domain for both splits, the equality of distances defined in (4.4) should be satisfied.

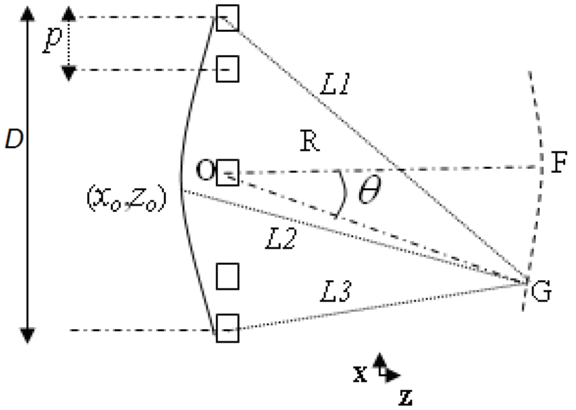

Figure 4.7: The geometry of a phased array transducer with aperture width (D), and element-to-element pitch (p) focused at focal point (F, f-number=F) on the main axis. The virtual curved aperture is used for calculating the distances between grating lobe point (G) and the aperture points ($L1$, $L2$, and $L3$) in order to account for the beamforming delays (*Torbatian et al.* (2010), Copyright ©2010, IEEE).

$$\begin{aligned} L2 - L3 &= L1 - L2 \\ L2 &= \frac{L1 + L3}{2} \end{aligned} \tag{4.4}$$

In order to solve (4.4), these Euclidean distances can be defined based on R, and the total array aperture (D). By using the first-order Taylor approximation of a square root, the element at which to split the aperture in order to obtain equal-length time-domain signals, x_0, can be expressed as:

$$x_0 = \left(\frac{F\sin\theta - \sqrt{F^2\sin^2\theta - (1-\cos\theta)(\frac{\cos\theta}{4} - \frac{F^2\cos^2\theta}{4F^2-1})}}{1-\cos\theta}\right)(Np) \tag{4.5}$$

which is a function of (N, F, p). The mathematical details are described in the appendix A.1. Generally, the expression for x_0 approaches zero at very large and very small grating lobe angles (i.e. the aperture is split at the central element). Intuitively, one can visualize a pulse arriving at the virtual curved aperture either from 90 degrees or from the main axis. These pulse echoes will 'see' a symmetric aperture where the difference between the closest and furthest elements in each sub-aperture (split at $x_0 = 0$) are the same. For all other angles, the element at which to split the array is generally within ±2 elements of the centre. Similar expressions can be obtained for splitting the aperture into 3, 4, 5, ..., etc based on these simple geometric principles, but again, it is a good approximation to simply split the aperture exactly into equal width sub-apertures. As a result of this, for the remainder of the chapter, the radiation patterns are simulated with equal width sub-apertures. Although this proposed split-aperture technique is very simple to implement, it does require K transmit events in order to generate one line of the image which decreases the frame-rate in proportion to K. To evaluate how effective the grating lobe suppression is with this technique, theoretical and experimental studies have been performed.

Theoretical Verification

For theoretical verification, 2-way radiation patterns of the proposed 40 MHz large-pitch phased array were simulated when K split transmit apertures were used for suppressing the grating lobe levels. MATLAB code (appendix C.1.2) was developed to trigger a sub-aperture on transmit that focuses to the desired point, receives on all the elements, inserts the proper receive delays, calculates the SCF weighting factors, and applies them to the beamformed signal. This is repeated until all K transmit apertures are used. These results are presented and discussed in section 4.3.1.

Experimental Verification

For experimental verification, the commercially available high frequency linear array ultrasound system, Vevo 2100 (Visualsonics, ON, CA) along with a 50 MHz, 256-element, 1.26λ pitch linear array transducer with 64-element sub-aperture (MS 700) was used to collect data. A sample of a B-mode image captured with this system from two 30 μm wire targets is shown in figure 4.8 when the beam is steered to 25 degrees. Since the pitch of this array is greater than .5λ, grating lobes are present in the field of view when the beam is steered. The Vevo 2100 has an engineering mode where some of the parameters of the system are accessible and can be rewritten to test special cases. Moreover, script codes can be developed to change the required parameters automatically and save the data on the system. The system is able to export the data in IQ format to reconstruct RF echoes.

The Vevo 2100 is designed for linear arrays where the beam is only focused along the main axis of active 64-element sub-apertures which is electronically translated along the full 256-element aperture to generate the 2D image. In order to mimic a 64-element phased array, the system had to be reprogrammed such that only one 64-element sub-aperture at the center of the 256 element array was active. This central 64-element aperture of the transducer was used to collect a single RF line along its main axis (line 128) (figure 4.9). A parameter, called steering angle is also available in the engineering mode which can be changed in the range of $(-35°, 35°)$ to steer the ultrasound beam to different angles. By changing this angle, one RF line was collected per steering angle as shown in figure 4.9. In figure 4.9, the image line is collected at a 20 degrees steering angle.

In order to test the proposed K-split transmit aperture technique with K=2, half of the 64-element aperture was turned OFF on transmit for each transmit event. In the engineering mode, two sets of four 16-bit registers were available which could control the status of

Study Name	Study (2012-08-27 12:00:18)
Series Name	Series 1
Animal ID	
Image Label	

Application	General Imaging
Preset	z-test
Transmit	
Frequency	50 MHz
Power	100 %
Acquisition	
Gain	20 dB
Frame Rate	235
Depth	9 mm
Width	9.73 mm
Line Density	Standard
Persistence	Off
Sensitivity	Standard
Height	6 mm
Steering	20 deg
Cycles	1
f-Number	2.5
VP1	1 V
BTOF	528
ECG/Resp Gate	Off/Off
Extended Buffer	Off
Receive	
Frequency	32 MHz
Sound Speed	1540 m/s
Display	
Dynamic Range	65 dB
Display Map	G5
Spatial Filter	TB1
Transfer Rate	78
Display Rate	30
Pixel Magnitude	22.37 dB (0)

Figure 4.8: B-mode image of two 30μm wire targets when the beam is steered to 20 degrees, captured with Vevo 2100. Since the pitch of this array is greater than .5λ, grating lobes are present in the field of view when the beam is steered.

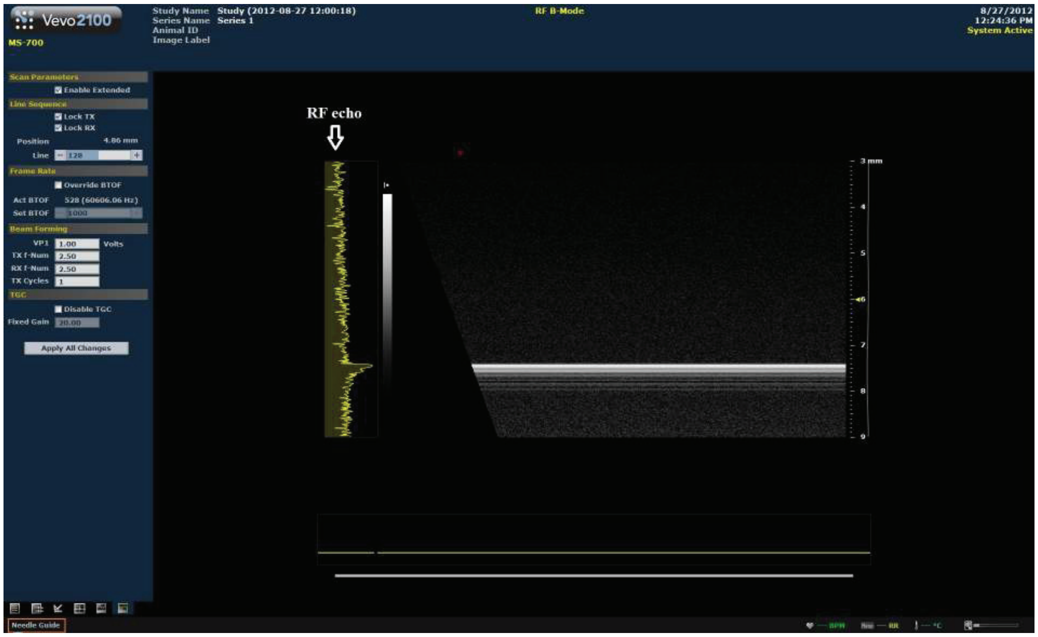

Study Name	Study (2012-08-27 12:00:18)
Series Name	Series 1
Animal ID	
Image Label	

Scan Parameters

☑ Enable Extended

Line Sequence

☑ Lock TX

☑ Lock RX

Position	4.86 mm
Line	120

Frame Rate

☐ Override BTOF

Act BTOF	528 (60606.06 Hz)
Set BTOF	1000

Beam Forming

VP1	1.00 Volts
TX f-Num	2.50
RX f-Num	2.50
TX Cycles	1

TGC

☐ Disable TGC

Fixed Gain	20.00

Figure 4.9: A screen shot of the extended engineering mode on the Vevo 2100. The central 64-elements of the array are collecting one focused RF line steered to 20 degrees. The RF echo is marked with the arrow and this line is repeated producing the B-mode image displayed.

elements of the active sub-aperture during receive or transmit separately (TX Channel Enbale, RX Channel Enbale). For instance, by assigning 1/0 to a bit of these registers the assigned transducer element could be turned ON/OFF during transmit or receive. Based on the technical documents of Vevo 2100, correct hexadecimal values were assigned to the TX Channel Enable registers to turn OFF half of the transmit aperture on each transmit event.

In order to calculate SCF weights, the delayed echoes are required on all elements of the aperture. The Vevo system could only provide the final RF echo after summing up all the delayed echoes of the elements. Therefore, on receive all elements except one had to be turned OFF to access the echo of that element individually. To do so, correct hexadecimal values were assigned to the RX Channel Enable registers which controlled the status of elements on receive. This step was repeated 64 times in order to receive each element echo individually. Since this procedure had to be repeated for each steering angle, the data collection was very time-consuming. A script code was developed to automate the whole process and save the required RF data for offline processing.

In the script code, the number of focal zones (1 at 6 mm), the gain (18 dB), and depth of the image (9 mm) was set first. Then, the steering angle was changed between $(-35°, 35°)$ in one degree intervals. At a given fixed steering angle, half of the aperture on transmit was turned ON and IQ data was collected and saved for each element of the 64-element aperture by turning only one element ON during receive. Then, the second half of the aperture was tuned ON on transmit and the receive loop was repeated again. This procedure was done for all steering angles which resulted in $(71\times2\times64)$ IQ files at the end that were exported for offline processing.

For offline processing, MATLAB code was developed to import the IQ data, calculate the SCF weights, and derive 2-way radiation patterns (appendix C.2.1). It was observed that in the reconstructed RF lines generated by the system, an artifact at 32 MHz was present which could affect the calculation of SCF weights. Therefore, before the SCF calculation, the RF signal was filtered with a stop-band finite impulse response (FIR) filter centred at 32 MHz, bandwidth 2 MHz, order 512 in order to remove this artifact. For each steering angle, the 64 element IQ data of the first transmit event (that corresponded to the RF echoes of 64 elements individually) was imported, the SCF weights were calculated, and then applied to the sum of the echoes. The same was done for the second set of 64 IQ data collected from the second transmit aperture. Then, the weighted echoes of these two transmit receive lines were added together to produce the final RF line for that angle. These steps were repeated for all steering angles and a 2-way radiation pattern was measured with the fixed phased array aperture.

In order emulate a point target and measure the 2-way radiation pattern, a glass wire target with 25 μm diameter was fabricated as follows: the tip of two glass rods were held close to each other and was heated up with a butane torch until it started to melt. Then the two rods were moved apart quickly so that they were only joined with a thin fibre and left to cool. The wire phantom was mounted on a fixture and placed in a water bath. Phased array images were also reconstructed for the wire phantom. These experimental results are presented and discussed in section 4.3.1.

4.2.2.3 The Pulse Probing Technique

An alternative technique that could potentially avoid the need to use multiple transmit pulses per A-scan line is to calculate the SCF weighting factors prior to imaging for each general region in the image, store in a look up table (LUT), and then apply to the echoes in conventional full aperture transmit beamforming. To do so, a broad defocused 'probing pulse' from the entire aperture is sent out first in order to generate a map of SCF values for all space prior to imaging. Then, conventional transmit beamforming is performed after which the map of SCF values is applied to the resulting image.

To generate a defocused pulse, it is suggested to use the entire aperture in order to increase the amount of energy sent into the tissue and hence maximize the signal amplitude (*Lockwood et al.*, 1998). As shown in figure 4.10a, beamforming delays corresponding to a virtual point source behind the array are required using (4.6). The echoes that are received from all points in space (including the grating lobe regions) are now temporally very short (figure 4.10b) and after receive beamforming delays are inserted along different A-scan lines, echoes from the grating lobe regions will have low phase coherence and corresponding SCF weighting factors.

$$\tau_{ti} = \sqrt{\mathrm{d}^2 + x_i^2} \tag{4.6}$$

where d is the depth of virtual point behind the transducer as shown in figure 4.10, τ_{ti}, and x_i are the time delay and lateral location of each element (i), respectively.

Since a broad defocused pulse is used upon transmission, dynamic receive focusing can be performed everywhere and hence a map of SCF weighting factors could potentially be computed and stored in memory for all space from a single probing pulse. Then, if conventional transmit beamforming is carried out (one A-Scan line at a time), the signals can be weighted with the previously computed weighting coefficients from the initial defocused probing pulse. This technique is possible since the weighting coefficients are slowly varying over different regions in space and therefore are not overly susceptible to small amounts of tissue motion during the relatively long pulsing sequence. Moreover, since

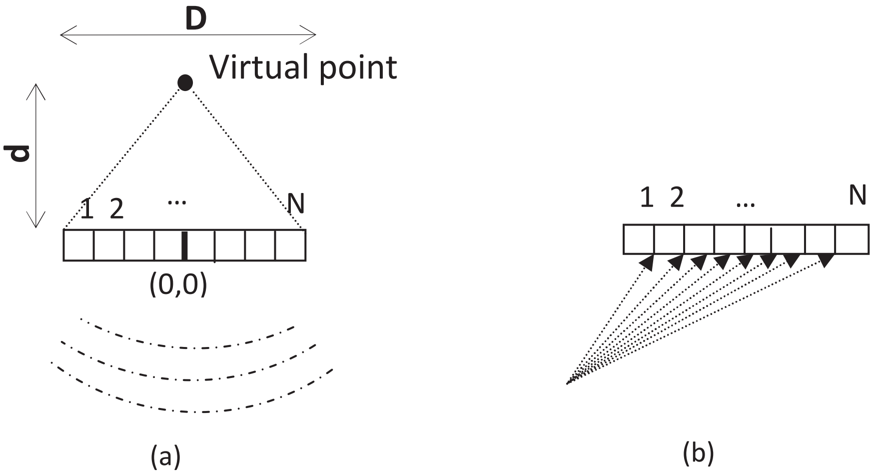

Figure 4.10: Diagram showing the proposed transmit and receive apertures for 'pulse-probing' technique to pre-calculate SCF weightings. An unfocused pulse is sent out during transmission (a) and the echoes are received by all elements (b) in order to pre-calculate SCF values in all general regions of space. Conventional full aperture beamforming is then used along with the pre-calculated SCF weighting factors (*Torbatian et al.* (2011a), with permission of the SPIE).

only one extra transmit event is required prior to the conventional transmit beamforming for SCF calculation, the frame-rate would not be affected significantly. To evaluate this technique in grating lobe suppression, theoretical and experimental studies have been performed.

Theoretical verification

For theoretical assessment, MATLAB code was developed to simulate the 2-way radiation pattern of a large-pitch phased array when the proposed pulse probing technique was applied (appendix C.1.3). In this code, the beamforming delays calculated from (4.6) were applied first to the elements of the transducer to generate a defocused pulse on transmit. The impulse-response technique described in section 2.2.4 was used to simulate the received echoes and proper receive delays were inserted to focus the beam at the focal point. The SCF weights were calculated based on (4.2) and stored. Then, conventional transmit beamforming echoes were simulated by transmitting a focused pulse at the focal point. The pre-calculated SCF weights were applied on the delayed echoes of this step and 2-way radiation patterns were calculated. The simulation results of pulse probing technique are presented and compared with K-split transmit aperture in section 4.3.2.

Experimental Verification

For experimental verification, the same high-frequency linear array system (Vevo 2100) and linear array transducer (MS 700) was used to collect the data. The system was used in the engineering mode to collect only the line along main axis of central 64 elements and

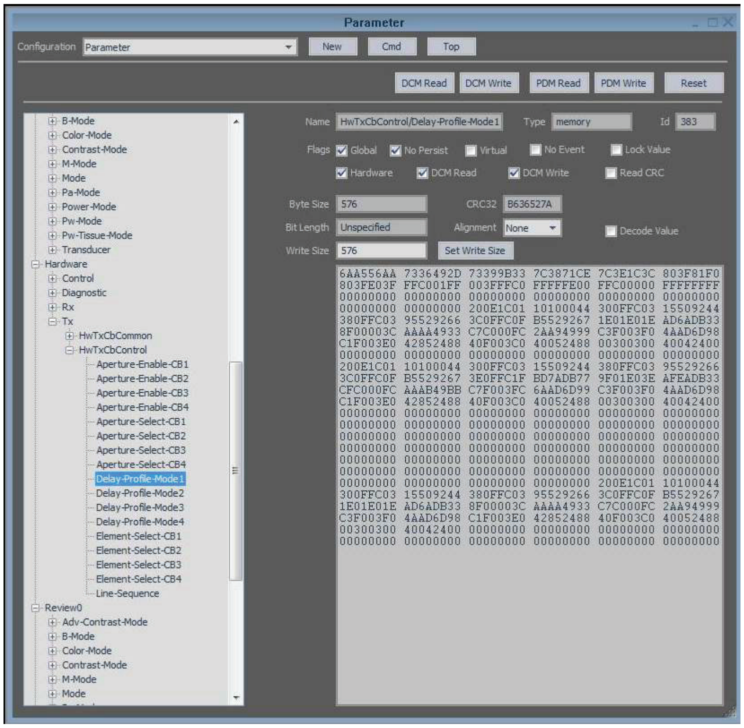

Configuration: Parameter

Name: HwTxCbControl/Delay-Profile-Mode1 Type: memory Id: 383

Flags: ☑ Global ☑ No Persist ☐ Virtual ☐ No Event ☐ Lock Value
☑ Hardware ☑ DCM Read ☑ DCM Write ☐ Read CRC

Byte Size: 576 CRC32: B636527A
Bit Length: Unspecified Alignment: None ☐ Decode Value
Write Size: 576

```
6AA556AA 7336492D 73399B33 7C3871CE 7C3E1C3C 803F81F0
803FE03F FFC001FF 003FFFC0 FFFFFE00 FFC00000 FFFFFFFF
00000000 00000000 00000000 00000000 00000000 00000000
00000000 00000000 200E1C01 10100044 300FFC03 15509244
380FFC03 95529266 3C0FFC0F B5529267 1E01E01E AD6ADB33
8F00003C AAAA4933 C7C000FC 2AA94999 C3F003F0 4AAD6D98
C1F003E0 42852488 40F003C0 40052488 00300300 40042400
00000000 00000000 00000000 00000000 00000000 00000000
200E1C01 10100044 300FFC03 15509244 380FFC03 95529266
3C0FFC0F B5529267 3E0FFC1F BD7ADB77 9F01E03E AFEADB33
CFC000FC AAAB49BB C7F003FC 6AAD6D99 C3F003F0 4AAD6D98
C1F003E0 42852488 40F003C0 40052488 00300300 40042400
00000000 00000000 00000000 00000000 00000000 00000000
00000000 00000000 00000000 00000000 00000000 00000000
00000000 00000000 00000000 00000000 00000000 00000000
00000000 00000000 00000000 00000000 00000000 00000000
00000000 00000000 00000000 00000000 00000000 00000000
00000000 00000000 00000000 00000000 00000000 00000000
00000000 00000000 00000000 00000000 200E1C01 10100044
300FFC03 15509244 380FFC03 95529266 3C0FFC0F B5529267
1E01E01E AD6ADB33 8F00003C AAAA4933 C7C000FC 2AA94999
C3F003F0 4AAD6D98 C1F003E0 42852488 40F003C0 40052488
00300300 40042400 00000000 00000000 00000000 00000000
00000000 00000000 00000000 00000000 00000000 00000000
```

Figure 4.11: The engineering mode of Vevo 2100 for updating the delay profile on transmit. For transmitting a defocused pulse, the delay profile of the system had to be updated.

the steering angle was changed in one degree intervals to mimic a phased array transducer as described in section 4.2.2.2.

For the SCF map calculation, a defocused pulse was required to be sent to the medium first. Therefore, a delay profile on transmit (figure 4.11) was programmed to trigger the transducer elements so as to generate a defocused pulse from 4 mm virtual point behind the transducer. The delays were calculated using (4.6) and they were coded according to the VisualSonics technical documents. On receive, the individual element echoes were required prior to the beamforming in order to apply proper delays for all the points in FOV and construct an entire map of SCF from one transmit shot. However, with this system the beamformed echo along each steering angle was only accessible. Therefore, the arrival time of the transmit defocused pulse was needed to be adjusted to be the same as that of focused pulse applied when the system was performing conventional transmit beamforming. For each steering angle in the range of $(-35°, 35°)$, the IQ data was collected on each transducer element individually to reconstruct RF echoes and calculate the SCF map offline. To get the element echo individually, the registers assigned to control the status of the elements on receive (RX Channel Enable) had to be updated in a way to turn OFF all elements except one (section 4.2.2.2). This batch of data was required to pre-calculate the SCF map. Then, the IQ data corresponding to conventional transmit beamforming was

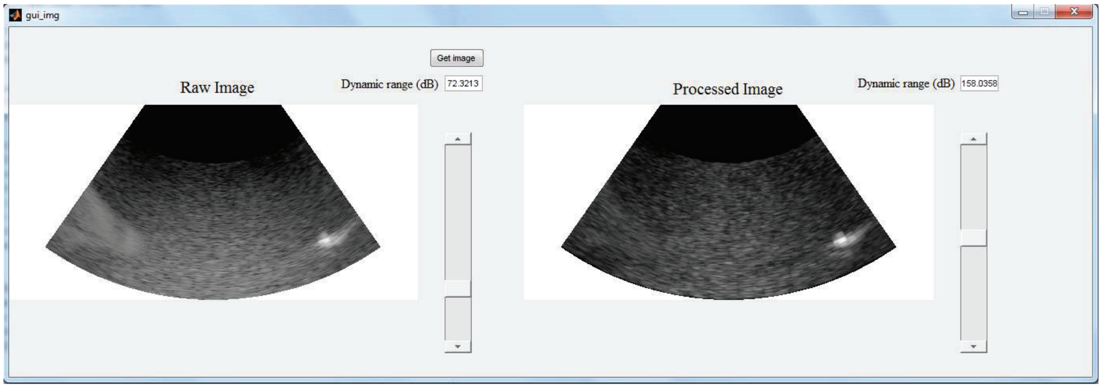

Dynamic range (dB) 72.3213

Dynamic range (dB) 158.0358

Figure 4.12: The GUI developed for offline processing of the experimental data with proposed pulse-probing technique. The raw and processed image with the desired dynamic range are shown.

quickly collected for each steering angle. In the end, there was $(71 \times 64 + 71)$ IQ data lines for offline processing.

In order to automate the data collection process, a script was developed to initialize the set-up, select a steering angle, program the delay profile, and collect the data repeatedly for the defocused probing pulse and then with the regular transmit beamforming. All of the data was transferred to a PC for offline processing.

MATLAB code was developed to import the data, calculate 2-way radiation patterns, and reconstruct phased array images of phantoms (appendix C.2.2). As mentioned in section 4.2.2.2, before the SCF calculation the RF signal was filtered with a stop-band finite impulse response (FIR) filter centred at 32 MHz, bandwidth 2 MHz, order 512 in order to remove a 32 MHz artifact which was affecting the RF echoes imported from the system. The 2-way radiation pattern was calculated based on the peak envelope of the weighted RF data along each steering angle. These echoes were also used to reconstruct phased array images. For generating the 2-way radiation pattern, the same wire target described in section 4.2.2.2 was placed in the water bath. To further investigate the capability of the proposed technique, multiple wire targets were mounted on a fixture and placed in the water to generate overlapping grating lobes. Moreover, tissue mimicking phantoms were made in the lab with wire targets embedded in them as explained in the appendix A.2.

The data was collected for each of these phantoms and they were processed with the described MATLAB code to reconstruct phased array images. A graphical user interface (GUI) was developed for these images in MATLAB which is shown in figure 4.12. Here, the raw and processed images are shown. It was possible to adjust the dynamic range for each image separately. The experimental results are presented and discussed in section 4.3.2.

4.3 Results and Discussion

4.3.1 Split-Aperture Transmit Beamforming Technique

Theoretical Verification

Although the SCF technique is generally effective for improving the lateral resolution and suppressing the side-lobes, its usefulness for grating lobe suppression is dependent on the temporal length of the transmit pulse in the grating lobe region. The shorter the transmit pulse in this region, the more effective the SCF method is for grating lobe suppression. In figure 4.13, 2-way radiation patterns for a 40 MHz, 64-element phased array transducer with element pitch p =1.25λ, focused to f/2, steered at 25 degrees are shown. One radiation pattern has no SCF weighting and this is compared with SCF-weighted transmit beamforming (K=1) and SCF-weighted synthetic aperture beamforming. As shown, the SCF technique is effective for suppressing the side-lobes and improving the lateral resolution while it is not very effective for suppressing grating lobes when conventional transmit beamforming is used. Yet, it suppresses the grating lobes in synthetic aperture beamforming more than 50 dB (from -35 dB to -90 dB). Again the underlying reason for the difference in effectiveness between the two transmit techniques is seen in figure 4.5a,b. In figure 4.5a, the grating lobe echoes in transmit beamforming are all in phase whereas they are not for synthetic aperture (figure 4.5b). For transmit beamforming, a weighting factor nearly equal to one results in the grating lobe region since all of the sign bits are the same at all time points. By splitting the aperture into two equal sub-apertures (K=2) however, the signals arriving from the grating lobe region are much shorter and as a result, the received echoes are not completely phase coherent after the receive beamforming delays are inserted. Figure 4.5c shows the received echoes on all 64 elements and it can clearly be seen that the sign bits are not all similar for the received signals and therefore the SCF weighting factor is low. Similar to the received signals in synthetic aperture beamforming, many of the signals are zero or random in phase at any given time point. By splitting the transmit aperture into more equal width sub-apertures, the length of the grating lobe signals becomes even shorter resulting in an even lower SCF weighting factor. Figure 4.14 shows 2-way radiation patterns for a 40 MHz, 64-element phased array transducer with pitch p =1.25λ, focused at f/2, and steering angle of 25 degrees. Radiation patterns are compared between transmit apertures with no weighting (No SCF), with SCF-weighting and no splitting (K=1), and SCF-weighting + splitting (K=2, 4, 8). This simulation clearly shows that split-transmit apertures are very effective in grating lobe suppression with SCF weighting factors (e.g. 20 dB grating lobe suppression is achieved with K equal to only 2). By increasing K, smaller apertures are pulsed during transmission resulting in shorter

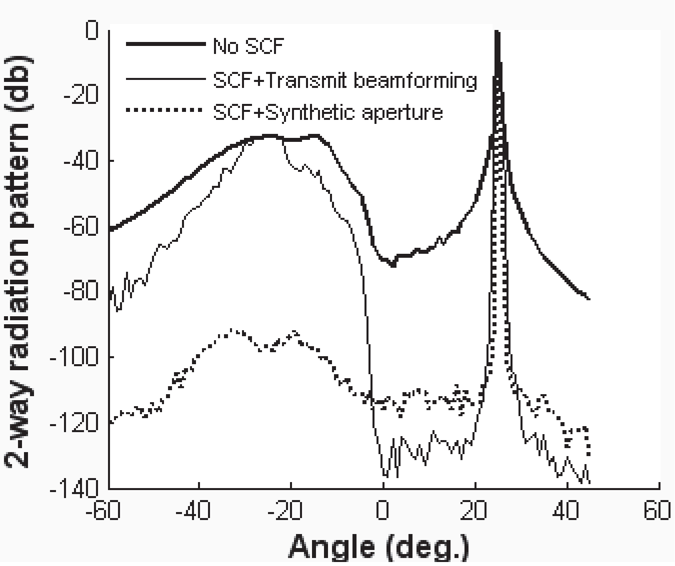

Figure 4.13: Comparison of grating lobe levels for a 40 MHz, 64-element phased array transducer with pitch p =1.25λ, focused to f/2, and steered at 25 degrees between no SCF, SCF-weighted transmit beamforming, and SCF-weighted synthetic aperture (*Torbatian et al.* (2010), Copyright ©2010, IEEE).

grating lobe echoes and as a result have less phase coherence. However, the frame-rate will obviously be decreased by increasing K and more transmit events are required before the signals are beamformed, increasing the severity of phase aberrations.

For a more quantitative evaluation of the effectiveness of the split-aperture method on grating lobe suppression, 2-way radiation patterns of 40 MHz, 64-element transducers with different pitches (0.75λ, λ, 1.25λ) steered at various angles (0, 15, 30, and 45 degrees) focused at f/2 are processed by SCF-weighting and different split-transmit apertures (K=1, 2, 4, 8). For each pitch value and split-aperture (K), the grating lobe level is plotted versus steering angle in order to observe the effect of increasing K on grating lobe suppression. Four different steering angles for each pitch value are shown on each graph in figure 4.15, summarizing the results for p=.75λ, λ, and 1.25λ respectively. At each angle, the grating lobe suppression increases by increasing the number of split-apertures (K). It can be seen from figure 4.15 that at large steering angles (30, 45 degrees), the amount of grating lobe suppression increases by approximately 20 dB for all element pitches (0.75λ, 1λ, and 1.25λ) by simply splitting the transmit aperture in half (K=2).

The important aspect of these graphs is that the K value should be chosen based on the range of steering angles in a given application and transducer pitch. For example in the case of p=λ, figure 4.15b shows that with K=2+SCF, it is possible to suppress the grating lobe to less than -60 dB below the main lobe at a 15 degree steering angle, while for a 45

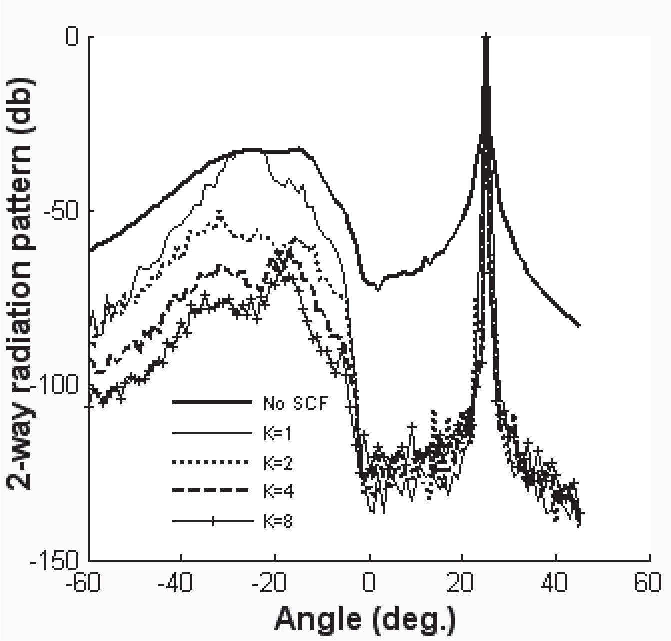

Figure 4.14: Comparison of grating lobe levels between split-aperture transmit beamforming with different number of splits (K=1, 2, 4, 8). The total aperture is a 40 MHz, 64-element transducer with pitch p =1.25λ, focused at f/2, and steered at 25 degrees. As shown, by increasing the number of transmit apertures 'K', grating lobe suppression is increased (*Torbatian et al.* (2010), Copyright ©2010, IEEE).

degrees steering angle, K must be increased to 8 in order to suppress the grating lobes to less than -60 dB.

As mentioned previously, increasing the K decreases the frame rate by 1/K, which is usually undesirable (total number of transmit pulsing for single frame increases K times). Therefore, a split aperture technique that could be used to recoup some of the decreased frame rate would be to gradually increase the 'K' value as the A-scan lines shift to larger steering angles. As shown in figure 4.15 even with an element pitch of 1.25λ, SCF weighting will suppress the grating lobe level approximately 60 dB below the main lobe at a 15 degrees steering angle with K=2. However, by the time 45 degrees of steering is reached, 8 sub-apertures with transmit focusing are required to maintain the same amount grating lobe suppression.

Experimental Verification

Initially, a 25 μm wire phantom was placed in a water bath and was imaged in a -33 to 33 degrees field-of-view. The phantom was situated 25 degrees from the center of the transducer at a depth of 6 mm. In figure 4.16, the 2-way experimentally measured radiation patterns are compared between raw data, data processed with SCF, and data processed with K=2 split-aperture technique along with SCF. As shown, the SCF was not overly effective for suppressing the grating lobes arising from the wire target. However, when it was used

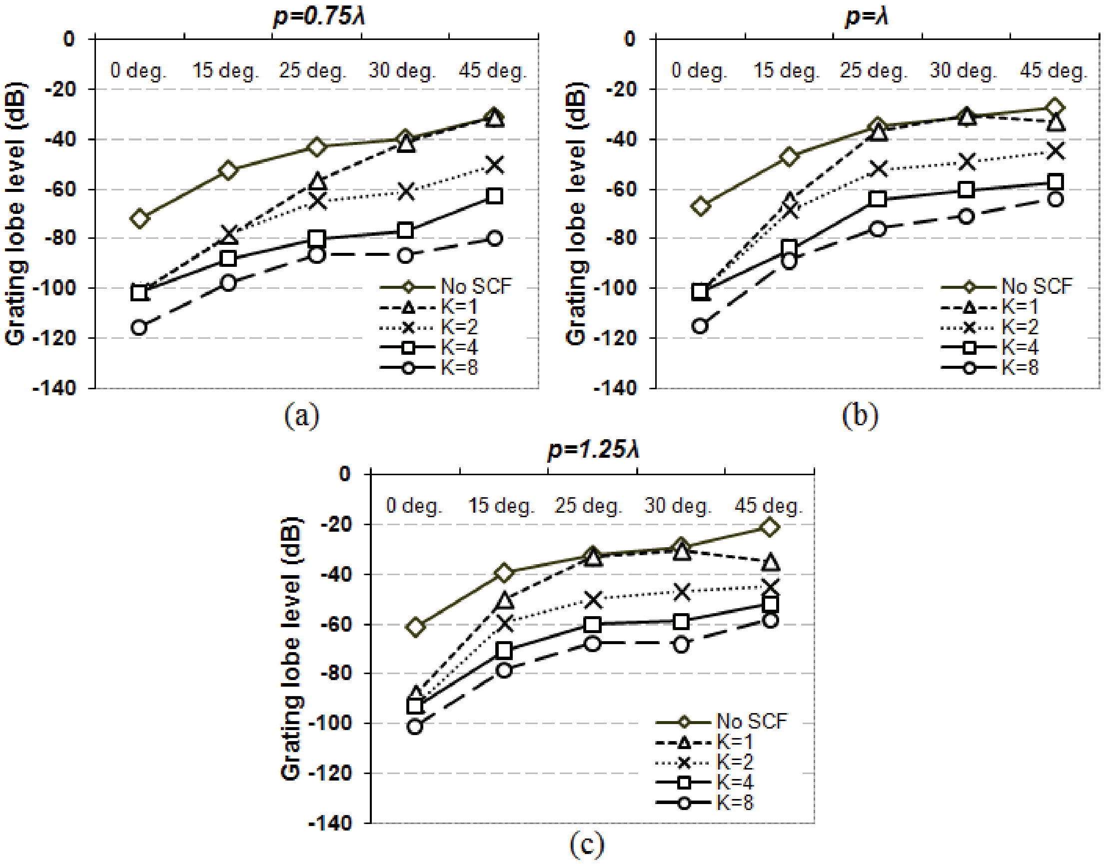

(a) (b)

(c)

Figure 4.15: The effect of K sub-apertures on grating lobe suppression for different element pitches and steering angles of a 40 MHz, 64-element phased array focused at f/2. The grating lobe level is plotted versus steering angles 0, 15, 30, and 45 degrees for K 'splits' (1, 2, 4, and 8) at element pitches of a) p=0.75λ, b) p=λ, and c) p=1.25λ. The regular value of grating lobe with no processing (No SCF) is also plotted for comparison (*Torbatian et al.* (2010), Copyright ©2010, IEEE).

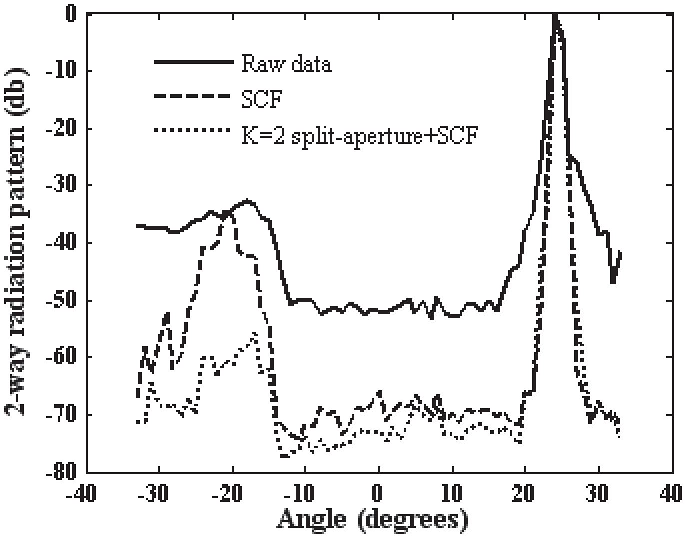

Figure 4.16: Experimental 2-way radiation patterns of a wire phantom for the raw data, SCF processed, and K=2 split-aperture+SCF. As shown, the proposed technique suppressed the grating lobe level about 20 dB while the SCF technique alone was not as effective (*Torbatian et al.* (2011b), Copyright ©2011, IEEE).

along with K=2 split-aperture transmit beamforming, the grating lobe level was suppressed about 20 dB. The improvement arises because the transmit pulse from the smaller aperture was shorter in the time domain, making SCF weighting more effective for grating lobe suppression. To compare with theory, simulated 2-way radiation patterns of raw data, SCF processed, and K=2 split-aperture processed are shown in figure 4.17. The simulated radiation patterns were generated using the impulse response method for an array of equal pitch, number of elements, and frequency as the MS 700. As shown, the experimental and simulated radiation patterns were consistent with each other and predicted a similar grating lobe level for K=2 split-aperture transmission ($\sim$ 20 dB suppression). Figure 4.18 shows images that were generated of the wire phantom for the three separate cases (raw data, SCF processed, and K=2 split-aperture processed) and are displayed with a 60 dB dynamic range. As seen in these images, there is a large spread out in the grating lobe region in the unprocessed image at an angle of approximately -20 degrees. When the SCF was applied on the raw data, much of the grating lobe artifact became suppressed, but there was still a narrow high amplitude region present. This was the region where grating lobe echoes on all the elements overlapped in the time domain. When the K=2 split-aperture transmit beamforming was used, however, the grating lobe was suppressed to less than 60 dB. Since the echo had to be collected on each channel individually for each sub-aperture as described in section 4.2.2.2, data collection was a time-consuming process.

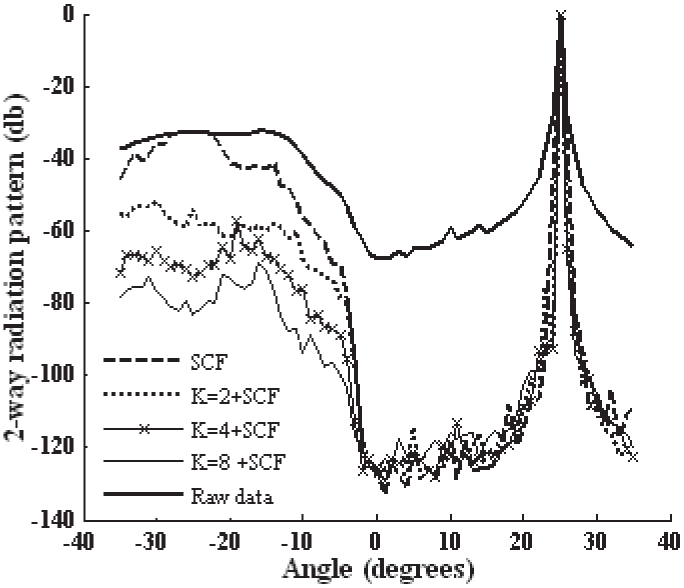

Figure 4.17: Simulated 2-way radiation patterns for a 50 MHz, 64-element, 1.26λ pitch phased array steered at 25 degrees. The radiation patterns are compared between raw data, SCF processed, and K=2, 4, 8 split-aperture+SCF. The split aperture technique suppressed the grating lobe level more than the SCF technique alone. The larger the number of sub-apertures (K), the greater the suppression (*Torbatian et al.* (2011b), Copyright ©2011, IEEE).

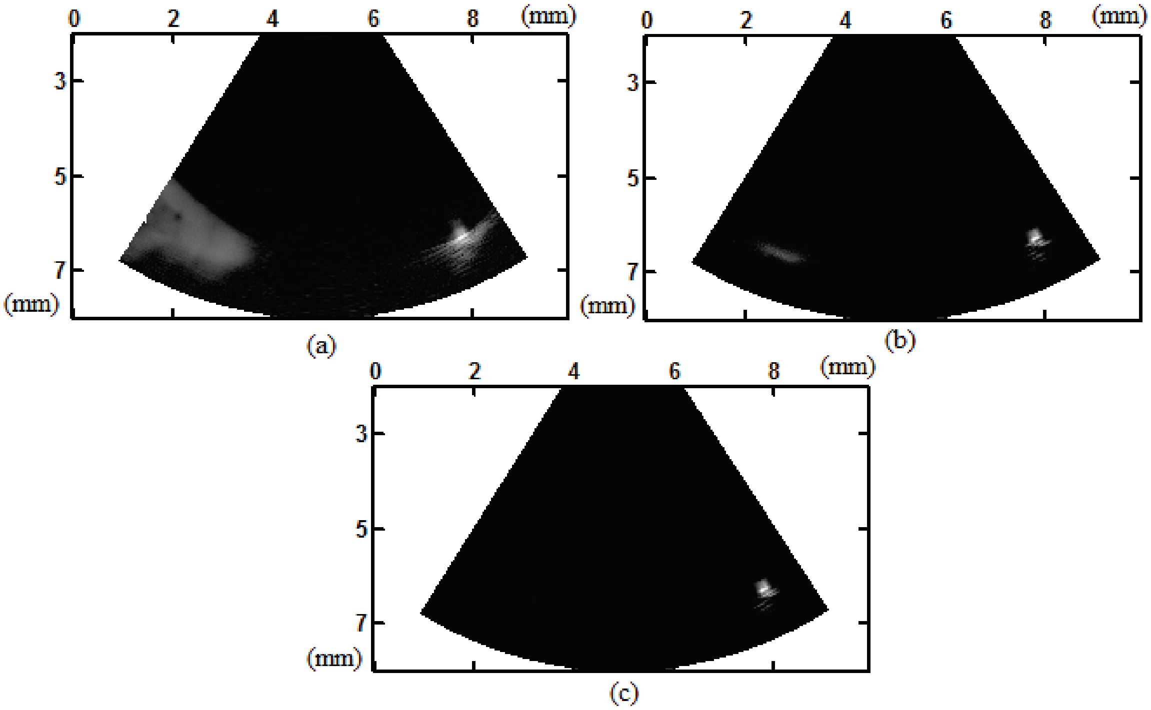

Figure 4.18: The experimental images of wire phantom with 60 dB dynamic range. a) Raw data, b) SCF processed, c) K=2 split-aperture transmit beamforming+SCF. As shown, there was a large grating lobe region on the left side of the raw data (a), the SCF suppressed the grating lobe region partially (b), while it was removed completely with the proposed split aprture technique (c) (*Torbatian et al.* (2011b), Copyright ©2011, IEEE).

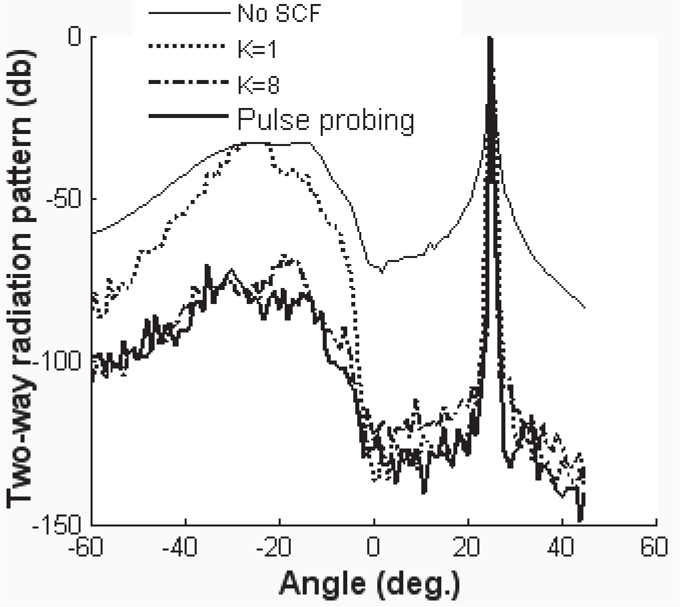

Figure 4.19: Comparison of grating lobe levels for a 40 MHz, 64-element phased array transducer with pitch p =1.25λ, focused to f/2, and steered at 25 degrees between no SCF, SCF-weighted transmit beamforming (K=1, 8) and suggested defocused 'pulse probing' technique. As shown, the 'pulse probing' method can be as effective as K=8 split-aperture in suppressing grating lobes (*Torbatian et al.* (2010), Copyright ©2010, IEEE).

4.3.2 Pulse Probing Technique

Theoretical Verification

The proposed 'pulse probing' technique avoids the decreased frame rate that is inherent to the split aperture technique. This is because only one single pulse probe is required per frame, to calculate the SCF map of the imaging region. In figure 4.19, the 2-way radiation pattern of the 'probing pulse' technique is compared with the split-aperture (K=1, K=8) for a 40 MHz, 64-element phased array transducer with pitch p =1.25λ, focused at f/2, and steering angle of 25 degrees. As shown, this technique is as effective as a K=8 split-aperture for suppressing the grating lobes. Again, by transmitting a broadband defocused pulse, broadband grating lobe echoes are generated which results in less overlap in the time domain and in return low phase coherence and low SCF-weighing factors. As a further quantitative study, 2-way radiation patterns of 40 MHz, 64-element transducers with different element pitches (0.75λ, λ, 1.25λ) steered at various angles (0, 15, 30, and 45 degrees) focused at f/2 are processed by the SCF-weighted 'pulse probing' technique, shown in figure 4.20. For each pitch value and steering angle, the grating lobe level of the proposed technique is compared with transmit beamforming phased arrays and K=8 transmit sub-apertures. As shown, the proposed 'pulse probing' technique is as effective as K=8 transmit sub-aperture technique in suppressing grating lobes in large pitch phased arrays while it effectively does not reduce the frame-rate. With this technique, the grating lobes of a 1.25λ pitch phased array can be suppressed more than -60 dB below the mainlobe at 30° steering angle. In this method, the theoretical maximum frame-rate is only decreased by one transmit event over conventional transmit beamforming (due to the initial probing pulse) and therefore is potentially more advantageous than the split aperture method. The main advantage of this technique over synthetic aperture is that it is not susceptible to motion artifacts. At first glance this might seem counter intuitive since the SCF values are pre-calculated for all space and then applied to each A-scan line as they are generated over time. The reason that this technique is not susceptible to motion artifacts is because the weighting coefficients are slowly varying over different regions in space. In fact the minimum spatial variance is equal to the length of the pulse envelope. Therefore, even if we were for example to apply SCF coefficients that were generated with a probing pulse that occurred 200 transmit events previous, the reflector would need to move on the order of wavelengths to invalidate the SCF weighting. On the other hand, with synthetic aperture beamforming, the actual beamforming might not be performed until after 200 transmit events occur, and therefore even a fraction of a wavelength reflector motion can distort the image. As a general rule beamforming delays should be accurate to within 1/30 of a wavelength.

Experimental Verification

Initially, the data was collected for a 30 μm glass fiber phantom in a water bath when the beam was steered from -35 to 35 degrees in order to generate a radiation pattern. The wire was placed at 25 degrees from the center of transducer at the depth of 6 mm. In figure 4.21, the measured 2-way radiation patterns are compared between raw data, data processed with SCF, and data processed with pulse probing+SCF. As predicted, the SCF weighting alone was not effective ($<$ 5dB suppression) for suppressing the grating lobe because the echoes from that region are narrowband. However, when the SCF weighting factors were calculated using the defocused pulse, the grating lobes were suppressed about 40 dB below the unweighted data.

This is consistent with simulated 2-way radiation patterns shown in figure 4.22 for a 50 MHz, 64-element, 1.26λ pitch phased array steered to 25 degrees. The simulated results again show approximately 40 dB suppression for the pulse probing technique but virtually no suppression for the SCF weighting technique alone. Figure 4.23 shows a phased array image generated of multiple wire phantoms placed in a water bath at different depths and beam angles, presented at 64 dB dynamic range. As shown in the raw phased array image (figure 4.23a), the grating lobe regions were very large and overlapping. When the map of SCF weighting factors generated with the pulse probing technique were applied however, the grating lobes were suppressed well below the dynamic range cut off in the image.

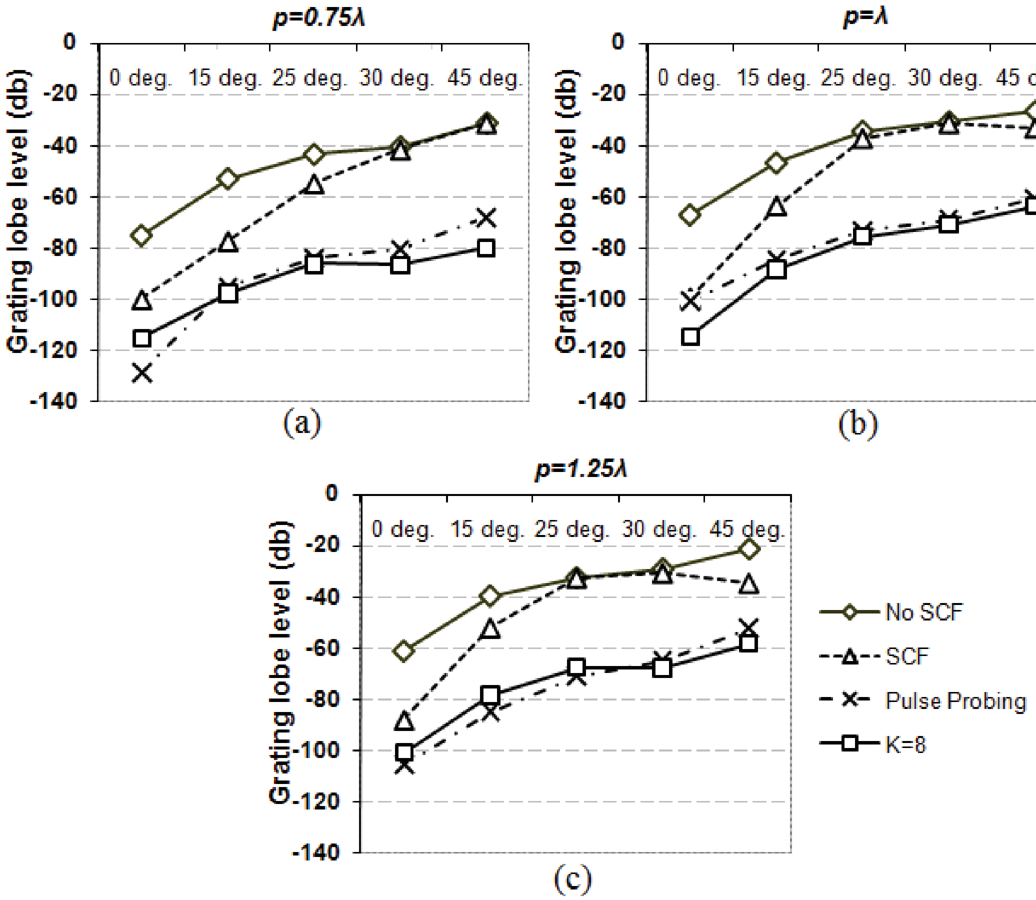

(a) (b) (c)

Figure 4.20: The effect of ’pulse probing’ technique and K=8 transmit sub-apertures on grating lobe suppression for different element pitches and steering angles of a 40 MHz, 64-element phased array focused at f/2. The grating lobe level is plotted versus steering angles 0, 15, 30, and 45 degrees for the ’pulse probing’ technique and K=8 splits at element pitches of a) p=0.75λ, b) p= λ, and c) p=1.25λ. The proposed ’pulse probing’ technique is as effective as K=8 split sub-apertures for suppressing grating lobes. The regular grating lobe levels with no processing (No SCF) are also plotted for comparison (*Torbatian et al.* (2011a) with permission of the SPIE).

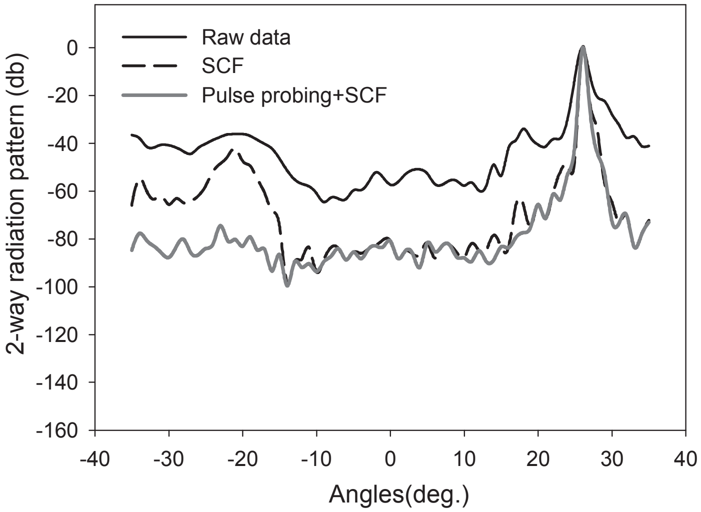

Figure 4.21: Experimental 2-way radiation patterns for a wire-phantom for the raw-data, SCF weighted, and pulse-probing+SCF weigthed. The proposed technique suppressed the grating lobe level approximately 40 dB (*Torbatian et al.* (2012a), Copyright ©2012, IEEE).

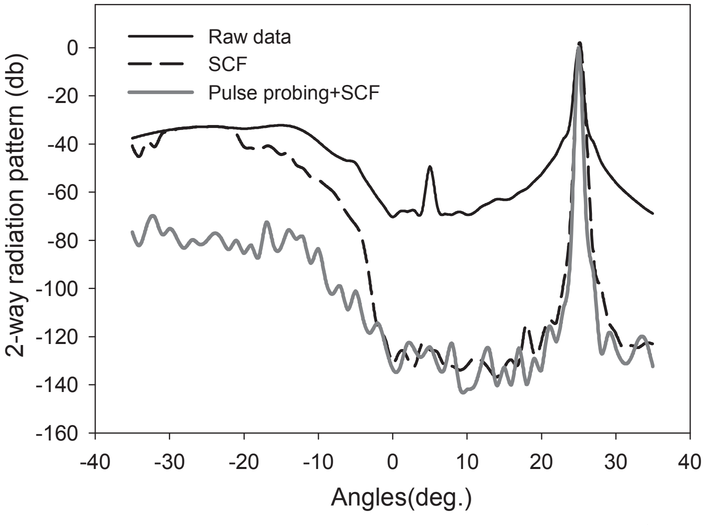

Figure 4.22: Simulated 2-way radiation patterns for a 50 MHz, 1.26λ pitch, 64-element phased array steered at 25 degrees. The radiation patterns are compared between raw data, SCF processed, and pulse-probing+SCF. As shown, the proposed technique suppressed the grating lobe level about 40 dB while the SCF was not effective (*Torbatian et al.* (2012a), Copyright ©2012, IEEE).

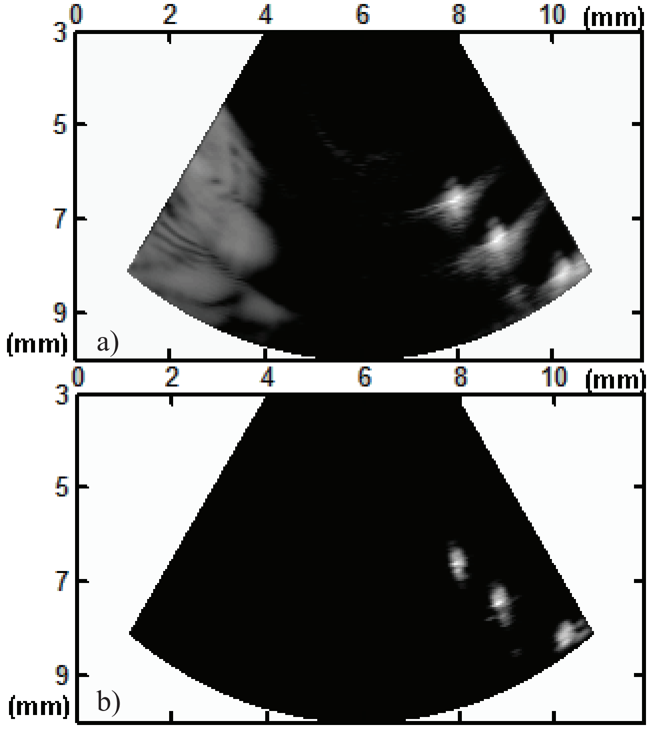

Figure 4.23: Experimental images of multiple wire phantoms in water with 64 dB dynamic range. a) Raw data, b) Processed image. As shown, the grating lobe was suppressed properly using proposed technique.

Although the technique is extremely effective in suppressing grating lobes from targets situated in a water bath, it was also necessary to verify that the technique will also work in tissue or a medium with many overlapping scatterers (speckles). In figure 4.24, the raw data (a) and the processed data (b) are shown for a similar 30 μm wire situated in a home-made tissue phantom (Appendix A.2) which was placed at 25 degrees from the center of the transducer. Although figure 4.24 shows that the proposed method was effective for suppressing the grating lobes while preserving the wire target embedded in the scattering medium, it was necessary to increase the dynamic range of the image after the SCF weights were applied in order to visualize the background speckle pattern of the raw image. The dynamic range plotted for the raw image (figure 4.24(a)) was 75 dB while it was 165 dB for the processed one (figure 4.24(b)). One reason for the suppression of the speckle pattern is related to the fact that the sizes of the speckle scatterers are much smaller than the ultrasound beamwidth and multiple scatterers at slightly different locations are present in the focal region. Therefore, the recorded echo from the focal region is the result of superposed echoes coming from many scatters and results in a small incoherency in the main lobe reflection. This incoherency caused by a population of scatterers reduces the SCF weights in all regions containing multiple scatterers within the

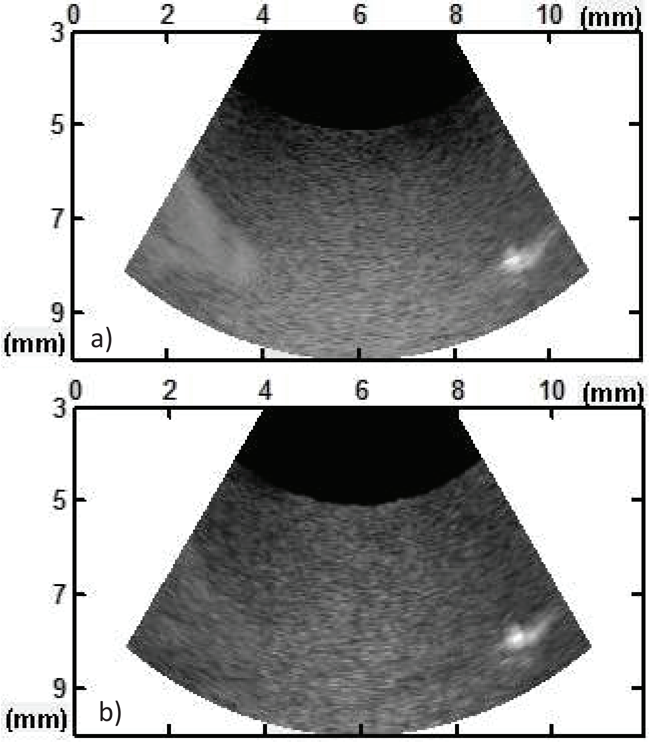

Figure 4.24: Experimental images of a wire target in a tissue phantom. a) Raw phased array image with 75 dB dynamic range and b) phased array image using pulse probing technique with 165 dB dynamic range. The grating lobe was suppressed properly with minimal effect on the tissue speckle (*Torbatian et al.* (2012a), Copyright ©2012, IEEE).

image. The other reason for increasing the dynamic range (to preserve the background speckle), is due to the grating lobe artifacts generated by the speckle on the opposite side of the tissue phantom. These grating lobe echoes are superimposed on the scatterer echoes which further reduces the phase coherency and in turn the SCF weighting of the tissue speckle. The reduced SCF weights for the speckle regions causes the suppression of echoes corresponding to these regions as compared to the coherent echoes that originate from specular reflectors. Therefore, in order to visualize regions containing these incoherent scatterers, the dynamic range of the image must be increased to account for their reduction by the SCF. For the experimental data shown in figure 4.24(a) the SCF weights calculated for the regions containing both speckle and grating lobes were on average approximately 0.0001 (a histogram of SCF weighting factors showed that over 90% were 0.0001 or smaller). Therefore in order to visualize all speckle regions plus all coherent scatterers with SCF weighting factors close to 1, it was necessary to increase the dynamic range in the processed image to at least $20 * \log(0.0001) = 80$ dB above the unprocessed image. The dynamic range was actually increased slightly more than 80 dB in order to qualitatively match the speckle pattern of the original image (90 dB) and compensate for the fact that even coherent scatterers do not result in perfect SCF weights $= 1$. This is due to small tissue aberrations, overlapping scatterers, and less than perfect beamforming delays.

In order to theoretically investigate the dependency of SCF weighting factor on the speckle and the required dynamic range for displaying the scatters on the processed image, a simplified version of simulation study was performed using the impulse-response method (*San Emeterio and Ullate*, 1992). The number of scatters in the in-house built tissue phantom (Appendix A.2) was calculated to be 1080 scatterers per 0.0047 mm^3 $(230,000/mm^3)$. This calculation is based on the density of the silicon dioxide and mixture ratios of the tissue phantom fabricated in house. In order to estimate the volume of the focal region for distributing the scatters, the lateral resolution at $f/2.5$ of the defocused transmit event was measured from the experimental 2-way radiation pattern. The passive elevation focus of the lens on the MS 700 probe was at $f/5$ according to its technical documents, and the depth considered in the simulation was at the elevation focal depth $(f/5\lambda)$. Instead of simulating in 3D, (in order to reduce computational power), for each scattering region it was decided to distribute the scatters randomly in a 2D sector region centered at a fixed radial distance and angle versus the center of the transducer. To mimic experimental situation, a scattering sector was considered centered at the focal point $f/2.5$ and steering angle 25 degrees, while several scattering regions were placed on the opposite side of the phantom at varying f-numbers ($f/2.4$ to $f/3.2$) and angles ($-30°$ to $30°$) in order to produce overlapping grating lobes. The pulse probing technique was first simulated to calculate the SCF weights at the focal point by transmitting a defocused pulse into the medium, calculating the element echoes generated from each scatterer, and inserting receive beamforming delays to focus at the focal point on receive. On each scattering region, the echoes of all scatters ($230,000/mm^3$) were added up to calculate the superimposed echo. In order to model the superposition effect, the echo of each array element was derived by summing up the echoes generated by all the scattering regions. Then, the SCF weights were calculated for the focal point and the histogram of the resulting SCF weights was plotted in order to visualize the distribution of weighting factors between 0 and 1. The histogram of the calculated weights for the echoes coming from the focal angle ($25°$) showed that more than 80$\%$ of the SCF weighting factors were 0.0001 or smaller, very similar to what was experimentally measured. It should be noted that in this simulation the presence of other scatters distributed along other angles and depths (f-number) were ignored to simplify calculation. These scatters would also generate overlapping echoes and cause reverberations which would affect the coherency of scatters at the focal region. However, based on this simplified simulation, most of the SCF values from general scattering media reduce the signal by approximately 80 dB suggesting that an equivalent increase in dynamic range is required in order to display the underlying tissue speckle.

It was also important to experimentally evaluate the pulse probing technique for a scenario where there are overlapping grating lobes and coherent reflectors. Two wires were placed at about 6 mm focal radius at $25°$ and -20° angles from the center of the transducer in order to generate overlapping grating lobes in a water bath. Figure 4.25 a,b show the unprocessed and processed image of overlapping wire phantoms and grating lobes. Upon application of the pulse probing technique, it was interesting that the SCF weights of the coherent wire targets were not completely preserved (i.e. $\sim$1) because of the incoherency of the overlapping grating lobes. Therefore, in order to preserve the coherent scattering events it was necessary to again increase the dynamic range of the weighted image. In this case, the dynamic range was increased 16 dB as this was the amount by which the coherent SCF weights were suppressed from the unprocessed image. As shown in figure 4.25b the proposed technique effectively suppresses the grating lobes while preserving the wire targets.

To further study the effect of overlapping grating lobes on SCF weights of the target echo, several radiation patterns were simulated when two targets were located at opposite sides (angles: -20 and 25 degrees) while the array was focused at 25 degrees, $f/2.5$ and the pulse probing technique was applied. It was shown that when there was a 9 dB difference in the intensity of two wire phantoms, this resulted in smaller SCF weights, and as a result

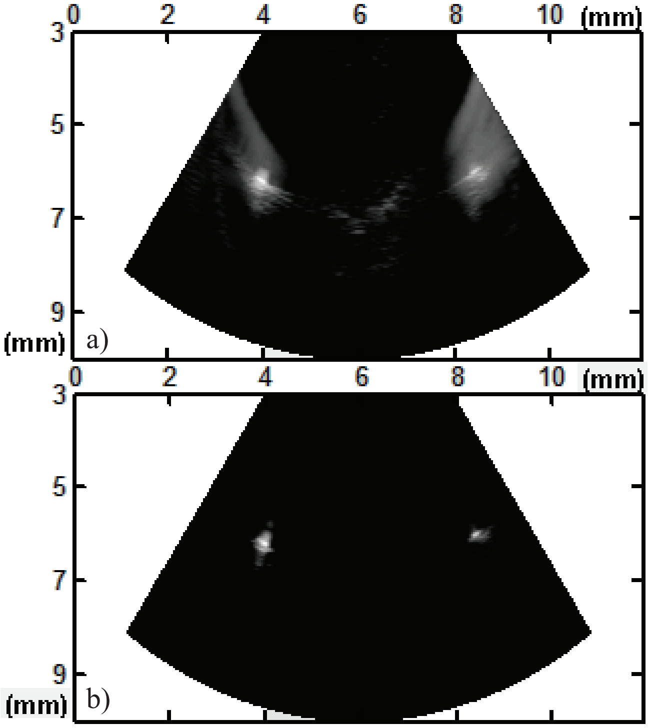

Figure 4.25: Experimental images of two wire phantoms in water with overlapping grating lobes. a) Conventional phased array image with 64 dB dynamic range and b) image generated with pulse probing technique, 80 dB dynamic range. The overlapping grating lobes were suppressed while the wire phantoms were preserved.

suppression of the wire target with lower intensity. Therefore, the SCF weights of the coherent target reflectors were reduced approximately 15 dB and in return the dynamic range needed to be increased to properly bring back the coherent targets. The difference between the intensity of two target wires in experiment might be the result of slightly different acoustic impedance of these home-made glass fibers due to variability in diameter or smaller directivity of transducer elements at larger angles (-20° vs. 25°). Although this is a substantial increase in dynamic range needed to properly visualize the wire targets after processing, it is still much lower than the increase needed to preserve the tissue speckle ($\geq$80 dB).

As a final validation experiment, the grating lobe suppression technique was tested in the scenario where there were overlapping grating lobes and wire targets in a scattering medium like a tissue phantom. Figure 4.26 shows the effectiveness of proposed technique for suppressing grating lobes resulting from glass fibers situated in a tissue phantom such that the grating lobes and reflectors overlap. Like in the previous tissue phantom experiment, the dynamic range of processed image had to be increased by approximately 100 dB in order to visualize the tissue speckle which was suppressed undesirably due to the incoherence of echoes from multiple scatterers within the focal region. As shown in

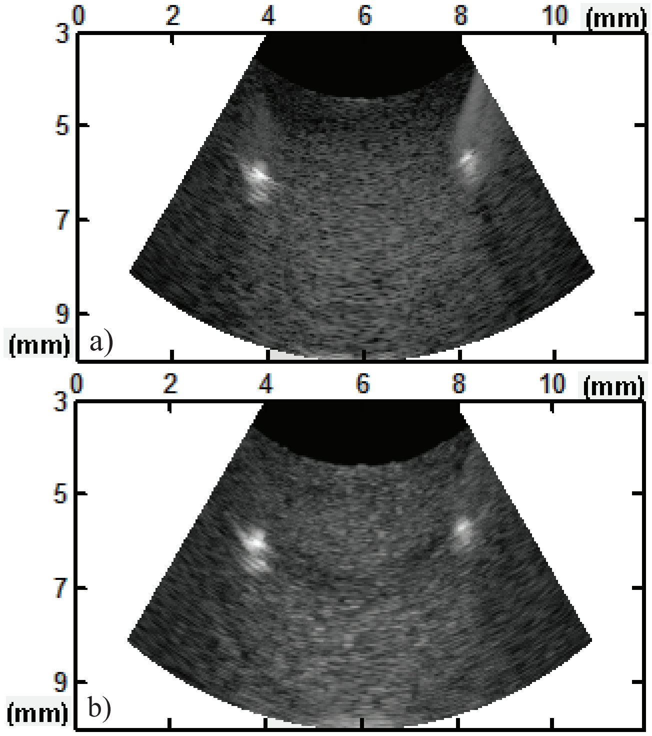

Figure 4.26: Experimental images of two glass wires embedded in a tissue phantom with overlapping grating lobes. a) Conventional phased array image with 62 dB dynamic range and b) image generated with pulse probing technique (162 dB dynamic range). The overlapping grating lobes were suppressed while the wire phantoms and tissue texture were preserved.

figure 4.26b, the wires and the tissue speckle were more coherent than the grating lobe regions and therefore were still well preserved on the processed image with increased dynamic range. An even larger increase in dynamic range was required in this case due to the overlapping coherent scatterers, grating lobes, and speckle.

Future study will be required in quantitatively determining how this increased dynamic range and non-linear compression is affecting the image. This will accomplished with a wide range of impulse response simulations of neighbouring coherent targets (with varying intensities) situated in a scattering medium. Simulating a large volume of densely packed scatterers however takes days to weeks on a PC computer and therefore a solution using a parallel server cluster will be required in order to perform multiple simulations in a realistic time frame. Experimental images between the array operating as a conventional 256 element linear array with no grating lobes or SCF processing to the 64 element phased array with SCF processing and increased dynamic range should also be compared in future experiments. As a general rule, however, if the SCF weighting factor multiplied by the amplitude of tissue speckle is larger than the SCF weighting factor multiplied by the grating lobe amplitude, the dynamic range of the image can be adjusted such that the grating lobes are removed and the tissue speckle is preserved.

4.4 Conclusion

Phased array transducers can provide a large field of view with a small aperture which is suitable for inner ear imaging through the narrow opening of the round window membrane. However, a small pitch is conventionally required ($\sim .5\lambda$) in order to avoid large grating lobes. This produces huge fabrication challenges for high frequency phased arrays. In this chapter, a 64-element, 50 MHz, 1.26λ pitch, phased array transducer which had 2.5 mm aperture was designed specifically for imaging the inner ear through the round window. It was shown that while the phase coherence imaging (PCI) was effective for improving the lateral resolution and suppressing the side-lobes of large-pitch phased arrays with conventional transmit beamforming, it was not effective for suppressing grating lobes. Two transmit beamforming techniques, called 'split aperture' and 'pulse probing' used in conjunction with PCI weighting were proposed in order to suppress grating lobes resulting from this large-pitch phased array. Impulse response simulation results of 2-way radiation patterns showed that the proposed techniques were potentially very effective for suppressing grating lobes inherent to large-pitch phased array transducers. Although some of these simulations were done for 40 MHz large-pitch phased arrays, the results can be generalized for large-pitch 50 MHz phased arrays since the pitches were defined based on a ratio of the wavelength ($k\lambda, k > 1$). These techniques could potentially alleviate some of the fabrication challenges associated with high-frequency phased array.

It has been shown that by splitting the transmit aperture into K sub-apertures to generate shorter grating lobe echoes, and applying SCF weighting coefficients, grating lobes can be significantly suppressed below their level in conventional transmit beamforming with large pitch arrays. Using basic geometric principles, an expression for the optimal aperture splitting location was derived that will produce equally short transmit pulses in the grating lobe region for the different sub-apertures. The simulation results have shown that splitting the aperture into equal-width sub-apertures is a good approximation to the optimal splitting locations for most f-numbers and grating lobe angles. It was also shown that a larger number of sub-apertures 'K' increases the amount of grating lobe suppression for different pitches and steering angles. At higher steering angles, greater values of K are required for acceptable grating lobe suppression which impact the frame-rate. Therefore, the minimum number of split apertures (K) should be chosen based on the steering angle and desired image contrast (grating lobe level) for the individual application. The experimental verification of the split-aperture along with SCF was performed using a high-frequency linear array transducer/system (MS 700/Vevo 2100). Radiation patterns from wire phantoms have shown that K=2 split-aperture technique along with SCF weighting was quite effective in suppressing the grating lobe levels to less than -60 dB as compared to performing SCF alone. The measured radiation patterns were in very good agreement with the simulation results. One should bear in mind that with split-aperture technique the frame-rate is reduced by a factor of 1/K.

With the second proposed technique, pulse probing, the frame-rate is not affected significantly since only one extra transmit event is required in order to pre-calculate the SCF weights. In the proposed 'pulse probing' technique, optimal SCF weights were pre-calculated based on broadband grating lobe echoes generated by transmission of a defocused pulse prior to imaging. These weights were later applied on the echoes received from conventional transmit beamforming. The simulation results have shown that this technique was as effective as using K=8 transmit sub-apertures in suppressing grating lobes while it did not decrease the frame-rate notably. It should be noted that the pulse probing technique would require more processing power than the split aperture technique as well as a large LUT. The experimental verification of the pulse-probing along with SCF was performed using a high-frequency linear array transducer/system (MS 700/Vevo 2100). It was experimentally validated that the proposed defocused pulse probing technique suppressed grating lobes approximately 40 dB on a 50 MHz linear array transducer with a 1.26λ pitch. It was further experimentally shown that the technique was effective for suppressing grating lobes resulting from multiple reflectors in a water bath and reflectors situated in a tissue phantom while preserving the tissue speckle. In a scattering medium, the dynamic range of the processed image needed to be increased in order to recapture tissue speckle which was suppressed undesirably due to the echo incoherence caused by many overlapping scatterers located in the focal region in addition to the grating lobes arising from the scatters at the opposing side. The technique had also been experimentally shown to be effective in suppressing grating lobes in the situation where reflectors and grating lobes overlapped however simulation studies suggested that strong overlapping grating lobes can result in much lower SCF values. This matter should be studied more carefully with more simulations and more experimental data/tissue imaging in the future. As presented in this study, the effectiveness of the split-aperture and pulse-probing techniques on grating lobe suppression were tested theoretically at different steering angles and inter-element pitches but at a fixed f-number (f/2) (figures 4.15,4.20), however, the results of these graphs were not validated for other f-numbers. The change of f-number would have effect on the amount of overlap between grating lobe echoes received on the array elements and the calculated delays for focusing. At lower f-numbers where the points are closer to the array, the difference between the distance of the focal point and each individual element is larger along the array which results in less overlap between grating lobe echoes and greater beamforming delays for focusing while at further depths where this difference is smaller, the overlap is greater and the delays are smaller. Therefore, the amount of overlap between grating lobe echoes after inserting delays should be very similar at various f-numbers which results in similar amount of grating lobe suppression in return. This matter can be further studied with more simulations at various f-numbers in the future.

In summary, in this chapter two transmit beamforming techniques were developed which were shown theoretically and experimentally to be effective in suppressing grating lobes of large-pitch phased arrays. The split-aperture technique is easy to implement however it affects the frame rate. The pulse-probing technique does not affect the frame-rate significantly however it requires more processing and more memory. In general, the proposed techniques create the possibility of developing high-frequency phased array transducers with linear array element pitch. This would significantly simplify the fabrication of phased arrays at high frequencies, suitable for intra-cochlear imaging.

CHAPTER 5

STUDY THREE: HIGH-FREQUENCY PULSED-WAVE DOPPLER ULTRASOUND FOR MEASURING BASILAR MEMBRANE VIBRATIONS

5.1 Introduction

Across its width, the cochlea is separated into three ducts, the scala vestibuli, scala media and scala tympani. The scala media and scala tympani are separated by the basilar membrane (BM), upon which sit the inner and outer hair cells which are responsible for, respectively, auditory transduction (*Møller*, 2006) and somatic motility (*Lagarde et al.*, 2008). The scala media is separated from the scala vestibuli by Reissner's membrane. When the eardrum and ossicles of the middle ear vibrate, the stapes footplate is pushed into the scala vestibuli, and the resulting pressure difference across the BM causes it to vibrate, setting up a travelling wave. Wave motion on the BM is dispersive, and the BM exhibits a varying stiffness along its length so that each point along the basilar membrane has a local resonant frequency for which the vibration amplitude is higher. The response of the BM rapidly decays to zero at points past the resonance. The point directly below the round window membrane has a resonance of approximately 18 KHz (*Stakhovskaya et al.*, 2007). Basilar membrane motion drives inner hair cell deflections, opening ion channels in the hair cells and releasing neurotransmitters. Because vibrations are carried by slow-moving waves on the basilar and tympanic membranes and because of the stiffnesses and inertia of the ossicles, significant phase shifts can accumulate between the ear canal sound pressure and the motion of various parts of the auditory system at acoustic frequencies.

Many forms of sensorineural hearing loss are associated with changes in basilar membrane motion in response to sound. Examples include the loss of cochlear non-linear amplification/compression when outer hair cells are lost (common in many disorders), or changes to BM vibration characteristics (ie Meniere's Disease (*Kim et al.*, 1994)). Therefore, direct measurement of basilar membrane vibration could be an important diagnostic tool for assessing and diagnosing hearing disorders (*Robles and Ruggero*, 2001). Intra-cochlear vibration measurements have been made in live animals and human cadaveric temporal bones using stroboscopic optical microscopy, laser Doppler interferometry, the Mossbauer technique, and Doppler Optical Coherence tomography (OCT) (*Robles and Ruggero*, 2001; *Dong and Olson*, 2009; *Lukashkin et al.*, 2005; *Kössl and Russell*, 1995; *Khanna*, 1991; *Ren et al.*, 2003; *Khanna and Leonard*, 1981; *Nuttall et al.*, 1991; *Ren*, 2002; *Overstreet et al.*, 2002; *Cooper*, 1999; *Stenfelt et al.*, 2003; *Johnstone and Boyle*, 1967; *Rhode*, 1971; *Gundersen et al.*, 1978; *Wang and Nuttall*, 2010; *Choudhury et al.*, 2008; *Hong and Freeman*, 2006; *Chen et al.*, 2011; *Gao et al.*, 2011). None of these techniques have so far allowed in-vivo imaging of the human BM due to their invasiveness, as any fenestration made into the cochlea carries an unacceptable risk of hearing and vestibular loss. Since both optical and ultrasonic techniques are unable to see through the thick, boney otic capsule surrounding the cochlea, non-invasive imaging with these modalities must be performed through the round window membrane (RWM). The RWM is an approximately 3 mm diameter membrane at the basal turn of the cochlea that acts to relieve pressure in the scala tympani when stapes footplate moves (*Møller*, 2006). From this access point, only the basal turn of basilar membrane can be monitored. The passive tuning of the cochlea/BM which is governed by the membrane stiffness is such that the local basilar membrane resonance directly under the RWM with the highest stiffness, is around 18 KHz (*Stakhovskaya et al.*, 2007). The basilar membrane has a nonlinear compressive amplification response about its local resonance frequency which is essential to expand the hearing dynamic range up to 120 dB (*Robles and Ruggero*, 2001).

Although OCT offers very high resolution, its depth of penetration through scattering tissue is very low. To the best knowledge of the author, OCT has not yet been used to measure the BM vibration through the RWM in human temporal bones. All optical techniques suffer from some common problems. The index of refraction of the BM is nearly identical to that of water, resulting in a very weak reflection of 0.0039-0.033% (*Khanna et al.*, 1989) that must be detected in the presence of stronger reflections from the RWM and the cochlear wall. The human round window differs from that of animals typically used for hearing research, by being much thicker than in most animals (*Roeser et al.*, 2007), and often covered by optically dense soft tissue folds that cause large optical reflection and scattering losses. Finally, any optical technique requires a direct line of sight between a microscope, the RWM and the BM, which is much harder to achieve under surgical conditions in humans than in small animals as the bony round window niche often covers the RWM (*Goycoolea*, 2001).

The overall goal of this third study was to develop an effective technique for measuring the vibration of the basilar membrane without damaging the cochlea with the potential for development into a clinical tool. To this end, a new approach, high-frequency pulsed-wave ultrasound Doppler vibrometry, was developed for studying the intra-cochlear dynamics through the round window. This technique has advantages in that pulsed ultrasound reflectometry automatically gives axial sectioning, suffers only a small loss at the soft tissue folds and RWM, and generates a large acoustic reflection (on the order of 30% (*Brown et al.*, 2009)(chapter 3) from the BM through the round window. Furthermore, the cochlear ultrasound probe is packaged into a miniature needle-mounted endoscope which makes orienting it in the round window niche feasible under minor clinic procedures and, as a result, the probe presents viable path to development as a minimally-invasive tool for measuring BM motion in living patients.

High-frequency pulsed-wave Doppler ultrasound is a relatively new area of ultrasonic imaging that can provide an order of magnitude better velocity resolution from dynamic structures than conventional ultrasound systems (*Christopher*, 1998; *Xu et al.*, 2008; *Zhou et al.*, 2007). In this technique, a high-frequency ultrasound pulse (center frequency >30MHz) propagates into the medium, and echoes reflect back when the pulse encounters structures with different acoustic properties. For example, when an ultrasound pulse is transmitted into the cochlea through the RWM, three distinct pulses are returned to the transducer; one from the RWM, one from the BM, and one from the far wall of the cochlear duct. Figure 5.1 shows a diagram of a probe transmitting an ultrasound pulse into the cochlea and the three main structures that reflect the pulse back to the probe. The distance between the round window and basilar membrane echoes was within the range reported for the RW and BM space (0.58-1.23 mm) (*Takahashi and Sando*, 1990). It has been previously shown in chapter 3 (figure 3.8) that the BM can be imaged with high-frequency ultrasound (*Brown et al.*, 2009). When a tone is applied in the ear canal however, BM vibrations also result. If the phase of the ultrasonic echogram is tracked over time, it will be observed to oscillate in proportion to the amplitude of the applied acoustic signal and with the same frequency.

In pulsed-wave Doppler velocimetry, the amplitude of each digitally sampled point of the echogram is recorded on each ultrasound pulse event and pulses are repeatedly sent into

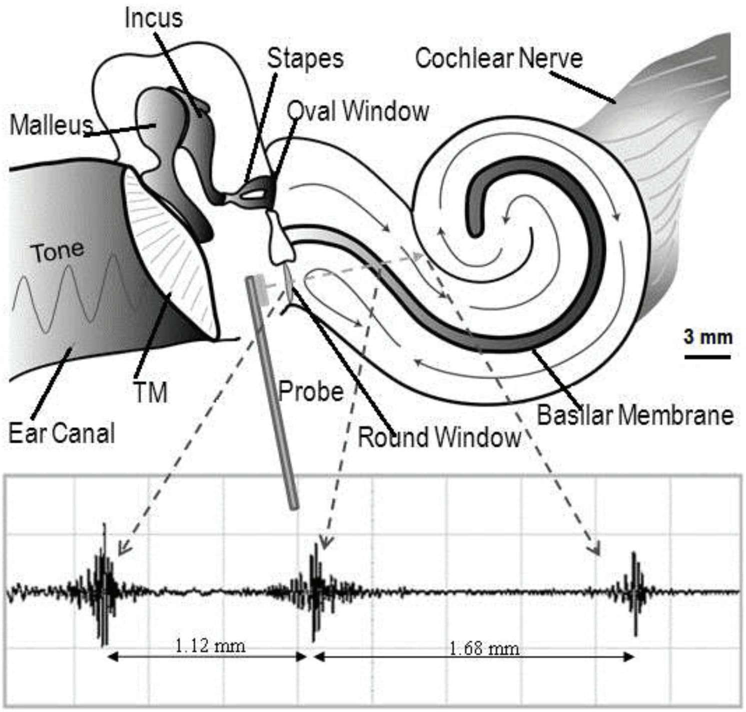

Figure 5.1: Schematic diagram of experimental Doppler measurements (*Torbatian et al.* (2012b), with permission of the Elsevier).

the tissue at a constant rate, the pulse repetition frequency (PRF). If a reflecting structure is vibrating, then it will be at a slightly different location on different pulses, and its reflection will occur at a slightly different delay relative to the pulse. This delay would cause a sinusoidal modulation in the amplitude of the sample taken at the zero-crossing of the echo over successive PRFs, so long as the acoustic displacement is small compared to the ultrasonic wavelength. For the ultrasound frequency of 45 MHz, the ultrasound wavelength is 33 μm while the largest observed displacements of membranes were just under 2 μm, so that they were always in the small displacement limit. The resulting sinusoidal variation can be detected in the fast Fourier transform of the sequence of amplitudes recorded for each pulse. By tracking the change of echo amplitude at the zero-crossing point over successive PRFs, the displacement curve can be measured. The velocity of a moving object is calculated based on the amplitude of this curve and the direction of motion is determined based on the phase of displacement curve, making possible the measurement of the phase of the acoustic displacement relative to the ear canal sound pressure.

To validate the method, a resonant vibrating piezoelectric actuator was measured with both LDV (CLV700, Polytec Inc., CA, USA) and pulsed-wave Doppler ultrasound and as shown in figure 5.2 the two measurements were found to be in good agreement over the frequency range from 100 Hz to 2 KHz. The magnitude of LDV was about 4.37±2.25 dB

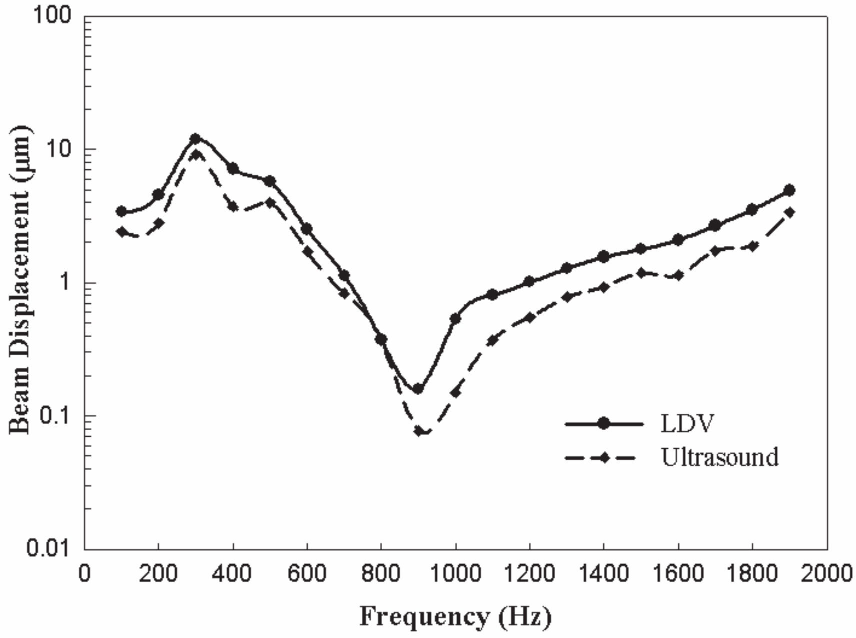

Figure 5.2: The displacement of piezoelectric actuator measured with the ultrasound and laser Doppler vibrometer. Both measurements showed the same response pattern while the LDV levels were higher.

higher than the ultrasound. This difference is believed to be due to damping caused by the ultrasound gel used for the ultrasound measurement but not the LDV measurement. The reproducibility of ultrasound measurements on the actuator was about $\pm 4.5\%$ which was corresponded to the 'cosine' of Doppler angle between the transducer and the vibrating object ($\pm 15°$).

5.2 Materials and Methods

5.2.1 Temporal Bone Preparation

In this study, measurements were performed on 8 human temporal bones (4 male, 4 female), with an average age of 64 (age range: 48-86). Six of the temporal bones were harvested within 48 hours of death at Dalhousie University and were refrigerated at $5°C$ in 10% Betadine or Salin and the others were purchased frozen from Anatomy Gifts Registry (MD, USA). The handling of the cadaveric tissues and the measurements described throughout this chapter were approved by the Ethics Review Board at Dalhousie University, Faculty of Medicine.

For each specimen, the bony ear canal was left intact to allow placement of the sound tube generating an acoustic pressure and a probe microphone (ER-7, Etymotic Research

Figure 5.3: Photograph of needle Doppler probe (*Torbatian et al.* (2012b), with permission of the Elsevier).

Inc., IL, USA) for the measurement of sound pressure level. To access the RWM, the mastoid portion of the facial nerve and surrounding bone were removed in a ”facial recess” approach. All of the middle ear structures, such as ossicles, ligaments, middle ear muscles, and any round window folds were left intact.

5.2.2 *Experimental Set-up*

An un-focused single-element transducer, based on PMN-32%PT single crystal substrate (*Park and Shrout*, 1997) was fabircated. It was fabricated by first lapping the substrate to a 47 μm thickness (45 MHz), sputtering a 1 micron Al electrode to the lapped surface, and then a 1 mm diameter disc was drilled out of the substrate using a diamond core bit. A conductive backing layer (EPO-TEK EE129-4) was deposited on the back face of the PMN-PT disk where the central conductor of a micro-coax cable was connected to the epoxy and fed through a 24 gauge needle. The needle was used as the ground/housing, and the front face of the transducer was connected to it by sputtering a layer of aluminium over the needle and front face of the transducer. A photograph of the fabricated probe is shown in figure 5.3.

The probe had to be rested up on the niche of round window in order to detect BM echo as shown in figure 5.1. This was a difficult job since the available space around the

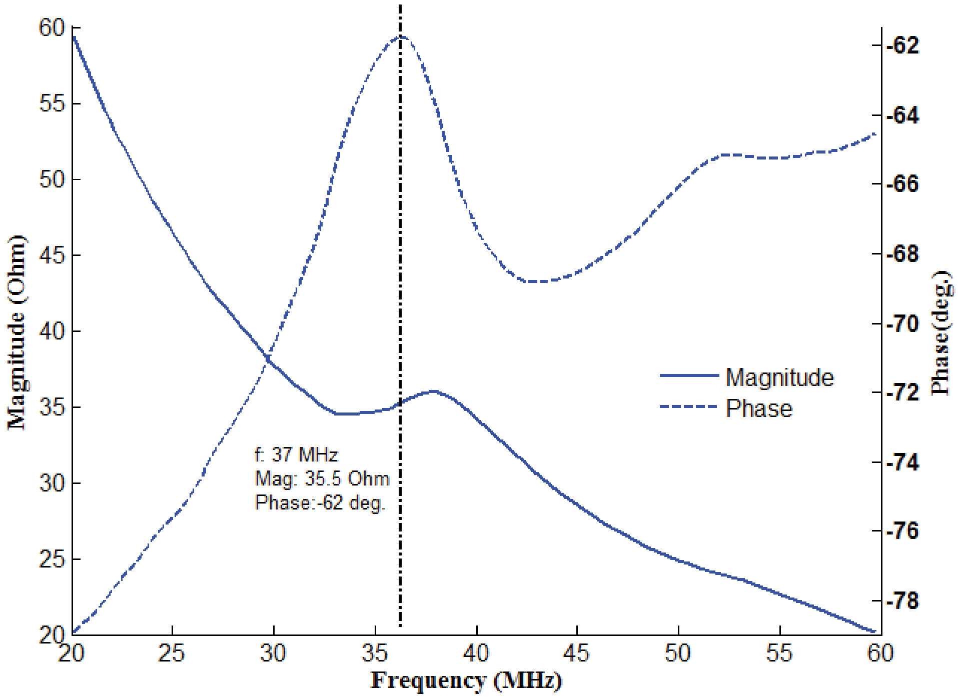

Figure 5.4: Electrical impedance of a typical in-house fabricated probe.

round window was quite limited and the probe had to be placed in a specific angle faced toward the stapes in order to detect required echoes. Therefore, during positioning of the probe, a precision position system and careful manipulation was required in order to avoid damaging of the front face by scratching on the bone. As the probes were somewhat sensitive to electrode damage, a batch of probes was usually fabricated with the described procedure in order to avoid any interruption during the experiment. In figure 5.4, the magnitude and phase of impedance of a typical in-house fabricated 1 mm unfocused probe measured using precision impedance analyzer (Agilent 4294A, Agilent Technologies Inc., CA, USA) is shown. As shown, the probe had 35.5 Ohm and -60 ° phase at the resonance peak. The effective electromechanical coupling coefficient of the fabricated probe (k_{eff}) can be estimated using the measured impedance as follows (*Cobbold*, 2007):

$$k_{eff} = \sqrt{\frac{\pi}{2}\frac{f_r}{f_a}\tan(\frac{\pi}{2}(\frac{f_a - f_r}{f_a}))} \tag{5.1}$$

where f_r called the resonance frequency is the minimum of magnitude impedance and f_a called anti-resonance frequency is the maximum of magnitude impedance in the neighbour of operating frequency of the probe. Based on the impedance measurements (figure 5.4), k_{eff} was 47% for this probe. In order to measure the pulse-echo response of the probe, a piece of glass was placed in the water and the echo was recorded on the oscilloscope

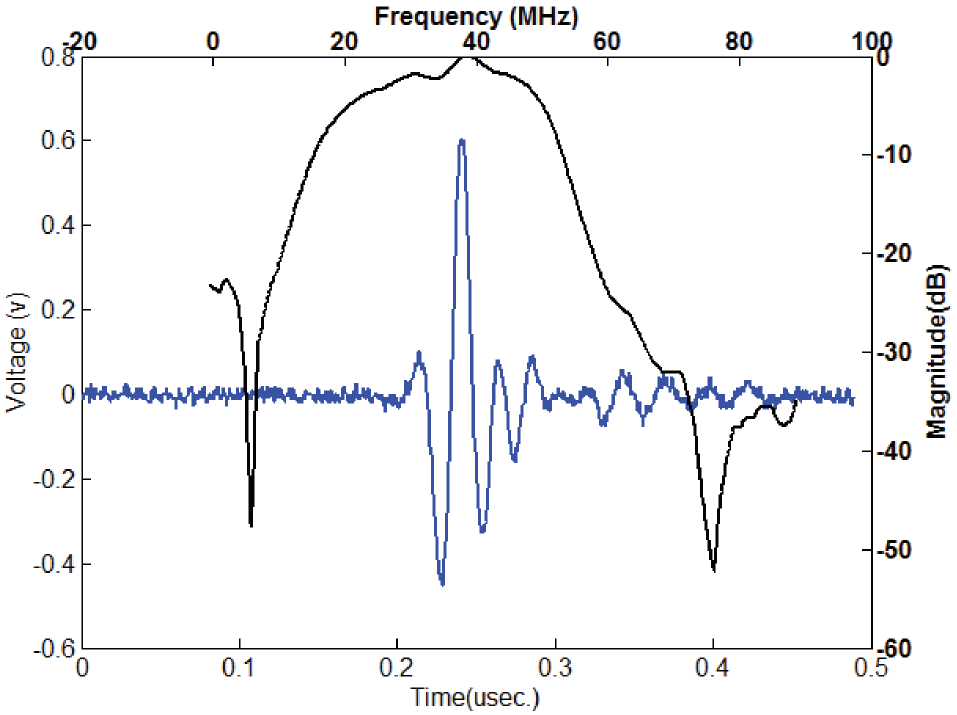

Figure 5.5: Pulse-echo of a fabricated probe operating at 37 MHz with 64% -6 dB bandwidth.

(Agilent DSO6014A, Agilent Technologies Inc., CA, USA) while it was triggered by a high frequency ultrasound pulser/receiver unit (Daxsonics 10ERS3., Halifax, Canada). In figure 5.5, the measured echo and its frequency response is shown. This particular probe had a 64% -6 dB bandwidth at 37 MHz.

Experiment set-up and Data analysis

The block diagram of the proposed set-up is shown in figure 5.6. To begin the measurements, the temporal bone was situated on an adjustable positioning stage, and the Doppler probe was positioned adjacent to the niche of RWM. Since the typical displacement response to the applied sound levels was on the order of tens of nanometers, the position of the probe was critical in order to ensure that a strong echo signal was obtained. The probe was positioned on the niche of round window to detect the first two echoes shown in figure 5.1 which were separated by about 1 mm distance, corresponding to the round window and basilar membrane. In order to distinguish reverberations from real echoes, the probe was moved forward and backward on the niche of round window in order to make sure that the distance between two echoes stayed the same while they were moving back and forth. This procedure helped to keep the probe positioning consistent throughout measurements on several temporal bones. A speaker, controlled by a signal generator (AFG3101, Tektronix Inc., OR, USA), was used to generate a pure-tone sinusoidal signal for stimulating the eardrum through a plastic sound tube. The applied sound pressure

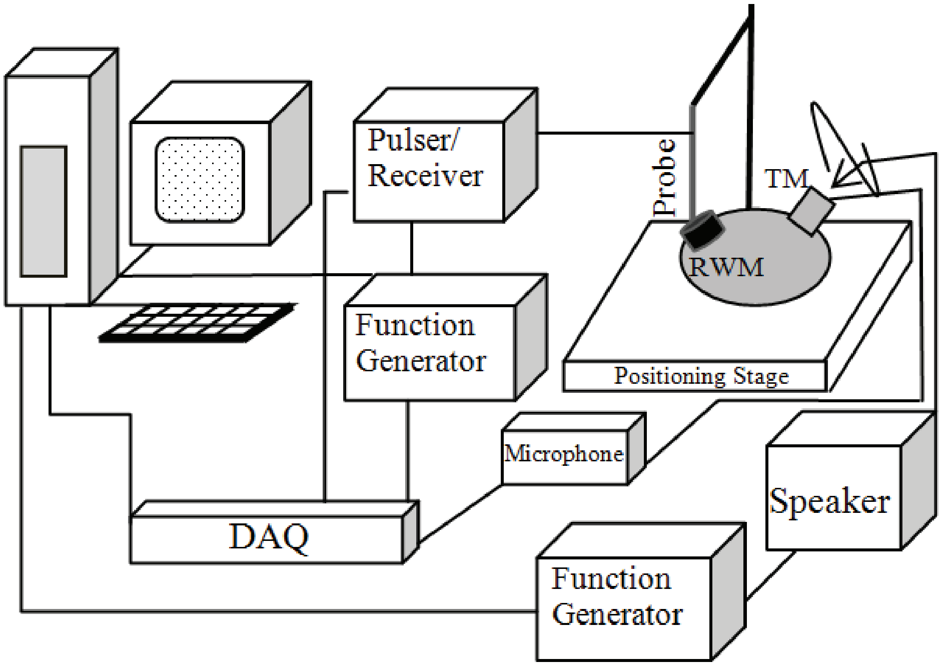

Figure 5.6: Block diagram of the proposed set-up. The sample was placed on the positioning stage where the high-frequency probe was positioned on the niche of round window membrane (RWM). The Doppler probe was controlled by a high-frequency pulser-receiver unit. A pure tone sound was generated by a speaker which was controlled by a signal generator to stimulate the tympanic membrane (TM). The applied sound pressure in the ear canal was measured by an ER-7 microphone. The pulse-echo and ER-7 output signals were sampled by a data aquisition card and transferred to a PC for Doppler processing. A second signal generator was used to set the PRF for triggering the pulser and synchronize the system (*Torbatian et al.* (2012b), with permission of the Elsevier).

level (SPL) in the ear canal was measured using a probe microphone (Etymotic Research ER-7) and adjusted to 120 dB SPL at the tympanic membrane. The ER-7 microphone was attached to the tip of the sound tube coming from the speaker while both were positioned in the ear canal close to the tympanic membrane. For the phase measurements between the membrane displacements and applied sound pressure in the ear canal (ER-7 output), a frequency-dependent correction factor was applied to the ER7 microphone data as this microphone does not have a linear phase response below 1 kHz. In Appendix B, the amount of required correction at each frequency is summarized in a table. The fabricated needle Doppler probe was controlled by a high-frequency ultrasound pulser/receiver unit (Daxsonics 10ERS3., Halifax, Canada) capable of generating ultrasound pulses in addition to receiving, bandpass filtering, and amplifying the echoes. The received echoes were sampled and recorded using either an Alazar RF data acquisition card (ATS9350, Alazar Tech Inc., QC, Canada) with a 16-bit depth 500 MHz sampling frequency or an oscilloscope with 8-bit depth and 2 GHz sampling frequency (Agilent DSO6014A, Agilent Technologies

Inc., CA, USA). A second function generator (Agilent 33220A, Agilent Technologies Inc., CA, USA) was used to trigger the pulser/receiver unit at the pulse-repetition-frequency (PRF) and to synchronize the acoustic signal to the ultrasound PRF. The PRF was adjusted to 20 times the frequency of the tone applied to the speaker in order to collect 20 points per cycle of the applied tone. The 2^{14}=16384 echoes from the membranes were collected for each acoustic frequency using Alazar card and the responses averaged in order to improve the signal-to-noise ratio. A MATLAB$^{\text{TM}}$ (The MathWorks Inc., Natick, Mass.,USA) script (which will be further explained later) was written to communicate with Alazar card, receive the digitized echoes, and perform analysis on it (appendix C.3).

In initial experiments, a broadband ultrasound pulse centred at 45 MHz was transmitted into the cochlea through the round window and the three echoes corresponding to the round window, basilar membrane, and the cochlear bone shown in figure 5.1 were detected using an oscilloscope. The probe was triggered at a constant PRF in order to collect a series of snapshots of the echoes over successive trigger events. When the sound was applied to the tympanic membrane, the membrane echoes were displaced over consecutive pulses while the echo of cochlear bone was still. When the membrane was moving toward the probe, the arrival time of corresponding echo was decreased while it was increased when the membrane was moving away from the probe. Therefore, by calculating the time-shifts of echoes recorded at consecutive PRFs, the amount of membrane displacement and its direction could be measured. One way to detect the displacement is by calculating the time-shifts of successive echoes using cross-correlation technique and scaling it properly (*Cobbold*, 2007). As an example, in figure 5.7a, successively recorded echoes of the BM are shown while applying a 120 dB SPL, 500 Hz sine-wave to the tympanic membrane. The recorded echoes and the calculated displacement of the basilar membrane vibrating at 500 Hz for one of the cadaveric temporal bones is shown in figure 5.7a-c. A special feature of Agilent oscilloscope called ”segmented memory” was used to record several snapshots of the membrane echo when the PRF was set to 20 times of the frequency of the stimulus (PRF $= 20f_{stim}$). Only 30 cycles of the applied stimulus were recorded due to the limited memory size of the scope. In order to improve the accuracy of detecting small phase shifts between echoes at higher frequencies, the recorded echoes were up-sampled 20 times after transferring to the PC. Then, the cross-correlation between the recorded echoes were calculated by considering the first echo as the reference to reveal the pattern of BM/RW displacement and calculate the phase shifts (2.21). Since the frequency of the pure-tone signal was known, a band-pass filter (based on linear phase finite impulse response (FIR) with 48 th order) centred at that frequency (f_{stim}) with ±10 Hz cut-off frequency was applied on the displacement signal to remove noise produced by building

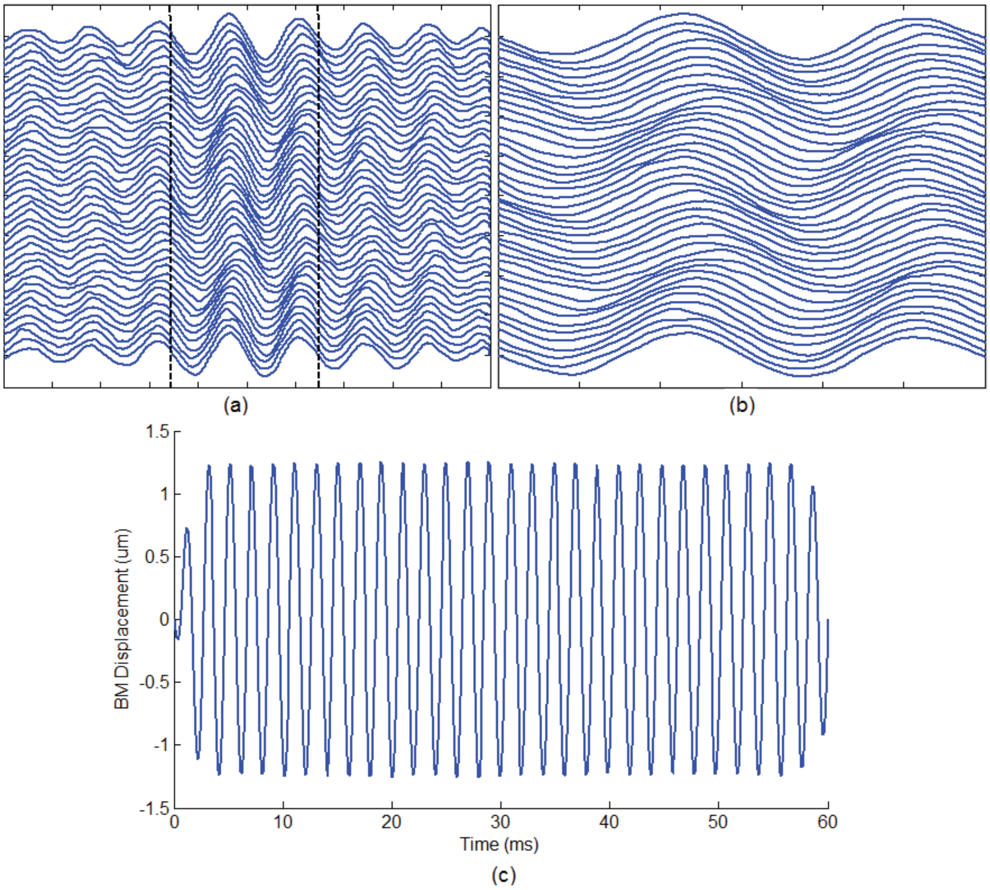

Figure 5.7: The recorded echoes and the calculated displacement of the vibrating basilar membrane, stimulated by a 500 Hz sine-wave tone which was applied to the tympanic membrane. a) Successive snapshots of the BM echoes when a 500 Hz sin-wave was applied to the tympanic membrane. b) The marked region in (a) is zoomed in order to show the pattern of the movement of echoes while applying the sound. c) The displacement of BM was derived by calculating the cross-correlation between upsampled echoes shown in (a) and applying band-pass FIR filter (*Torbatian et al.* (2012b), with permission of the Elsevier).

vibrations. The displacement ($\triangle x_j$) and maximum velocity of the membranes $max(\triangle v_j)$ were calculated using the detected time-shifts ($\triangle t_j$) as follows:

$$\begin{aligned}\triangle x_j &= \frac{c \triangle t_j}{2} \\ max(\triangle v_j) &= 2\pi f_{stim} max(\triangle x_j)\end{aligned} \tag{5.2}$$

where c is the speed of sound in water. As shown in figure 5.7b, the wavy pattern of BM displacement could be visualized by following an echo point along the y-axis. The cross-correlation between the echoes shown in figure 5.7a was calculated to derive the time-shift between echoes, proper scaling was done based on (5.2), and a bandpass filter was applied to filter out the noise and reveal accurate values for BM displacement shown in figure 5.7c. In this method, the recorded resolution of echoes are needed to be high enough in order to detect very small motion. Therefore, it was usually necessary to upsample the echoes prior to time-shift calculation which imposed a high computational cost to the processing.

To avoid high computational cost and long data transfer time from the oscilloscope, another approach which is very sensitive to small displacements and fast in processing, was implemented with a 500 MHz 16-bit PCIe Alazar data acquisition card in place of the oscilloscope. This technique was based on tracking the change of signal amplitude of an individual echo point which corresponds to a particular depth in the tissue, over many ultrasound pulses. The fast Fourier transform (FFT) of this changing amplitude was calculated to generate a time-frequency spectrum. The points in the echo that move strongly in response to the stimulus are expected to show high FFT magnitudes at the applied frequency while the non-moving points have FFT amplitudes close to zero. In figure 5.8a, echograms are shown along the y-axis (corresponding to depth in tissue) for 16384 transmit pulse events (along the x axis) when the ear canal was stimulated with a 1 KHz sinusoidal wave. In figure 5.8b, the time-frequency spectrum is shown which is obtained by taking the FFT along the x-axis of figure 5.8a. As shown, two bright regions separated by about 1 mm were detected at the stimulation frequency of 1KHz that corresponded to the reflections from the RWM and BM . A corresponding wavy pattern with a 1 KHz frequency can be seen in the same regions of figure 5.8a.

Close examination of the bright regions in figure 5.8b shows a sinusoidal modulation in the amplitude as a function of depth. This modulation corresponds to the ultrasound phase shift over successive PRFs. Points near a zero-crossing in the echogram exhibit large amplitude changes in response to reflector displacement because they have a large local

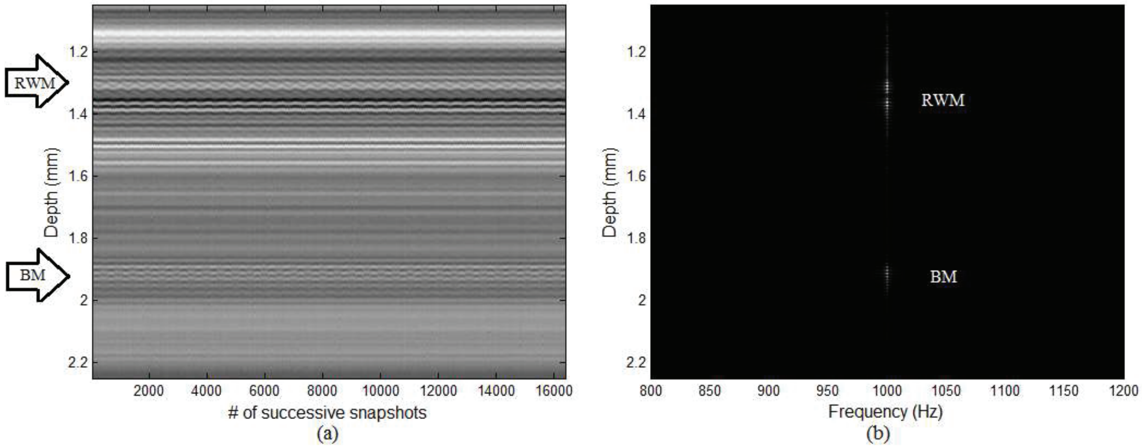

(a) (b)

Figure 5.8: a) The echoes recorded from the niche of round window over 16384 PRFs (snapshots) of a temporal bone when the tympanic membrane was stimulated with a 1 KHz sinusoidal wave. Each echo snapshot is shown along the x-axis. The voltage amplitude of each echo is mapped to gray scale values shown along the y axis (Depth). The two arrows show the location of round window and basilar membrane which were separated by about 1 mm distance. The wavy patterns visualized in these regions indicate the time-shifts of successive echoes when the sound was applied. b) The time-frequency spectrum of the recorded echoes. At each depth (y-axis), the FFT of echo points shown in (a) over many snapshots (x-axis) was calculated. As shown, two bright regions corresponding to the round window and basilar membrane were detected at 1 KHz when the stimulator was applied (*Torbatian et al.* (2012b), with permission of the Elsevier).

slope. In contrast, at maxima and minima of the echogram there is very little response to reflector displacement because the local slope is zero. For this reason in order to obtain the displacement amplitude, the point with the largest amplitude in the time-frequency spectrogram within the RWM and BM regions at the excitation frequency was taken to be representative of the motion of the structure. To calculate the displacement from the spectrogram, the ultrasonic echogram is modelled as a Gaussian modulated cosine wave with full width at half maximum (FWHM) bandwidth of $BW_{FWHM} = \frac{2.36\sigma_W}{2\pi f_u}$ (*Cobbold*, 2007) and is expressed as follows:

$$V_{PRF}(t,i) = A\cos(2\pi f_u t + \phi_a(t + \frac{i}{PRF})) \cdot e^{-\sigma_W^2 (t^2/2)} \tag{5.3}$$

where $V_{PRF}(t,i)$ is the instantaneous echogram amplitude, t is the time in the ultrasound signal (corresponding to tissue depth), A is the peak amplitude, f_u is the ultrasound pulse center frequency, ϕ_a is the time dependent phase caused by the motion of the membrane in response to sound, PRF is the pulse repetition frequency, and i indexes the pulse number (corresponding to time for the acoustic signal). Using a trigonometric identities this can be rewritten as

$$V_{PRF}(t,i) = (A\cos(2\pi f_u t)\cos(\phi_a(t+\frac{i}{PRF})) - A\sin(2\pi f_u t)\sin(\phi_a(t+\frac{i}{PRF})))\cdot e^{-\sigma_W^2(t^2/2)} \tag{5.4}$$

If the applied sound pressure at the tympanic membrane is sinusoidal, then the membranes will also move sinusoidally and so will induce a sinusoidal phase shift $\phi_a(t) = \frac{2\pi f_u(2d_{max})}{c}\sin(2\pi f_{stim}t)$ on the echogram. Here d_{max} is the peak displacement of the membrane and c is the speed of sound so that $\frac{2d_{max}}{c}$ is the ultrasound time delay generated on reflection and $\frac{4\pi f_u d_{max}}{c}$ is the peak induced by the phase shift. The factor of two accounts for the fact that sound must travel to the reflector and then back to the source. f_{stim} is the acoustic stimulation frequency. Since the membrane displacements ($<$2 μm) for the sound level of 120 dB SPL) are much smaller than an ultrasound wavelength (33.4 μm), $\phi_a << 1$ and the small angle approximation becomes valid so that $\sin\phi_a \sim \phi_a$ and $\cos\phi_a \sim 1$. It follows that

$$V_{PRF}(t,i) \sim A(\cos(2\pi f_u t) + \frac{4\pi f_u d_{max}}{c}\sin(2\pi f_{stim}(t+\frac{i}{PRF}))\sin(2\pi f_u t))\cdot e^{-\sigma_W^2(t^2/2)} \tag{5.5}$$

V_{PRF} is most sensitive to the acoustic phase at depths for which $2\pi f_u t = \frac{n\pi}{2}$ so that $\cos(2\pi f_u t) = 0$ and $\sin(2\pi f_u t) = 1$ (i.e. the zero-crossings of $V_{PRF}(t,i)$). When this is the case, and assuming that $BW_{FWHM} \sim 50\%$ and that a zero-crossing near the center of the envelope was chosen where $e^{-\sigma_W^2(t^2/2)} \sim 1$, the amplitude of the response becomes

$$V_{PRF}(i) \sim \frac{4\pi f_u A d_{max}}{c}\sin(2\pi f_{stim}(\frac{i}{PRF})) \tag{5.6}$$

By calculating the FFT of the echo amplitude over many pulses i, a peak at f_{stim} will be detected whose amplitude is directly proportional to the displacement caused by the sound. Since f_u and c =1500 m/s for tissue are known and A can be obtained from the amplitude of echogram, this information is sufficient to measure the displacement of the membrane. Moreover, the phase of the FFT at the acoustic frequency provides the phase of the membrane displacement which can be compared to the phase of a simultaneously measured ear canal pressure.

Using the above approach, the time-frequency spectrum of the recorded echoes over many pulses was calculated and the brightest regions corresponding to the round window and basilar membrane were located. For each region, the echo point with the highest FFT amplitude was identified and was scaled based on the technique described above to calculate the membrane displacement at each tone frequency. The peak to peak velocity magnitude values ($velocity_{pk-pk}$) were then calculated from the displacement magnitude (d_{max}) and known input frequency (f_{stim}) using the following equations and were normalized to the applied sound pressure measured by the ER-7 microphone.

$$velocity_{pk-pk} = 2\pi f_{stim}(2d_{max}) \tag{5.7}$$

To measure the phase difference between the ear canal pressure and the membrane motion, the sound pressure signal from the ER7 microphone was recorded on the second channel of the Alazar data acquisition card during the experiment. The phase angle of the BM or RWM motion was subtracted from the measured phase of the pressure signal to obtain the plotted phases.

Once the sound pressure level was adjusted to 120 dB by controlling the amplitude of speaker signal and getting feedback from ER-7, the MATLAB-based GUI shown in figure 5.9 was executed. As shown, the inputs were the tone applied to the ear canal (Frequency), number of points per cycle (PtsPerCycle) for adjusting the PRF, the start point of the echoes (Acquire After), number of samples per record of each echo (Samples Per Record), and number of snapshots (Number of Samples). The snapshots of the echoes and the sound pressure level measured by ER-7 were plotted and saved for calculating the corresponding displacements/velocities offline. Moreover, the time-frequency spectrum of the snapshots of the echoes were plotted in order to visualize the portion of the echo corresponding to the membrane which was vibrating while the tone was applied. The setting for the experiments in this study was Frequency= the desired tone of speaker, PRF=20×Frequency (PtsPerCycle=20), (Acquire After) and (Samples Per Record) adjusted in order to capture both membrane echoes in each snapshot, and number of snapshots= 2^{14} limited by the size of Alazar on board memory.

5.3 Results and Discussion

Figures 5.10 (a) and (b) show the velocity measured for the RWM and BM, normalized to the sound pressure input in the ear canal, of the eight temporal bones (grey lines) and their average (black line) used in this study. The velocity of both the RWM and BM show peak values ranging between 700 and 1300 Hz. This range of peak values, along with the overall characteristic shape of the curves, is consistent with previously measured middle ear transfer function results (*Goode et al.*, 1994; *Voss et al.*, 2000; *Aibara et al.*, 2001). At the peak values (400-1500 Hz), the mean velocity levels of the RWM were 6.80±2.96 times larger than the mean BM velocity levels. The maximum of normalized mean RWM

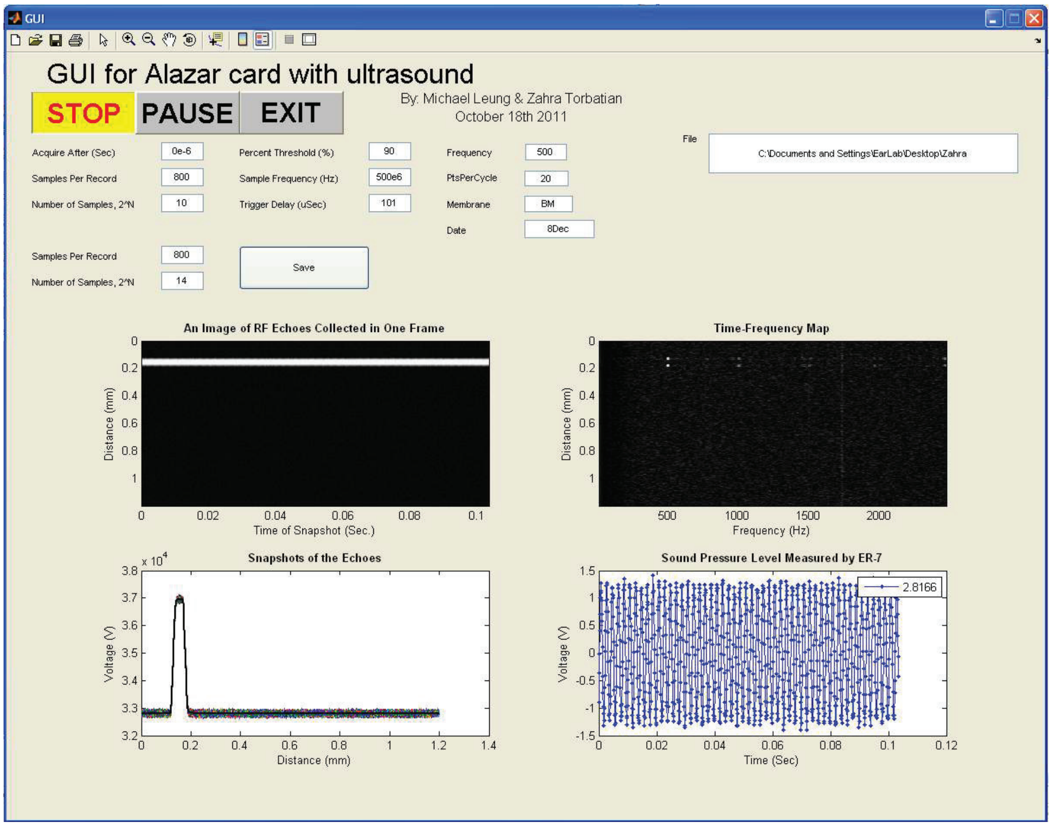

GUI for Alazar card with ultrasound

By: Michael Leung & Zahra Torbatian
October 18th 2011

Acquire After (Sec): 0e-6
Samples Per Record: 800
Number of Samples, 2^N: 10
Percent Threshold (%): 90
Sample Frequency (Hz): 500e6
Trigger Delay (uSec): 101
Frequency: 500
PtsPerCycle: 20
Membrane: BM
Date: 8Dec
File: C:\Documents and Settings\EarLab\Desktop\Zahra
Samples Per Record: 800
Number of Samples, 2^N: 14

Figure 5.9: The MATLAB-based GUI developed for controlling the proposed pulsed-wave Doppler study.

displacement at 120 dB SPL in the ear canal which occurred about 800 Hz was measured to be 715.64±479.96 nm corresponding to a RWM response of 179.86±120.62 μm/s/Pa. To figure out the noise floor inherent to the system, the FFT of the membrane displacements were calculated to measure the level of signal on all frequencies except that of the applied tone. The noise floor (dashed line) shown in figure 5.10 is the average of noise levels of all measurements and is well below the measured signal level except for some bones at the high end of the frequency range. The measured mean value of RWM velocity is consistent with results reported by *Stenfelt et al.* (2004) who observed velocities at 31 points on the round window of a single temporal bone to range from 100 to 750 μm/s/Pa at 800 Hz (figure 2.7a), using an LDV through a hole drilled into the temporal bone near the round window. That technique used spatially-resolved velocity measurements whereas the unfocused ultrasound transducer used in the present study effectively averages the velocity over a $(\pi(0.5\ mm)^2)$ 0.78 mm^2 area in the central portion of the RWM surface.

In order to estimate the effect of placing ultrasound gel on the round window membrane on cochlear mechanics, RWM vibration was measured with an LDV system (CLV700, Polytec Inc., CA, US) prior to placing the probe on the RWM. As shown in figure 5.11, the normalized velocity magnitude of the RWM measured with LDV was found to have the same response pattern as the ultrasound measurements showed in figure 5.10a however the LDV levels were 7.62±3.63 dB higher over the measured frequency range. This difference can be likely attributed to damping and inertia effects of the ultrasound gel. Moreover, as mentioned above with LDV the vibration of a single point was measured on the RWM while with ultrasound it was an average of vibration of points located at a spot with various phases. These measurements are reproducible as long as the mechanical characteristics of the middle ear and inner ear structures (e.g. stiffness) have not changed significantly over time. As measured with the piezoelectric bending actuator, the positioning of the probe can introduce about 4.5% variation to the amplitude of membrane responses corresponding to the Doppler angle (up to 15°) however freshness of the bone decays over time and might shift the resonance peak to lower frequencies (*Robles and Ruggero*, 2001).

The maximum measured displacement of the BM which occurred about 800 Hz was 106.8±30.63 nm at 120 dB SPL corresponding to a normalized velocity of 26.84±7.69 (μm/s/Pa). Surprisingly, there are no direct reports of basilar membrane velocity in human temporal bones at a location directly underneath the round window in the literature. *Stenfelt et al.* (2003) reported the BM vibration measured in one temporal bone with an LDV system at a point 12 mm apical to the BM to be on average 12 dB higher than the stapes footplate motion at 1 KHz (absolute velocity was not reported, figure 2.6 (a)). Based on *Hato et al.* (2003) measurements of stapes footplate vibration in 10 temporal bones,

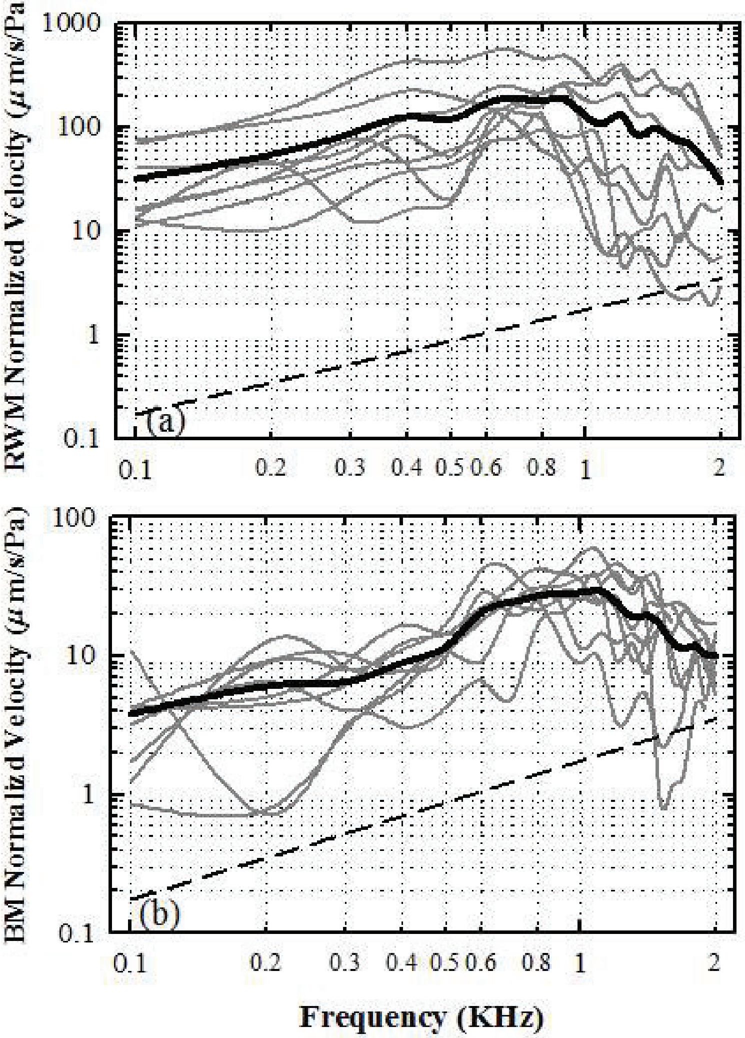

Figure 5.10: Normalized velocities of (a) RWM and (b) BM. (Grey individual measurements; Black average measurements over 8 temporal bones, Dashed line-Mean noise floor) (*Torbatian et al.* (2012b), with permission of the Elsevier).

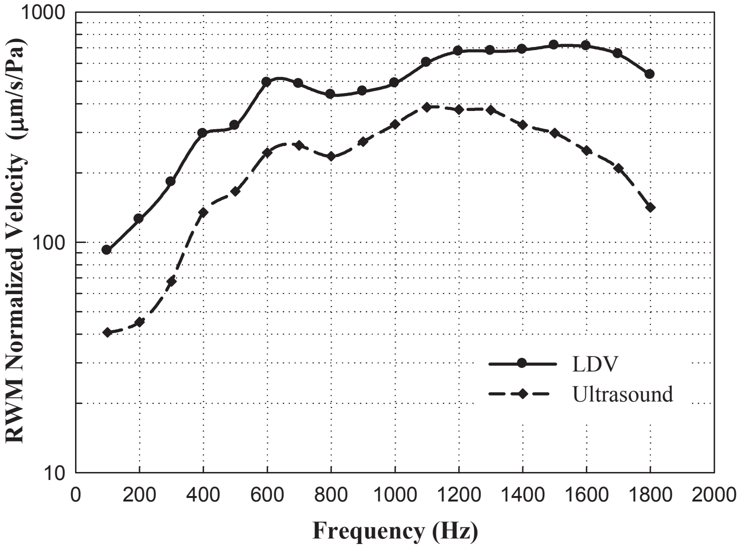

Figure 5.11: The normalized velocity of the RWM measured with the ultrasound and laser Doppler vibrometer for a human cadaveric temporal bone. Both measurements showed the same response pattern while the LDV levels were higher.

this corresponds to a normalized BM velocity range of between 750 μm/s/Pa and 1500 μm/s/Pa, between 28 and 35 dB higher than the measured amplitude in this study. Much of this discrepancy can be accounted for by the fact that the BM's stiffness decreases as one moves closer to the apex, increasing its response at low frequencies, but it may also indicate that some of the beam is hitting portions of the cochlea that are not moving or not moving as much as the BM such as the osseous spiral lamina (*Stenfelt et al.*, 2003).

A limitation of the unfocused Doppler probe arises from the fact that it is a unfocused, planar piezoelectric disk. Since the transducer is unfocused, the beamwidth is approximately the same size as the disk i.e. a 1 mm diameter over the full imaging distance. It is quite likely that the ultrasound spot covers a significant fraction of the osseous spiral lamina in addition to the basilar membrane which is likely a source of the low measured vibration and the large bone-to-bone variability. The portion of the osseous spiral lamina adjacent to the cochlear wall has been shown to move much less than the BM (*Stenfelt et al.*, 2003) (figure 2.6 a), and since the measured Doppler vibration amplitude is effectively an average over all reflections contributing at a point in time, this will result in a reduced measured velocity. Furthermore, as measurements have previously shown (*Stenfelt et al.*, 2004), the vibration of the round window can exhibit two or more regions that move out of phase with each other at frequencies above 1.5 kHz. Since the probe is unfocused, it effectively averages the RWM vibration level over its surface area, and when multiple regions are out of phase, a low vibration level is recorded even if each region is moving substantially. Similarly, measured BM motion will begin to decay when the wavelength of the travelling wave at the basal turn becomes comparable to the ultrasound spot size on the BM. From the frequency roll-off of data, this appears to prevent any measurements above 2 KHz. Figures 5.12 (a) and (b) show the measured displacement phase relative to sound pressure level in the ear canal for the RWM and BM of the eight bones (grey lines) and their average (black line), respectively. A negative phase indicates that the membrane was moving toward the ultrasound probe and lagged the ear canal pressure. Phase values were only calculated if the amplitude of the measured signal at the acoustic frequency exceeded the acoustic noise floor associated with structural vibrations of the lab and apparatus, typically 7 nm. The dashed lines on figure 5.10 show the level of noise floor over the frequency range. The RWM phase results shown in figure 5.12a are in relatively good agreement to a previous study by Stenfelt (*Stenfelt et al.*, 2004) of the RWM using an LDV system which reported a relatively constant phase region at frequencies below 0.6 KHz followed by more rapid phase accumulation indicative of a transition to continuous wave-propagation behavior (figure 2.7b). The constant phase region around -180 degrees (figure 5.12a) indicates that the RWM bulged outward into the middle ear (toward the ultrasound probe) while positive sound pressure was applied into the ear canal. It has been shown that the middle ear acts as a linear phase bandpass filter with group delay of 83 μs for frequencies above 1 KHz (*Nakajima et al.*, 2009). Moreover, LDV measurements of the relative phase between a point on the basilar membrane 12 mm apical to the round window region and the stapes footplate show that a large group delay is evident for frequencies above 0.5 KHz (*Stenfelt et al.*, 2003) (figure 2.6b). Therefore, the increase of phase shown in the measurements with a mean group delay of 844 μs for frequencies above 0.5 KHz corresponds to the delays caused from the TM through the ossicular chain, and the basilar membrane. As shown in *Stenfelt et al.* (2004), the RWM phase characteristics at lower frequencies changes when the stapes is damaged or replaced by a piston. This might be the reason that the constant phase of one temporal bone was lower than the rest in the measurement (figure 5.12a). The BM phase shown in figure 5.12b remains relatively constant for all bones up until a resonance occurs at between 550 Hz and 1500 Hz. This resonance can likely be identified with the middle ear resonance reported by *Homma et al.* (2009) to occur between 800 and 1200 Hz for air conducted sound. The higher variability in the BM phase results may be due to loading of the RWM by the transducer and the ultrasound gel, differences in the preparation of the temporal bones, the possibility of the ultrasound beam hitting multiple structures within the BM, and possibility of a non-normal angle of incidence between the beam and the basilar membrane. More consistent basilar membrane displacement phase measurements may be possible with a focused probe. The above facts might explain why no clear relationship between BM motion and RWM motion was found

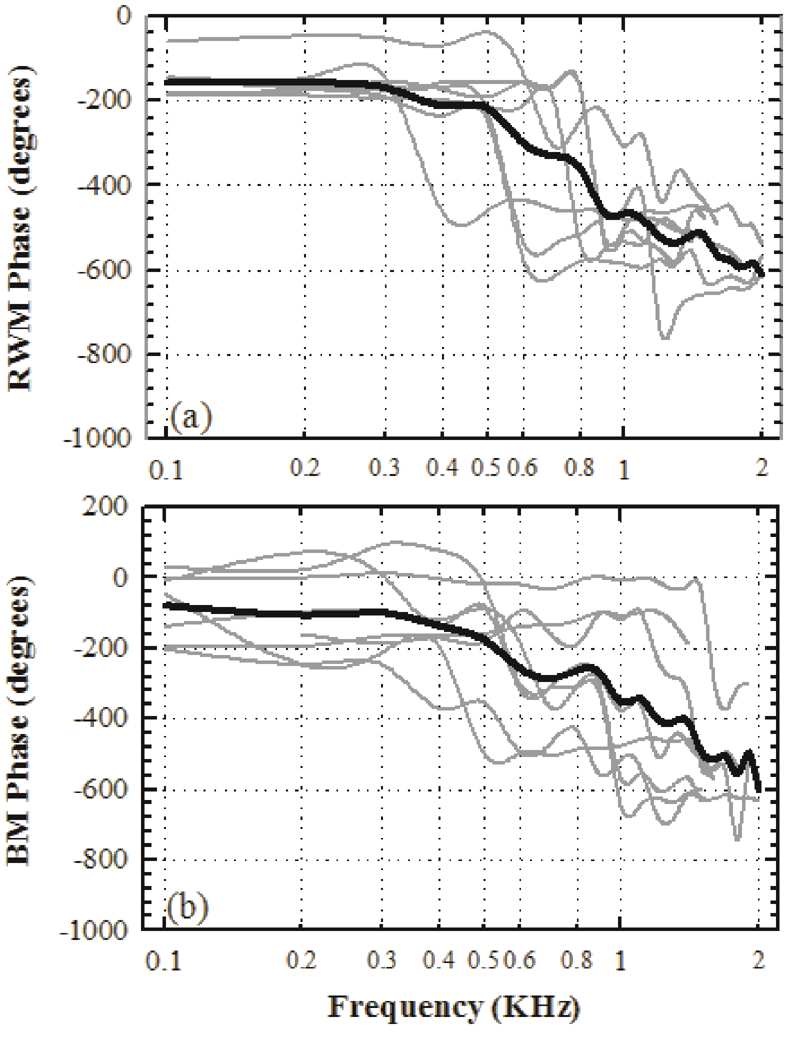

Figure 5.12: Phase difference of (a) RWM and (b) BM displacements versus the applied sound pressure in the ear canal measured by ER-7. (Grey individual measurements; Black average over 8 temporal bones) (*Torbatian et al.* (2012b), with permission of the Elsevier).

in this study. No data was available in the literature for the BM phase characteristics at the basal turn on human temporal bones in order to compare with the results of this work.

5.4 Conclusion

This chapter reports results on measuring the vibration of BM and RWM without violating the cochlea using high-frequency pulsed-wave Doppler ultrasound. This experiment represents proof of concept for a possible clinical measurement of intracochelar structure motion because it was done without fenestrating or otherwise damaging the cochlea. This is the first time that this technique has been used for measuring the intra-cochlea dynamics. The use of ultrasound entails three main benefits. 1) The technique introduces no damage to the cochlea, so it should be a viable approach to making in-vivo human measurements, 2) it produces a much larger BM reflection (with minimal attenuation/scattering from the RWM), giving it an advantage over optical techniques, and 3) it can be done with a small (< 1 mm diameter) probe suitable for clinical use that does not require a line of sight through a microscope. For an in-vivo procedure, the probe would be inserted through the eardrum and rested up against the RWM after a minimally-invasive myringotomy (the same procedure described in chapter 3 for the imaging probe).

One of the major limitations of the current system is that, since an unfocused transducer was used, the minimum detectable acoustic wavelength is limited by the ultrasound beamwidth. The wavelength of the traveling wave on the basilar membrane becomes small at higher frequencies and so within the ultrasound beam there are regions of both positive and negative Doppler shift. The received signal averages over these and receives little net signal. A probe with higher lateral resolution is required to obtain accurate Doppler information at higher acoustic frequencies. A focused needle-based transducer can offer finer beamwidth at the same measuring depth. In future studies, a focused 45 MHZ needle Doppler probe focused at f/3 will be fabricated to improve the lateral resolution to $\sim$90 μm (*Lockwood et al.*, 1993), allowing BM response measurements to be made over the full frequency range of human hearing (20 Hz to 20 KHz). This will also allow the BM response to be measured near the local resonance frequency in the basal turn which would allow study of non-linear BM response when used in living patients. A focused probe may also eliminate signal artifacts due to the spot lying on both on and off the basilar membrane and may improve the measurements of BM displacement phase. This technology has the potential to provide the first direct, objective diagnostic information about cochlear mechanics not based on inferences from behavioural or electrophysiological tests or on otoacoustic emissions. The clinical value of such information has a great potential to improve our understanding of the cochlear pathologies that lead to sensorineural hearing loss. For instance, in case of Meniere's disease where extra pressure is applied on the basilar membrane due to the over-pressurization of the endolymph in the scala media, the velocity of vibrating membrane would be different from a normal case which can lead to diagnosis of this disorder at different levels.

CHAPTER 6

SUMMARY AND CONCLUSION

In a clinical setting, the diagnosis of hearing disorders is often inaccurate since it is mostly based on symptoms reported by the patient, otoscopic examination, and audiometric tests. None of these techniques provide direct visualization of middle and inner ear pathologies. Physiological tests such as ABR are also available for measuring signals generated by the auditory system in response to acoustic stimulation. However, it is not possible to assign a particular pattern of the measured parameter to a known disorder disease because of large signal variation within the patients and normal subject populations. These techniques mostly just indicate the presence of an abnormality, and the type of disorder cannot be decided with accuracy. CT and MRI are sometimes used for imaging the auditory system, but they do not offer sufficient spatial resolution for visualizing the small structures within the middle ear and the inner ear. Moreover, the dynamics of auditory system cannot be studied with these techniques because of the low temporal resolution. Thus, the aim of this dissertation was to develop an accurate and minimally-invasive technique for in-vivo exploration of the auditory system. Such a technique could potentially revolutionize diagnostics in otology. The first focus of this dissertation was on developing a high-resolution imaging technique for real-time visualization of the inner ear structures. The second focus was to develop a technique which would be practical for measuring the dynamics of inner ear structures in-vivo. For these purposes, three separate but related studies were conducted in order to explore the potential of high-frequency ultrasound in addressing the objectives of this work.

High-frequency ultrasound has shown promising results in imaging sub-surface micro-structures in several applications such as ophthalmic imaging, intravascular imaging, and small animal imaging. Since this technique can provide high-resolution, real-time images with a minimally invasive procedure, it was hypothesized that the same would be true for imaging the auditory system. The first study of this dissertation was conducted to explore this hypothesis.

Development of high-frequency phased array ultrasound transducers is challenging due to the small element-to-element pitch required in order to avoid the introduction of grating lobe artifacts. In fact no phased array imaging probe operating above 30 MHz has been reported in the literature to date. In the second study, a feasible high-frequency phased array ultrasound transducer for imaging the inner ear was designed, which could be developed using current array fabrication processes.

High-frequency pulsed wave Doppler ultrasound has been widely used for measuring the velocity of blood cells within the small vessels through the skin. Since this technique has high temporal and spatial resolution, it was hypothesized that this technique might be applicable for measuring the dynamics of the auditory system. The third study of this dissertation focused on the application of high-frequency pulsed-wave Doppler ultrasound for measuring basilar membrane vibrations without violating the cochlea.

The objectives and key findings of the three proposed studies are summarized below:

6.1 Review of Objectives

Objective One (Study One)

The first objective (chapter 3) determined that high-frequency ultrasound could provide sufficient resolution for visualizing important middle ear and inner ear structures. An in-house 50 MHz annular array ultrasound system was used to image individual ossicles placed in a water bath, the middle ear cavity through the tympanic membrane, and the cochlear structures through the round window (ex-vivo). The comparison between high-frequency ultrasound images and the corresponding microscopic photos revealed that this modality was excellent for visualizing details of the ossicles on the reconstructed 3D ultrasound images. In the middle ear cross-sectional ultrasound image, malleus attached to the tympanic membrane (umbo) and the stapes footplate which were in plane with the 2D image could be clearly visualized. With respect to the intra-cochlear ultrasound image, the basal turn of basilar membrane could be clearly visualized through the round window without damaging the cochlea. Based on these findings, it was concluded that high-frequency ultrasound could offer higher resolution than CT or MRI for visualizing some of the most important auditory structures. However, since the space for placing the probe (eg. through the ear canal to the round window niche) is very limited, an application specific endoscopic probe would be required for in-vivo implementation. This issue was addressed by objective two of this dissertation.

Objective Two (Study two)

The second objective (chapter 4) was to design an endoscopic ultrasound transducer specifically for in-vivo imaging of the cochlea through the round window. Since a large field of view was desired through the small opening of the round window, a phased array transducer was designed with large-element-to-element pitch so that established micro-fabrication techniques could be used to fabricate the array. The radiation profile of the phased array was simulated using the impulse-response method in order to optimize the design. To reduce grating lobes in this large-pitch phased array, two beamforming techniques were developed and verified theoretically and experimentally. The results showed that the K=8 split aperture or pulse probing technique along with phase coherence imaging was effective in suppressing the grating lobe levels by more than 40 dB without affecting the frame-rate significantly. Moreover, the application of PCI technique improved the lateral resolution and side-lobes suppression, resulting in higher image contrast. A 50 MHz, 1.26λ pitch phased array was proposed as an endoscopic intra-cochlear imaging probe which could be used along with the computationally efficient split-aperture/pulse probing technique in order to suppress grating lobes properly.

Objective Three (Study Three)

The third objective (chapter 5) of this dissertation was to develop a technique applicable to in-vivo measurements of the basilar membrane vibrations across the round window. In the first study it was shown that the basilar membrane could be visualized through the round window. It was therefore hypothesized that high-frequency pulsed-wave Doppler ultrasound might be able to measure membrane dynamics when an acoustic stimulus was applied at the ear canal. To prove this, a 45 MHz unfocused single-element disk transducer with 1 mm diameter was fabricated small enough so that it could be placed on the tip of a needle and into the niche of the round window to measure the vibrations of the basilar membrane and round window. These measurements were performed while stimulating the auditory system with pure tone sounds in the frequency range of 100 Hz-2 KHz. Hardware and software were developed to acquire data and generate the Doppler information. It was shown that the magnitude of membrane velocities normalized to the applied sound pressure had a peak around 1 KHz which was due to the resonance frequency of the middle ear. The phase shift between the membrane displacement and the applied sound in the ear canal had a flat region up to about .5 KHz after which it had a steep downward slope. These findings were in good agreement with the measurements reported in the literature performed using laser Doppler vibrometry. Therefore, it was concluded that high-frequency pulsed wave Doppler had the potential to be used for in-vivo measurement of the basilar membrane vibration without the need to open the cochlea.

6.2 Limitations

Current imaging technologies such as CT or MRI do not offer sufficient spatial and temporal resolution for visualizing and dynamically assessing the auditory structures, in-vivo. In this dissertation, several ex-vivo experiments were performed to show that high-frequency ultrasound can provide enough spatial resolution for imaging the micro-structures within the middle ear/inner ear and enough temporal resolution for measuring the vibrations of intra-cochlear structures such as basilar membrane without violating the cochlea. Therefore, this modality could be developed into an endoscopic form factor and be suitable for in-vivo monitoring of the auditory system. The key limitations of the current studies however should first be addressed before any future development of this technology.

Limitations-Study One

In the described ex-vivo high frequency ultrasound imaging experiments, the packaging size of the annular array probe was large and mechanical scanning was required for 2D imaging. Therefore, some parts of the cadaveric temporal bones had to be removed to have direct access for intra-cochlear imaging. An additional issue with the current imaging system was that the aperture of the annular array was 2 mm in diameter while the round window niche is $\sim$3 mm. Thus, the ultrasound beam became distorted due to the presence of the temporal bone on the edge of the round window after only 1 mm of linear translation. These limitations can be avoided through the fabrication of the endoscopic phased array probe proposed in study two for intra-cochlear imaging. No beam distortion would be present if the fixed aperture is limited to the width of round window.

A drawback of intra-cochlear imaging through the round window is that only the basal turn of intra-cochlear structures (eg. basilar membrane) could be visualized. This problem might be avoided by thinning out the cochlear bone at the desired spot along the cochlea in order to decrease the amount of ultrasound beam attenuation, but this would be a surgical procedure and not useful in the clinic.

Another unknown question is whether the acoustic waves of the ultrasound beam sent to the cochlea during imaging could potentially damage the cochlear structures. This question can only be answered through in-vivo animal studies which are planned for the future.

The other concern about inner ear imaging is that whether the characteristics of ultrasound wave such as velocity and attenuation within intra-cochlear fluids are similar to those of soft tissues. Since perilymph and endolymph are very similar to extracellular and intracellular fluids, these values are expected to be almost the same as those of the soft tissues, however it should be confirmed by measurement.

In middle ear imaging, the major limitation is that the middle ear cavity needs to be filled with water to create an acoustic coupling medium for the imaging probe. This is a relatively common procedure called a transtympanic injection.

Limitations-Study Two

The imaging results in study one were based on an annular array transducer which provides symmetrical beamwidth in the elevation direction at all imaging depths. In study two where a phased array transducer was designed for inner ear imaging, the elevation focusing is provided by a lens at a fixed f-number. This could degrade the resolution of in-vivo images captured with the proposed phased array in comparison with the ex-vivo images presented in this dissertation. However, since the required depth of field for intra-cochlear imaging through round window is limited, high resolution in the elevation axis can be provided by fabricating a lens with a small f-number.

The main limitation of this study was that the proposed grating lobe suppression techniques (split aperture, pulse probing) could not be tested in real-time. The current version of the Vevo 2100 imaging system only provided the final beamformed echo on each steering angle while the SCF calculation requires individual element data. Therefore, at each steering angle, each channel was collected individually by turning off all channels on receive except one. This greatly increased the time of data collection and did not allow anywhere close to real-time acquisition. In future software versions of the Vevo 2100, a new feature is going to be added to the system which allows accessing each channel in parallel prior to the beamforming. In this case, code could potentially be developed on the system to process the data and test the applicability of proposed techniques in real-time.

Another issue with these techniques was associated with the effect of SCF weighting on the speckle pattern of tissue-like phantoms. Since the scatterer size of tissue-like phantoms was smaller than the beamwidth of ultrasound transducer at the focal point, superposition of multiple scatter echoes within the focal region affected the phase information of recorded echoes. The coherency of the echoes was further distorted due to the overlapping grating lobes generated from other speckle. For these reasons, the detected echoes from the speckle regions was found to be much less in phase and therefore the SCF weighting factors suppressed them. The speckle could be brought back by increasing the dynamic range of the image as long as the speckle suppression was less than the grating lobe suppression. A major question is what effect this non-linear compression has on the image quality. Although qualitatively the processed images look very good, it will be necessary to do a more quantitative study in which processed phased array images of tissue phantoms are correlated with images generated with unprocessed linear array images operating in the linear array mode (ie. no grating lobes).

Limitations-Study Three

The main limitation in this study was that the fabricated single-element transducer was unfocused which had a beamwidth approximately equal to the size of its diameter (1 mm). Therefore, the measured echoes from the membranes corresponded to the average of echoes coming from multiple points located within the ultrasound beam rather than a single spatial point. This limited the maximum Doppler frequency measured to 2 KHz since it has been shown that the wavelength of membrane motion becomes comparable with the current ultrasound beamwidth for frequencies above 1.5 KHz. Therefore, it is essential to develop a focused version of the needle mounted transducers in order to decrease the ultrasound beamwidth and increase the Doppler frequency range up to 20 KHz. This would include the resonance frequency (CF) of basilar membrane at the basal turn.

In this study, all measurements were based on ex-vivo experiments where there was sufficient time to place the probe on the niche of round window at the right angle. For in-vivo application, it should be studied if placing the probe with the current design is feasible and time-efficient or whether some modifications are required for designing the probe (eg. with flexible tip) in order to optimize this procedure.

The other concern with an in-vivo measurement is whether the blood microcirculation within the cochlea can affect the Doppler signal of the vibrating membrane. Since the probe is pointing at the membrane with a small deviation from the right angle, the blood vessels which are assumed to be laid on the surface of membranes would have negligible effect on the recorded signal (Doppler angle$\sim 90^\circ$), however this matter has to be studied carefully in in-vivo measurements.

The presented ex-vivo measurements were based on a pure-tone stimulator to trigger only one spot on the basilar membrane. For an in-vivo pure-tone study, the measurements have to be done in an audio booth in order to avoid any effect of inter-modulation distortions due to the nonlinear characteristics of the basilar membrane. Some other artifacts such as breathing or motion might affect the recorded signals in-vivo, however, since the frequencies of these artifacts are low and the applied tone is known, they can be removed with band-pass filtering as described in chapter 5.

Another point is that in this ex-vivo study, the postmortem responses of the membranes were measured. The compressive nonlinearity of the BM disappears within minutes after death which results in the decrease of sensitivity of responses to low-level stimuli, downward shift of the CF, and a loss in sharpness of tuning (*Robles and Ruggero*, 2001). Therefore, only the passive mechanical response of the basilar membrane could be measured in this work. To investigate active amplification effect of outer hair cells, in-vivo measurements are required.

In addition, the temporal bones used in this study were frozen and thawed after dissectioning. It has been shown that the stiffness of basilar membrane in animals degrades after a freeze-thaw cycle in comparison with fresh ones (*Ketten and Mountain*, 2009). In another study, it has been shown that freezing and thawing can change the middle-ear and inner ear mechanics by affecting the mechanical properties of the annular ligament or allowing air into the inner ear (*Ravicz et al.*, 2000). Therefore, the velocity of round window and basilar membrane presented in this dissertation might change when measured on fresh temporal bones.

6.3 Future Directions

In this dissertation, it was shown that high frequency ultrasound offers sufficient spatial and temporal resolutions for studying the status of micro-structures within the auditory system, ex-vivo. Since the ultimate goal is to apply this technique in-vivo, the following future directions are suggested.

Future Direction-Study One

In study one, ex-vivo imaging experiments showed that the basilar membrane could be visualized through the round window with high-frequency ultrasound. However, it was also discovered that for an in-vivo approach it would be essential to develop an endoscopic probe with dimensions less than 3 mm. This led me to the second proposed study focused on designing such a miniaturized endoscopic phased array. The phased array was designed with an unconventionally large inter-element pitch and as a result two novel beamforming techniques were developed in order to suppress the grating lobe artifacts. Although the effectiveness of the proposed techniques were verified experimentally by collecting data using the Vevo 2100, it was not possible to test these techniques in real-time. The next step for this research would be to implement the proposed techniques on updated version of the imaging system and generate images in real-time. I have been informed that the next version of the Vevo 2100 will have a function in which individual element echoes can be accessed prior to the beamforming in parallel.

Future Directions-Study Two

In study two, a 50 MHz 1.26λ pitch phased array was designed as an endoscopic probe specifically for in-vivo intra-cochlear imaging through the round window. The reason for choosing large-pitch array was to simplify the fabrication procedure making the arrays a possibility using current fabrication technology. The next obvious step in the phased array development would be to fabricate the proposed large-pitch phased array transducer in a

miniaturized form factor. This probe can be connected to Vevo 2100 system in order to do the initial testing with the proposed grating lobe suppression techniques.
Upon successful fabrication of the miniaturized phased array endoscope, the feasibility of placing the probe on the niche of round window in intact temporal bones can be studied. Then, the quality of intra-cochlear images such as the lateral resolution, depth of field, directivity, and presence of grating lobes can be investigated through ex-vivo studies. If the results are promising, a 64-channel high-speed beamformer should be designed and implemented specifically for triggering the proposed intra-cochlear imaging array and processing the received echoes based on either the split-aperture or pulse probing technique.

Future Directions-Study Three

In the third study of this dissertation, it was shown that the vibration of basilar membrane could be measured using high-frequency pulsed-wave Doppler ultrasound through the round window however the measured frequency range was limited. The next step for this study would be to fabricate a focused single-element transducer in order to improve the spatial resolution of measuring point by reducing the size of ultrasound beamwidth on the membrane and extend the acoustic frequency range in return. This can be done by placing a lens with proper curvature on the front face of transducer to focus the beam at the desired focal point (f/3). At higher acoustic frequencies, the PRF should be increased (>2f) because of the Nyquist criteria. The fabrication of a focused transducer and optimized Doppler software would allow measuring the vibration of basal turn of basilar membrane up to 20 KHz in order to study the nonlinear compressive behaviour of this membrane about its resonance frequency in-vivo on small animals and eventually on humans. Lastly, the Doppler technology should simply be incorporated into the imaging array when the imaging array is combined with the grating lobe suppression technique and incorporated into a high speed parallel channel data acquisition system.

6.4 Concluding Remarks

Diagnostic technology for hearing disorders is currently lacking in many ways. Available diagnostic tools such as optical otoscopy, audiometry, and physiological tests do not provide enough direct information about the status or dynamics of auditory structures within the middle ear or the inner ear. Considering the large unmet need for accurate diagnostic tools in otology, and the ability of high-frequency ultrasound to capture real-time images from micro-scaled subsurface structures, the motivation behind this thesis was to demonstrate its potential through three separate studies. First, the potential of high-resolution ultrasound was demonstrated through an ex-vivo imaging study of cadaveric tissues. Second, the feasibility of a miniature phased array endoscope with large element pitch was demonstrated. Third, Doppler velocimetry measurements were successfully performed with high-frequency ultrasound for the first time on human temporal bones without compromising the cochlea.

The intention of this thesis was to show that this technology could be developed into a diagnostic tool suitable for use in the clinic. This dissertation was a series of pioneering ’first of a kind’ imaging studies and prototype technology development that has laid the groundwork for development into a full clinical system. Although being able to visualize intra-cochlear structures and their dynamics is very exciting, there is much clinical work to be done in quantifying how this can help identify different pathologies. The future recommendations have quantified the remaining technological hurdles before a useful imaging system is realized. These future developments will be continued by the research group at Dalhousie and will build on top of the very promising pilot research described in this thesis. In summary the novelty of my PhD work is listed as follows:

- Demonstrating the feasibility of high-frequency ultrasound for visualizing fine details of ossciles
- Demonstrating the feasibility of high-frequency ultrasound for middle-ear imaging (visualizing the ossciles across the tympanic membrane)
- Demonstrating the feasibility of high-frequency ultrasound for inner-ear imaging (visualizing the basilar membrane through the round window membrane)
- Designing a large-pitch high-frequency phased array, suitable for in-vivo inner ear imaging
- Developing two effective transmit beamforming techniques for suppressing grating lobes in large-pitch phased arrays
- Demonstrating the feasibility of high-frequency pulsed-wave Doppler ultrasound for measuring the vibration of basilar membrane through the round window, without opening the cochlea

BIBLIOGRAPHY

ER-7C Series B Microphone System Datasheet, `http://www.etymotic.com/pdf/er7c_series_b_datasheet.pdf`.

Agrawal, V., Grating-lobe suppression in phased arrays by subarray rotation, *Proceedings of the IEEE*, *66*, 347–349, 1978.

Aibara, R., J. Welsh, S. Puria, and R. Goode, Human middle-ear sound transfer function and cochlear input impedance, *Hearing Research*, *152*, 100–109, 2001.

Alvord, L., and P. Fine, Real-time b-scan ultrasound in middle ear assessment. a preliminary report., *Journal of Ultrasound in Medicine*, *9*, 91–94, 1990.

Arditi, M., F. Foster, and J. Hunt, Transient fields of concave annular arrays, *Ultrasonic Imaging*, *3*, 37–61, 1981.

Asai, M., A. Huber, and R. Goode, Analysis of the best site on the stapes footplate for ossicular chain reconstruction, *Acta Oto-Laryngologica*, *119*, 356–361, 1999.

Asl, B., and A. Mahloojifar, Eigenspace-based minimum variance beamforming applied to medical ultrasound imaging, *IEEE Transactions on Ultrasonics, Ferroelectrics and Frequency Control*, *57*, 2381–2390, 2010.

Belinchon, A., H. Perez-Garrigues, J. Tenias, and A. Lopez, Hearing assessment in Meniere's disease, *The Laryngoscope*, *121*, 622–626, 2011.

Berson, M., F. Patat, Z. Wang, D. Besse, and L. Pourcelot, Very high frequency pulsed doppler apparatus, *Ultrasound in Medicine & Biology*, *15*, 121–131, 1989.

Bess, F., and L. Humes, *Audiology: the fundamentals*, vol. 67, Recherche, 2003.

Braun, M., Impediment of basilar membrane motion reduces overload protection but not threshold sensitivity: evidence from clinical and experimental hydrops, *Hearing Research*, *97*, 1–10, 1996.

Brown, J., Design, fabrication, and performance of a high-frequency annular-array-based ultrasound imaging system, Ph.D. thesis, Queen's University, Canada, 2005.

Brown, J., and G. Lockwood, A digital beamformer for high-frequency annular arrays, *IEEE Transactions on Ultrasonics, Ferroelectrics and Frequency Control*, *52*, 1262–1269, 2005.

Brown, J., C. Démoré, and G. Lockwood, Design and fabrication of annular arrays for high-frequency ultrasound, *IEEE Transactions on Ultrasonics, Ferroelectrics and Frequency Control*, *51*, 1010–1017, 2004a.

Brown, J., C. Morton-Démoré, F. Foster, and G. Lockwood, Performance of a 50 MHz annular array based imaging system, in *IEEE Ultrasonics Symposium Proceedings*, vol. 1, pp. 760–763, IEEE, 2004b.

Brown, J., F. Foster, A. Needles, E. Cherin, and G. Lockwood, Fabrication and performance of a 40 MHz linear array based on a 1-3 composite with geometric elevation focusing, *IEEE Transactions on Ultrasonics, Ferroelectrics and Frequency Control*, *54*, 1888–1894, 2007.

Brown, J., Z. Torbatian, R. Adamson, R. Van Wijhe, R. Pennings, G. Lockwood, and M. Bance, High-frequency ex vivo ultrasound imaging of the auditory system, *Ultrasound in Medicine & Biology*, *35*, 1899–1907, 2009.

Burkard, R., J. Eggermont, and M. Don, *Auditory evoked potentials: Basic principles and clinical application*, Lippincott Williams & Wilkins, 2007.

Bushberg, J., *The essential physics of medical imaging*, Williams & Wilkins, 2002.

Camacho, J., M. Parrilla, and C. Fritsch, Phase coherence imaging, *IEEE Transactions on Ultrasonics, Ferroelectrics and Frequency Control*, *56*, 958–974, 2009.

Cannata, J., J. Williams, and K. Shung, A kerfless 30 MHz linear ultrasonic array, in *IEEE Ultrasonics Symposium Proceedings*, pp. 109–112, IEEE, 2005.

Cannata, J., J. Williams, Q. Zhou, T. Ritter, and K. Shung, Development of a 35 MHz piezo-composite ultrasound array for medical imaging, *IEEE Transactions on Ultrasonics, Ferroelectrics and Frequency Control*, *53*, 224–236, 2006.

Cannata, J., J. Williams, L. Zhang, C. Hu, and K. Shung, A high-frequency linear ultrasonic array utilizing an interdigitally bonded 2-2 piezo-composite, *IEEE Transactions on Ultrasonics, Ferroelectrics and Frequency Control*, *58*, 2202–2212, 2011.

Chabok, H., J. Cannata, H. Kim, J. Williams, J. Park, and K. Shung, A high-frequency annular-array transducer using an interdigital bonded 1-3 composite, *IEEE Transactions on Ultrasonics, Ferroelectrics and Frequency Control*, *58*, 206–214, 2011.

Chen, F., D. Zha, A. Fridberger, J. Zheng, N. Choudhury, S. Jacques, R. Wang, X. Shi, and A. Nuttall, A differentially amplified motion in the ear for near-threshold sound detection, *Nature Neuroscience*, *14*, 770–774, 2011.

Choudhury, N., F. Chen, J. Zheng, A. Nuttall, and S. Jacques, In vivo imaging and vibration measurement of guinea pig cochlea, in *Proceedings of SPIE*, pp. 68471V–01, SPIE, 2008.

Christopher, D., Detecting, measuring, and imaging the microcirculation with high-frequency doppler ultrasound, Ph.D. thesis, University of Toronto, 1998.

Christopher, D., P. Burns, B. Starkoski, and F. Foster, A high-frequency pulsed-wave doppler ultrasound system for the detection and imaging of blood flow in the microcirculation, *Ultrasound in Medicine & Biology*, *23*, 997–1015, 1997.

Claes, G., M. Wyndaele, C. De Valck, J. Claes, P. Govaerts, F. Wuyts, and P. Van de Heyning, Travelling wave velocity test and Meniere's disease revisited, *European Archives of Oto-Rhino-Laryngology*, *265*, 517–523, 2008.

Cobbold, R., *Foundations of biomedical ultrasound*, Oxford University Press, USA, 2007.

Cook, J., R. Bouchard, and S. Emelianov, Tissue-mimicking phantoms for photoacoustic and ultrasonic imaging, *Biomedical Optics Express*, *2*, 3193–3206, 2011.

Cooper, N., An improved heterodyne laser interferometer for use in studies of cochlear mechanics, *Journal of Neuroscience Methods*, *88*, 93–102, 1999.

Couzos, S., R. Murray, and S. Metcalf, Systematic review of existing evidence and primary care guidelines on the management of otitis media in aboriginal and torres strait islander populations, *National Aboriginal Community Controlled Health Organisation and Australia*, 2001.

Dalebout, S., *The Praeger Guide to Hearing and Hearing Loss: Assessment, Treatment, and Prevention*, Praeger Cloth A Titles, 2008.

Davis, H., Advances in the neurophysiology and neuroanatomy of the cochlea, *The Journal of the Acoustical Society of America*, *34*, 1377–1385, 1962.

de Kleine, E., D. Mateijsen, H. Wit, and F. Albers, Evoked otoacoustic emissions in patients with Meniere's disease, *Otology & Neurotology*, *23*, 510, 2002.

Desilets, C., J. Fraser, and G. Kino, The design of efficient broad-band piezoelectric transducers, *IEEE Transactions on Sonics and Ultrasonics*, *25*, 115–125, 1978.

Discolo, C., M. Byrd, T. Bates, D. Hazony, J. Lewandowski, and P. Koltai, Ultrasonic detection of middle ear effusion: a preliminary study, *Archives of Otolaryngology- Head and Neck Surgery*, *130*, 1407, 2004.

Don, M., B. Kwong, and C. Tanaka, A diagnostic test for Ménière's disease and cochlear hydrops: impaired high-pass noise masking of auditory brainstem responses, *Otology & Neurotology*, *26*, 711, 2005.

Don, M., B. Kwong, and C. Tanaka, An alternative diagnostic test for active Meniere's disease and cochlear hydrops using high-pass noise masked responses: the complex amplitude ratio, *Audiology and Neurotology*, *12*, 359–370, 2007.

Dong, W., and E. Olson, In vivo impedance of the gerbil cochlear partition at auditory frequencies, *Biophysical Journal*, *97*, 1233–1243, 2009.

Ear Anatomy, `http://www.edoctoronline.com/medical-atlas.asp?c=4&id=21693`.

Ergun, A., G. Yaralioglu, and B. Khuri-Yakub, Capacitive micromachined ultrasonic transducers: Theory and technology, *Journal of Aerospace Engineering*, *16*, 76, 2003.

Ergun, A., et al., Broadband capacitive micromachined ultrasonic transducers ranging from 10 khz to 60 MHz for imaging arrays and more, in *IEEE Ultrasonics Symposium Proceedings*, vol. 2, pp. 1039–1043, IEEE, 2002.

Evans, D., *Doppler ultrasound: physics, instrumentation, and clinical applications*, A Wiley Medical Publication, Wiley, 1989.

Feeney, M., I. Grant, and D. Mills, Wideband energy reflectance measurements of ossicular chain discontinuity and repair in human temporal bone, *Ear and Hearing*, *30*, 391, 2009.

Ferrara, K., B. Zager, J. Sokil-Melgar, R. Silverman, and I. Aslanidis, Estimation of blood velocity with high frequency ultrasound, *IEEE Transactions on Ultrasonics, Ferroelectrics and Frequency Control*, *43*, 149–157, 1996.

Foster, F., C. Pavlin, K. Harasiewicz, D. Christopher, and D. Turnbull, Advances in ultrasound biomicroscopy, *Ultrasound in Medicine & Biology*, *26*, 1–27, 2000.

Foster, F., J. Mehi, M. Lukacs, D. Hirson, C. White, C. Chaggares, and A. Needles, A new 15-50 MHz array-based micro-ultrasound scanner for preclinical imaging, *Ultrasound in Medicine & Biology*, *35*, 1700–1708, 2009.

Gao, S., A. Xia, T. Yuan, P. Raphael, R. Shelton, B. Applegate, and J. Oghalai, Quantitative imaging of cochlear soft tissues in wild-type and hearing-impaired transgenic mice by spectral domain optical coherence tomography, *Optics Express*, *19*, 15415–15428, 2011.

Gavrilov, L., and J. Hand, A theoretical assessment of the relative performance of spherical phased arrays for ultrasound surgery, *IEEE Transactions on Ultrasonics, Ferroelectrics and Frequency Control*, *47*, 125–139, 2000.

Gavrilov, L., J. Hand, P. Abel, and C. Cain, A method of reducing grating lobes associated with an ultrasound linear phased array intended for transrectal thermotherapy, *IEEE Transactions on Ultrasonics, Ferroelectrics and Frequency Control*, *44*, 1010–1017, 1997.

Ghiz, A., A. Salt, J. DeMott, M. Henson, O. Henson, and S. Gewalt, Quantitative anatomy of the round window and cochlear aqueduct in guinea pigs, *Hearing Research*, *162*, 105–112, 2001.

Goode, R., M. Killion, K. Nakamura, and S. Nishihara, New knowledge about the function of the human middle ear: development of an improved analog model, *American Journal of Otology*, *15*, 145–145, 1994.

Goss, S., L. Frizzell, J. Kouzmanoff, J. Barich, and J. Yang, Sparse random ultrasound phased array for focal surgery, *IEEE Transactions on Ultrasonics, Ferroelectrics and Frequency Control*, *43*, 1111–1121, 1996.

Goycoolea, M., Clinical aspects of round window membrane permeability under normal and pathological conditions, *Acta Oto-Laryngologica*, *121*, 437–447, 2001.

Gundersen, T., ø. Skarstein, and T. Sikkeland, A study of the vibration of the basilar membrane in human temporal bone preparations by the use of the mossbauer effect, *Acta Oto-Laryngologica*, *86*, 225–232, 1978.

Harneja, N., and R. Chaturvedi, A study of the human ear ossicles, *Indian Journal of Otolaryngology and Head & Neck Surgery*, *25*, 154–160, 1973.

Harris, J., *Meniere's disease*, Kugler Publications, 1999.

Harris, J., and A. Salt, Meniere's disease, in *The Senses: A Comprehensive Reference. Vol. 3 : Audition*, pp. 157–163, Oxford, Great Britain: Elsevier, 2008.

Hato, N., S. Stenfelt, and R. Goode, Three-dimensional stapes footplate motion in human temporal bones, *Audiology and Neurotology*, *8*, 140–152, 2003.

Hoen, P., Systematic analysis of the grating lobe of ultrasonographic array directivity, in *SPIE Medical Imaging and Image Interpretation*, pp. 94–713, SPIE, 1982.

Homma, K., Y. Du, Y. Shimizu, and S. Puria, Ossicular resonance modes of the human middle ear for bone and air conduction, *The Journal of the Acoustical Society of America*, *125*, 968, 2009.

Hong, S., and D. Freeman, Doppler optical coherence microscopy for studies of cochlear mechanics, *Journal of Biomedical Optics*, *11*, 054014, 2006.

Horii, A., Y. Osaki, T. Kitahara, T. Imai, A. Uno, S. Nishiike, N. Fujita, and H. Inohara, Endolymphatic hydrops in Meniere's disease detected by MRI after intratympanic administration of gadolinium: Comparison with sudden deafness, *Acta Oto-Laryngologica*, *131*, 602–609, 2011.

Hu, C., K. Snook, P. Cao, and K. Kirk Shung, High-frequency ultrasound annular array imaging. part ii: Digital beamformer design and imaging, *IEEE Transactions on Ultrasonics, Ferroelectrics and Frequency Control*, *53*, 309–316, 2006a.

Hu, C., X. Xu, J. Cannata, J. Yen, and K. Shung, Development of a real-time, high-frequency ultrasound digital beamformer for high-frequency linear array transducers, *IEEE Transactions on Ultrasonics, Ferroelectrics and Frequency Control*, *53*, 317–323, 2006b.

Hu, C., L. Zhang, J. Cannata, J. Yen, K. Shung, et al., Development of a 64 channel ultrasonic high frequency linear array imaging system., *Ultrasonics*, *51*, 953, 2011.

Hutchinson, E., M. Buchanan, and K. Hynynen, Design and optimization of an aperiodic ultrasound phased array for intracavitary prostate thermal therapies, *Medical Physics*, *23*, 767, 1996.

Iseli, C., and W. Gibson, A comparison of three methods of using transtympanic electrocochleography for the diagnosis of Meniere's disease: Click summating potential measurements, tone burst summating potential amplitude measurements, and biasing of the summating potential using a low frequency tone, *Acta Oto-Laryngologica*, *130*, 95–101, 2010.

Jahn, A., and J. Santos-Sacchi, *Physiology of the Ear*, Singular Pub Group, 2001.

Jensen, J., S. Nikolov, K. Gammelmark, and M. Pedersen, Synthetic aperture ultrasound imaging, *Ultrasonics*, *44*, e5–e15, 2006.

Johnstone, B., and A. Boyle, Basilar membrane vibration examined with the Mössbauer technique, *Science*, *158*, 389, 1967.

Ketten, D., and D. Mountain, Beaked and baleen whale hearing: modeling responses to underwater noise, *Monterey, California: Naval Postgraduate School*, 2009.

Ketterling, J., O. Aristizábal, D. Turnbull, and F. Lizzi, Design and fabrication of a 40 MHz annular array transducer, *IEEE Transactions on Ultrasonics, Ferroelectrics and Frequency Control*, *52*, 672–681, 2005.

Khanna, S., Cellular vibration measurement with a noninvasive optical system, in *Proceedings of SPIE*, vol. 1429, p. 9, 1991.

Khanna, S., and D. Leonard, Laser interferometric measurements of basilar membrane vibrations in cats using a round window approach, *The Journal of the Acoustical Society of America*, *69*, S51, 1981.

Khanna, S., J. Willemin, and M. Ulfendahl, Measurement of optical reflectivity in cells of the inner ear, *Acta Oto-Laryngologica. Supplementum*, pp. 69–75, 1989.

Khanna, S., M. Ulfendahl, and C. Steele, Vibration of reflective beads placed on the basilar membrane, *Hearing Research*, *116*, 71–85, 1998.

Kim, H., J. Cannata, J. Williams, J. Chang, and K. Shung, Fabrication of 20 MHz convex array transducers for high frequency ophthalmic imaging, in *IEEE Ultrasonics Symposium Proceedings*, pp. 1130–1133, IEEE, 2009.

Kim, Y., M. Aoyagi, and Y. Koike, Measurement of cochlear basilar membrane traveling wave velocity by derived ABR, *Acta Oto-Laryngologica*, *114*, 71–76, 1994.

Kinsler, L., A. Frey, A. Coppens, and J. Sanders, *Fundamentals of acoustics*, Wiley-VCH, 1999.

Kliauga, P., and S. Khanna, Dose rate to the inner ear during mossbauer experiments, *Physics in Medicine and Biology*, *28*, 359, 1983.

Koizuka, I., Micro-magnetic resonance imaging of the inner ear., *Journal Code: Y0852B*, *12*, 80–85, 2002.

Kössl, M., and I. Russell, Basilar membrane resonance in the cochlea of the mustached bat, *Proceedings of the National Academy of Sciences*, *92*, 276, 1995.

Lagarde, M., M. Drexl, V. Lukashkina, A. Lukashkin, and I. Russell, Outer hair cell somatic, not hair bundle, motility is the basis of the cochlear amplifier, *Nature Neuroscience*, *11*, 746–748, 2008.

Li, P., and M. Li, Adaptive imaging using the generalized coherence factor, *IEEE Transactions on Ultrasonics, Ferroelectrics and Frequency Control*, *50*, 128–141, 2003.

Lin, J., H. Staecker, and M. Samir Jafri, Optical coherence tomography imaging of the inner ear: a feasibility study with implications for cochlear implantation, *The Annals of Otology, Rhinology & Laryngology*, *117*, 341–346, 2008.

Liu, C., D. Wu, Q. Zhou, F. Djuth, and K. Shung, High-frequency (50-100 MHz) medical ultrasound transducer arrays produced by micromachining bulk PZT materials, in *IEEE Ultrasonics Symposium Proceedings*, pp. 690–693, IEEE, 2008.

Liu, C., Q. Zhou, F. Djuth, and K. Shung, High-frequency ($>$ 50 MHz) medical ultrasound linear arrays fabricated from micromachined bulk PZT materials, *IEEE Transactions on Ultrasonics, Ferroelectrics and Frequency Control*, *59*, 315–318, 2012.

Liu, R., K. Harasiewicz, and F. Foster, Interdigital pair bonding for high frequency (20-50 MHz) ultrasonic composite transducers, *IEEE Transactions on Ultrasonics, Ferroelectrics and Frequency Control*, *48*, 299–306, 2001.

Lockwood, G., L. Ryan, and F. Foster, A 45 to 55 MHz needle-based ultrasound system for invasive imaging, *Ultrasonic Imaging*, *15*, 1–13, 1993.

Lockwood, G., D. Turnbull, D. Christopher, and F. Foster, Beyond 30 MHz applications of high-frequency ultrasound imaging, *Engineering in Medicine and Biology Magazine, IEEE*, *15*, 60–71, 1996.

Lockwood, G., J. Talman, and S. Brunke, Real-time 3-D ultrasound imaging using sparse synthetic aperture beamforming, *IEEE Transactions on Ultrasonics, Ferroelectrics and Frequency Control*, *45*, 980–988, 1998.

Lukacs, M., M. Sayer, G. Lockwood, and S. Foster, Laser micromachined high frequency ultrasonic arrays, in *IEEE Ultrasonics Symposium Proceedings*, vol. 2, pp. 1209–1212, IEEE, 1999.

Lukacs, M., J. Yin, G. Pang, R. Garcia, E. Cherin, R. Williams, F. Foster, and J. Mehi, Performance and characterization of high frequency linear arrays, in *IEEE Ultrasonics Symposium Proceedings*, vol. 1, pp. 105–108, IEEE, 2005.

Lukacs, M., J. Yin, G. Pang, R. Garcia, E. Cherin, R. Williams, J. Mehi, and F. Foster, Performance and characterization of new micromachined high-frequency linear arrays, *IEEE Transactions on Ultrasonics, Ferroelectrics and Frequency Control*, *53*, 1719–1729, 2006.

Lukashkin, A., M. Bashtanov, and I. Russell, A self-mixing laser-diode interferometer for measuring basilar membrane vibrations without opening the cochlea, *Journal of Neuroscience Methods*, *148*, 122–129, 2005.

Mancini, F., M. Catalani, M. Carru, and B. Monti, History of Meniere's disease and its clinical presentation, *Otolaryngologic Clinics of North America*, *35*, 2002.

Manes, G., P. Tortoli, F. Andreuccetti, G. Avitabile, and C. Atzeni, Synchronous dynamic focusing for ultrasound imaging, *IEEE Transactions on Ultrasonics, Ferroelectrics and Frequency Control*, *35*, 14–21, 1988.

Martin, F., and J. Clark, *Introduction to audiology*, Allyn and Bacon Boston, 1997.

Møller, A., *Hearing: Anatomy, physiology and disorders of the auditory system*, Academic Press, 2006.

Morton, C., and G. Lockwood, Evaluation of kerfless linear arrays, in *IEEE Ultrasonics Symposium Proceedings*, vol. 2, pp. 1257–1260, IEEE, 2002.

Mucci, R., A comparison of efficient beamforming algorithms, *IEEE Transactions on Acoustics, Speech and Signal Processing*, *32*, 548–558, 1984.

Muzzi, E., A. Rinaldo, and A. Ferlito, Méniere disease: diagnostic instrumental support, *American Journal of Otolaryngology*, *29*, 188–194, 2008.

Nageris, B., J. Adams, and S. Merchant, A human temporal bone study of changes in the basilar membrane of the apical turn in endolymphatic hydrops, *Otology & Neurotology*, *17*, 245, 1996.

Nakajima, H., W. Dong, E. Olson, S. Merchant, M. Ravicz, and J. Rosowski, Differential intracochlear sound pressure measurements in normal human temporal bones, *Journal of the Association for Research in Otolaryngology*, *10*, 23–36, 2009.

Nilsen, K., and I. Russell, The spatial and temporal representation of a tone on the guinea pig basilar membrane, *Proceedings of the National Academy of Sciences*, *97*, 11751, 2000.

Nuttall, A., D. Dolan, and G. Avinash, Laser doppler velocimetry of basilar membrane vibration, *Hearing Research*, *51*, 203–213, 1991.

Oralkan, O., A. Ergun, J. Johnson, M. Karaman, U. Demirci, K. Kaviani, T. Lee, and B. Khuri-Yakub, Capacitive micromachined ultrasonic transducers: Next-generation arrays for acoustic imaging, *IEEE Transactions on Ultrasonics, Ferroelectrics and Frequency Control*, *49*, 1596–1610, 2002.

Overstreet, E., A. Temchin, and M. Ruggero, Basilar membrane vibrations near the round window of the gerbil cochlea, *Journal of the Association for Research in Otolaryngology*, *3*, 351–361, 2002.

Park, S., and T. Shrout, Ultrahigh strain and piezoelectric behavior in relaxor based ferroelectric single crystals, *Journal of Applied Physics*, *82*, 1804, 1997.

Pitris, C., K. Saunders, J. Fujimoto, and M. Brezinski, High-resolution imaging of the middle ear with optical coherence tomography: a feasibility study, *Archives of Otolaryngology- Head and Neck Surgery*, *127*, 637, 2001.

Postnov, A., A. Zarowski, N. De Clerck, F. Vanpoucke, F. Offeciers, D. Van Dyck, and S. Peeters, High resolution micro-CT scanning as an innovatory tool for evaluation of the surgical positioning of cochlear implant electrodes, *Acta Oto-Laryngologica*, *126*, 467–474, 2006.

Ravicz, M., S. Merchant, and J. Rosowski, Effect of freezing and thawing on stapes-cochlear input impedance in human temporal bones, *Hearing Research*, *150*, 215–224, 2000.

Ren, T., Longitudinal pattern of basilar membrane vibration in the sensitive cochlea, *Proceedings of the National Academy of Sciences*, *99*, 17101, 2002.

Ren, T., Y. Zou, J. Zheng, A. Nutall, E. Porsov, and S. Matthews, Measurements of basilar membrane vibration using a scanning laser interferometer, *Biophysics of the Cochlea*, pp. 211–219, 2003.

Rew, C., S. Park, and J. Ra, Elimination of all grating lobes in ultrasonic synthetic focusing using a linear array, *Electronics Letters*, *29*, 1729, 1993.

Rhode, W., Observations of the vibration of the basilar membrane in squirrel monkeys using the Mössbauer technique, *The Journal of the Acoustical Society of America*, *49*, 1218, 1971.

Ritter, T., T. Shrout, R. Tutwiler, and K. Shung, A 30 MHz piezo-composite ultrasound array for medical imaging applications, *IEEE Transactions on Ultrasonics, Ferroelectrics and Frequency Control*, *49*, 217–230, 2002.

Robles, L., and M. Ruggero, Mechanics of the mammalian cochlea, *Physiological Reviews*, *81*, 1305–1352, 2001.

Roeser, R., M. Valente, and H. Hosford-Dunn, *Audiology: diagnosis*, Thieme Medical Pub, 2007.

Rosowski, J., R. Mehta, and S. Merchant, Diagnostic utility of laser-doppler vibrometry in conductive hearing loss with normal tympanic membrane, *Otology & Neurotology*, *24*, 165, 2003.

Rosowski, J., H. Nakajima, and S. Merchant, Clinical utility of laser-doppler vibrometer measurements in live normal and pathologic human ears, *Ear and Hearing*, *29*, 3, 2008.

Rothbaum, D., et al., High-resolution ultrasonography of the cochlea, *Johns Hopkins University*.

Ruggero, M., N. Rich, A. Recio, S. Narayan, and L. Robles, Basilar-membrane responses to tones at the base of the chinchilla cochlea, *The Journal of the Acoustical Society of America*, *101*, 2151, 1997.

Ryan, L., and F. Foster, Tissue equivalent vessel phantoms for intravascular ultrasound, *Ultrasound in Medicine & Biology*, *23*, 261–273, 1997.

Salt, A., and S. Plontke, Endolymphatic hydrops: pathophysiology and experimental models, *Otolaryngologic Clinics of North America*, *43*, 971–983, 2010.

San Emeterio, J., and L. Ullate, Diffraction impulse response of rectangular transducers, *The Journal of the Acoustical Society of America*, *92*, 651, 1992.

Sando, I., Y. Orita, and B. Hirsch, Pathology and pathophysiology of Meniere's disease., *Otolaryngologic Clinics of North America*, *35*, 517, 2002.

Satomura, S., Ultrasonic doppler method for the inspection of cardiac functions, *Classic Papers In Modern Diagnostic Radiology*, p. 224, 2005.

Sennaroglu, L., I. Saatci, A. Aralasmak, B. Gursel, and E. Turan, Magnetic resonance imaging versus computed tomography in pre-operative evaluation of cochlear implant candidates with congenital hearing loss, *The Journal of Laryngology & Otology*, *116*, 804–810, 2002.

Sepehr, A., H. Djalilian, J. Chang, Z. Chen, and B. Wong, Optical coherence tomography of the cochlea in the porcine model, *The Laryngoscope*, *118*, 1449–1451, 2008.

Shield, B., Evaluation of the social and economic costs of hearing impairment, *A Report for Hear-it*, 2006.

Shung, K., J. Cannata, and Q. Zhou, Piezoelectric materials for high frequency medical imaging applications: A review, *Journal of Electroceramics*, *19*, 141–147, 2007.

Silver, R., H. Djalilian, S. Levine, and F. Rimell, High-resolution magnetic resonance imaging of human cochlea, *The Laryngoscope*, *112*, 1737–1741, 2002.

Sisman, A., J. Zahorian, G. Gurun, M. Karaman, M. Balantekin, F. Degertekin, and P. Hasler, Evaluation of CMUT annular arrays for side-looking IVUS, in *IEEE Ultrasonics Symposium Proceedings*, pp. 2774–2777, IEEE, 2009.

Snook, K., T. Shrout, and K. Shung, Development of high frequency annular arrays for medical imaging, in *IEEE Ultrasonics Symposium*, vol. 1, pp. 865–868, IEEE, 2003.

Stakhovskaya, O., D. Sridhar, B. Bonham, and P. Leake, Frequency map for the human cochlear spiral ganglion: implications for cochlear implants, *Journal of the Association for Research in Otolaryngology*, *8*, 220–233, 2007.

Statistics Canada PLAS, Facts on Hearing Limitations, `http://www.statcan.gc.ca/pub/89-628-x/2009012/fs-fi/fs-fi-eng.htm`, 2006.

Stenfelt, S., S. Puria, N. Hato, and R. Goode, Basilar membrane and osseous spiral lamina motion in human cadavers with air and bone conduction stimuli, *Hearing Research*, *181*, 131–143, 2003.

Stenfelt, S., N. Hato, and R. Goode, Round window membrane motion with air conduction and bone conduction stimulation, *Hearing Research*, *198*, 10–24, 2004.

Stepanishen, P., Transient radiation from pistons in an infinite planar baffle, *The Journal of the Acoustical Society of America*, *49*, 1629, 1971.

Stieger, C., C. Candreia, M. Kompis, G. Herrmann, F. Pfiffner, D. Widmer, and A. Arnold, Laser doppler vibrometric assessment of middle ear motion in thiel-embalmed heads, *Otology & Neurotology*, *33*, 311–318, 2012.

Subhash, H., N. Choudhury, S. Jacques, R. Wang, F. Chen, D. Zha, and A. Nuttall, Absolute measurement of subnanometer scale vibration of cochlear partition of an excised guinea pig cochlea using spectral-domain phase-sensitive optical coherence tomography, in *Proceedings of SPIE*, vol. 8213, p. 82131V, 2012.

Synnevag, J., A. Austeng, and S. Holm, Adaptive beamforming applied to medical ultrasound imaging, *IEEE Transactions on Ultrasonics, Ferroelectrics and Frequency Control*, *54*, 1606–1613, 2007.

Takahashi, H., and I. Sando, Computer-aided 3-D temporal bone anatomy for cochlear implant surgery, *The Laryngoscope*, *100*, 417–421, 1990.

Talman, J., and G. Lockwood, Evaluation of the radiation pattern of a split aperture linear phased array for high frequency imaging, *IEEE Transactions on Ultrasonics, Ferroelectrics and Frequency Control*, *47*, 117–124, 2000.

The Hearing Foundation of Canada, `http://www.thfc.ca/cms/en/KeyStatistics/KeyStatistics.aspx?menuid=87`, 2010.

Thomenius, K., Evolution of ultrasound beamformers, in *IEEE Ultrasonics Symposium Proceedings*, vol. 2, pp. 1615–1622, IEEE, 1996.

Tonndorf, J., Modern methods for measurement of basilar membrane displacements., *Acta Oto-Laryngologica*, *83*, 113, 1977.

Torbatian, Z., R. Adamson, R. van Wijhe, R. Pennings, M. Bance, and J. Brown, Imaging the auditory system: A new application of high-frequency ultrasound, in *IEEE Ultrasonics Symposium Proceedings (Copyright ©2009, IEEE)*, pp. 236–239, IEEE, 2009.

Torbatian, Z., R. Adamson, M. Bance, and J. Brown, A split-aperture transmit beamforming technique with phase coherence grating lobe suppression, *IEEE Transactions on Ultrasonics, Ferroelectrics and Frequency Control (Copyright ©2010, IEEE)*, *57*, 2588–2595, 2010.

Torbatian, Z., R. Adamson, M. Bance, and J. Brown, Transmit beamforming techniques for suppressing grating lobes in large pitch ultrasonic phased arrays, in *Proceedings of SPIE*, vol. 7968, p. 79680R, 2011a.

Torbatian, Z., R. Adamson, and M. Brown, Experimental verification of a split-aperture transmit beamforming technique for suppressing grating lobes in large pitch phased arrays, in *IEEE Ultrasonics Symposium Proceedings (Copyright ©2011, IEEE)*, pp. 1139– 1142, 2011b.

Torbatian, Z., R. Adamson, and J. Brown, A virtual point source pulse probing technique for suppressing grating lobes in large pitch phased arrays, in *IEEE Ultrasonics Symposium Proceedings (Copyright ©2012, IEEE)*, IEEE, 2012a.

Torbatian, Z., R. Adamson, J. Savage, and B. J. Bance, M.L., Listening to the cochlea with high-frequency ultrasound, *Ultrasound in Medicine & Biology*, 2012b.

Turnbull, D., and F. Foster, Beam steering with pulsed two-dimensional transducer arrays, *IEEE Transactions on Ultrasonics, Ferroelectrics and Frequency Control*, *38*, 320–333, 1991.

Ustuner, K., and A. Gee, Adaptive grating lobe suppression in ultrasound imaging, 2007, US Patent 7,207,942.

Vassiliou, A., P. Vlastarakos, P. Maragoudakis, D. Candiloros, and T. Nikolopoulos, Menieres disease: Still a mystery disease with difficult differential diagnosis, *Annals of Indian Academy of Neurology*, *14*, 12, 2011.

Von Békésy, G., *Experiments in hearing.*, McGraw Hill, 1960.

Voss, S., J. Rosowski, S. Merchant, and W. Peake, Acoustic responses of the human middle ear, *Hearing Research*, *150*, 43–69, 2000.

Wang, H., D. Fang, and Y. Chow, Grating lobe reduction in a phased array of limited scanning, *IEEE Transactions on Antennas and Propagation*, *56*, 1581–1586, 2008.

Wang, R., and A. Nuttall, Phase-sensitive optical coherence tomography imaging of the tissue motion within the organ of Corti at a subnanometer scale: a preliminary study, *Journal of Biomedical Optics*, *15*, 056005, 2010.

Wild, J., The use of ultrasonic pulses for the measurement of biologic tissues and the detection of tissue density changes, *Surgery*, *27*, 183, 1950.

Wong, B., Y. Zhao, M. Yamaguchi, N. Nassif, Z. Chen, and J. De Boer, Imaging the internal structure of the rat cochlea using optical coherence tomography at 0.827 μm and 1.3 μm, *Otolaryngology-Head and Neck Surgery*, *130*, 334–338, 2004.

Wu, C., C. Hsu, and F. Hsieh, Preliminary use of endoluminal ultrasonography in assessment of middle ear with effusion., *Journal of Ultrasound in Medicine*, *17*, 427–430, 1998.

Wu, D., Q. Zhou, X. Geng, C. Liu, F. Djuth, and K. Shung, Very high frequency (beyond 100 MHz) PZT kerfless linear arrays, *IEEE Transactions on Ultrasonics, Ferroelectrics and Frequency Control*, *56*, 2304–2310, 2009.

Wysocki, J., Dimensions of the human vestibular and tympanic scalae, *Hearing Research*, *135*, 39–46, 1999.

Xenellis, J., F. Linthicum Jr, P. Webster, and R. Lopez, Basilar membrane displacement related to endolymphatic sac volume, *The Laryngoscope*, *114*, 1953–1959, 2004.

Xu, X., L. Sun, J. Cannata, J. Yen, and K. Shung, High-frequency ultrasound doppler system for biomedical applications with a 30 MHz linear array, *Ultrasound in Medicine & Biology*, *34*, 638–646, 2008.

Yeh, D., O. Oralkan, A. Ergun, X. Zhuang, I. Wygant, and B. Khuri-Yakub, High-frequency CMUT arrays for high-resolution medical imaging, *Proceeding SPIE Medical Imaging*, *5750*, 87–98, 2005.

Yin, J., M. Lukacs, K. Harasiewicz, and S. Foster, Ultra-fine piezoelectric composites for high frequency ultrasonic transducers, in *IEEE Ultrasonics Symposium Proceedings*, vol. 3, pp. 1962–1965, IEEE, 2004.

Zemp, R., L. Song, R. Bitton, K. Shung, and L. Wang, Real-time photoacoustic microscopy in vivo with a 30 MHz ultrasound array transducer, *Optics Express*, *16*, 7915–7928, 2008.

Zhou, Q., X. Xu, E. Gottlieb, L. Sun, J. Cannata, H. Ameri, M. Humayun, P. Han, and S. Shung, PMN-PT single crystal, high-frequency ultrasonic needle transducers for pulsed-wave doppler application, *IEEE Transactions on Ultrasonics, Ferroelectrics and Frequency Control*, *54*, 668–675, 2007.

Zhou, Q., D. Wu, C. Liu, B. Zhu, F. Djuth, and K. Shung, Micro-machined high-frequency (80 MHz) PZT thick film linear arrays, *IEEE Transactions on Ultrasonics, Ferroelectrics and Frequency Control*, *57*, 2213–2220, 2010.

Ziomek, L. J., *Fundamentals of acoustic field theory and space-time signal processing*, CRC, 1995.

APPENDIX A

DETAILS RELATED TO STUDY TWO

A.1 Derivation of Optimal Aperture in Split Aperture Technique

As mentioned in section 4.2.2.2, it is essential to find the optimum point for splitting the array aperture on transmit in order to obtain grating lobe echoes with equal length in each transmit event. In order to account for the effect of an array of elements with transmit beamforming delays inserted to focus to F, a virtual curved aperture is considered for the rest of the derivation as shown in figure 4.7. $L1, L2,$ and $L3$ are the distances between the grating lobe point (G) and the points on the virtual curved aperture. In order to have transmit pulses with the same length in the time domain for both splits, the equality of distances defined in the following equation should be satisfied.

$$\begin{aligned} L2 - L3 &= L1 - L2 \\ L2 &= \frac{L1 + L3}{2} \end{aligned} \tag{A.1}$$

where the distances between grating lobe and the virtual aperture points are:

$$\begin{aligned} L1 &= \sqrt{(R\sin\theta - \frac{D}{2})^2 + (R\cos\theta)^2} \\ L3 &= \sqrt{(R\sin\theta - (-\frac{D}{2}))^2 + (R\cos\theta)^2} \\ L2 &= \sqrt{(R\sin\theta - x_0)^2 + (R\cos\theta - z_0)^2} \end{aligned} \tag{A.2}$$

where D is the total array aperture and (x_0, z_0) is point on the virtual curved aperture. It can be shown that for $L2$, z_0 can be replaced as a function of x_0, reducing $L2$ to:

$$L2(x_0) = \sqrt{(R\sin\theta - x_0)^2 + (R\cos\theta - (R - \sqrt{R^2 + (\frac{D}{2})^2 - x_0^2}))^2} \tag{A.3}$$

and $L1$ and $L3$ are simply $L2(\frac{D}{2})$ and $L2(-\frac{D}{2})$, respectively. The following derivation is based on the assumption that $R >> \frac{D}{2}$ which is a reasonable assumption at f-numbers greater than 2. By squaring the right side of equation (A.1), we obtain:

$$\frac{(\sqrt{(R\sin\theta - \frac{D}{2})^2 + (R\cos\theta)^2} + \sqrt{(R\sin\theta - (-\frac{D}{2}))^2 + (R\cos\theta)^2})^2}{4} \tag{A.4}$$
$$\sim R^2 + \frac{R^2\cos^2\theta\frac{D^2}{4}}{(R^2 - \frac{D^2}{4})}$$

The approximation is based on the first-order Taylor approximation of a square:

$$\sqrt{x^2 + a} = x + \frac{a}{2x} \tag{A.5}$$

By squaring the left side of equation (A.1), and again using the Taylor approximation in equation (A.5), we obtain the expression:

$$(R\sin\theta - x_0)^2 + (R\cos\theta - (R - \sqrt{R^2 + (\frac{D}{2})^2 - x_0^2}))^2 \tag{A.6}$$
$$\sim (1 - \cos\theta)x_0^2 - (2R\sin\theta)x_0 + (\cos\theta\frac{D^2}{4} + R^2)$$

The equality of equation (A.4) and equation (A.6) therefore results in

$$(1 - \cos\theta)x_0^2 - (2R\sin\theta)x_0 + (\cos\theta\frac{D^2}{4} - \frac{R^2\cos^2(\theta)\frac{D^2}{4}}{(R^2 - \frac{D^2}{4})}) = 0 \tag{A.7}$$

By solving the root of (A.7) and substituting $R = FD$ and $D = Np$, we obtain an expression for x_0 or rather the element at which to split the aperture in order to obtain equal-length time-domain signals:

$$x_0 = (\frac{F\sin\theta - \sqrt{F^2\sin^2\theta - (1 - \cos\theta)(\frac{\cos\theta}{4} - \frac{F^2\cos^2\theta}{4F^2 - 1})}}{1 - \cos\theta})(Np) \tag{A.8}$$

A.2 In-house Tissue Phantom and its Characteristics

To develop the tissue phantom, 6% gelatine (from porcine skin, G2500-1KG, Sigma) was mixed with cold deionized water first using a magnetic stirrer. The mixture was microwaved to get to $80°C$ temperature and was placed on a hotplate with magnetic stirrer for about 5 minutes to get the gas bubble on top of the liquid. The gas bubbles were removed from the surface with a spoon and 4% (by weight) silicon dioxide (S5631-500G, Sigma) already diluted in a small amount of water was added to the gelatin mixture. The hotplate was turned off while the stirrer was still on and the mixture was let to cool down to about $80°C$. Then it was poured in a container which had a wire target placed at the bottom of it. Lastly, it was placed in the fridge to harden (*Ryan and Foster*, 1997).

The techniques described in *Cook et al.* (2011) were used to measure the speed of sound, attenuation, and scattering coefficients of this home-made phantom. For this purpose, an in-house 45 MHz single-element transducer with 2.5 mm diameter and $f/2.7$ was used. The transducer was triggered by a high frequency ultrasound pulser/receiver unit (Daxsonics 10ERS3., Halifax, Canada) and the received echo was monitored and saved with an oscilloscope (Agilent MSO-X-3052A, Agilent Technologies Inc., CA, USA).

To measure the speed of sound in the phantom, a piece of aluminium was placed at depth of 12.75 mm (z) from the front face of the transducer in a water bath. A section of phantom with 4 mm thickness (d_{ph}) was then inserted between the transducer and the aluminium with 5 mm distance (z_2) from the metal. The arrival time of aluminium echo (τ) was measured on the scope. By knowing the speed of sound in water to be 1500 m/s (c_w) and distances, the sound velocity in phantom (c_{ph}) was calculated to be 1472 m/s using following equation:

$$\frac{(z-d_{ph})}{c_w}+\frac{d_{ph}}{c_{ph}}=\frac{\tau}{2} \tag{A.9}$$

The ultrasound attenuation coefficient of the phantom (α_s) was estimated using Fourier analysis of the aluminium echoes located at distance z collected once with no phantom in between of the metal and the transducer ($V_r(f,z)$) and the other time with phantom in between ($V_s(f,z)$) (*Cook et al.*, 2011). Each echo was measured ten times in different spots to average. By knowing the attenuation coefficient in water (α_w) to be 0.0022 dB/MHz cm and the thickness of the phantom d_{ph} in cm, α_s was calculated in dB/cm to be 0.32 MHz^{-1}cm^{-1} using (A.10).

$$\alpha_s=\frac{10}{d_{ph}}\log\left(\frac{V_s(f,z)}{V_r(f,z)}10^{\frac{-d_{ph}\alpha_w f}{10}}\right) \tag{A.10}$$

where f is the frequency and z is the distance of the echo versus the transducer. For the backscatter coefficient ($\eta(f)$), a short-time Fourier transform (STFT) technique was used (*Cook et al.*, 2011). For this part, a set of echo was collected from the aluminim while it was embedded inside the phantom to simulate an ideal ultrasound scatter. The height of the transducer was adjusted in a way to place the metal at its focal point (F). With the same setting a second set of measurements was done from the phantom itself at the same distance from the transducer. Then the following equation was used to estimate the backscatter coefficient of the phantom.

$$\eta(f) = \frac{S_s(f,F)}{S_r(f,F)} \frac{R^2k^2a^2}{8\pi d[1+(\frac{ka^2}{4F})^2]} \tag{A.11}$$

where $S_s(f,F)$ is the STFT of the phantom signal at the focus of the transducer, $S_r(f,F)$ is the STFT of the aluminium echo at the focal point, R is the reflection coeffiecient (i.e. 0.71) between water and metal, k is the wavelength number in cm^{-1}, a is the radius of transducer in cm, d is the gate length in cm, and F is the focal length of the transducer in cm (*Cook et al.*, 2011). The scattering coefficient of our home made phantom was calculated to be 1.3 cm^{-1}sr^{-1} at 45 MHz.

In soft tissue, the speed of sound is 1540m/s, the attenuation coefficient range is between 0.5 to 3.3 dB cm^{-1}MHz^{-1}, and the backscatter coefficient varies between 10^{-5} to 10^{-1}cm^{-1}sr^{-1} (*Cook et al.*, 2011). Although the in-house developed tissue phantom has about 4.5% lower speed of sound, 36 % lower attenuation coefficient, and slightly higher backscattering coefficient in comparison with soft tissue, it is still a useful sub-wavelength scattering medium for our measurements.

APPENDIX B

PHASE CORRECTION FOR ER-7 PROBE MICROPHONE (RELATED TO STUDY THREE)

As mentioned in section 5.2, an ER-7 probe microphone (Etymotic Research Inc., IL, USA) was used to measure the sound pressure applied into the tympanic membrane during experiment. ER-7 probe microphone has a .95 mm probe tube which is inserted into the ear canal to pick up the sound and is connected to an electronic box as an input (*ER-7C Series B Microphone System Datasheet*). The output of ER-7 is a voltage signal which its amplitude and frequency is a function of applied sound pressure and its frequency components, respectively. The amount of pressure is calculated based on the amplitude of output voltage using equation (B.1).

$$V_{pk-pk} = 2\sqrt{2}(1e^{-6})10^{(\frac{SPL}{20})} \tag{B.1}$$

where V_{pk-pk} is the peak-to-peak value of ER-7 output voltage and SPL is the desired sound pressure level in dB. Since it was desired to measure the phase difference between the applied sound and the vibration of membranes, it was important to figure out if any lag was inserted between the input and output of ER-7 microphone due to the pre-amplifier built in ER-7. For this purpose, a small experiment was conducted where the probe microphone was placed in a tube attached to a speaker which was controlled with a signal generator. The signal at the input and output terminals of ER-7 were monitored simultaneously using two channels of oscilloscope in order to measure the phase lag while a pure tone sound was generated with the speaker. It was shown that the output was lagging the input between 50 to 90 degrees for the applied frequency between 100 Hz-2 KHz. The measured phase difference between the membrane displacement and the applied sound pressure were corrected based on the phase lags summarized in the following table.

Table B.1: Measured phase-lag between input and output of ER-7

Frequency (Hz)	Phase Lag (Degree)	Frequency (Hz)	Phase Lag (Degree)
100	77	1100	70
200	50	1200	70
300	50	1300	80
400	50	1400	70
500	50	1500	80
600	50	1600	80
700	60	1700	70
800	60	1800	80
900	60	1900	80
1000	70	2000	90

APPENDIX C

CODE

This Appendix includes part of the MATLAB code and Script code that were developed to collect data for study two and three of this dissertation.

C.1 MATLAB Code for Theoretical Simulations of Proposed Array and Grating Lobe Suppression Techniques (Study Two)

C.1.1 Simulation of a N-element Rectangular Phased Array Transducer

```
clear
%---------
f=40e6;%----operating frequency
c=1500;
lambda=(1500/f);
N=64;%------------number of elements
dd=1.26*lambda;%----pitch
a=(dd-0.25*dd)/2;%---half of element width
b=(40*dd)/2;%----half of elemnt length
D=(N-1)*dd+2*a;%---aperture
TS=1e-6/(c);%---time resolution of the simulation
gg=0;
%-------------------------
if mod(N,2)~=0
    el_up=(N-1)/2;
    el_down=(N-1)/2;
else
    el_up=fix((N-1)/2)+1;
    el_down=fix((N-1)/2);
end
%-----
y=0;
j=0;
%------velocity pulse
BW=.4;%---38%
l= (BW*2*pi*f/(2.36))^2;
%l=1.7E15;
t2=[1:4*800];
t2o=TS.*(t2-4*200);
v=sin(2*pi*f*(t2o-7E-9)).*exp(-(t2o-7E-9).^2*l);
devv2=diff(v);
devv2=devv2/max(devv2);
devv=devv2(740:900);
```

```
%-------------
j1=0;
F=2.5;%------f-number
theta=25;%-----focal angle
xf=F*D*sin(theta*pi/180);yf=0;zf=F*D*cos(theta*pi/180);%---focal
    point
%-----delay center to center delay each element
for i=1:el_up+1%----with center
    del(i,1)=round((sqrt((xf-(i-1)*dd)^2+zf^2+yf^2)/c)/TS);%----
       element 1
    del(i,2)=del(i,1);
end
%--down
for i=1:el_down
    del(el_up+1+i,1)=round((sqrt((xf+i*dd)^2+zf^2+(yf)^2)/c)/TS)
       ;%---element 18
    del(el_up+1+i,2)=del(el_up+1+i,1);
end
%------points for calculating radiation patterns
% %-----for plotting contour map
% Xrange=-2e-3:0.05e-3:2e-3;
% Zrange=0.5e-3:.1e-3:zf+2e-3;
%-----for calculating radiation pattern
Theta=(-90:1:90)*pi/180;
R=2.5*D:.1*D:2.5*D;
%-------calculating impulse-reponse for each element at each
   space point
for rrz=F*D
    bbz=1;
    j1=j1+1;
    j=0;
    for theta2=Theta
        x=rrz*sin(theta2);
        z=rrz*cos(theta2);
        xsave(bbz)=x;
        zsave(bbz)=z;
        bbz=bbz+1;
        rrz
```

```
theta2*180/pi
j=j+1;
for upe=1:el_up+1
    %---------elemet 1
    clear alpha alphab tt1 radius
    %-----d
    d(1)=abs(x-(upe-1)*dd)-a;
    d(2)=abs(y)-b;
    d(3)=abs(x-(upe-1)*dd)+a;
    d(4)=abs(y)+b;
    d;
    %-----tau
    tauA=(d(1)^2+d(2)^2+z^2)^.5/c;
    tauB=(d(2)^2+d(3)^2+z^2)^.5/c;
    tauC=(d(1)^2+d(4)^2+z^2)^.5/c;
    tauD=(d(3)^2+d(4)^2+z^2)^.5/c;
    tauS=(d.^2+z^2).^.5./c;
    tau0=z/c;
    taum=min(tauB,tauC);
    tauM=max(tauB,tauC);
    %-------------Define time window
    nnn(upe,1)=fix(tau0/TS)+1;nnn(upe,2)=fix(tauD/TS)+1;
    tt1=((nnn(upe,1))*TS:TS:(nnn(upe,2))*TS);
    %-----alpha, alphab
    radius=((c*tt1).^2-z^2).^.5;
    alpha(1,:)=asin(d(1)./radius);
    alpha(2,:)=asin(d(2)./radius);
    alpha(3,:)=asin(d(3)./radius);
    alpha(4,:)=asin(d(4)./radius);

    alphab(1,:)=(sign(d(1)))*asin(min(abs(d(1))./radius
       ,1));
    alphab(2,:)=(sign(d(2)))*asin(min(abs(d(2))./radius
       ,1));
    alphab(3,:)=(sign(d(3)))*asin(min(abs(d(3))./radius
       ,1));
    alphab(4,:)=(sign(d(4)))*asin(min(abs(d(4))./radius
       ,1));
```

```
    %----impulse response
    h{upe}=impres2(abs(x-(upe-1)*dd),abs(y),a,b,tt1,tauA
       ,taum,tauM,tauB,tauC,tauD,tau0,tauS,alpha,alphab,
       c);
end
%--------------------
%_____________________________________Down arrays
%-----------element 18
for dwe=1:el_down
    clear alpha alphab tt18 radius
    %-----d
    d(1)=abs(x+(dwe)*dd)-a;
    d(2)=abs(y)-b;
    d(3)=abs(x+(dwe)*dd)+a;
    d(4)=abs(y)+b;
    d;
    %-----tau
    tauA=(d(1)^2+d(2)^2+z^2)^.5/c;
    tauB=(d(2)^2+d(3)^2+z^2)^.5/c;
    tauC=(d(1)^2+d(4)^2+z^2)^.5/c;
    tauD=(d(3)^2+d(4)^2+z^2)^.5/c;
    tauS=(d.^2+z^2).^.5./c;
    tau0=z/c;
    taum=min(tauB,tauC);
    tauM=max(tauB,tauC);
    %-------------Define time window
    nnn(upe+dwe,1)=fix(tau0/TS)+1;nnn(upe+dwe,2)=fix(
       tauD/TS)+1;
    tt18=(nnn(upe+dwe,1)*TS:TS:nnn(upe+dwe,2)*TS);
    %-----alpha, alphab
    radius=((c*tt18).^2-z^2).^.5;
    alpha(1,:)=asin(d(1)./radius);
    alpha(2,:)=asin(d(2)./radius);
    alpha(3,:)=asin(d(3)./radius);
    alpha(4,:)=asin(d(4)./radius);

    alphab(1,:)=(sign(d(1)))*asin(min(abs(d(1))./radius
       ,1));
```

```
            alphab(2,:)=(sign(d(2)))*asin(min(abs(d(2))./radius
               ,1));
            alphab(3,:)=(sign(d(3)))*asin(min(abs(d(3))./radius
               ,1));
            alphab(4,:)=(sign(d(4)))*asin(min(abs(d(4))./radius
               ,1));
            %----impulse response
            h{upe+dwe}=impres2(abs(x+(dwe)*dd),abs(y),a,b,tt18,
               tauA,taum,tauM,tauB,tauC,tauD,tau0,tauS,alpha,
               alphab,c);
        end
        %--------------------------------insert delays
        del=del-max(max(del));
        nnew=nnn-del;
        nnew=nnew-min(min(nnew))+1;
        htot=zeros(N,max(max(nnew)));
        for i=1:N
            htot(i,nnew(i,1):nnew(i,2))=h{i};
        end
        htotf=sum(htot,1);%---final impulse-reponse of the array
        lenhtot(j,j1)=length(htot);
        %-------------------------------
        p{j,j1,:}=conv(devv,htotf);%----transmit pulse
        p{j,j1,:}=conv(p{j,j1,:},htotf);%---receive pulse
        %--------------------
        htt{j,j1,:}=htotf/c;
        amp(j,j1)=max(abs(p{j,j1,:}));
        hold on
        clear bbbb
        bbbb=find(htotf>0);
        clear  htotf htot h nnew nnn
    end
    figure(3)
    hold on
    plot((Theta*180/pi),20*log10(amp/max(amp)),'r')
end
% %--------for plotting contour maps
% figure
```

```
% XX=fix(20*log10(amp'/max(max(amp))));
% [C,h] =contour(Zrange*1e3,Xrange*1e3,XX
   ,[[0:-1:-5],[-7:-12:-100]]);
% clabel(C,h,'FontSize',12)
% hh = findobj('Type','patch');
% set(hh,'LineWidth',2)
% xlabel('Distance from the transducer (mm)');
% ylabel('Distance from axis (mm)');
% colorbar
%%%%%%%%%%%%%%%%%%%%%%%%%%%%%%%%%%%
%CALCULATING IMPULSE-RESPONSE OF EACH RECTANGULAR ELEMENT
function [gg]=impres2(x,y,a,b,tt,tauA,taum,tauM,tauB,tauC,tauD,
   tau0,tauS,alpha,alphab,c);
%----calculating impulse-reponse of array elements based on
   analytical
%formulas in (San Emeterio 1992)
gg=zeros(1,size(tt,2));
clear z1 z2 z3 z4
if (x>=a & y>=b)%---region I
    z1=find(tt>=tauA & tt<=taum);
    gg(z1)=c*(pi/2-alpha(1,z1)-alpha(2,z1))/(2*pi);
    z2=find(tt>=taum & tt<=tauM);
    if tauB<=tauC
        gg(z2)=c*(alpha(3,z2)-alpha(1,z2))/(2*pi);
    else
        gg(z2)=c*(alpha(4,z2)-alpha(2,z2))/(2*pi);
    end
    z3=find(tt>=tauM & tt<=tauD);
    gg(z3)=c*(-pi/2+alpha(3,z3)+alpha(4,z3))/(2*pi);

elseif (x<=a & y>=b)%---regioin II
    z1=find(tt>=tauS(2) & tt<tauA);
    gg(z1)=c*(pi-2*alpha(2,z1))/(2*pi);
    z2=find(tt>=tauA & tt<=taum);
    gg(z2)=c*(pi/2-alpha(1,z2)-alpha(2,z2))/(2*pi);
    z3=find(tt>=taum & tt<=tauM);
    gg(z3)=c*(-pi-alpha(1,z3)+alpha(3,z3)+2*alphab(4,z3))/(2*pi)
       ;
```

```
    z4=find(tt>=tauM & tt<=tauD);
    gg(z4)=c*(-pi/2+alpha(3,z4)+alpha(4,z4))/(2*pi);
elseif (x>=a & y<=b)%---region III
    z1=find(tt>=tauS(1) & tt<tauA);
    gg(z1)=c*(2*alphab(3,z1)-2*alpha(1,z1))/(2*pi);
    z2=find(tt>=tauA & tt<=taum);
    gg(z2)=c*(-pi/2-alpha(1,z2)-alpha(2,z2)+2*alphab(3,z2))/(2*
       pi);
    z3=find(tt>=taum & tt<=tauM);
    if tauB<=tauC
        gg(z3)=c*(-alpha(1,z3)+alpha(3,z3))/(2*pi);
    else
        gg(z3)=c*(-pi-alpha(2,z3)+2*alphab(3,z3)+alpha(4,z3))
           /(2*pi);
    end
    z4=find(tt>=tauM & tt<=tauD);
    gg(z4)=c*(-pi/2+alpha(3,z4)+alpha(4,z4))/(2*pi);

elseif (x<=a & y<=b)%---region IV
    z1=find(tt>=tau0 & tt<tauA);
    gg(z1)=c*(-2*pi-2*alphab(1,z1)-2*alphab(2,z1)+2*alphab(3,z1)
       +2*alphab(4,z1))/(2*pi);
    z2=find(tt>=tauA & tt<=taum);
    gg(z2)=c*(-3*pi/2-alpha(1,z2)-alpha(2,z2)+2*alphab(3,z2)+2*
       alphab(4,z2))/(2*pi);
    z3=find(tt>=taum & tt<=tauM);
    if tauB<=tauC
        gg(z3)=c*(-pi-alpha(1,z3)+alpha(3,z3)+2*alphab(4,z3))
           /(2*pi);
    else
        gg(z3)=c*(-pi-alpha(2,z3)+2*alphab(3,z3)+alpha(4,z3))
           /(2*pi);
    end
    z4=find(tt>=tauM & tt<=tauD);
    gg(z4)=c*(-pi/2+alpha(3,z4)+alpha(4,z4))/(2*pi);
end
```

C.1.2 Simulation of K Split-Aperture Transmit Beamforming Technique for Suppressing Grating Lobes of Large-pitch Phased Arrays

```
clear
%close all
%---------consider for three elements
f=40e6;
c=1500;
lambda=(1500/f);
N=64;
%cof_lamb=[0.75,1,1.5];
cof_lamb=1.25;%----pitch=1.25*lambda
for a_lamb=1:1;
    a=cof_lamb(a_lamb)*lambda/2;
    dd=cof_lamb(a_lamb)*lambda;
    TS=1e-6/(c);
    gg=0;
    D=(N-1)*dd+2*a;
    b=(3*D/4)/2;
    if mod(N,2)~=0
        el_up=(N-1)/2;
        el_down=(N-1)/2;
    else
        el_up=fix((N-1)/2)+1;
        el_down=fix((N-1)/2);
    end
    %-----point field
    y=0;
    j=0;
    %------jeremy
    BW=.4;%---38%
    l= (BW*2*pi*f/(2.36))^2;
    %l=1.7E15;
    t2=[1:4*800];
    t2o=TS.*(t2-4*200);
    v=sin(2*pi*f*(t2o-7E-9)).*exp(-(t2o-7E-9).^2*l);
    devv=diff(v);
    devv=devv/max(devv);
```

```
%-------
j1=1;
F=2;
%th_fo=[0 15 25 30 45];
th_fo=25;%----focal angle
for i_fo=1:1
    theta=th_fo(i_fo);
    xf=F*D*sin(theta*pi/180);yf=0;zf=F*D*cos(theta*pi/180);%
       ---focal point
    %-----delay center to center delay each element
    for i=1:el_up+1%----with center
        del(i,1)=fix((sqrt((xf-(i-1)*dd)^2+zf^2+yf^2)/c-sqrt
           ((xf)^2+zf^2+yf^2)/c)/TS);%----element 1
        del(i,2)=del(i,1);
    end
    %--down
    for i=1:el_down
        del(el_up+1+i,1)=fix((sqrt((xf+i*dd)^2+zf^2+(yf)^2)/
           c-sqrt((xf)^2+zf^2+yf^2)/c)/TS);%---element 18
        del(el_up+1+i,2)=del(el_up+1+i,1);
    end
    theta=-60:1:45;
    Xrange=F*D*sin(theta*pi/180);%---on the same R
    Zrange=zf:.02e-3:zf;
    el_loc=[N:-1:el_up+2,1:el_up+1];
    %spl_co=[1 2 4 8];
    spl_co=4;%---------splitting the transmit aperture
    for spl=1:1
        for j=1:length(theta)
            [cof_lamb(a_lamb) th_fo(i_fo) spl_co(spl) theta(
               j)]
            x=F*D*sin(theta(j)*pi/180);
            z=F*D*cos(theta(j)*pi/180);
            clear len
            for upe=1:el_up+1
                %---------elemet 1
                clear alpha alphab tt1 radius
                %-----d
```

```
    d(1)=abs(x-(upe-1)*dd)-a;
    d(2)=abs(y)-b;
    d(3)=abs(x-(upe-1)*dd)+a;
    d(4)=abs(y)+b;
    d;
    %-----tau
    tauA=(d(1)^2+d(2)^2+z^2)^.5/c;
    tauB=(d(2)^2+d(3)^2+z^2)^.5/c;
    tauC=(d(1)^2+d(4)^2+z^2)^.5/c;
    tauD=(d(3)^2+d(4)^2+z^2)^.5/c;
    tauS=(d.^2+z^2).^.5./c;
    tau0=z/c;
    taum=min(tauB,tauC);
    tauM=max(tauB,tauC);
    %-------------Define time window
    nnn(upe,1)=fix(tau0/TS)+1;nnn(upe,2)=fix(
       tauD/TS)+1;
    tt1=((nnn(upe,1))*TS:TS:(nnn(upe,2))*TS);
    %-----alpha, alphab
    radius=((c*tt1).^2-z^2).^.5;
    alpha(1,:)=asin(d(1)./radius);
    alpha(2,:)=asin(d(2)./radius);
    alpha(3,:)=asin(d(3)./radius);
    alpha(4,:)=asin(d(4)./radius);
    alphab(1,:)=(sign(d(1)))*asin(min(abs(d(1))
       ./radius,1));
    alphab(2,:)=(sign(d(2)))*asin(min(abs(d(2))
       ./radius,1));
    alphab(3,:)=(sign(d(3)))*asin(min(abs(d(3))
       ./radius,1));
    alphab(4,:)=(sign(d(4)))*asin(min(abs(d(4))
       ./radius,1));
    %----impulse response
    h{upe}=impres2(abs(x-(upe-1)*dd),abs(y),a,b,
       tt1,tauA,taum,tauM,tauB,tauC,tauD,tau0,
       tauS,alpha,alphab,c);
    len(upe)=length(h{upe});
end
```

```
%---------------------
%___________________________________________Down
   arrays
%-----------element 18
for dwe=1:el_down
    clear alpha alphab tt18 radius
    %-----d
    d(1)=abs(x+(dwe)*dd)-a;
    d(2)=abs(y)-b;
    d(3)=abs(x+(dwe)*dd)+a;
    d(4)=abs(y)+b;
    d;
    %-----tau
    tauA=(d(1)^2+d(2)^2+z^2)^.5/c;
    tauB=(d(2)^2+d(3)^2+z^2)^.5/c;
    tauC=(d(1)^2+d(4)^2+z^2)^.5/c;
    tauD=(d(3)^2+d(4)^2+z^2)^.5/c;
    tauS=(d.^2+z^2).^.5./c;
    tau0=z/c;
    taum=min(tauB,tauC);
    tauM=max(tauB,tauC);
    %-------------Define time window
    nnn(upe+dwe,1)=fix(tau0/TS)+1;nnn(upe+dwe,2)
       =fix(tauD/TS)+1;
    tt18=(nnn(upe+dwe,1)*TS:TS:nnn(upe+dwe,2)*TS
       );
    %-----alpha, alphab
    radius=((c*tt18).^2-z^2).^.5;
    alpha(1,:)=asin(d(1)./radius);
    alpha(2,:)=asin(d(2)./radius);
    alpha(3,:)=asin(d(3)./radius);
    alpha(4,:)=asin(d(4)./radius);
    alphab(1,:)=(sign(d(1)))*asin(min(abs(d(1))
       ./radius,1));
    alphab(2,:)=(sign(d(2)))*asin(min(abs(d(2))
       ./radius,1));
    alphab(3,:)=(sign(d(3)))*asin(min(abs(d(3))
       ./radius,1));
```

```
    alphab(4,:)=(sign(d(4)))*asin(min(abs(d(4))
       ./radius,1));
    %----impulse response
    h{upe+dwe}=impres2(abs(x+(dwe)*dd),abs(y),a,
       b,tt18,tauA,taum,tauM,tauB,tauC,tauD,tau0
       ,tauS,alpha,alphab,c);
    len(upe+dwe)=length(h{upe+dwe});
end
del=del-max(max(del));
nnew=nnn-del;
htot=zeros(N,max(max(nnew)));
% applying delay to all elements
for i=1:N
    htot(i,nnew(i,1):nnew(i,2))=h{i};
end
Transmit=zeros(N,max(max(nnew)));
%--------------------split transmit aperture
split=spl_co(spl);
lim=fix(N/split);
for sp=1:split
    st=(sp-1)*lim+1;
    spp=min([(sp)*lim,N]);
    Transmit(sp,:)=sum(htot(el_loc(st:spp),:),1)
       ;
end
k1=conv(devv,zeros(1,max(max(nnew))));
element=conv(k1,htot(1,:));
%-------calculating SCF for each split
for i=1:split
    clear ggg hhh
    i
    hhh=zeros(1,max(max(nnew)));
    ggg=conv(devv,Transmit(i,:)/c);%--- transmit
        pulse is coming back
    clear bb b_k

    for jjj=1:N%---Receive by each element
```

```
        htot(jjj,nnew(jjj,1):nnew(jjj,2))=real(h{jjj});
        bb(jjj,:)=conv(ggg,htot(jjj,:)/c);
        nn= sqrt(0.000000004) * randn(1, size(bb,2));
        bb(jjj,:)=bb(jjj,:)+nn;
        %-------SCF
        clear v1 v2
        b_k(jjj,:)=bb(jjj,:);
        v1=find(bb(jjj,:)>=0);
        b_k(jjj,v1)=1;
        v2=find(bb(jjj,:)<0);
        b_k(jjj,v2)=-1;
    end
    %-----SCF
    sig=1-(mean(b_k)).^2;
    SCF=(abs(1-sig.^(.5))).^2;
    pp=SCF.*sum(bb,1);
    element(i,:)=[sum(pp,1),zeros(1,size(element,2)-size(bb,2))];%---adding weighted echoes of all splits
    el_ref(i,:)=[sum(bb,1),zeros(1,size(element,2)-size(bb,2))];
    clear pp sig SCF nn
end
%-------------------------------organize hi s
htotf=sum(htot,1);%-----for transmit
p_SCF{j,:}=sum(element,1);
amp_SCF(j)=max(abs(p_SCF{j,:}));
%-------For reference (Original)
% htotf=sum(htot,1);
pp2{j,:}=sum(el_ref,1);
amp2(j)=max(abs(pp2{j,:}));
lenhtot(j)=length(htot);
%-----figure
clear element angg angg_A sf PCF ggg b_k SCF sig el_ref
clear  htotf htot h nnew nnn Transmit
```

```
            end
            figure(10+a_lamb+th_fo(i_fo))
            hold on
            plot(theta,20*log10(amp2/max(amp2)),’g’)%---
               Reference
            plot(theta,20*log10(amp_SCF/max(amp_SCF)),’r’)
            save (['D:\zahra\z-rectangular\phase.co\’,num2str(
               i_fo+25+125),num2str(a_lamb),num2str(spl)],’amp2’
               ,’amp_SCF’)
        end
    end
end
```

C.1.3 Simulation of Pulse-Probing Technique for Suppressing Grating Lobes of Large-Pitch Phased Arrays

```
clear
%---------
f=40e6;
c=1500;
lambda=(1500/f);
N=64;
cof_lamb=[0.75,1,1.25,1.5];
for a_lamb=1:4
    a=cof_lamb(a_lamb)*lambda/2;
    dd=cof_lamb(a_lamb)*lambda;
    TS=1e-6/(c);
    gg=0;
    D=(N-1)*dd+2*a;
    b=(3*D/4)/2;
    if mod(N,2)~=0
        el_up=(N-1)/2;
        el_down=(N-1)/2;
    else
        el_up=fix((N-1)/2)+1;
        el_down=fix((N-1)/2);
    end
    %-----velocity pulse
    y=0;
    j=0;
    BW=.4;%---38%
    l= ((BW*2*pi*f/(2.36))^2)/2;
    %l=1.7E15;
    t2=[1:4*800];
    t2o=TS.*(t2-4*200);
    v=sin(2*pi*f*(t2o-7E-9)).*exp(-(t2o-7E-9).^2*l);
    devv=diff(v);
    devv=devv/max(devv);
    %--------
    j1=1;
    F=2;
```

```
th_fo=[0 15 25 30 45];
i_fo=1:1
for i_fo=1:5
    theta=th_fo(i_fo);
    xf=(F*D)*sin(theta*pi/180);yf=0;zf=(F*D)*cos(theta*pi
       /180);
    %----------------------delay for defocused transmit
    %-----delay center to center delay each element
    for i=1:el_up+1%----with center
        del_trans(i,1)=fix((sqrt(((i-1)*dd)^2+(4e-3)^2+yf^2)
           /c)/TS);%----element 1
        del_trans(i,2)=del_trans(i,1);
    end
    %--down
    for i=1:el_down
        del_trans(el_up+1+i,1)=fix((sqrt((i*dd)^2+(4e-3)^2+(
           yf)^2)/c)/TS);%---element 18
        del_trans(el_up+1+i,2)=del_trans(el_up+1+i,1);
    end
    %-------------------------------------------
    %-----delay center to center delay each element
    for i=1:el_up+1%----with center
        del(i,1)=fix((sqrt((xf-(i-1)*dd)^2+zf^2+yf^2)/c)/TS)
           ;%----element 1
        del(i,2)=del(i,1);
    end
    %--down
    for i=1:el_down
        del(el_up+1+i,1)=fix((sqrt((xf+i*dd)^2+zf^2+(yf)^2)/
           c)/TS);%---element 18
        del(el_up+1+i,2)=del(el_up+1+i,1);
    end
    theta=-60:1:45;
    Xrange=F*D*sin(theta*pi/180);%---on the same R
    Zrange=zf:.02e-3:zf;
    el_loc=[N:-1:el_up+2,1:el_up+1];
    spl_co=1;
    spl=1:1
```

```
for j=1:length(theta)
    [cof_lamb(a_lamb) th_fo(i_fo) spl_co(spl) theta(j)]
    %                 %-------------------------virtual is
        the center
    x=(F*D)*sin(theta(j)*pi/180);
    z=(F*D)*cos(theta(j)*pi/180);
    clear len
    for upe=1:el_up+1
        %---------elemet 1
        clear alpha alphab tt1 radius
        %-----d
        d(1)=abs(x-(upe-1)*dd)-a;
        d(2)=abs(y)-b;
        d(3)=abs(x-(upe-1)*dd)+a;
        d(4)=abs(y)+b;
        d;
        %-----tau
        tauA=(d(1)^2+d(2)^2+z^2)^.5/c;
        tauB=(d(2)^2+d(3)^2+z^2)^.5/c;
        tauC=(d(1)^2+d(4)^2+z^2)^.5/c;
        tauD=(d(3)^2+d(4)^2+z^2)^.5/c;
        tauS=(d.^2+z^2).^.5./c;
        tau0=z/c;
        taum=min(tauB,tauC);
        tauM=max(tauB,tauC);
        %-------------Define time window
        nnn(upe,1)=fix(tau0/TS)+1;nnn(upe,2)=fix(tauD/TS
           )+1;
        tt1=((nnn(upe,1))*TS:TS:(nnn(upe,2))*TS);
        %-----alpha, alphab
        radius=((c*tt1).^2-z^2).^.5;
        alpha(1,:)=asin(d(1)./radius);
        alpha(2,:)=asin(d(2)./radius);
        alpha(3,:)=asin(d(3)./radius);
        alpha(4,:)=asin(d(4)./radius);

        alphab(1,:)=(sign(d(1)))*asin(min(abs(d(1))./
           radius,1));
```

```
    alphab(2,:)=(sign(d(2)))*asin(min(abs(d(2))./
       radius,1));
    alphab(3,:)=(sign(d(3)))*asin(min(abs(d(3))./
       radius,1));
    alphab(4,:)=(sign(d(4)))*asin(min(abs(d(4))./
       radius,1));
    %----impulse response

    h{upe}=impres2(abs(x-(upe-1)*dd),abs(y),a,b,tt1,
       tauA,taum,tauM,tauB,tauC,tauD,tau0,tauS,alpha
       ,alphab,c);
    len(upe)=length(h{upe});
end
%---------------------
%______________________________________Down arrays
%-----------element 18
for dwe=1:el_down
    clear alpha alphab tt18 radius
    %-----d
    d(1)=abs(x+(dwe)*dd)-a;
    d(2)=abs(y)-b;
    d(3)=abs(x+(dwe)*dd)+a;
    d(4)=abs(y)+b;
    d;
    %-----tau
    tauA=(d(1)^2+d(2)^2+z^2)^.5/c;
    tauB=(d(2)^2+d(3)^2+z^2)^.5/c;
    tauC=(d(1)^2+d(4)^2+z^2)^.5/c;
    tauD=(d(3)^2+d(4)^2+z^2)^.5/c;
    tauS=(d.^2+z^2).^.5./c;
    tau0=z/c;
    taum=min(tauB,tauC);
    tauM=max(tauB,tauC);
    %-------------Define time window
    nnn(upe+dwe,1)=fix(tau0/TS)+1;nnn(upe+dwe,2)=fix
       (tauD/TS)+1;
    tt18=(nnn(upe+dwe,1)*TS:TS:nnn(upe+dwe,2)*TS);
    %-----alpha, alphab
```

```
    radius=((c*tt18).^2-z^2).^.5;
    alpha(1,:)=asin(d(1)./radius);
    alpha(2,:)=asin(d(2)./radius);
    alpha(3,:)=asin(d(3)./radius);
    alpha(4,:)=asin(d(4)./radius);
    alphab(1,:)=(sign(d(1)))*asin(min(abs(d(1))./
       radius,1));
    alphab(2,:)=(sign(d(2)))*asin(min(abs(d(2))./
       radius,1));
    alphab(3,:)=(sign(d(3)))*asin(min(abs(d(3))./
       radius,1));
    alphab(4,:)=(sign(d(4)))*asin(min(abs(d(4))./
       radius,1));
    %----impulse response
    h{upe+dwe}=impres2(abs(x+(dwe)*dd),abs(y),a,b,
       tt18,tauA,taum,tauM,tauB,tauC,tauD,tau0,tauS,
       alpha,alphab,c);
    len(upe+dwe)=length(h{upe+dwe});
end
nnew_trans=nnn+del_trans;
del=del-max(max(del));
nnew=nnn-del;
htot=zeros(N,max(max(nnew)));
htot_trans=zeros(N,max(max(nnew_trans)));
% applying delay to all elements
for i=1:N
    htot(i,nnew(i,1):nnew(i,2))=h{i};
    htot_trans(i,nnew_trans(i,1):nnew_trans(i,2))=h{
       i};
end
Transmit=zeros(1,max(max(nnew_trans)));
Transmit_rev=zeros(1,max(max(nnew)));
Rec=zeros(1,max(max(nnew)));
Transmit=sum(htot_trans,1);%---transmit defocused
   pulse
Rec=sum(htot,1);%----impulse-respone of transmit
   beamforming
```

```
%---------Correspond the defocus to transmit beamforming
%------------I want to find the start point of the impulse response for the phased array and defocused to copy them on tope of each other. This is needed when I want to multiply the SCF of defocused with the signal of phased array to refer to the same location.
clear dis zzz dis2 zzz2 dis_unfoc
%---find the closest element to the point
for xx=1:el_up+1%----with center
    dis(xx)=fix((sqrt((x-(xx-1)*dd)^2+z^2)/c)/TS);%----element 1
end
%--down
for xx=1:el_down
    dis(el_up+1+xx)=fix((sqrt((x+xx*dd)^2+z^2)/c)/TS);%---element 18
end
dis2=dis-del(:,1)';
zzz=find(dis2==min(dis2));
lll2=dis2(zzz(1));
dis_unfoc=dis+del_trans(:,1)';
zzz2=find(dis_unfoc==min(dis_unfoc));
lll=dis_unfoc(zzz2(1));
ll2=max(nnew_trans);
ll_b=ll2(2)-lll(1);
Transmit_rev(lll2:lll2+ll_b)=Transmit(lll(1):ll2(2));
Trans_sig=conv(devv,Transmit_rev);
Rec_sig=conv(devv,Rec);
hh=conv(Trans_sig,htot(1,:));
bb_phased=zeros(N,size(hh,2));
llb=length(conv(Rec_sig,htot(1,:)));
for jjj=1:N%---Receive by each element
    htot(jjj,nnew(jjj,1):nnew(jjj,2))=real(h{jjj});
    bb(jjj,:)=conv(Trans_sig,htot(jjj,:)/c);%-----defocused echo
```

```
    %---compare with phased
    bb_phased(jjj,1:llb)=conv(Rec_sig,htot(jjj,:)/c)
       ;%---transmit beamformed echo
    %-------
    nn= sqrt(0.000000004) * randn(1, size(bb,2));
    nn2= sqrt(0.000000004) * randn(1, size(bb_phased
       ,2));
    bb(jjj,:)=bb(jjj,:)+nn;
    bb_phased(jjj,:)=bb_phased(jjj,:)+nn2;
    %-------SCF
    clear v1 v2 v3 v4
    b_k(jjj,:)=bb(jjj,:);
    v1=find(bb(jjj,:)>=0);
    b_k(jjj,v1)=1;
    v2=find(bb(jjj,:)<0);
    b_k(jjj,v2)=-1;
    %----compared with phased
    b_k_p(jjj,:)=bb_phased(jjj,:);
    v3=find(bb_phased(jjj,:)>=0);
    b_k_p(jjj,v3)=1;
    v4=find(bb_phased(jjj,:)<0);
    b_k_p(jjj,v4)=-1;
end
%%-----SCF+defocused
sig=1-(mean(b_k)).^2;
SCF=(abs(1-sig.^(.5))).^2;
pp=SCF.*sum(bb_phased,1);
%-----SCF phased for comparison
sig_p=1-(mean(b_k_p)).^2;
SCF_p=(abs(1-sig_p.^(.5))).^2;
pp_p=SCF_p.*sum(bb_phased,1);
%-----radiation patterns
amp2(j)=max(abs(pp));%---------defocused +SCF
amp2_rec(j)=max(abs(pp_p));%----SCF on phase
amp2_ref(j)=max(abs(sum(bb_phased,1)));%---No SCF
lenhtot(j)=length(htot);
%-----figure
```

```
            clear element angg angg_A sf PCF ggg b_k SCF sig
               el_ref
            clear b_k_p SCF_p sig_p  pp pp_p bb bb_phased
            clear  htotf htot h nnew nnn Transmit Trans_sig Rec
               Rec_sig
        end
        figure
        hold on
        plot(theta,20*log10(amp2/max(amp2)),’r’)%---defocused
        plot(theta,20*log10(amp2_ref/max(amp2_ref)),’b’)%---No
           SCF
        plot(theta,20*log10(amp2_rec/max(amp2_rec)),’g’)%---SCF
        save (['D:\zahra\z-rectangular\phase.co\unfocused’,
           num2str(i_fo),num2str(a_lamb),num2str(spl)],’amp2’,’
           amp2_rec’,’amp2_ref’)
    end
end
```

C.2 MATLAB Code for Experimental Verification of Proposed Grating lobes Suppression Techniques (Study Two)

The script code developed for Vevo 2100 system in study two are not included in this appendix due to the non-disclosure agreement between the author and VisualSonics.

C.2.1 MATLAB Code for Offline Processing of Experimental Data Collected for K=2 Split-Aperture Technique

```
%These are part of the codes developed for analyzing the
   experimental data using K=2 split-aperture technique.
clear
pp=[-32:1:33];
L=1:4500;   %4500 for upsampled,580 fo no sample
M=length(L);
P_scf=zeros(66,M);
P_raw=zeros(66,M);
P_scf_split=zeros(66,M);
P_scf_mean=zeros(66,M);
P_raw_mean=zeros(66,M);
P_scf_split_mean=zeros(66,M);
env_raw=zeros(66,M);
for i=1:66
    K=pp(i)
    load (['K:\zahra\phase3-visualsonic\Data-visulasonic\test\',
       num2str(i),'\data4'])
    amp_scf(i)=max(abs(p_scf(L)));
    amp_raw(i)=max(abs(p_raw(L)));
    amp_scf_split(i)=max(abs(p_scf_split(L)));
    gg=length(p_scf(L));
    P_scf(i,1:gg)=p_scf(L);
    P_raw(i,1:gg)=p_raw(L);
    P_scf_split(i,1:gg)=p_scf_split(L);
    amp_scf_mean(i)=max(abs(p_scf_mean(L)));
    amp_raw_mean(i)=max(abs(p_raw_mean(L)));
    amp_scf_split_mean(i)=max(abs(p_scf_split_mean(L)));
    gg=length(p_scf_mean(L));
    P_scf_mean(i,1:gg)=p_scf_mean(L);
```

```
    P_raw_mean(i,1:gg)=p_raw_mean(L);
    P_scf_split_mean(i,1:gg)=p_scf_split_mean(L);
    env_raw(i,1:gg)=abs(hilbert(p_raw(L)));
    env_scf_split(i,1:gg)=abs(hilbert(p_scf_split(L)));
    clear  p_raw p_scf  p_scf_split RfData RfData2 RF_l RF_l2
       RF_l_mean RF_l2_mean  p_raw_mean p_scf_mean
       p_scf_split_mean
end
figure
plot(pp,20*log10(amp_raw/max(amp_raw)))
hold on
plot(pp,20*log10(amp_scf/max(amp_scf)),'r')
plot(pp,20*log10(amp_scf_split/max(amp_scf_split)),'g')
figure
plot(pp,20*log10(amp_raw_mean/max(amp_raw_mean)))
hold on
plot(pp,20*log10(amp_scf_mean/max(amp_scf_mean)),'r')
plot(pp,20*log10(amp_scf_split_mean/max(amp_scf_split_mean)),'g'
   )
%%%%%%%%%%%%%%%%%%%%%%%%%%%%%%%%%%%%%%%%%%%%%%%%%%%%%%%%%%%%%%%
    LOADING Split-aperture RF DATA
function [p_raw, p_scf,p_scf_split,amp_raw,amp_scf,amp_scf_split
   ,p_raw_mean, p_scf_mean,p_scf_split_mean,amp_raw_mean,
   amp_scf_mean,amp_scf_split_mean]=main(K);
lineNumber=20;
%----------------------------------------------------
fbase=['D:\zahra\phase3-visualsonic\Data-visulasonic\test\',
   num2str(K),'\Image',num2str(K),num2str(1)]
fbase2=['D:\zahra\phase3-visualsonic\Data-visulasonic\test\',
   num2str(K),'\Image',num2str(K),num2str(2)]
ftrans_on=[];
fref=[];
fl=[fbase,num2str(1),'.iq'];
[BmodeNumLines]=RF(fl,lineNumber);
fl2=[fbase,num2str(1),'.iq'];
[BmodeNumLines2]=RF(fl2,lineNumber);
for i=1:64
    i;
```

```
    %---image 1
    fl=[fbase,num2str(i),’.iq’];
    [BmodeNumLines,RF_l(i,:), Idatam, Qdatam,cc1,BmodeNumSamples
       ,IntFac,fs_int1,RfData]=RF(fl,lineNumber);
    [BmodeNumLines,RF_l_mean(i,:),Idata(i,:), Qdata(i,:)]=
       RF_mean(fl,lineNumber);
    %    Mean_RF_l(i,:)=mean(real(RfData),2);
    if size(fbase2)>0
        %---image 2
        fl2=[fbase2,num2str(i),’.iq’];
        [BmodeNumLines2,RF_l2(i,:), Idata2m, Qdata2m,cc,
           BmodeNumSamples,IntFac,fs_int2, RfData2]=RF(fl2,
           lineNumber);
        [BmodeNumLines,RF_l2_mean(i,:),Idata2(i,:),Qdata2(i,:),
           cc,BmodeNumSamples,IntFac,fs_int,RfData,RFl2,f_rf,t]=
           RF_mean(fl2,lineNumber);
    end
end
%-------------------------SCF processing
[p_raw,p_scf,p_scf_split,amp_scf_split,amp_scf,amp_raw]=SCF_cal(
   RF_l, RF_l2);
[p_raw_mean,p_scf_mean,p_scf_split_mean,amp_scf_split_mean,
   amp_scf_mean,amp_raw_mean,SCF3]=SCF_cal(RF_l_mean, RF_l2_mean
   );
save([’D:\zahra\phase3-visualsonic\Data-visulasonic\test\’,
   num2str(K),’\data4’], ’p_raw’,’p_scf’,’p_scf_split’,’RfData’,
   ’RfData2’,’RF_l’,’RF_l2’,’RF_l_mean’,’RF_l2_mean’,’p_raw_mean
   ’,’p_scf_mean’,’p_scf_split_mean’);
%%%%%%%%%%%%%%%%%%%%%%%%%%%%%%%%%%%%%%%%%%%%%%%%%%%%%%%%%%%%%
%%%%%%%%%%%%%%%%%%%%%%%%%%%%%%%%%%%%%%%%%%%%%%%%%%%%%%%%%%%%
%The functions "RF.m" and "RF_mean.m" were developed based on "
   VsiBModeReconstructRF.m" provided by the VisuaSonics for
   importing the IQ data (not included in this appendix).
%%%%%%%%%%%%%%%%%%%%%%%%%%%%%%%%%%%%%%%%%%%%%%%%%%%%%%%%%%%%
%%%%%%%%%%%%%%%%%%%%%%%%%%%%%%%%%%%%%%%%%%%%%%%%%%%%%%%%%%%%%%
   CALCULATING SCF WEIGHTS FROM SPLIT-APERTURE ECHOES
function [p_raw,p_scf,p_scf_split,amp_scf_split,amp_scf,amp_raw,
   SCF3]=SCF_cal(RF_l, RF_l2)
```

```
for i=1:64
    %--1st half
    clear v1 v2
    element(i,:)=RF_l(i,:);
    b_k(i,:)=element(i,:);
    v1=find(element(i,:)>=0);
    b_k(i,v1)=1;
    v2=find(element(i,:)<0);
    b_k(i,v2)=-1;
    %---2nd half
    clear v3 v4
    element2(i,:)=RF_l2(i,:);
    b_k2(i,:)=element2(i,:);
    v3=find(element2(i,:)>=0);
    b_k2(i,v3)=1;
    v4=find(element2(i,:)<0);
    b_k2(i,v4)=-1;
    %-----full aperture
    clear v3 v4
    %element3(i,:)=RF_l3(i,:);
    element3(i,:)=RF_l(i,:)+RF_l2(i,:);
    b_k3(i,:)=element3(i,:);
    v3=find(element3(i,:)>=0);
    b_k3(i,v3)=1;
    v4=find(element3(i,:)<0);
    b_k3(i,v4)=-1;
end
%-----------------------split
%-----SCF
sig=1-(mean(b_k)).^2;
SCF=(abs(1-sig.^(.5))).^2;
p_SCF=SCF.*sum(RF_l,1);
amp_SCF=max(abs(p_SCF));
%-----SCF2
sig2=1-(mean(b_k2)).^2;
SCF2=(abs(1-sig2.^(.5))).^2;
p_SCF2=SCF2.*sum(RF_l2,1);
amp_SCF2=max(abs(p_SCF2));
```

```
%----------------------regular SCF
%-----SCF3
sig3=1-(mean(b_k3)).^2;
SCF3=(abs(1-sig3.^(.5))).^2;
p_SCF3=SCF3.*(sum(RF_l2,1)+ sum(RF_l,1));
amp_SCF3=max(abs(p_SCF3));
%-----
amp_scf_split=max(abs(p_SCF+p_SCF2));
amp_scf=amp_SCF3;
amp_raw=max(abs((sum(RF_l2,1)+ sum(RF_l,1))));
p_scf_split=p_SCF+p_SCF2;
p_scf=p_SCF3;
p_raw=(sum(RF_l2,1)+ sum(RF_l,1));
%%%%%%%%%%%%%%%%%%%%%%%%%%%%%%%%%%%%%%%%%%%%%%%%%%%%%%%%%%%%%%
   PlOTTING THE PHASED ARRAY DATA IN PIE SHAPE
clear j1 jj h1 I I2
sig=P_scf_mean;
%-----for data4
[b,a]=butter(3,.15,'low');%.2 for upsampled
for i=1:size(P_scf_mean,1)
    jj1(i,:)=sqrt(abs(2*filtfilt(b,a,sig(i,:).^2)));
    %----if upsampled
    j1(i,:)=resample(jj1(i,:),2,8);
end
d1=size(j1,2);
f1=fix(d1/6); %6 mm (2-8)
ff2=2*f1;%---2mm offset
for i=1:size(P_raw_mean,1)
    jjj=[zeros(1,ff2),j1(i,:)];%--add the offset as like zeros
    jj(i,:)=20*log10(jjj);
    clear bb bb1
    bb=find(jjj<=0);
    jj(i,bb)=0;
end
j2=find(jj<=(max(max(jj))-80)); %---65 for upsampled
jj(j2)=(max(max(jj))-80);
jj=(jj-min(min(jj)))*255/(max(max(jj))-min(min(jj)));
figure
```

```
imshow(jj',[])
RFd=jj;
Ref2=jj;
x2=size(RFd,2);
x2=x2;
x1=fix(2*tan(33*pi/180)*x2);
Theta=-32:1:33;
R=1:round(sqrt(x1^2+x2^2));
x2=x2;
I=zeros(x1,x2);
I3=zeros(x1,x2);
xlim=fix(x2*tan(33*pi/(2*180)));
for i=1:x1
    i;
    for j=1:x2
        xm=(i-x1/2);
        r=((sqrt((xm).^2+(j).^2)));
        theta=(atan(xm/(j))*180/pi);
        rr(i,j)=r;
        tt(i,j)=theta;
        if ((theta)>=0 & (theta)<=33 & r<size(RFd,2))
            clear gg1 gg2
            gg1=find(r>=R);
            gg2=find(theta>=Theta);
            Lr=gg1(length(gg1));
            w1=1-abs(R(Lr)-r);w2=1-abs(R(Lr+1)-r);
            Lt=Theta(gg2(length(gg2)));
            Ltind=(gg2(length(gg2)));
            w3=1-abs(Lt-theta);w4=1-abs(Lt+1-theta);
            if Lt<=33 & Lr<=x2
                I2(i,j)=w1*w3*Ref2(Ltind,Lr)+ w4*w1*Ref2(Ltind
                   +1,Lr)+w3*w2*Ref2(Ltind,Lr+1)+w4*w2*Ref2(
                   Ltind+1,Lr+1);
            else
                I2(i,j)=0;
            end
        elseif (theta<=0 & theta>=-32 & r<size(RFd,2))
            clear gg1 gg2
```

```
            gg1=find(r>=R);
            gg2=find(theta>=Theta);
            Lr=gg1(length(gg1));
            w1=1-abs(R(Lr)-r);w2=1-abs(R(Lr+1)-r);
            Lt=Theta(gg2(length(gg2)));
            Ltind=(gg2(length(gg2)));
            w3=1-abs(Lt-theta);w4=1-abs(Lt+1-theta);
            %---
            if Lt>=-33 & Lr<=x2
                I2(i,j)=w1*w3*Ref2(Ltind,Lr)+ w4*w1*Ref2(Ltind
                   +1,Lr)+w3*w2*Ref2(Ltind,Lr+1)+w4*w2*Ref2(
                   Ltind+1,Lr+1);
            else
                I2(i,j)=0;
            end
        else
            I2(i,j)=0;
            I3(i,j)=50;
        end
    end
end
I4=I2;
x2=x2-ff2;
clear ggg
ggg=find(I3==0);
I3(ggg)=I4(ggg);
I3=I3(:,ff2+1:size(I3,2));
TS=8/512e6;
M=2.59e-3/6e-3;
figure
B = imresize(I3, [fix(x2*.43*2) fix(x2)/2]);
imshow(B’,[])
```

C.2.2 MATLAB Code for Offline Processing of Experimental Data Collected for Pulse-Probing Technique

```
%These are part of the codes developed for analyzing the
   experimental data using pulse-probing technique.
clear
pp=[-35:1:35];
L=1:4000;
%--------------------Load the focused & defocused echoes
add_foc='K:\zahra\phase3-visualsonic\Data-visulasonic\Defocuse\
   tissueph-wire\Foc\';
add_def='K:\zahra\phase3-visualsonic\Data-visulasonic\Defocuse\
   tissueph-wire\';
for i=1:length(pp)
    add2_foc=[add_foc,'data',num2str(i),'_foc'];
    load(add2_foc)
    amp_raw_mean_foc(i)=max(p_raw_mean_foc(L));
    p_raw_mean_focc{i}=p_raw_mean_foc(L);
    add2_def=[add_def,'data',num2str(i),'_def'];
    load(add2_def)
    SCF_mean_def{i}=SCF_mean(L);
    amp_raw_mean_def(i)=max(p_raw_mean(L));
    p_raw_mean_deff{i}=p_raw_mean(L);
    p_scf_mean_deff{i}=SCF_mean(L).*p_raw_mean(L);
    amp_scf_mean_def(i)=max(p_scf_mean_deff{i});
    p_scf_mean_foc2{i}=SCF_mean_def{i}'.*p_raw_mean_focc{i};
    amp_scf_mean_foc2(i)=max(p_scf_mean_foc2{i});
    P_raw_mean(i,:)=p_raw_mean_focc{i};
    P_scf_mean(i,:)=p_scf_mean_foc2{i};
    clear PPP PPP2
    PPP=p_raw_mean_deff{i};
    %-----push the def to the right
    P_raw_mean_def(i,:)=[zeros(1,NN),PPP(1:length(PPP)-NN)];
    P_scf_def(i,:)=p_scf_mean_deff{i};
    SCFF(i,:)=WT2;
end
figure
plot(pp,20*log10(amp_raw_mean_foc/max(amp_raw_mean_foc)))
```

```
hold on
plot(pp,20*log10(amp_scf_mean_foc2/max(amp_scf_mean_foc2)),'g')
figure
plot(pp,20*log10(amp_raw_mean_foc/max(amp_raw_mean_foc)))
hold on
plot(pp,20*log10(amp_raw_mean_def/max(amp_raw_mean_def)),'r')
%%%%%%%%%%%%%%%%%%%%%%%%%%%%%%%%%%%%%%%%%%%%%%%%%%%%%%%%%%%%%%%%
    LOADING DEFOUCUSED RF DATA
function [p_raw,p_scf_def,amp_raw,amp_scf_def,p_raw_mean,
   p_scf_def_mean,amp_raw_mean,amp_scf_def_mean,SCF,SCF_mean,
   RF_l_mean]=main(K);
lineNumber=20;
fbase=['K:\zahra\phase3-visualsonic\Data-visulasonic\Defocuse\
   tissueph-wire\','Image',num2str(K),'ph',num2str(1),'tx']
add='K:\zahra\phase3-visualsonic\Data-visulasonic\Defocuse\
   tissueph-wire\'
ftrans_on=[];
fref=[];
fl=[fbase,num2str(1),'.iq'];
[BmodeNumLines]=RF(fl,lineNumber);
for i=1:64
    %---image 1
    fl=[fbase,num2str(i),'.iq'];
    [BmodeNumLines,RF_l_mean(i,:),Idata(i,:), Qdata(i,:),cc2,
       BmodeNumSamples2,IntFac2,fs_int2,RfData2,RFl2(i,:)]=
       RF_mean(fl,lineNumber);%--- importing IQ data
end
%-------------------------SCF processing
[p_raw_mean,p_scf_def_mean,amp_scf_def_mean,amp_raw_mean,
   SCF_mean]=SCF_cal(RF_l_mean);
%----------------
save([add,'data',num2str(K),'_def_5'],'RF_l_mean','p_raw_mean','
   p_scf_def_mean','SCF','SCF_mean','RFl2');
%%%%%%%%%%%%%%%%%%%%%%%%%%%%%%%%%%%%%%%%%%%%%%%%%%%%%%%%%%%%%%%
   LOADING FOCUSED RF DATA
function [p_raw_foc,amp_raw_foc,p_raw_mean_foc,amp_raw_mean_foc
   ]=main_foc(K);
lineNumber=20;
```

```
fbase=['K:\zahra\phase3-visualsonic\Data-visulasonic\Defocuse\
   tissueph-wire\Foc\','ImageF',num2str(K),'ph']
add='K:\zahra\phase3-visualsonic\Data-visulasonic\Defocuse\
   tissueph-wire\Foc\'
ftrans_on=[];
fref=[];
fl=[fbase,'.iq'];
[BmodeNumLines]=RF(fl,lineNumber);
[BmodeNumLines,RF_l_mean_foc,Idata, Qdata]=RF_mean(fl,lineNumber
   );
amp_raw_foc=max(RF_l_foc);
p_raw_foc=(RF_l_foc);
amp_raw_mean_foc=max(RF_l_mean_foc);
p_raw_mean_foc=(RF_l_mean_foc);
save([add,'data',num2str(K),'_foc'], 'p_raw_foc','RfData_foc','
   RF_l_foc','RF_l_mean_foc','p_raw_mean_foc');
%%%%%%%%%%%%%%%%%%%%%%%%%%%%%%%%%%%%%%%%%%%%%%%%%%%%%%%%%%%%%%
%%%%%%%%%%%%%%%%%%%%%%%%%%%%%%%%%%%%%%%%%%%%%%%%%%%%%%%%%%%%%
%The function "RF_mean.m" was developed based on "
   VsiBModeReconstructRF.m" provided by the VisuaSonics for
   importing the IQ data (not included in this appendix).
%%%%%%%%%%%%%%%%%%%%%%%%%%%%%%%%%%%%%%%%%%%%%%%%%%%%%%%%%%%%%
%%%%%%%%%%%%%%%%%%%%%%%%%%%%%%%%%%%%%%%%%%%%%%%%%%%%%%%%%%%%%%%
   CALCULATING SCF WEIGHTS FROM DEFOCUSED ECHOES
function [p_raw,p_scf_def,amp_scf_def,amp_raw,SCF]=SCF_cal(RF_l)
for i=1:64
    %--1st half
    clear v1 v2
    element(i,:)=RF_l(i,:);
    b_k(i,:)=element(i,:);
    v1=find(element(i,:)>=0);
    b_k(i,v1)=1;
    v2=find(element(i,:)<0);
    b_k(i,v2)=-1;
end
%-----SCF
sig=1-(mean(b_k)).^2;
SCF=(abs(1-sig.^(.5))).^2;
```

```
p_SCF=SCF.*sum(RF_l,1);
amp_SCF=max(abs(p_SCF));
amp_scf_def=max(abs(p_SCF));
amp_raw=max(sum(RF_l,1));
p_scf_def=p_SCF;
p_raw=(sum(RF_l,1));
%%%%%%%%%%%%%%%%%%%%%%%%%%%%%%%%%%%%%%%%%%%%%%%%%%%%%%%%%%%%%%%%%%%%%%%%
   PlOTTING THE PHASED ARRAY DATA IN PIE SHAPE
sig=P_raw_mean;
clear jj1 jj2 j1 jjj jj
fil=0;
%-----for data4
[b,a]=butter(3,.2,'low');%.2 for upsampled
for i=1:size(P_raw_mean,1)
    sig(i,1:1200)=zeros(1,1200);
    jj1(i,:)=sqrt(abs(2*filtfilt(b,a,sig(i,:).^2)));
    %----if upsampled
    j1(i,:)=resample(jj1(i,:),2,8);
end
d1=size(j1,2);
f1=fix(d1/6); %7 mm (3-9 mm)
ff2=3*f1;%--3 mm
for i=1:size(P_raw_mean,1)
    clear jjj
    jjj=[zeros(1,ff2),j1(i,:)];%--add the offset as like zeros
    jj(i,:)=(jjj);%+0+.001*randn(size(jjj,1),size(jjj,2));
    clear bb bb1
    bb=find(jjj<=0);
    jj(i,bb)=0;
end
figure
imshow(jj',[])
RFd=jj;
Ref2=jj;
x2=size(RFd,2);
x2=x2;
x1=fix(2*tan(35*pi/180)*x2);
Theta=-35:1:35;
```

```
R=1:round(sqrt(x1^2+x2^2));
x2=x2;
I=zeros(x1,x2);
I3=zeros(x1,x2);
xlim=fix(x2*tan(35*pi/(2*180)));
for i=1:x1
    i;
    for j=1:x2
        xm=(i-x1/2);
        r=((sqrt((xm).^2+(j).^2)));
        theta=(atan(xm/(j))*180/pi);
        rr(i,j)=r;
        tt(i,j)=theta;
        %---
        if ((theta)>=0 & (theta)<=35 & r<size(RFd,2))
            clear gg1 gg2
            gg1=find(r>=R);
            gg2=find(theta>=Theta);
            Lr=gg1(length(gg1));
            w1=(1-abs(R(Lr)-r));w2=(1-abs(R(Lr+1)-r));
            Lt=Theta(gg2(length(gg2)));
            Ltind=(gg2(length(gg2)));
            w3=(1-abs(Lt-theta));w4=(1-abs(Lt+1-theta));
            %             %---
            if (Lt<=35 & Lr<=x2 & j>zth)
                I2(i,j)=w1*w3*Ref2(Ltind,Lr)+ w4*w1*Ref2(Ltind
                   +1,Lr)+w3*w2*Ref2(Ltind,Lr+1)+w4*w2*Ref2(
                   Ltind+1,Lr+1);
            else
                I2(i,j)=0;
            end
        elseif (theta<=0 & theta>=-35 & r<size(RFd,2))
            clear gg1 gg2
            gg1=find(r>=R);
            gg2=find(theta>=Theta);
            Lr=gg1(length(gg1));
            w1=(1-abs(R(Lr)-r));w2=(1-abs(R(Lr+1)-r));
            Lt=Theta(gg2(length(gg2)));
```

```
            Ltind=(gg2(length(gg2)));
            w3=(1-abs(Lt-theta));w4=(1-abs(Lt+1-theta));
            %---
            if (Lt>=-35 & Lr<=x2 & j>zth)
                I2(i,j)=w1*w3*Ref2(Ltind,Lr)+ w4*w1*Ref2(Ltind
                   +1,Lr)+w3*w2*Ref2(Ltind,Lr+1)+w4*w2*Ref2(
                   Ltind+1,Lr+1);
            else
                I2(i,j)=0;
            end
        else
            I2(i,j)=0;
            I3(i,j)=-300;
        end
    end
end
clear I4
Iref=I2;
I4=I2;
I3_ref=I3;
x2=size(Iref,2);
x2=x2-ff2;
clear ggg
ggg=find(I3==0);
I3(ggg)=I4(ggg);
I3_ref(ggg)=I2(ggg);
I3=I3(:,ff2+1:size(I3,2));
I3_ref=I3_ref(:,ff2+1:size(I3_ref,2));
TS=8/512e6;
M=2.59e-3/6e-3;
I5=I3;
kkk=find(I3˜=-300);
I3_s=I3(kkk);
I5(kkk)=20*log10(I3(kkk)/max(max(I3_s)));
clear fff
fff=find(I5==-100000);
I5(fff)=min(min(I5(kkk)))-10;
I4=I5;
```

```
clear fff
fff=find(I5==-300);
I4(fff)=-50;
figure
B = imresize(real(I4), [fix(x2*0.52*2) fix(x2/2)]);
imshow(B’,[])
```

C.3 MATLAB Code For Collecting and Processing of Doppler Ultrasound Membrane Echoes (Study Three)

C.3.1 MATLAB code For Collecting the Data using Alazar Card

```
%%%%%%Part of the GUI developed for communicating with Alazar card to collect the membrane echoes.
% --- Executes on button press in Enable.
function Enable_Callback(hObject, eventdata, handles)
% hObject    handle to Enable (see GCBO)
% eventdata  reserved - to be defined in a future version of MATLAB
% handles    structure with handles and user data (see GUIDATA)
% Hint: get(hObject,'Value') returns toggle state of Enable
global Go Pau SaveData
SaveData = false;
button_state = get(hObject,'Value');
if button_state == get(hObject,'Max')
    % toggle button is pressed
    % To pass these variables to the function ctscan
    Per = str2double(get(handles.Per, 'String') )/100; % Percent - Include lines above this percent threshold
    SPR = str2double(get(handles.SPR, 'String') ); % samplesPerRecord = 800; % Multiple of 32
    SPR = 32 * round(SPR/32);
    NS = 2^(str2double(get(handles.NS, 'String') ) ); % NumSteps = 2^12; % 2^10 = 1024
    SF = 1/(str2double(get(handles.SF, 'String') ) ); % SampleFreq = 1/(500e6);
    % TD = str2double(get(handles.TD, 'String') ); % TriggerDelay = 70e-6;
    AA = str2double(get(handles.AA, 'String') ); % AcquireAfter = 1.7e-6;
    set(handles.Enable,...
        'String','STOP', ...
        'ForegroundColor', [1 0 0], ... % Red
        'BackgroundColor', [1 1 0]); % Yellow
    Go = true;
```

```
    Pau = false;
    freqq=freqq_Callback(hObject, eventdata, handles);
    np_cycle=npoint_percycle_Callback(hObject, eventdata,
       handles);
    TD=TrigGen (freqq,np_cycle);%---trigger interval (TD)(us)
    trigger_interval=TD*1e6;
    TD_Callback(hObject, eventdata, handles,trigger_interval);
    memb=memb_Callback(hObject, eventdata, handles);
    root=root_Callback(hObject, eventdata, handles);
    date=date_Callback(hObject, eventdata, handles);
    init_tek(freqq)
    ctscan(handles, Per, SPR, NS, SF, TD, AA, freqq, memb, root,
        date)
elseif button_state == get(hObject,'Min')
    % toggle button is not pressed
    set(handles.Enable,...
        'String','START', ...
        'ForegroundColor', [0 0 0], ... % Black
        'BackgroundColor', [0.753 0.753 0.753]); % Grey
    Go = false;
end
%
   %%%%%%%%%%%%%%%%%%%%%%%%%%%%%%%%%%%%%%%%%%%%%%%%%%%%%%%%%%%%%%%%%%%%%%%%%

%PART of the ctscan.m FUNCTION
function ctscan(handles, Percent, samplesPerRecord, NumSteps,
   SampleFreq, TriggerDelay, AcquireAfter,freqq,memb,root,date)
BuffersBeforeUpdate = 1;
% Load driver library
if ~libisloaded('ATSApi')
    loadlibrary('ATSApi.dll',@AlazarInclude)
    if ~libisloaded('ATSApi')
        fprintf('ATSApi.dll not loaded\n');
        return
    end
end
AlazarDefs
....
```

```
    //
....
if bufferFull
    clear data dataout dataSPL VoltsSPL
    setdatatype(bufferOut, 'uint16Ptr', 1, samplesPerBuffer);
    % Display the buffer on screen
    data =double(bufferOut.Value);
    clear bufferOut
    % Chanel A
    % Data is dumped in a long vector, break vector into matrix
       by
    % number of samples per trigger.
    data1=data(1:recordsPerBuffer*samplesPerRecord);
    dataout=reshape(data1,samplesPerRecord,recordsPerBuffer);
    clear data1
    % Chanel B
    dataSPL = (data(recordsPerBuffer*samplesPerRecord+1:
       samplesPerRecord:end)); % Pull out first datapoint of
       channel B
    clear data
    InputRange = 8; %200 mV (100mV * 2)
    VoltsSPL =((dataSPL-2^15) * InputRange) / (2^16) ; % Scaling
        factor to display in Volts, since input is -32 768 to +
       32 768
    Rtio=[6.37, 8.05  14.76  16.24  12.65  11.80  11.07  10.41
         9.78 9.84 9.78  9.32  9.67   9.47  9.41 9.73  9.78
       9.47  9.37  9.52];
    fff=100:100:2000;
    nn=find(fff==freqq);
    VoltsSPL=(VoltsSPL-mean(VoltsSPL))*Rtio(nn);
    dataRMS=(max(VoltsSPL)-min(VoltsSPL))/(2*sqrt(2));
    SPL = 20*log10((dataRMS) / (20e-6)); % Bring to dB scale, 20
        uPa = 0 dB  through amp use ->24.5
    % Make the buffer available to be filled again by the board
    retCode = calllib('ATSApi', 'AlazarPostAsyncBuffer',
       boardHandle, pbuffer, bytesPerBuffer);
    if retCode ~= ApiSuccess
```

```
    fprintf('Error: AlazarPostAsyncBuffer failed -- %s\n',
       errorToText(retCode));
    captureDone = true;
end
% Save the transfer time
transferTime_sec = toc(startTickCount);
% Abort the acquisition
retCode = calllib('ATSApi', 'AlazarAbortAsyncRead',
   boardHandle);
if retCode ~= ApiSuccess
    fprintf('Error: AlazarAbortAsyncRead failed -- %s\n',
       errorToText(retCode));
end
if (SaveData)
    time = clock;
    fl=[root,'\2012\',date,'\',memb,'_',num2str(freqq)]
    save(fl, 'dataout','VoltsSPL','freqq','memb','date','
       samplesPerRecord', 'NumSteps', 'SampleFreq', '
       TriggerDelay', 'AcquireAfter')
    SaveData = false;
    Go = false;
    clear dataout
    clear VoltsSPL
else
    % Display results
    if buffersCompleted > 0
        buffersPerSec = buffersCompleted / transferTime_sec;
    end
    [a,b] = size(dataout); % a is samples per record, after
       1 trigger event; b is number of triggers in record
    fs=1/TriggerDelay;
    Nt=recordsPerBuffer;
    Freq = linspace(0, 0.5* 1/TriggerDelay, recordsPerBuffer
       /2);
    Time = AcquireAfter:SampleFreq:(AcquireAfter+SampleFreq*
       samplesPerRecord);
    Dist = Time*1500/2; % Time * velocity of sound in water
       (1500m/s) / 2 (since wave travels twice the path)
```

```
DataFFT = zeros(a,recordsPerBuffer); % Preallocation of
   memory
Window = hanning(b);
bbbb=fir1(64,2*80/fs,'high');
for nn = 1:a
    clear n_lag
    %---------High pass
    n_lag = filtfilt(bbbb,1,dataout(nn,:));
    %----------No filter
    %n_lag=dataout(nn,:);
    DataFFT(nn,:) = fft(Window' .* n_lag);
end
F1=round(recordsPerBuffer/300); %ignore dc & 60Hz
F2=round(b/4);
length(Freq);
T1=1;
T2=a; %a
AbsDataFFT = DataFFT(T1:T2,F1:F2) .* conj(DataFFT(T1:T2,
   F1:F2));
[maxecho,maxpos]=max(dataout,[],1);
FFTecho=abs(fft(maxpos));
[maxFFTperline,l1] = max(AbsDataFFT,[],2); %finds the
   max across a row. returns the max value for each row
[maxFFT,l2] = max(maxFFTperline); %find the frequency at
    which the abs max occurs at
pline = l1(l2); %row number where the max is found
[l1,s1]=max([1,pline-1]); % To avoid it acessing out of
   bounds index
[l2,s2]=min([a,pline+1]); %
Thresh = Percent*maxFFT; %Threshold
Vector = maxFFTperline >= Thresh;
index = 0;
for nn = 1:a
    if Vector(nn)
        index = index+1;
        PowerData(index,:) = AbsDataFFT(nn,:);
    end
end
```

```
        aPowerData = mean(PowerData);
        clear PowerData
        [abcd,loc]=max(aPowerData);
        clear abcd
        subplot(3,2,4);
        cla
        imagesc([Freq(F1) Freq(F2)],[Dist(T1) Dist(T2)],abs(
           DataFFT(T1:T2,F1:F2)))
        xlabel(’Frequency, Hz’)
        ylabel(’Distance’)
        subplot(3,2,5);
        cla
        size((Dist(1:length(Dist)-1)));
        plot((Dist(1:length(Dist)-1)),(dataout))
        hold on
        plot((Dist(1:length(Dist)-1)),mean(dataout,2),’k’,’
           LineWidth’,2)
        subplot(3,2,6);
        cla
        plot(linspace(0,b*TriggerDelay,b),VoltsSPL,’.-’)
        legend([num2str(max(VoltsSPL)-min(VoltsSPL))])
        xlabel(’Time, Sec’)
        ylabel(’Volts’)
        pause(eps); % Let plots update and display
    end
end
```

C.3.2 MATLAB code For Doppler Processing of the Data

```
clear
close all
F=100;
fl=['K:\zahra\Doppler study_second PC\2012\Alazar collection\
   Doppler_meas_15Feb\16Feb\1set\BM_',num2str(F)];
load(fl);
Fs=1/(TriggerDelay*1e-6);
bb=dataout;
SPL=VoltsSPL;
sound_pa=2*max(SPL)/(2*sqrt(2)*50e-3)
InputRange = 800e-3; %(400mV * 2)
for i=1:size(bb,2)
    bb(:,i) = ((bb(:,i)-2^15) * InputRange) / (2^16) ;
end
PRF=20*F;
X=((1:size(bb,1))/500e6)*1500/2+AcquireAfter*1500/2;
figure
imagesc((1:size(bb,2)),X*1e3,bb)
xlabel('# of successive snapshots')
ylabel('Depth (mm)')
colormap('gray')
clear vv
for i=1:size(bb,1)
    lag_a=bb(i,:);
    lag_a=lag_a-mean(lag_a);
    Nt=length(lag_a);
    fs=Fs;
    clear y_a mag
    y_a = fft(lag_a,length(lag_a));
    mag =2*(abs(y_a))/(length(y_a));      %compute magnitude
    mag_a(i,:)=mag(1:((Nt/2)+1));
end
freq_a = (0:(Nt/2))*(fs/Nt);
gg=1;
gg2=length(freq_a)%find(fix(freq_a)==2001);
figure
X=((1:size(bb,1))/500e6)*1500/2+AcquireAfter*1500/2;
```

```
imagesc(freq_a(gg:gg2),X*1e3,mag_a(:,gg:gg2))
imagesc(freq_a(gg:gg2),(1:size(bb,1)),mag_a(:,gg:gg2))
xlabel('Frequency (Hz)')
ylabel('Depth (mm)')
colormap('gray')
%----------------choose RW & BM partition
clear vv
st=100;sp=400;
vv=mag_a(st:sp,:);
[p1,p2]=find(vv==max(max(vv)));
p1=p1+st-1
%---plotthe signal & fft for the highest RW point
figure
plot(st:sp,bb(st:sp,1))
hold on
plot(p1,bb(p1,1),'r*')
plot(st:sp,bb(st:sp,2),'g')
plot(st:sp,bb(st:sp,3),'m')
figure
plot(bb(p1,1:20))
sig_RW=bb(p1,:);
Nt=length(sig_RW);
fs=Fs;
clear y_a mag mag_a_sig
y_a = fft(sig_RW,length(sig_RW));
mag =2*(abs(y_a))/(length(y_a));     %compute magnitude
mag_a_sig=mag(1:((Nt/2)+1));
freq_a = (0:(Nt/2))*(fs/Nt);
figure(10)
plot(freq_a,mag_a_sig)
title('FFT of RW')
clear g1 ppp
g1=find(abs(freq_a-F)<=25);
ppp=find((mag_a_sig(g1))==max(mag_a_sig(g1)));
freq_a(g1);
max(mag_a_sig(g1));
mg_ff=2*max(mag_a_sig(g1));%--pk-pk
fu=45e6;
```

```
delta_t_RW=mg_ff/(2*pi*fu);
disp_RW=delta_t_RW*1500*1e6/2
title(['Max=',num2str(max(mag_a_sig(g1)))])
%-----------Filter vibration for phase
% % %-----FIR
Fn=freq_a(g1(ppp));
b=fir1(505,2*[Fn-5,Fn+5]/Fs);
y_filt1_RW = filtfilt(b,1,sig_RW);
y_filt1_RW=y_filt1_RW*-1;
%---
Nt=length(y_filt1_RW);
fs=Fs;
y = fft(y_filt1_RW,length(y_filt1_RW));
mag =2*(abs(y))/(length(y));                      %compute
   magnitude
freq = (0:(Nt/2))*(fs/Nt);               %compute discrete freq.
    range
figure(10)
hold on
plot(freq,mag(1:((Nt/2)+1)),'g')
%-----------------------BM
clear vv
st=550;sp=750;
vv=mag_a(st:sp,:);
[p1,p2]=find(vv==max(max(vv)));
p1=p1+st-1
%---plotthe signal & fft for the highest RW point
sig_BM=bb(p1,:);
Nt=length(sig_BM);
fs=Fs;
clear y_a mag mag_a_sig
y_a = fft(sig_BM,length(sig_BM));
mag =2*(abs(y_a))/(length(y_a));     %compute magnitude
mag_a_sig=mag(1:((Nt/2)+1));
freq_a = (0:(Nt/2))*(fs/Nt);
figure(12)
plot(freq_a,mag_a_sig)
title('FFT of BM')
```

```
clear g1 ppp
g1=find(abs(freq_a-F)<=15);
ppp=find((mag_a_sig(g1))==max(mag_a_sig(g1)));
max(mag_a_sig(g1));
mg_ff=2*max(mag_a_sig(g1));%--pk-pk
fu=45e6;
delta_t_BM=mg_ff/(2*pi*fu);
disp_BM=delta_t_BM*1500*1e6/2
title(['Max=',num2str(max(mag_a_sig(g1)))])
%-----------FIlter vibration for phase
% % %-----FIR
Fn=freq_a(g1(ppp));
b=fir1(505,2*[Fn-5,Fn+5]/Fs);
y_filt1_BM = filtfilt(b,1,sig_BM);
%---
Nt=length(y_filt1_BM);
fs=Fs;
y = fft(y_filt1_BM,length(y_filt1_BM));
mag =2*(abs(y))/(length(y));                      %compute
   magnitude
freq = (0:(Nt/2))*(fs/Nt);               %compute discrete freq.
    range
figure(12)
hold on
plot(freq,mag(1:((Nt/2)+1)),'g')
%-------------------SPl
%----SPL
figure(13)
plot(SPL)
title('sound pressure')
y_a = fft(SPL,length(SPL));
clear mag
mag =2*(abs(y_a))/(length(y_a));     %compute magnitude
mag_SPL=mag(1:((Nt/2)+1));
figure(14)
plot(freq_a,mag_SPL)
title('FFT of sound pressure')
clear g1 ppp
```

```
g1=find(abs(freq_a-F)<=15);
ppp=find((mag_SPL(g1))==max(mag_SPL(g1)));
Fn=freq_a(g1(ppp));
b=fir1(505,2*[Fn-5,Fn+5]/Fs);
y_SPL = filtfilt(b,1,SPL);
figure(13)
hold on
plot(y_SPL,'g')
title('Filtered SPL')
y_a_SPL = fft(y_SPL,length(y_SPL));
clear mag
mag =2*(abs(y_a_SPL))/(length(y_a_SPL));     %compute magnitude
mag_SPL2=mag(1:((Nt/2)+1));
figure(14)
hold on
plot(freq_a,mag_SPL2,'g')
%--------------------------Phase
k=fix(Fs/F);
for i=1:fix(length(y_filt1_RW)/k)
    % figure(20)
   clear ss l gg h1 h2
    h1=y_SPL((i-1)*k+1:min([i*k, length(y_SPL)]))';
    h2=y_filt1_RW((i-1)*k+1:min([i*k, length(y_filt1_RW)]));
    %---Mine;
    [ss,l]=xcorr(h2,h1);
    gg=find(ss==max(ss));
    L2(i)=l(gg);
    ph2(i)=l(gg)*F*360/Fs;
end
L2;
clear cc
cc=find(L2<=0);
L2(cc)=L2(cc)+k;
mode(abs(L2(5:length(L2)-1)));
ph_RW=mode(abs(L2(5:length(L2)-1)))*F*360/Fs
%
   -----------------------------------------------------------------
    Ph_BM
```

```
for i=1:fix(length(y_filt1_BM)/k)
    clear ss l gg h1 h2
    h1=y_SPL((i-1)*k+1:min([i*k, length(y_SPL)]))’;
    h2=y_filt1_BM((i-1)*k+1:min([i*k, length(y_filt1_BM)]));
   %---Mine;
    [ss,l]=xcorr(h2,h1);
    gg=find(ss==max(ss));
    L2_BM(i)=l(gg);
    ph2_BM(i)=l(gg)*F*360/Fs;
end
L2_BM;
clear cc
cc=find(L2_BM<=0);
L2_BM(cc)=L2_BM(cc)+k;
mode(abs(L2_BM(5:length(L2_BM)-1)));
ph_BM=mode(abs(L2_BM(5:length(L2_BM)-1)))*F*360/Fs
figure
plot(y_SPL/50)
hold on
plot(y_filt1_RW,’r’)
plot(y_filt1_BM,’g’)
legend(’SPL’,’RW’,’BM’)
```

APPENDIX D

COPYRIGHT PERMISSION LETTERS

D.1 Publications

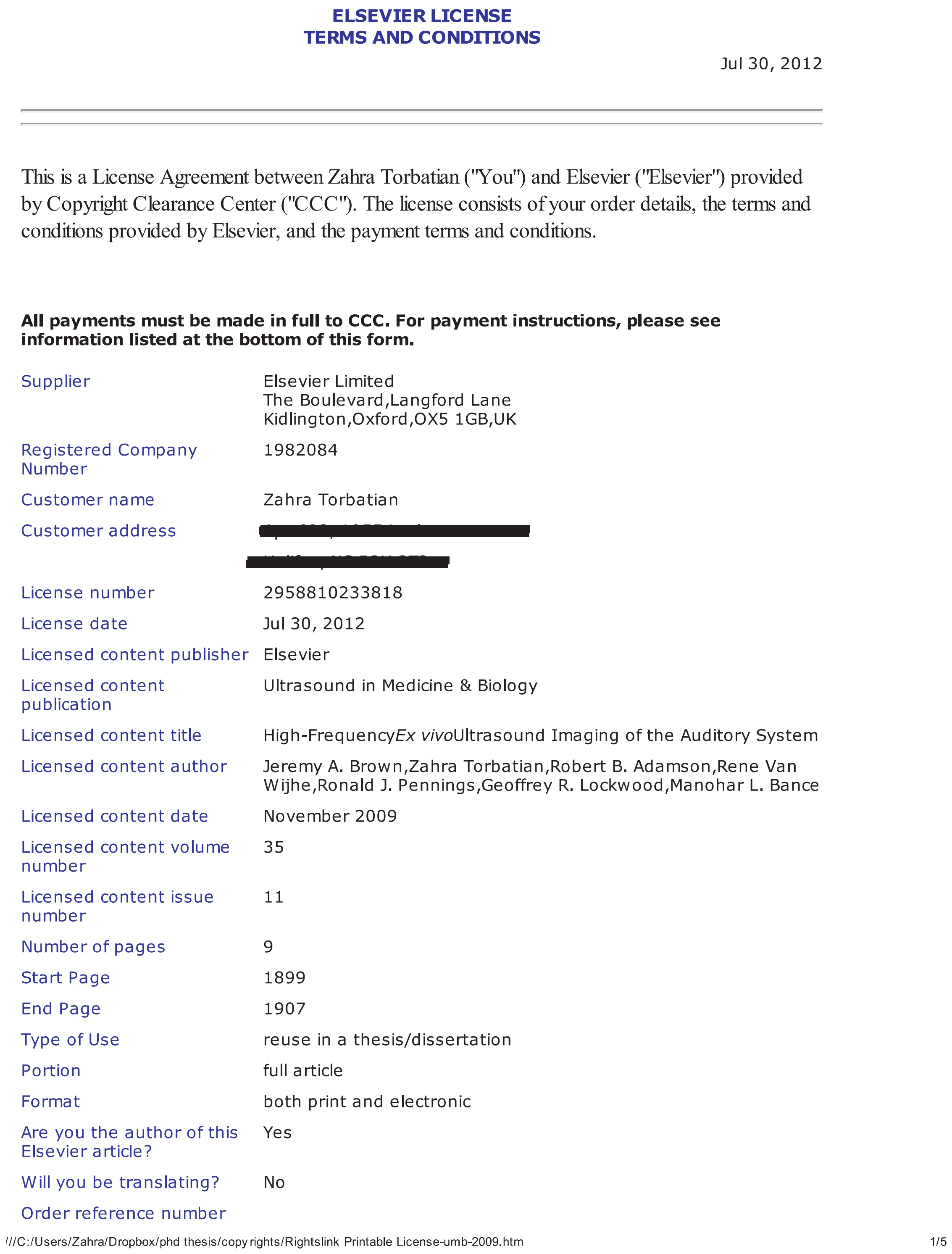

ELSEVIER LICENSE
TERMS AND CONDITIONS

Jul 30, 2012

This is a License Agreement between Zahra Torbatian ("You") and Elsevier ("Elsevier") provided by Copyright Clearance Center ("CCC"). The license consists of your order details, the terms and conditions provided by Elsevier, and the payment terms and conditions.

All payments must be made in full to CCC. For payment instructions, please see information listed at the bottom of this form.

Supplier	Elsevier Limited The Boulevard,Langford Lane Kidlington,Oxford,OX5 1GB,UK
Registered Company Number	1982084
Customer name	Zahra Torbatian
Customer address	[redacted]
License number	2958810233818
License date	Jul 30, 2012
Licensed content publisher	Elsevier
Licensed content publication	Ultrasound in Medicine & Biology
Licensed content title	High-Frequency*Ex vivo*Ultrasound Imaging of the Auditory System
Licensed content author	Jeremy A. Brown,Zahra Torbatian,Robert B. Adamson,Rene Van Wijhe,Ronald J. Pennings,Geoffrey R. Lockwood,Manohar L. Bance
Licensed content date	November 2009
Licensed content volume number	35
Licensed content issue number	11
Number of pages	9
Start Page	1899
End Page	1907
Type of Use	reuse in a thesis/dissertation
Portion	full article
Format	both print and electronic
Are you the author of this Elsevier article?	Yes
Will you be translating?	No
Order reference number	

Title of your thesis/dissertation	High-frequency Ultrasound Imaging of the Auditory System
Expected completion date	Oct 2012
Estimated size (number of pages)	200
Elsevier VAT number	GB 494 6272 12
Permissions price	0.00 USD
VAT/Local Sales Tax	0.00 USD / GBP
Total	0.00 USD
Terms and Conditions	

INTRODUCTION

1. The publisher for this copyrighted material is Elsevier. By clicking "accept" in connection with completing this licensing transaction, you agree that the following terms and conditions apply to this transaction (along with the Billing and Payment terms and conditions established by Copyright Clearance Center, Inc. ("CCC"), at the time that you opened your Rightslink account and that are available at any time at http://myaccount.copyright.com).

GENERAL TERMS

2. Elsevier hereby grants you permission to reproduce the aforementioned material subject to the terms and conditions indicated.

3. Acknowledgement: If any part of the material to be used (for example, figures) has appeared in our publication with credit or acknowledgement to another source, permission must also be sought from that source. If such permission is not obtained then that material may not be included in your publication/copies. Suitable acknowledgement to the source must be made, either as a footnote or in a reference list at the end of your publication, as follows:

“Reprinted from Publication title, Vol /edition number, Author(s), Title of article / title of chapter, Pages No., Copyright (Year), with permission from Elsevier [OR APPLICABLE SOCIETY COPYRIGHT OWNER].” Also Lancet special credit - “Reprinted from The Lancet, Vol. number, Author(s), Title of article, Pages No., Copyright (Year), with permission from Elsevier.”

4. Reproduction of this material is confined to the purpose and/or media for which permission is hereby given.

5. Altering/Modifying Material: Not Permitted. However figures and illustrations may be altered/adapted minimally to serve your work. Any other abbreviations, additions, deletions and/or any other alterations shall be made only with prior written authorization of Elsevier Ltd. (Please contact Elsevier at permissions@elsevier.com)

6. If the permission fee for the requested use of our material is waived in this instance, please be advised that your future requests for Elsevier materials may attract a fee.

Copyright
Clearance
Center

RightsLink®

Home | Create Account | Help

IEEE
Requesting permission to reuse content from an IEEE publication

Title:	Imaging the auditory system: A new application of high-frequency ultrasound
Conference Proceedings:	Ultrasonics Symposium (IUS), 2009 IEEE International
Author:	Torbatian, Z.; Adamson, R.; van Wijhe, R.; Pennings, R.; Bance, M.; Brown, J.
Publisher:	IEEE
Date:	20-23 Sept. 2009

User ID

Password

☐ Enable Auto Login

LOGIN

Forgot Password/User ID?

If you're a copyright.com user, you can login to RightsLink using your copyright.com credentials. Already **a RightsLink user** or want to learn more?

Thesis / Dissertation Reuse

The IEEE does not require individuals working on a thesis to obtain a formal reuse license, however, you may print out this statement to be used as a permission grant:

Requirements to be followed when using any portion (e.g., figure, graph, table, or textual material) of an IEEE copyrighted paper in a thesis:

1) In the case of textual material (e.g., using short quotes or referring to the work within these papers) users must give full credit to the original source (author, paper, publication) followed by the IEEE copyright line © 2011 IEEE.
2) In the case of illustrations or tabular material, we require that the copyright line © [Year of original publication] IEEE appear prominently with each reprinted figure and/or table.
3) If a substantial portion of the original paper is to be used, and if you are not the senior author, also obtain the senior author's approval.

Requirements to be followed when using an entire IEEE copyrighted paper in a thesis:

1) The following IEEE copyright/ credit notice should be placed prominently in the references: © [year of original publication] IEEE. Reprinted, with permission, from [author names, paper title, IEEE publication title, and month/year of publication]
2) Only the accepted version of an IEEE copyrighted paper can be used when posting the paper or your thesis on-line.
3) In placing the thesis on the author's university website, please display the following message in a prominent place on the website: In reference to IEEE copyrighted material which is used with permission in this thesis, the IEEE does not endorse any of [university/educational entity's name goes here]'s products or services. Internal or personal use of this material is permitted. If interested in reprinting/republishing IEEE copyrighted material for advertising or promotional purposes or for creating new collective works for resale or redistribution, please go to http://www.ieee.org/publications_standards/publications/rights/rights_link.html to learn how to obtain a License from RightsLink.

If applicable, University Microfilms and/or ProQuest Library, or the Archives of Canada may supply single copies of the dissertation.

BACK | CLOSE WINDOW

Copyright Clearance Center RightsLink®

Home Create Account Help

IEEE Requesting permission to reuse content from an IEEE publication

Title: A split-aperture transmit beamforming technique with phase coherence grating lobe suppression
Author: Torbatian, Z.; Adamson, R.; Bance, M.; Brown, J.A.
Publication: Ultrasonics, Ferroelectrics and Frequency Control, IEEE Transactions on
Publisher: IEEE
Date: November 2010

User ID
Password
☐ Enable Auto Login
LOGIN
Forgot Password/User ID?
If you're a copyright.com user, you can login to RightsLink using your copyright.com credentials. Already **a RightsLink user** or want to learn more?

Thesis / Dissertation Reuse

The IEEE does not require individuals working on a thesis to obtain a formal reuse license, however, you may print out this statement to be used as a permission grant:

Requirements to be followed when using any portion (e.g., figure, graph, table, or textual material) of an IEEE copyrighted paper in a thesis:

1) In the case of textual material (e.g., using short quotes or referring to the work within these papers) users must give full credit to the original source (author, paper, publication) followed by the IEEE copyright line © 2011 IEEE.
2) In the case of illustrations or tabular material, we require that the copyright line © [Year of original publication] IEEE appear prominently with each reprinted figure and/or table.
3) If a substantial portion of the original paper is to be used, and if you are not the senior author, also obtain the senior author's approval.

Requirements to be followed when using an entire IEEE copyrighted paper in a thesis:

1) The following IEEE copyright/ credit notice should be placed prominently in the references: © [year of original publication] IEEE. Reprinted, with permission, from [author names, paper title, IEEE publication title, and month/year of publication]
2) Only the accepted version of an IEEE copyrighted paper can be used when posting the paper or your thesis on-line.
3) In placing the thesis on the author's university website, please display the following message in a prominent place on the website: In reference to IEEE copyrighted material which is used with permission in this thesis, the IEEE does not endorse any of [university/educational entity's name goes here]'s products or services. Internal or personal use of this material is permitted. If interested in reprinting/republishing IEEE copyrighted material for advertising or promotional purposes or for creating new collective works for resale or redistribution, please go to http://www.ieee.org/publications_standards/publications/rights/rights_link.html to learn how to obtain a License from RightsLink.

If applicable, University Microfilms and/or ProQuest Library, or the Archives of Canada may supply single copies of the dissertation.

BACK CLOSE WINDOW

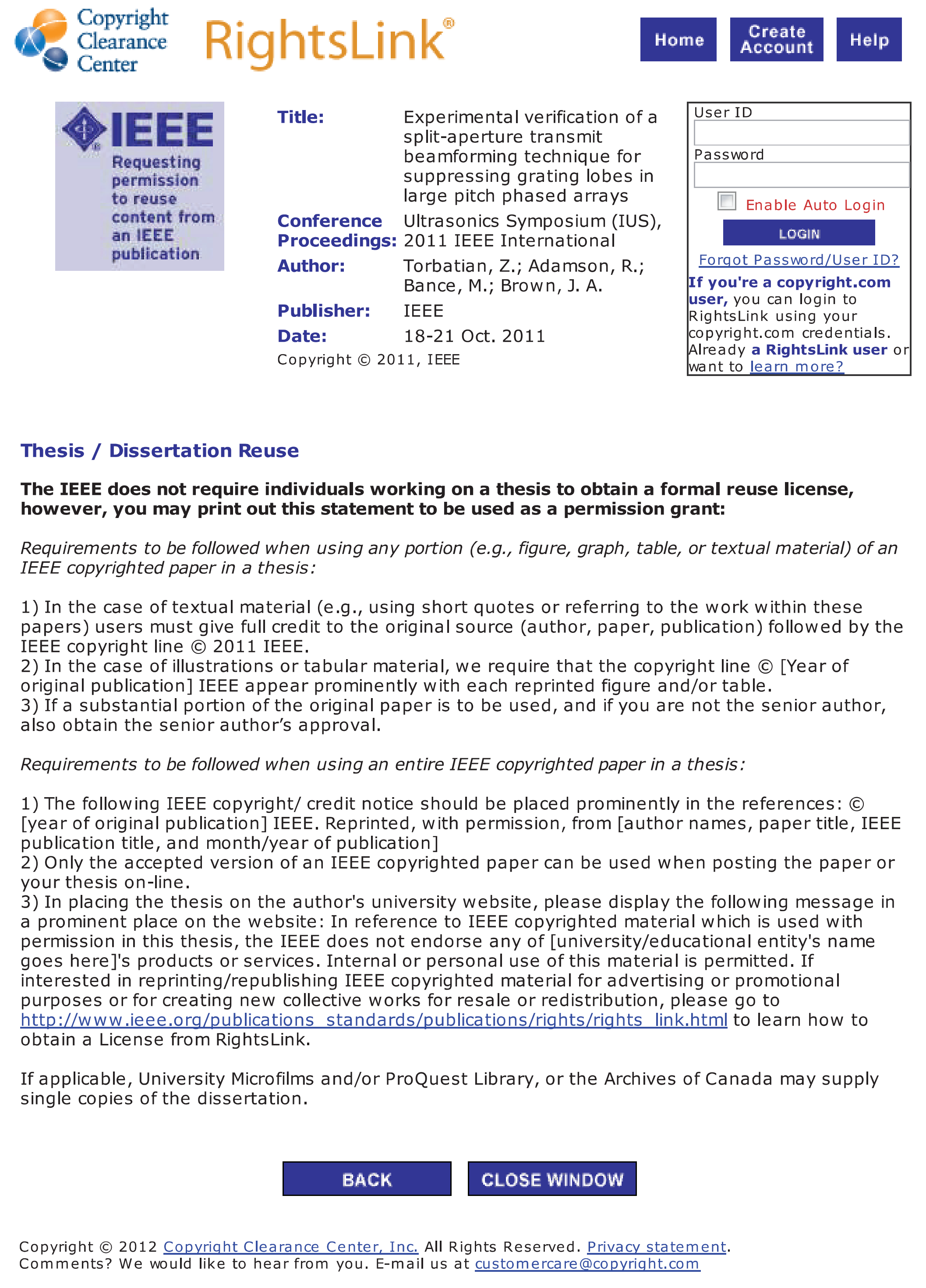

Title: Experimental verification of a split-aperture transmit beamforming technique for suppressing grating lobes in large pitch phased arrays

Conference Proceedings: Ultrasonics Symposium (IUS), 2011 IEEE International

Author: Torbatian, Z.; Adamson, R.; Bance, M.; Brown, J. A.

Publisher: IEEE

Date: 18-21 Oct. 2011

Copyright © 2011, IEEE

If you're a copyright.com user, you can login to RightsLink using your copyright.com credentials. Already **a RightsLink user** or want to learn more?

Thesis / Dissertation Reuse

The IEEE does not require individuals working on a thesis to obtain a formal reuse license, however, you may print out this statement to be used as a permission grant:

Requirements to be followed when using any portion (e.g., figure, graph, table, or textual material) of an IEEE copyrighted paper in a thesis:

1) In the case of textual material (e.g., using short quotes or referring to the work within these papers) users must give full credit to the original source (author, paper, publication) followed by the IEEE copyright line © 2011 IEEE.
2) In the case of illustrations or tabular material, we require that the copyright line © [Year of original publication] IEEE appear prominently with each reprinted figure and/or table.
3) If a substantial portion of the original paper is to be used, and if you are not the senior author, also obtain the senior author's approval.

Requirements to be followed when using an entire IEEE copyrighted paper in a thesis:

1) The following IEEE copyright/ credit notice should be placed prominently in the references: © [year of original publication] IEEE. Reprinted, with permission, from [author names, paper title, IEEE publication title, and month/year of publication]
2) Only the accepted version of an IEEE copyrighted paper can be used when posting the paper or your thesis on-line.
3) In placing the thesis on the author's university website, please display the following message in a prominent place on the website: In reference to IEEE copyrighted material which is used with permission in this thesis, the IEEE does not endorse any of [university/educational entity's name goes here]'s products or services. Internal or personal use of this material is permitted. If interested in reprinting/republishing IEEE copyrighted material for advertising or promotional purposes or for creating new collective works for resale or redistribution, please go to http://www.ieee.org/publications_standards/publications/rights/rights_link.html to learn how to obtain a License from RightsLink.

If applicable, University Microfilms and/or ProQuest Library, or the Archives of Canada may supply single copies of the dissertation.

Request for reprint permission

Z T [redacted] Wed, Jul 4, 2012 at 3:01 P
To: reprint_permission@spie.org

Dear Sir/Madam,

I am preparing my PhD thesis for submission to the Faculty of Graduate Studies at Dalhousie University, Halifax, Nova Scotia, Canada. I am seeking your permission to include a manuscript version of the following paper(s) as a chapter in the thesis:

Transmit beamforming techniques for suppressing grating lobes in large pitch ultrasonic phased arrays

Torbatian, Zahra; Adamson, Rob; Bance, Manohar; Brown, Jeremy A.

Medical Imaging 2011: Ultrasonic Imaging, Tomography, and Therapy. Edited by D'Hooge, Jan; Doyley, Marvin M. Proceedings of the SPIE, Volume 7968, pp. 79680R-79680R-8 (2011).

Canadian graduate theses are reproduced by the Library and Archives of Canada (formerly National Library of Canada) through a non-exclusive, world-wide license to reproduce, loan, distribute, or sell theses. I am also seeking your permission for the material described above to be reproduced and distributed by the LAC(NLC). Further details about the LAC(NLC) thesis program are available on the LAC(NLC) website (www.nlc-bnc.ca).
Full publication details and a copy of this permission letter will be included in the thesis.

Yours sincerely,

Zahra Torbatian

Scott McNeill <scottm@spie.org> Wed, Jul 11, 2012 at 12:26 P
To: Z T [redacted]

Dear Zahra Torbatian,

Thank you for seeking permission from SPIE to reprint material from our publications. As an author of the cited work, you retain co-owner rights to the original content therein. Publisher's permission is hereby granted under the following conditions: (1) the material to be used has appeared in our publication without credit or acknowledgment to another source; and (2) you credit the original SPIE publication. Include the authors' names, title of paper, volume title, SPIE volume number, and year of publication in your credit statement.

Sincerely,

Scott McNeill for

Eric Pepper, Director of Publications

SPIE

P.O. Box 10, Bellingham WA 98227-0010 USA

360/676-3290 (Pacific Time) eric@spie.org

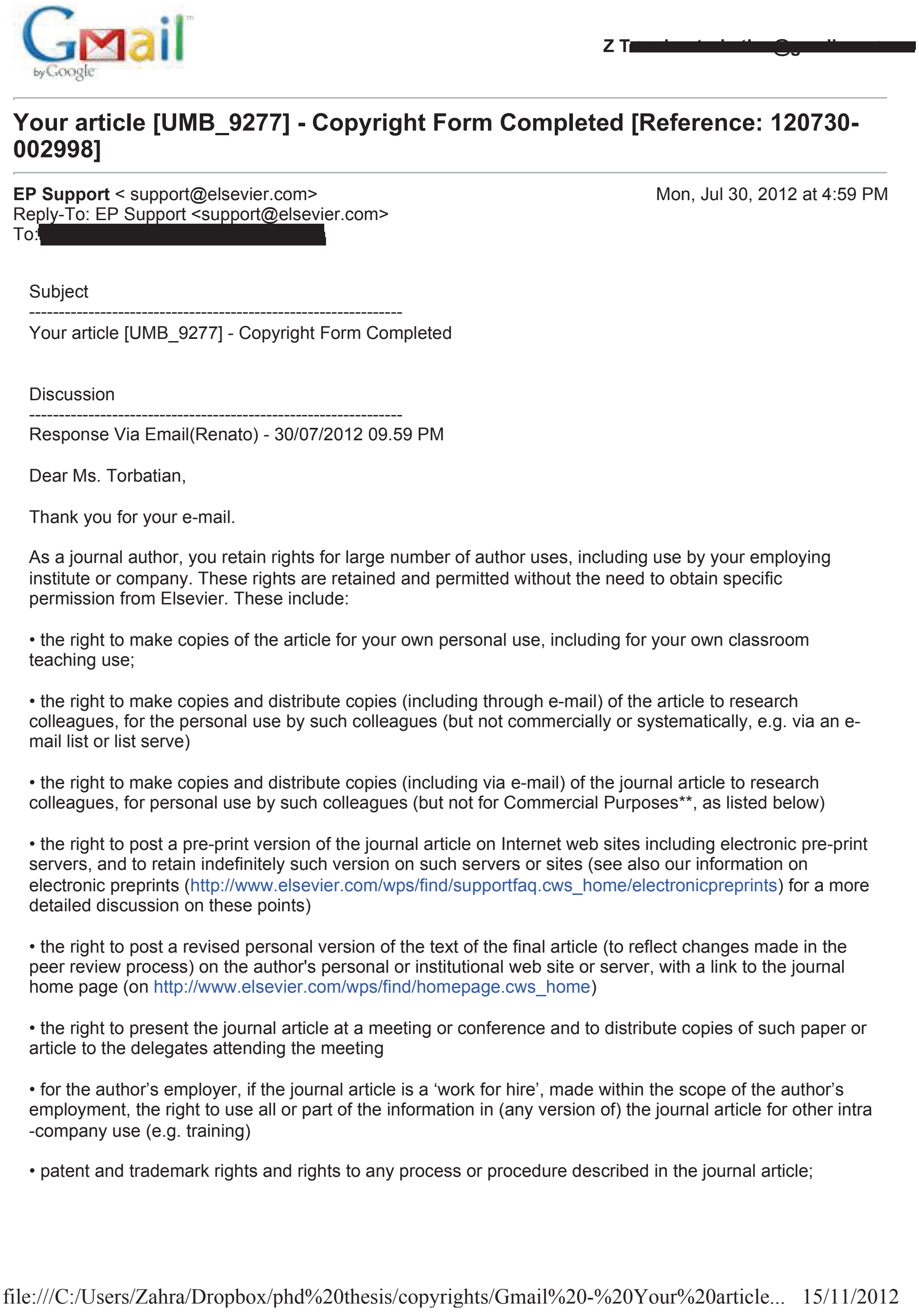

Z T[redacted]

Your article [UMB_9277] - Copyright Form Completed [Reference: 120730-002998]

EP Support < support@elsevier.com> Mon, Jul 30, 2012 at 4:59 PM
Reply-To: EP Support <support@elsevier.com>
To:[redacted]

Subject

Your article [UMB_9277] - Copyright Form Completed

Discussion

Response Via Email(Renato) - 30/07/2012 09.59 PM

Dear Ms. Torbatian,

Thank you for your e-mail.

As a journal author, you retain rights for large number of author uses, including use by your employing institute or company. These rights are retained and permitted without the need to obtain specific permission from Elsevier. These include:

• the right to make copies of the article for your own personal use, including for your own classroom teaching use;

• the right to make copies and distribute copies (including through e-mail) of the article to research colleagues, for the personal use by such colleagues (but not commercially or systematically, e.g. via an e-mail list or list serve)

• the right to make copies and distribute copies (including via e-mail) of the journal article to research colleagues, for personal use by such colleagues (but not for Commercial Purposes**, as listed below)

• the right to post a pre-print version of the journal article on Internet web sites including electronic pre-print servers, and to retain indefinitely such version on such servers or sites (see also our information on electronic preprints (http://www.elsevier.com/wps/find/supportfaq.cws_home/electronicpreprints) for a more detailed discussion on these points)

• the right to post a revised personal version of the text of the final article (to reflect changes made in the peer review process) on the author's personal or institutional web site or server, with a link to the journal home page (on http://www.elsevier.com/wps/find/homepage.cws_home)

• the right to present the journal article at a meeting or conference and to distribute copies of such paper or article to the delegates attending the meeting

• for the author's employer, if the journal article is a 'work for hire', made within the scope of the author's employment, the right to use all or part of the information in (any version of) the journal article for other intra-company use (e.g. training)

• patent and trademark rights and rights to any process or procedure described in the journal article;

file:///C:/Users/Zahra/Dropbox/phd%20thesis/copyrights/Gmail%20-%20Your%20article... 15/11/2012

- the right to include the journal article, in full or in part, in a thesis or dissertation;

- the right to include the article in full or in part in a thesis or dissertation (provided that this is not to be published commercially)

- the right to use the article or any part there of in a printed compilation of works of the author, such as collected writings or lecture notes (subsequent to publication of the article in the journal)

- the right to prepare other derivative works, to extend the article into book-length form, or to otherwise re-use portions or excerpts in other works, with full acknowledgement of its original publication in the journal.

Other uses by authors should be authorized by Elsevier through the Global Rights Department, and journal authors are encouraged to let Elsevier know of any particular needs or requirements:

http://www.elsevier.com/wps/find/supportfaq.cws_home/permissionusematerial

To learn more about Author's rights please go to:

http://www.elsevier.com/wps/find/authorsview.authors/copyright#whatrights

You may find the following solution from our support and help site of interest:

http://support.elsevier.com/app/answers/detail/a_id/565

If responding to this e-mail, please ensure that the reference number remains in the subject line.

Should you have any additional questions or concerns, please visit our self-help site at: http://support.elsevier.com/. Here you will be able to search for solutions on a range of topics, find answers to frequently asked questions and learn more about EES via interactive tutorials. You will also find our 24/7 support contact details should you need further assistance from one of our customer service representatives.

Yours sincerely,

Renato Madriaga

Elsevier Customer Support

……………………………………………………
Customer By Email (Zahra Torbatian) - 30/07/2012 04.01 PM

Hello,

I want to use this article (UMB9277) as a chapter in my PhD thesis. I
completed a permission form online but since this article is
not published yet, I was wondering if it is the right way to do.

Thanks,
Zahra

On Mon, Jul 30, 2012 at 10:37 AM, Author Services <support@elsevier.com>wrote:

>
> Article title: Listening to the Cochlea with High-Frequency Ultrasound
> Reference: UMB9277
> Journal title: Ultrasound in Medicine & Biology
> Corresponding author: Ms. Zahra Torbatian

Zahra T <

Re: Fwd: Seeking reprint permission-urgent

j.hansson@ieee.org <j.hansson@ieee.org> Tue, Nov 20, 2012 at 3:19 PM
Reply-To: Copyrights@ieee.org
To: Zahra T

Comments/Response to Case ID: **005E4B76**

ReplyTo: Copyrights@ieee.org

From: Jacqueline Hansson	**Date:** 11/20/2012
Subject: Re: Fwd: Seeking reprint permission-urgent	**Send To:** Zahra T
	cc:

Dear Zahra Torbatian :

The IEEE does not require individuals working on a thesis to obtain a formal reuse license, but a statement that can be used as a permission grant can be obtained by going to RightsLink. However, since an IEEE copyrighted paper that you're requesting doesn't appear in Xplore yet, you may print out this statement to be used as a permission grant: At the end of this letter will be instructions as to how to go to RightsLInk in the future for your IEEE copyrighted material reuse needs.

Requirements to be followed when using any portion (e.g., figure, graph, table, or textual material) of an IEEE copyrighted paper in a thesis:

1) In the case of textual material (e.g., using short quotes or referring to the work within these papers) users must give full credit to the original source (author, paper, publication) followed by the IEEE copyright line ©© [year of original publication] IEEE.

2) In the case of illustrations or tabular material, we require that the copyright line © 2012 IEEE appear prominently with each reprinted figure and/or table

3) If you expect to use a substantial portion of the original paper, and if you are not the senior author, please obtain the senior author's approval.

Requirements to be followed when using an entire IEEE copyrighted paper in a thesis:

1) The following IEEE copyright/ credit notice should be placed prominently in the references: © 2012 IEEE. Reprinted, with permission, from [author names, paper title, IEEE publication title, and month/year of publication]

2) The published version of an IEEE copyrighted paper can be used when posting the paper or your thesis on-line.

3) In placing the thesis on the author's university website, please display the following message in a prominent place on the website: In reference to IEEE copyrighted material which is used with permission in this thesis, the IEEE does not endorse any of [university/educational entity's name goes here]'s products or services. Internal or personal use of this material is permitted. If interested in reprinting/republishing IEEE copyrighted material for advertising or promotional purposes or for creating new collective works for resale or redistribution, please go to http://www.ieee.org/publications_standards/publications/rights/rights_link.html to learn how to obtain a License from RightsLink.

If applicable, University Microfilms and/or ProQuest Library, or the Archives of Canada may supply single copies of the

In regards to future requests for IEEE copyrighted material, the IEEE has recently implemented a policy that provides an automated means for handling reuse permission of IEEE content through the Copyright Clearance Center RightsLink permission service. You can facilitate this process by taking the steps provided below for any IEEE copyrighted material that can be found in IEEE Xplore. . Should assistance be needed with this new service, users are encouraged to contact the Copyright Customer Care staff at CustomerCare@copyright.com provided by the Copyright Clearance Center. If you still have further questions after your contact with the Copyright Customer Care staff, please contact Nancy A. Blair-DeLeon, Senior Program Manager, n.blair-deleon@ieee.org

1. Go to http://ieeexplore.ieee.org/Xplore/guesthome.jsp
2. Type the title of the IEEE copyrighted paper into the IEEE Xplore Search Bar and click on the word "Search" .
3. Click on the underlined IEEE copyrighted paper's title that's in orange and blue print.
4. The title will appear again in orange print under the empty Search bar..
5. Next, click on the orange “Request Permissions” link, which can be found under the IEEE paper title and above the Abstract area.
6. Create a RightsLink account, if you don't already have one.
6. When you reach the "Welcome to RightLink page, begin to make your selections. If the reuse is not for the author's personal use or for the author's employer's use, then "I am a author of this content" doesn't apply and one of the other phrases should be selected, since the IEEE copyrighted material is being reused by a third party.
7. Continue the process to obtain permission for any material desired from each additional IEEE copyrighted paper.

Sincerely,

Jacqueline Hansson, Coordinator
IEEE Intellectual Property Rights Office
445 Hoes Lane
Piscataway, NJ 08855-1331 USA
+1 732 562 3828 (phone)
+1 732 562 1746(fax)
e-mail: j.hansson@ieee.org
IEEE Fostering technological innovation
and excellence for the benefit of humanity.

©©©©©©©©©©©©©©©©©©©©©©©©©©©©©©

---------- Forwarded message ----------
From: **Zahra T**
Date: Mon, Nov 19, 2012 at 12:02 PM
Subject: Seeking reprint permission-urgent
To: pubs-permissions@ieee.org

Dear Sir/Madam,

I am preparing my PhD thesis for submission to the Faculty of Graduate Studies at Dalhousie University, Halifax, Nova Scotia, Canada. I am seeking the permission to include the following paper (which is going to be published in IEEE) as part of a chapter in my thesis. I am the first author of this paper.

Z. Torbatian, R. Adamson, J. Brown "A Virtual Point Source Pulse Probing Technique for Suppressing Grating Lobes in Large Pitch Phased Arrays", IEEE International Ultrasonics Symposium, 2012.

I have a deadline to hand in my thesis by Wednesday (21 st Dec.).

D.2 Figures

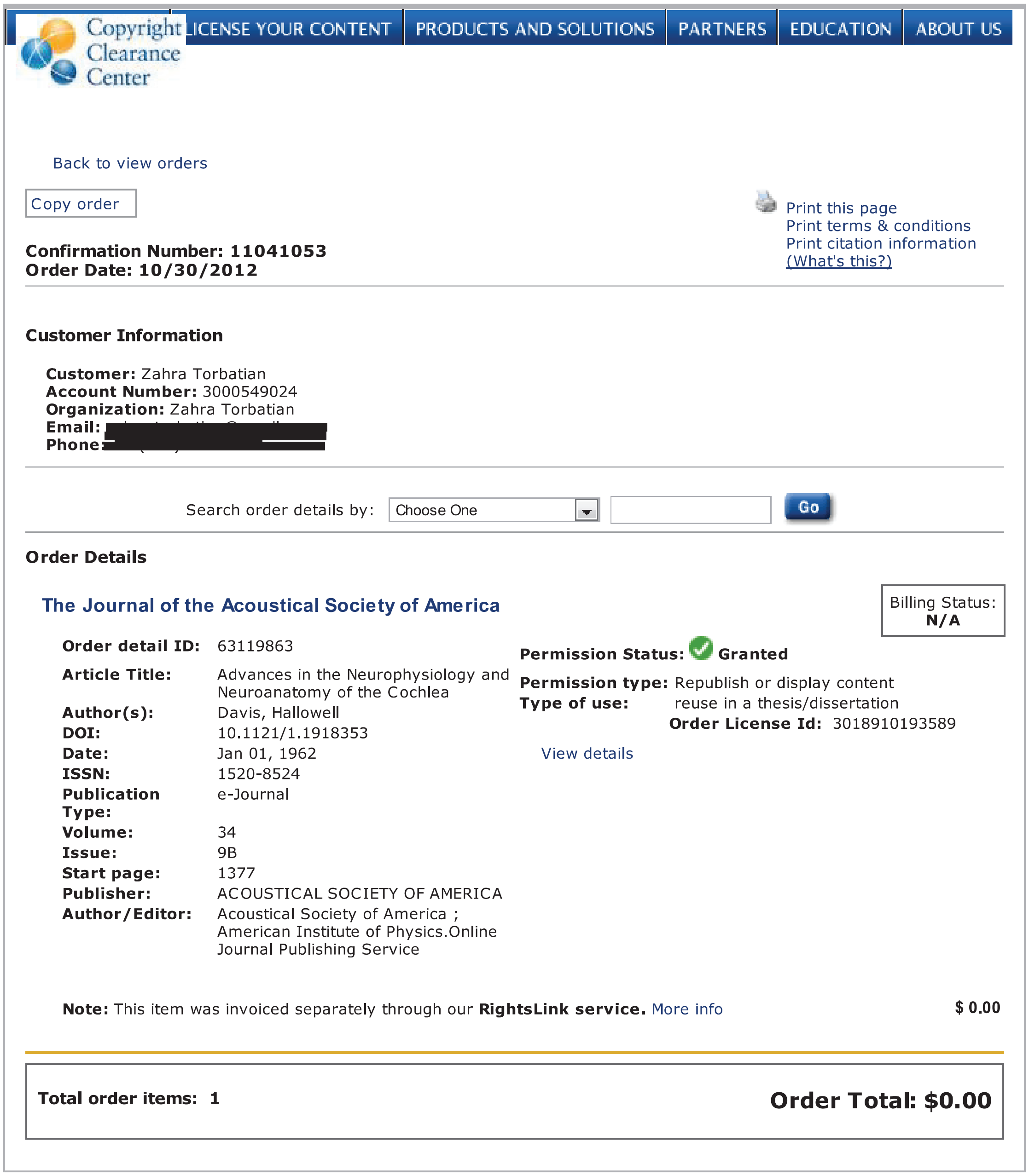

Confirmation Number: 11041053
Order Date: 10/30/2012

Customer Information

Customer: Zahra Torbatian
Account Number: 3000549024
Organization: Zahra Torbatian
Email: [redacted]
Phone: [redacted]

Order Details

The Journal of the Acoustical Society of America

Billing Status: **N/A**

Order detail ID:	63119863
Article Title:	Advances in the Neurophysiology and Neuroanatomy of the Cochlea
Author(s):	Davis, Hallowell
DOI:	10.1121/1.1918353
Date:	Jan 01, 1962
ISSN:	1520-8524
Publication Type:	e-Journal
Volume:	34
Issue:	9B
Start page:	1377
Publisher:	ACOUSTICAL SOCIETY OF AMERICA
Author/Editor:	Acoustical Society of America ; American Institute of Physics.Online Journal Publishing Service

Permission Status: ✓ **Granted**

Permission type: Republish or display content
Type of use: reuse in a thesis/dissertation
Order License Id: 3018910193589

Note: This item was invoiced separately through our **RightsLink service.** More info $ 0.00

Total order items: 1 **Order Total: $0.00**

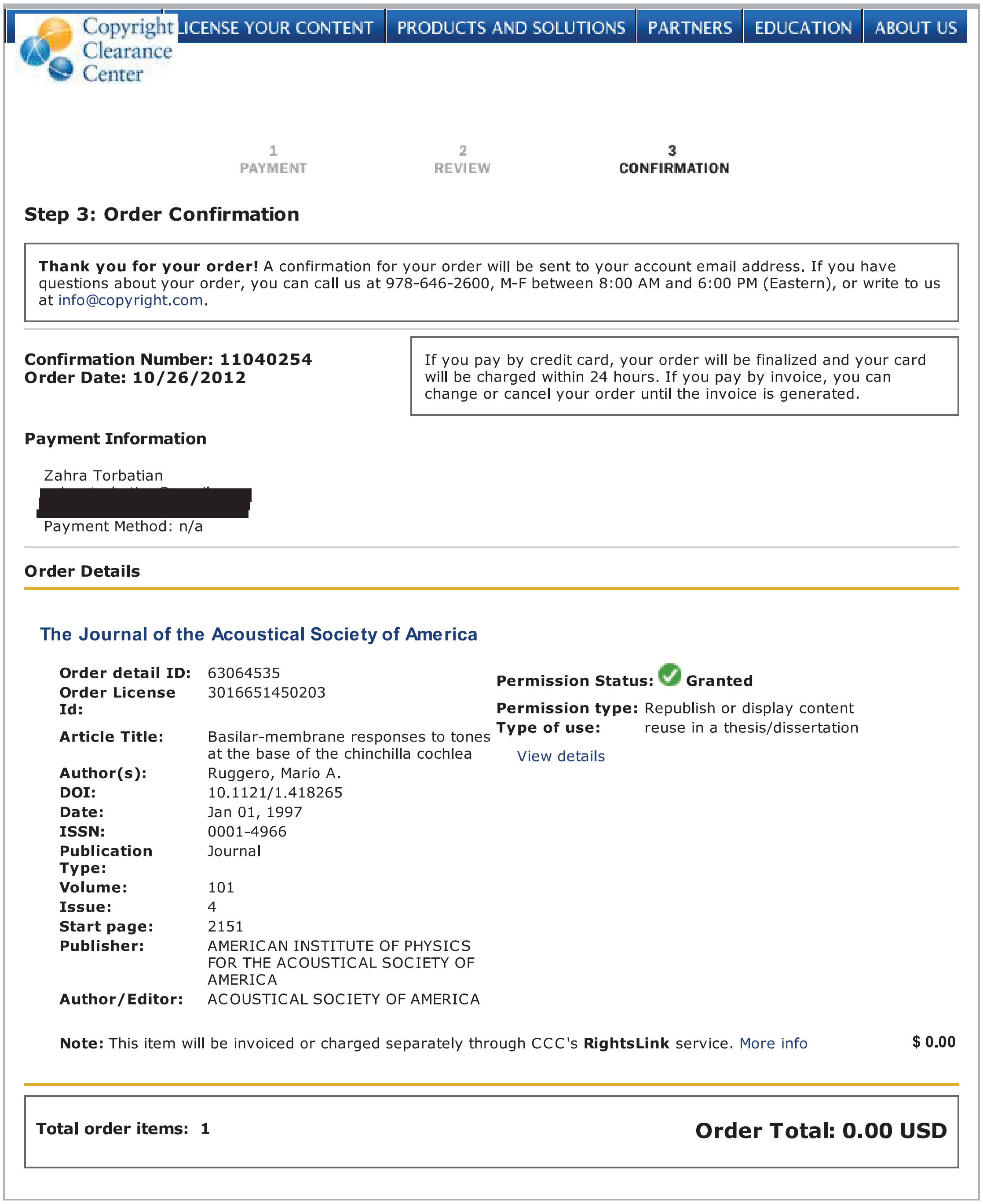

Step 3: Order Confirmation

Thank you for your order! A confirmation for your order will be sent to your account email address. If you have questions about your order, you can call us at 978-646-2600, M-F between 8:00 AM and 6:00 PM (Eastern), or write to us at info@copyright.com.

Confirmation Number: 11040254
Order Date: 10/26/2012

If you pay by credit card, your order will be finalized and your card will be charged within 24 hours. If you pay by invoice, you can change or cancel your order until the invoice is generated.

Payment Information

Zahra Torbatian
[redacted]
Payment Method: n/a

Order Details

The Journal of the Acoustical Society of America

Order detail ID: 63064535
Order License Id: 3016651450203
Article Title: Basilar-membrane responses to tones at the base of the chinchilla cochlea
Author(s): Ruggero, Mario A.
DOI: 10.1121/1.418265
Date: Jan 01, 1997
ISSN: 0001-4966
Publication Type: Journal
Volume: 101
Issue: 4
Start page: 2151
Publisher: AMERICAN INSTITUTE OF PHYSICS FOR THE ACOUSTICAL SOCIETY OF AMERICA
Author/Editor: ACOUSTICAL SOCIETY OF AMERICA

Permission Status: ✓ **Granted**
Permission type: Republish or display content
Type of use: reuse in a thesis/dissertation

View details

Note: This item will be invoiced or charged separately through CCC's **RightsLink** service. More info $ 0.00

Total order items: 1
Order Total: 0.00 USD

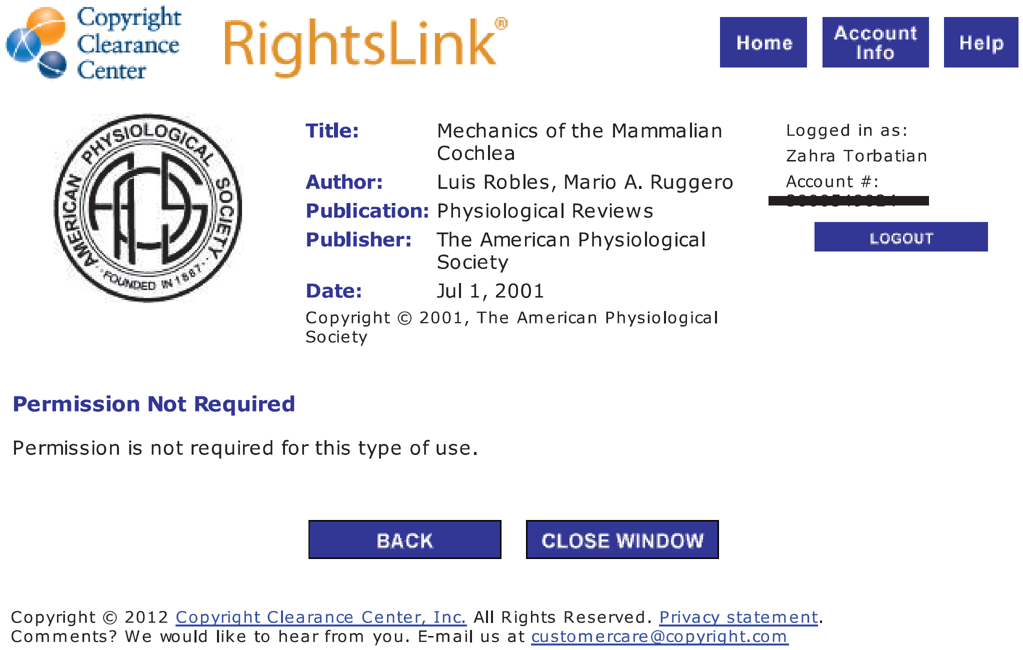

Title: Mechanics of the Mammalian Cochlea
Author: Luis Robles, Mario A. Ruggero
Publication: Physiological Reviews
Publisher: The American Physiological Society
Date: Jul 1, 2001

Copyright © 2001, The American Physiological Society

Logged in as:
Zahra Torbatian
Account #:
[redacted]

Permission Not Required

Permission is not required for this type of use.

Copyright Clearance Center RightsLink®

Home | Account Info | Help

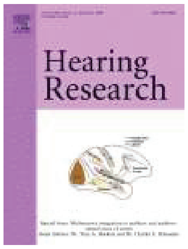

Title: Basilar membrane and osseous spiral lamina motion in human cadavers with air and bone conduction stimuli

Author: Stefan Stenfelt,Sunil Puria,Naohito Hato,Richard L. Goode

Publication: Hearing Research

Publisher: Elsevier

Date: July 2003

Logged in as:
Zahra Torbatian
Account #:
[redacted]

LOGOUT

Order Completed

Thank you very much for your order.

This is a License Agreement between Zahra Torbatian ("You") and Elsevier ("Elsevier"). The license consists of your order details, the terms and conditions provided by Elsevier, and the payment terms and conditions.

Get the printable license.

License Number	3015501445590
License date	Oct 24, 2012
Licensed content publisher	Elsevier
Licensed content publication	Hearing Research
Licensed content title	Basilar membrane and osseous spiral lamina motion in human cadavers with air and bone conduction stimuli
Licensed content author	Stefan Stenfelt,Sunil Puria,Naohito Hato,Richard L. Goode
Licensed content date	July 2003
Licensed content volume number	181
Licensed content issue number	1–2
Number of pages	13
Type of Use	reuse in a thesis/dissertation
Portion	figures/tables/illustrations
Number of figures/tables/illustrations	1
Format	both print and electronic
Are you the author of this Elsevier article?	No
Will you be translating?	No
Order reference number	
Title of your thesis/dissertation	High-frequency Ultrasound Imaging of the Auditory System
Expected completion date	Oct 2012
Estimated size (number of pages)	200
Elsevier VAT number	GB 494 6272 12
Permissions price	0.00 USD
VAT/Local Sales Tax	0.0 USD / 0.0 GBP
Total	0.00 USD

Title:	Round window membrane motion with air conduction and bone conduction stimulation
Author:	Stefan Stenfelt,Naohito Hato,Richard L. Goode
Publication:	Hearing Research
Publisher:	Elsevier
Date:	December 2004

Copyright © 2004, Elsevier

Logged in as:
Zahra Torbatian
Account #:
[redacted]

Order Completed

Thank you very much for your order.

This is a License Agreement between Zahra Torbatian ("You") and Elsevier ("Elsevier"). The license consists of your order details, the terms and conditions provided by Elsevier, and the payment terms and conditions.

Get the printable license.

License Number	3015510074860
License date	Oct 24, 2012
Licensed content publisher	Elsevier
Licensed content publication	Hearing Research
Licensed content title	Round window membrane motion with air conduction and bone conduction stimulation
Licensed content author	Stefan Stenfelt,Naohito Hato,Richard L. Goode
Licensed content date	December 2004
Licensed content volume number	198
Licensed content issue number	1–2
Number of pages	15
Type of Use	reuse in a thesis/dissertation
Portion	figures/tables/illustrations
Number of figures/tables/illustrations	1
Format	both print and electronic
Are you the author of this Elsevier article?	No
Will you be translating?	No
Order reference number	
Title of your thesis/dissertation	High-frequency Ultrasound Imaging of the Auditory System
Expected completion date	Oct 2012
Estimated size (number of pages)	200
Elsevier VAT number	GB 494 6272 12
Permissions price	0.00 USD
VAT/Local Sales Tax	0.0 USD / 0.0 GBP
Total	0.00 USD

Jsers/Zahra/Dropbox/phd thesis/copyright-figure/Rightslink® by Copyright Clearance Center3.htm